Background Subtraction

Definition

With background subtraction the background in an image is removed. Thus it is done when a very uniform background is needed (e. g. for ►PIV algorithms). Hereby only relatively sharp objects remain and the background is removed with morphological algorithms. A non-uniform background results from non-uniform illumination and/or image capturing.

Backpressure

► Pump Head

Band Broadening

► Hydrodynamic Dispersion

Bead Based Assays

► Bead Based Microfluidic Platforms

Bead Based Microfluidic Platforms

SUNG YANG[1], JEFFREY D. ZAHN[2]
[1] Department of Mechatronics, School of Information and Mechatronics, Gwangju Institute of Science and Technology (GIST), Gwangju, Buk-gu, Republic of Korea
[2] Department of Biomedical Engineering, The State University of New Jersey, Piscataway, NJ, USA
syang@gist.ac.kr, jdzahn@rci.rutgers.edu

Synonyms

Bead based assays; Cytometric bead immunoassay; Particle manipulation

Definition

Bead based microfluidic platforms may be used for either particle manipulation or bead based sensing especially in cytometric bead based immunoassays. Bead based microfluidic platforms are often geared to biomedical research and diagnostics particularly in protein diagnostics through immunosorbent assays. For instance, in bead based immunosorbent assays, antigen–antibody reactions are induced on the surface of the bead in the solution and then, the binding event of the antigen–antibody is monitored by fluorescent labeling of either a secondary antigen or antibody. These assays are used to detect biomolecules by utilizing specific ligand-receptor binding reactions. The ligand-receptor binding events may then be quantified by quantifying changes in bead properties using either optical or physical sensing mechanisms. In order to optimize bead based reactions, there has also been considerable interest in developing microfluidic systems for efficient bead handling and manipulation.

Overview

Recently, there have been enormous efforts to transform conventional biological analysis methods into more efficient or sensitive assays through the use of Lab-on-a-Chip platforms. One of these representative efforts is found in the increased development of bead based microfluidic platforms [1]. The majority of bead based microfluidic platforms have been developed to detect specific biomolecules in an unknown sample by utilizing a ligand-receptor binding event. Bead based platforms have several potential advantages over conventional techniques. Bead based microfluidic platforms provide a larger binding surface area to sample volume ratio and thus may yield an improvement in the detection limit of a specific biomolecule over conventional techniques by allow-

ing more available binding surface area per unit volume. This change in relative surface to volume ratio may also limit nonspecific binding and background interference due to other contaminating molecules which may also lead to improvements in detection limits of the desired analyte. In addition, bead based microfluidic platforms require less consumption of analyte sample as well as reagent volumes which may lead to less expensive assay platforms. There have been several reports which describe bead based microfluidic platforms for biomolecule detections [2–6] as well as novel methods which may be used for multiple particle manipulation and steering [7] within microfluidic environments. In the basic methodology section, the standard enzyme-linked immunosorbent assay (ELISA) is briefly introduced as a working principle for bead based microfluidic sensing platforms and the fundamentals of enzyme kinetics for ligand-receptor binding is also discussed as a theoretical background. Detailed discussions of case studies are presented in the Key Research Finding section.

Basic Methodology

ELISA (Enzyme-Linked Immunosorbent Assay)

The enzyme-linked immunosorbent assay (ELISA or EIA) is one of the most commonly utilized methods used in protein detection and analysis. An ELISA can provide quantitative information about antigen or antibody concentrations in solution by comparing the results of an unknown sample assay to a calibration curve based on known standard concentrations of the antibody or antigen of interest. Although, there are many variations in how ELISA may be performed, three of the most commonly used representative methods are discussed here (Fig. 1). The choice of which ELISA technique is used often depends on the nature of the antigen or antibody of interest, the availability of appropriate binding pairs, and the specificity of only the antigen of interest to a monoclonal antibody.

1. Indirect ELISA
   The concentration of an antibody (especially in blood plasma) can be quantitatively determined through the use of the indirect ELISA technique. In the indirect ELISA, an antigen is pre-coated within a microtiter well. Then a solution (e. g., blood plasma) containing the primary antibody of interest is added to the antigen coated microtiter well and allowed to incubate so that the two components may bind with each other. Afterwards a washing step removes any free primary antibody. Next, an enzyme-linked secondary antibody is added to produce a binding between the primary and secondary antibodies. The enzyme linked antibody often contains the catalytic protein of a horseradish peroxidase which cleaves a colorimetric substrate (such as *o*-phenylenediamine dihydrochloride) causing a color change in the substrate solution which may be monitored in a spectrophotometer by the optical density of the transmission spectra at the appropriate wavelength of light. Since the substrate produces a color change which is proportional to the amount of enzyme present through the binding reactions, the measured color change may be correlated with the concentration of the antibody of interest initially present in the solution which was analyzed. The concentration of antibody of interest can be determined by comparing the color change of the unknown sample against standards of known concentration.
2. Sandwich ELISA
   In a related technique, an antigen concentration can be determined by using a sandwich ELISA. In this technique, the antibody which binds to the antigen of interest is pre-coated in the microtiter well. Next, the sample containing the antigen of interest is added and allowed to bind with the pre-coated antibody. After the well is washed, an enzyme-linked secondary antibody specific to the antigen of interest is added and allowed to bind with the bound antigen. After washing any free secondary antibody away, the colormetric substrate for the enzyme is added. Again, by measuring the change of color in the enzyme reaction, as discussed before, the concentration of antigen can be determined by comparison with the color shifts of a predetermined standard calibration curve.
3. Competitive ELISA
   Another method to determine the concentration of an antigen is through the use of a competitive ELISA. In the competitive ELISA, a primary antibody is first incubated in a solution containing the antigen of interest. Through antibody-antigen binding the free antigen is captured by the antibody in solution. The larger the antigen concentration in the initial solution, the less free primary antibody that will be left after the antigen–antibody binding reaction. Next, the antigen–primary antibody mixture is added into an antigen pre-coated microtiter well. Now, only the free primary antibody left in the mixture will be able to bind with the antigen within the microtiter well. After a washing step, the antigen–primary antibody complex in the solution is removed and an enzyme-linked secondary antibody is added to produce a binding between the primary and secondary antibodies. As a final step, the colormetric substrate is added to the microtiter well and the amount of color change is measured and correlated to the known calibration curve. In the competitive assay, however, the concentration of the antigen of interest

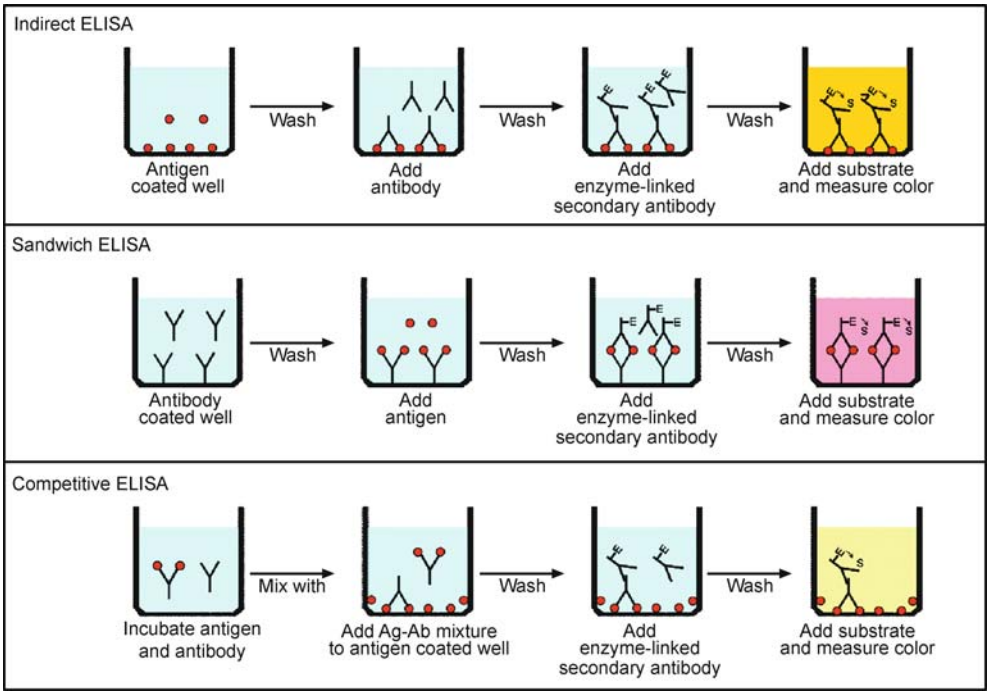

Bead Based Microfluidic Platforms, Figure 1 Variations in the ELISA technique. Each assay can be used not only for qualitative but also for quantitative determination of the presence of antigen or antibody by comparison with standard curves prepared with known concentrations of antibody or antigen. The indirect ELISA is useful to determine antibody concentrations in solution. On the other hand, the sandwich ELISA is useful in determining antigen concentrations. In the competitive ELISA, the concentration of antigen is inversely proportional to the color produced by the substrate because the competitive ELISA is an inhibition-type assay

in the original sample is inversely proportional to the amount of color change because the antigen in solution reduces the amount of free antibody which is able to bind to the antigen coated in the microtiter well.

Key Research Findings

Many research groups have pursued bead based immunosorbent assays within microfluidic platforms. Here, instead of coating antigen or antibodies within microtiter wells, they are coated onto the surface of micron sized beads which act as the reaction vessels. Sato et al. [2] demonstrated a bead based immunosorbent microfluidic platform (Fig. 2). In their system, they used polystyrene beads for the solid phase reaction in order to maximize the available surface area for antigen–antibody binding. First, the beads were introduced into the microfluidic channel, which was designed with a barrier to trap the beads at a specific location within the device and create a packed bed. Next, an antigen (human secretory immunoglobulin A (s-IgA)) was infused through the microdevice to allow nonspecific adsorption of the antigen to the packed beads. After the unbound antigen is washed away, an antibody (anti-s-IgA) which had been conjugated with colloidal gold was infused to produce the antigen–antibody binding reaction. After a final wash step to remove the unbound antibody, the amount of binding between the antigen and antibody was detected by a thermal lens microscope (TLM). The TLM uses an excitation laser and a probe laser which is focused through the objective lens. The colloidal gold absorbs some of the excitation light and the rest of the energy is dissipated in the solution as thermal energy. The temperature change is monitored by a change in the solution refractive index monitored through a thermal lens. The larger the amount of colloidal gold, the lower the temperature change in the solution and thus a smaller change in the refractive index of the solution so the initial antigen concentration may be correlated to the temperature change in the solution monitored by the thermal lens. Based on this procedure, they were able to obtain a thermal lens signal down to 1 μg/ml of antigen (s-IgA) concentration with a linear dependency of thermal lens signal on the initial antigen concentration. In addition, the time needed for the antigen–antibody binding reaction was reduced by 90 fold which resulted in a shortening of the overall analysis time to less than 1 hr compared to 24 h for the standard procedure.

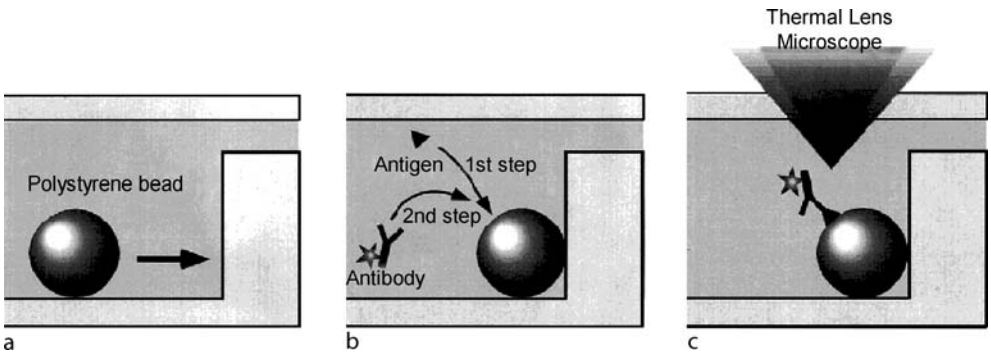

Bead Based Microfluidic Platforms, Figure 2 Schematic illustrations of integrated immunosorbent assay. (**a**) bead in (**b**) antigen and antibody binding (**c**) measurement [2]

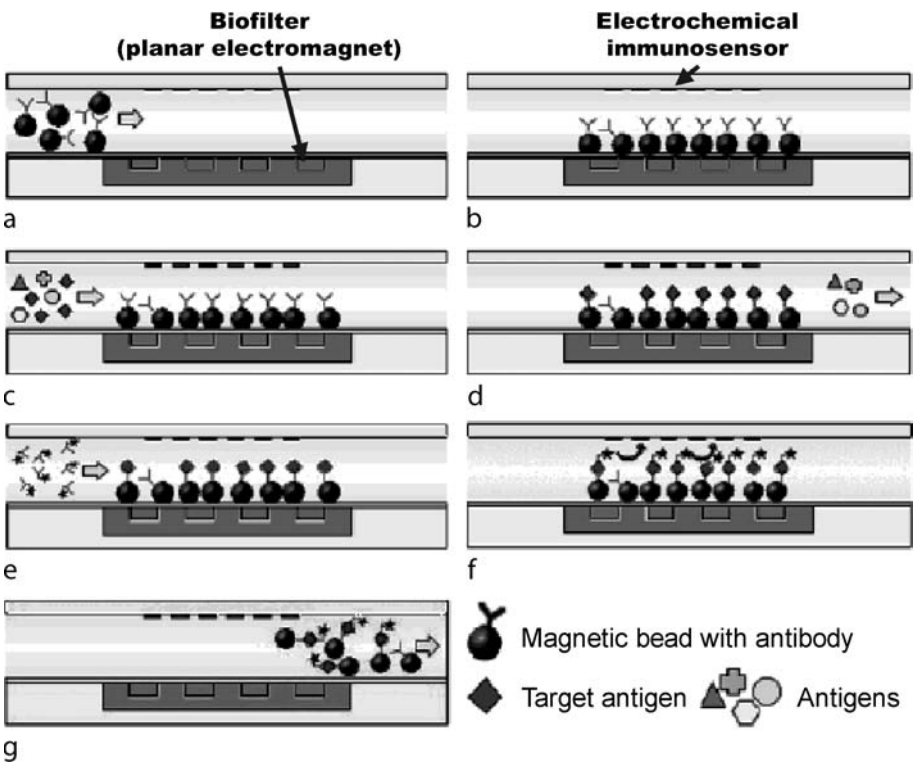

Bead Based Microfluidic Platforms, Figure 3 Conceptual illustration of bio-sampling and immunoassay procedure using magnetic bead approach: (**a**) injection of magnetic beads; (**b**) separation and holding of beads; (**c**) flowing sample; (**d**) immobilization of target antigen; (**e**) flowing labeled antibody; (**f**) electrochemical detection after adding enzyme substrate; and (**g**) washing out magnetic beads and ready for another immunoassay [3]

Next, Choi et al. [3] reported an integrated microfluidic biochemical detection system for rapid low-volume immunoassays. They utilized magnetic core beads as the solid support phase for the capture antibodies, and as carriers of captured target antigens. In order to detect target antigens, the working principle is based on a sandwich ELISA (Fig. 3). The antibody coated beads are first infused into the microfluidic channel with an integrated electromagnet. Once the magnetic beads are introduced, then they are attracted to the electromagnet and held in place. While holding the primary antibody coated magnetic beads within the magnetic field, target antigens are infused into the microfluidic channel. The antigen–antibody binding occurs while other free antigens not specific to the antibody used are washed away with the continuous flow. Next, enzyme-linked secondary antibodies are infused to produce a binding event between the bound antigen and secondary antibodies. The microfluidic channel is

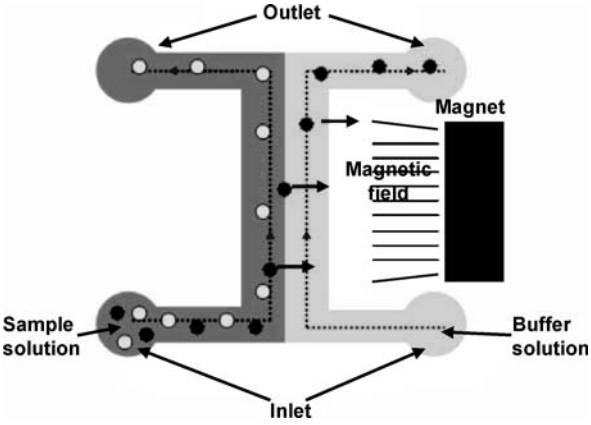

Bead Based Microfluidic Platforms, Figure 4 Proposed detection principle. Microbead conjugated with superparamagnetic nanoparticles (●). Unconjugated microbead (○) [4]

then washed to remove all unbound secondary antibodies. As a final step, a substrate solution, which reacts with the conjugated enzyme on the secondary antibody, is injected into the microfluidic channel. Electrochemistry is used as a detection method. To demonstrate this concept, they have used alkaline phosphatase (AP) and *p*-aminophenyl phosphate (PAPP) as the antibody bound enzyme and electrochemical substrate, respectively. AP converts PAPP to *p*-aminophenol (PAP). Thus, by applying an oxidizing potential to the patterned detection electrodes, PAP is converted into 4-quinoneimine (4-QI) by a 2-electron oxidation reaction. Therefore, by measuring the electrical current change by amperometry, it is possible to determine the concentration of the enzyme (AP) bound to the magnetic beads. By using mouse IgG as an analyte and applying the electrochemical detection principle, they were able to show a detection limit within their device of around 100 ng/ml of mouse IgG. Also, the total time required for an immunoassay was less than 20 min including sample incubation time, and sample volume wasted was less than 50 μl during five repeated assays.

Another good example of a bead based immunoassay is based on superparamagnetic nanoparticles (50 nm diameter) handling in microfluidic environments which was reported by Kim et al. [4]. In their report, the binding of antigen conjugated with superparamagnetic nanoparticles to antibody coated fluorescent microbeads (1 μm diameter) and the subsequent deflection of the magnetic nanoparticle bound fluorescent microbeads within a magnetic field were used as the signal for measuring the presence of analyte. To test their principle, the target analyte sample was conjugated with the superparamagnetic nanoparticles. The fluorescent microbeads were conjugated with antibodies to the analyte of interest by nonspecific adsorption. Then, the target nanoparticle conjugated analyte and the antibody coated microbeads are mixed together to produce antigen–antibody binding. Since the target analyte molecules are conjugated with the superparamagnetic nanoparticles, the fluorescent microbeads will be indirectly conjugated with the nanoparticles. The total amount of the superparamagnetic nanoparticles bound with the microbeads depends on the concentration of the target antigen. As shown in Fig. 4, a buffer and sample solution are both infused into a converging channel geometry where the sample solution contains the fluorescent microbeads with the bound superparamagnetic nanoparticles. A permanent magnet is placed on the buffer side of the microchannel geometry. Due to the presence of the magnetic field gradient, the nanoparticle bound microbead will be deflected towards the magnet and the deflection force will depend on the number of superparamagnetic nanoparticles presented on the microbeads. In this study, Kim, et al., assumed that if the concentration of the superparamagnetic nanoparticles bound to the fluorescent microbead increases, the velocity of the bead towards the magnet will increase. This implies that the bead velocity in the microchannel may be correlated back to the initial concentration of the target analyte. In addition, since the microbeads have specific optical properties, a multiplex analysis is also possible. Using this method, the magnetic force-based microfluidic immunoassay was successfully applied to detect both rabbit IgG and mouse IgG as model analytes. The detection limit of the system was determined to be 244 pg/ml and 15.6 ng/ml for rabbit IgG and mouse IgG, respectively.

Yang et al. [5] reported a novel concept in bead handling and serial reaction processing using a technique named "particle cross over" in microfluidic channels to accomplish continuous cytometric bead processing within a microfluidic device for bead based sensing platforms. The operating principle of the continuous biosensing is based on adapting the Zweifach–Fung effect [8, 9] in a novel manner. The Zweifach–Fung effect has shown that when a particle approaches a bifurcating region that all particles will flow into the daughter branch with the higher flow rate if the flow rate ratio between the two branches are greater than 2.5 : 1 when the particle diameter approaches the vessel diameter. Utilizing this mechanism involves moving cytometric beads through different regions within the microfluidic device where the bead is exposed to different solution environments so that antigen–antibody binding, washing and detection can occur without any significant sample dilution. When a micron-sized bead approaches a bifurcating region of microfluidic channel, it is possible for the bead to cross over from a carrier

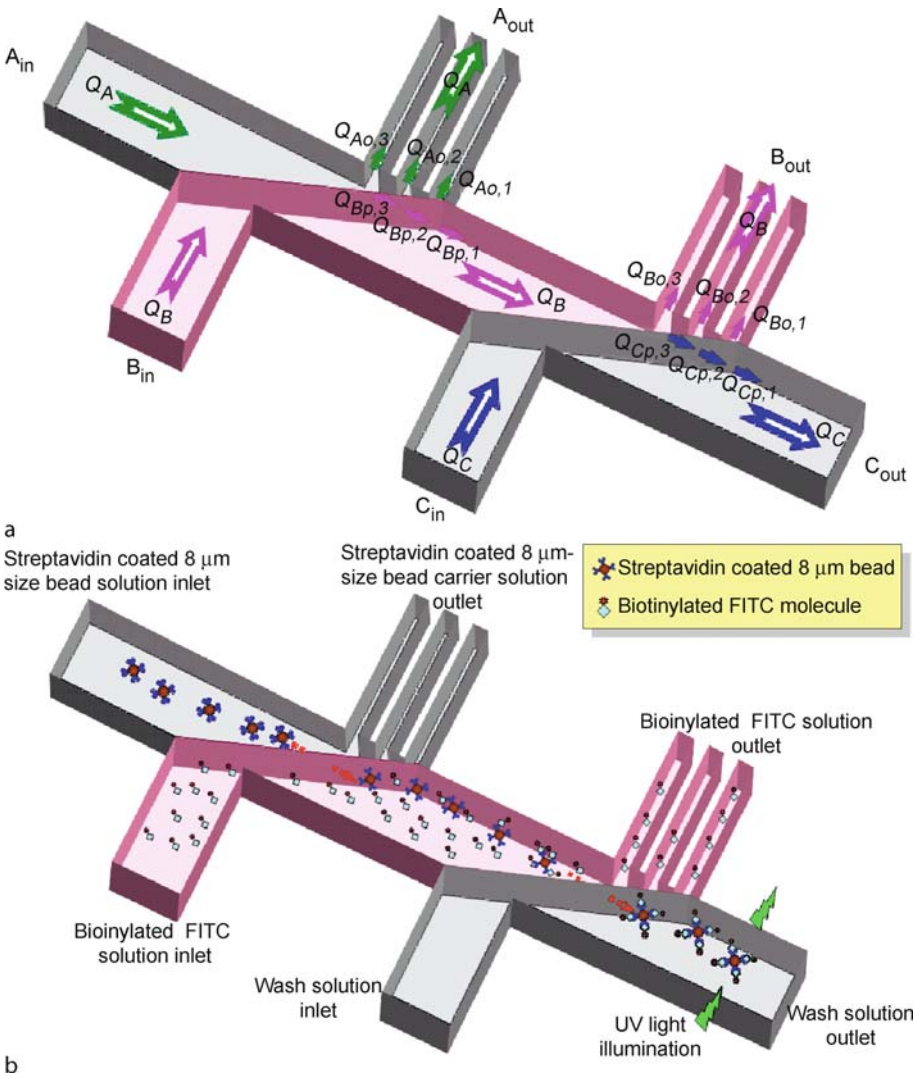

Bead Based Microfluidic Platforms, Figure 5 (**a**) Conceptual drawing of microflow structures within a microfluidic network for the particle cross over within microfluidic channels. It is possible to achieve the particle cross over from one to another fluid streams without losing particles into multiple parallel channels. (**b**) Schematic sketch of a representative example of continuous biosensing using the particle cross over mechanism. The concentration of biotinylated FITC molecules can be determined by measuring the fluorescence intensity of the biotinylated FITC bound streptavidin coated 8 μm-diameter particle at the detection window using an epifluorescence microscope [5]

fluid into a recipient fluid streams by precisely controlling flow rate ratio between the two downstream channels. For instance, as shown in Fig. 5a, a microfluidic device can be designed to have a 1 to 1 of total flow rate ratio ($Q_A = Q_B = Q_C$) at each bifurcation region. Thus, all three fluid streams which are infused from each inlet can be transported into each designated outlet ($A_{in} \rightarrow A_{out}$, $B_{in} \rightarrow B_{out}$, $C_{in} \rightarrow C_{out}$). At the same time, it is also possible to design the outlets as a series of multiple parallel channels at each bifurcation region so that a micron-sized particle infused from the inlet is not able to follow its original fluid stream of the carrier fluid into the outlet and will cross over into the recipient fluid stream (A→B) because of the Zweifach–Fung effect. In this study, a streptavidin coated 8 μm-diameter particles and biotinylated FITC dye were used as a test system for demonstrating continuous biosensing in microfluidic channels. The biotinylated FITC molecules produce fluorescence light (532 nm) under UV light exposure due to the presence of the FITC (fluorescence dye). Thus, the higher concentration of biotinylated FITC in solution, the more biotinylated FITC which is bound to a bead through biotin-streptavidin binding, the higher the fluorescence intensity which can be detected. Figure 5b represents a concep-

tual sketch of continuous biosensing based on the particle cross over mechanism. Once the streptavidin coated 8 μm-diameter beads in buffer media travel toward the 1st bifurcation region, then they can cross over into the biotinylated FITC solution without significant mixing of the two fluid streams. Once the streptavidin coated bead enters into the biotinylated FITC solution, the binding between the biotinylated FITC molecules and the streptavidin coated 8 μm-diameter beads occurs within the main channel. In addition, no significant serial dilution effect on biotinylated FITC solution is expected as would be expected by simply mixing the fluids together through a converging channel geometry and passive micromixing region because the old fluid infused from upstream of the main channel is removed at the bifurcation by maintaining a 1 to 1 total flow rate ratio between the two fluid streams. At the 2nd bifurcation, the biotinylated FITC bound streptavidin beads can then cross over to a wash solution by producing the same microflow structures. Finally, the fluorescence intensity of the biotinylated FITC bound streptavidin beads can be measured at a downstream detection window by an epifluorescence microscope. The fluorescence intensity of the beads can be assumed to be proportional to the concentration of biotinylated FITC dye in the solution. Since beads are continuously infused into the device from the bead inlet, it is expected that the bead fluorescence intensity will change in response to changes in biotinylated FITC dye concentration which can be tracked by plotting the bead fluorescence intensity as a function of time. Thus, the system can dynamically respond to changes in analyte concentration allowing continuous biosensing. Based on this concept, Yang, et al. demonstrated that the fluorescence intensity of the bead measured is linearly proportional to the analyte (biotinylated-FITC) concentration. The detection limit of the device was determined as a 50 ng/ml of biotinylated FITC concentration.

Another application area of bead based microfluidic platforms includes bead based DNA detections. Han et al. [6] reported quantum-dot-tagged microbeads for multiplexed optical coding of DNAs. Multicolor optical coding for DNA hybridization assays has been achieved by embedding different-sized quantum dots into polymeric microbeads at precisely controlled ratios. And then, as shown in Fig. 6, probe oligos were conjugated to the beads by cross linking. The target oligos were detected with Cascade Blue. After hybridization, nonspecifically bonded molecules and excess reagents were removed by a washing process. For multiplexed assays, they have optimized the oligo lengths and sequences so that all probes had similar melting temperatures ($T_m = 66\,°C - 99\,°C$) and hybridization kinetics (30 min). As a result, they have shown that the coding and target signals can be simultaneously read at the single-bead level with high uniformity and reproducibility. Also, they have shown that bead identification accuracies were as high as 99.99 % under favorable conditions.

A final example of bead based microfluidic platforms is a novel concept in particle handling and steering. Armani et al. [7] recently reported very attractive results on steering multiple particles simultaneously within microfluidic environments. They combined electrokinetic based microfluidic platforms with vision-based feedback control to independently steer multiple particles with micrometer accuracy in two spatial dimensions. In their method, they have steered particles by creating an electroosmotic flow field that carries all the particles from where the particles are to where particles should be at the next time step. The flow is created by the biasing of multiple electrodes arranged around the active test area. In order to steer each particle independently, they constructed a vision-based feedback loop comprised of sensing, computation, and actuation to steer particles along user-input trajectories. Particle locations were identified in real-time by an optical system and transferred to a control algorithm that then determined each electrode voltage necessary to create the proper electroosmotic flow pattern to carry all the particles to their next desired locations. They have experimentally demonstrated that it is possible to steer not only neutral particles but also charged particles simultaneously by precisely controlling electroosmotic flow patterns. The neutral particles can be carried by the electroosmotic flow by controlling voltage applied on each electrode. The charged particles can be also steered by both electroosmotic and electrophoretic forces by controlling voltage applied on each electrode. For instance, as shown in Fig. 7, they were able to steer three yeast cells (5 μm diameter), which have a small surface charge (electrophoretic mobility $c = -23.3 \pm 6.9 \times 10^{-9}\ m^2V^{-1}s^{-1}$) within an accuracy of less than 1 μm by controlling the potentials of eight electrodes. Since this type of particle steering permits noninvasive steering of any visible particle regardless of the charge status of particles, it is expected that this technique is useful for navigating beads and particles to localized sensors for cell sorting, sample preparation, and for combinatory testing of particle interactions with other particles, chemical species, and distributed sensors.

Future Directions for Research

Although a variety of technologies related to bead based microfluidic platforms are introduced here, there are still many challenges to producing efficient Lab-on-a-Chip bead based sensor technologies over the conven-

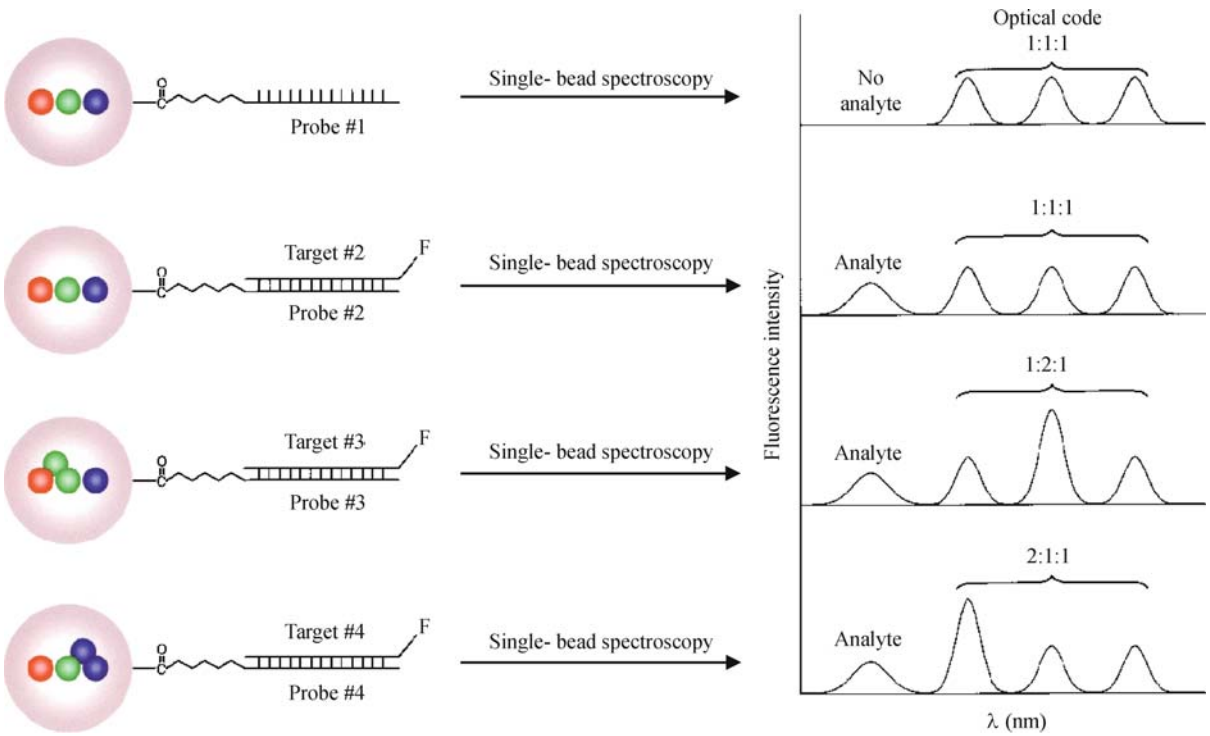

Bead Based Microfluidic Platforms, Figure 6 Schematic illustration of DNA hybridization assays using QD-tagged beads [6]

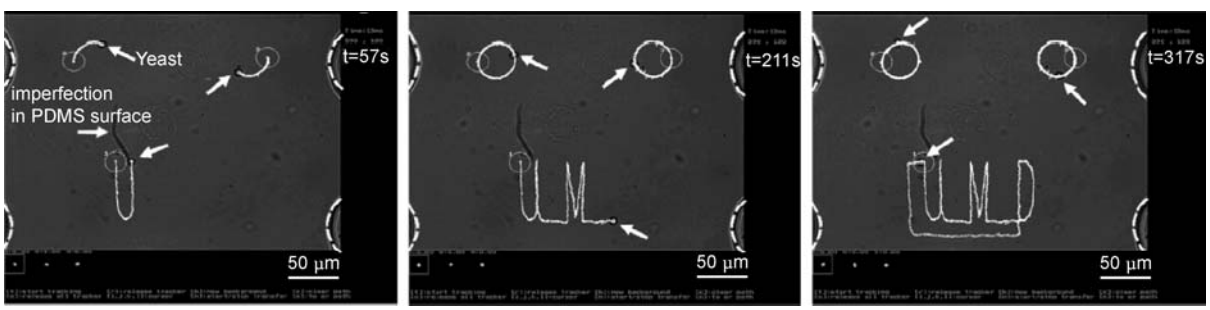

Bead Based Microfluidic Platforms, Figure 7 Steering of three yeast cells (5 μm diameter, Red Star, Giant Food) with small surface charge (electrophoretic mobility, $c = -23.3 \pm 6.9 \times 10^{-9}\ m^2V^{-1}s^{-1}$) around two circles and a *UMD* path. The yeast cells are visible as small black dots with a white center (the three target cells are marked with a white arrow in each image), and the white curves are the trajectories that the target cells have traced out. The three beads are being steered to within an accuracy of one pixel (corresponding to less than 1 μm) [7]

tional sensing methods. For instance, although many bead based microfluidic immunosensing technologies have been demonstrated with faster throughput over conventional methods, these microdevices often still have higher concentration detection limits and higher variability when compared with the conventional macroscale methods. Thus, most laboratories still utilize standard ELISA protocols or more recently cytometric bead based flow cytometry assays. This implies that there still needs to be substantial improvement and standardization in the future development of these bead based platforms for truly realizing the promise of Lab-on-a-Chip bead based microfluidic sensing and handling platforms which can outperform the standard macroscale technologies.

Cross References

- ► Biosensors Using Magnetics
- ► Cell Sorting
- ► Lab-on-Chip Devices for Immunoassay
- ► Lab-on-Chip Devices for Particle and Cell Separation
- ► Sample Purification Using Magnetic Particles

References

1. Verpoorte E (2003) Beads and Chips: new recipes for analysis. Lab Chip 3:60N–68N
2. Sato K, Tokeshi M, Odake T, Kimura H, Ooi T, Nakao M, Kitamori T (2000) Integration of an Immunosorbent Assay System: Analysis of Secretory Human Immunoglobulin A on Polystyrene Beads in a Microchip. Anal Chem 72:1144–1147
3. Choi J-W, Oh KW, Thomas JH, Heineman WR, Halsall HB, Nevin JH, Helmicki AJ, Henderson HT, Ahn CH (2002) An integrated microfluidic biochemical detection system for protein analysis with magnetic bead-based sampling capabilities. Lab Chip 2:27–30
4. Kim KS, Park J-K (2005) Magnetic force-based multiplexed immunoassay using superparamagnetic nanoparticles in microfluidic channel. Lab Chip 5:657–664
5. Yang S, Ündar A, Zahn JD (2007) Continuous cytometric bead processing within a microfluidic device for bead based sensing platforms. Lab Chip 7(5):588–595
6. Han M, Gao X, Su JZ, Nie S (2001) Quantum-dot-tagged microbeads for multiplexed optical coding of biomolecules. Nature Biotechnol 19:631–635
7. Armani MD, Chaudhary SV, Probst R, Shapiro B (2006) Using Feedback Control of Microflows to Independently Steer Multiple Particles. J MEMS 15(4):945–956
8. Yen RT, Fung YC (1978) Effects of Velocity Distribution on Red Cell Distribution in Capillary Blood Vessel. Am J Physiol 235(2):H251–H257
9. Fung YC (1973) Stochastic Flow in Capillary Blood Vessels. Microvasc Res 5:34–48

Behavioral Model

Definition

The behavioral models are a set of equations derived directly from the underlying domain-physics. They are the most generic and effective forms describing the response of the system.

Bias Voltage

Definition

The application of a steady voltage to a system to improve its performance.

Cross References

► Sputtering for Film Deposition

Bifurcating Microchannel

► Flow Bifurcation in Microchannel

Bimorph

B

Definition

A structure composed of two active layers and one or more passive layers. Typically the active layers work through either thermal expansion, hygrothermal expansion, or piezoelectric expansion via an externally-applied electrical field. Bimorphs are used in the latter case to amplify the low maximum strain possible in piezoelectric materials while reducing the output force.

Cross References

► Unimorph
► Piezoelectric Valves

Biocatalytic Fuel Cell

► Biofuel Cell

Biochip

Synonyms

DNA array; Protein array; Cell array

Definition

►Microarray

Cross References

► Cell Culture (2D and 3D) on Chip
► Cell Patterning on Chip
► DNA Micro-arrays
► Droplet Dispensing
► Droplet Evaporation
► Evanescent-Wave Sensing
► Fluorescence Measurements
► Fluorescent Labeling
► Hydrophilic/Hydrophobic Patterning
► Lab-on-Chip Devices for Protein Analysis
► Methods for Surface Modification
► Microarray
► Supersonic Micro-Nozzles
► Proteomics in Microfluidic Devices
► Surface Tension, Capillarity and Contact Angle
► Van der Waals Interaction Forces

Biochip Printing

► Bioprinting on Chip

Bioengineering

► Biomimetics

Biofuel Cell

Synonyms

Biocatalytic fuel cell; Enzymatic fuel cell; Microbial fuel cell

Definition

Conceptually similar to a battery, a fuel cell is an electrochemical device that converts chemical energy stored in a fuel and an oxidant into electrical energy. The fundamental difference between a fuel cell and a battery is that fuel and oxidant are supplied from outside the reaction chamber and waste products are removed. Fuel cells that utilize biological catalysts are collectively termed biofuel cells. There is a common misinterpretation that biofuel cells are named as such because they use biological fuels, which is ambiguous as the same fuel (e.g., methanol) may originate from both biological and non-biological sources. A biofuel cell mimics electrochemical processes occurring in nature to harvest a useful electrical current, without the use of precious electrocatalysts such as platinum. There are two main categories of biofuel cells: microbial biofuel cells and enzymatic biofuel cells. Microbial biofuel cells utilize entire living cells or microorganisms combined with redox intermediates to catalyze the oxidation of a fuel. Enzymatic biofuel cells, on the other hand, catalyze the chemical reactions using biological redox enzymes that can be isolated and purified from suitable organisms, thus extracting the core part of the cell that enables catalytic activity.

Cross References

► Microfluidic Fuel Cells
► MEMS-Based Biosensor

Biognosis

► Biomimetics

Bioimmobilization

Definition

Bioimmobilization is the process of immobilizing biomolecules onto sensor surface to provide the biospecificity to the biosensor. Biospecificty is the property of the biorecognition membrane of the biotransducer that is conferred by the purposeful use of a bioactive receptor. The major purpose of bioimmobilization is to confer the molecular recognition and specificity inherent to the bioactive receptor to the biotransducer in a manner that maximizes the sensitivity of the physicochemical transducer that lies beneath. Amongst the various bioimmobilization approaches are:

- adsorption (physical, chemical and electrostatic),
- adsorption followed by covalent cross-linking,
- covalent tethering, and
- entrapment (physical or covalent) within host matrices (e. g. polymers, polymeric hydrogels and sol-gels).

Regardless of the specific linking chemistry and substrate employed, the key goals in all biomolecule immobilization strategies are:

- reproducible, high density coverage of the biomolecule on the substrate,
- the orientation of the biomolecule for efficient kinetics of the biological reaction,
- minimal background and non-specific adsorption to the support or substrate,
- improved sensitivity, and
- long term stability (retained bioactivity) of the immobilized biomolecule.

Cross References

► Impedimetric Biosensors for Micro and Nano Fluidics

Bio-Inspired Design

► Biomimetics

Biological Sensors

► Impedimetric Biosensors for Nano- and Microfluidics

Biomedical Microdevices

► Integrated Microdevices for Medical Diagnostics

Bio-MicroElectroMechanical Systems (BioMEMS)

► Droplet Based Lab-on-Chip Devices

Biomicrofluidics

► Electrokinetic Transport with Biochemical Reactions

Biomimesis

► Biomimetics

Biomimetics

DUSTIN HOUSE , DONGQING LI
Department of Mechanical Engineering,
Vanderbilt University, Nashville, TN, USA
dustin.l.house@vanderbilt.edu

Synonyms

Biomimicry; Bionics; Biognosis; Biotechnology; Bioengineering; Biophysics; Bio-inspired design; Biomimesis

Definition

Biomimetics is the study of how to apply the methods and principles found in nature to modern science and engineering.

Overview

Biomimetics has become a more modern approach in various fields of engineering design. Advocates of the field believe optimized solutions for ecological systems resulting from thousands of years of natural evolution can provide today's engineers with limitless applicable technologies. Julian Vincent, a well-established researcher and the director of the Centre for Biomimetics and Natural Technologies proclaims that there is only a 10% overlap between biology and technology in terms of the mechanisms used [1]. This vast technological potential has resulted in many innovative creations throughout history.

Possibly the most well-known application of biomimetics was by a Swiss inventor, George de Mestral, who observed the efficient manner in which cockleburs adhered themselves to clothing and fur and designed a material capable of mimicking the plant's trait, ultimately leading to the patent of VELCRO® [2]. Another familiar application can been seen in the parallel field of bionics which focuses heavily on the anatomy and physiology of humans and animals in the design of robotic components to obtain stable fluid-like motions while reducing energy expenditure [3, 4]. In the area of computer science, many forms of imitating nature to optimize engineering systems are utilized. Genetic algorithms utilize evolutionary theories formulated by Charles Darwin that force a program to iterate toward optimal solutions. Often used concurrently with genetic algorithms are artificial neural networks. Modeled after biological neural networks, this form of software design can adapt to closely model relationships between inputs and outputs of a system. On a smaller scale, biomimetics is used in the area of nanostructured materials as Wendell et al. observe cellular processes and apply novel phenomena to synthetic polymer membrane systems [5]. In the field of BioMEMS, the physiological process of hemostasis is being recreated chemically in a microfluidic system to design self-repairing devices [6]. Another area that is having significant influences on microfluidics is electrowetting-based actuation. The idea of optimizing the wetting properties of a surface to control a fluid is utilized by the lotus plant to self-clean itself as water droplets roll off the leaves [7].

Cross References

► Self-Assembly Fabrication

References

1. Hooper R (2004) Ideas Stolen Right From Nature. Wired Nov 9. http://www.wired.com/science/discoveries/news/2004/11/65642. Accessed 27 Nov 2007
2. Vincent F, Bogatyreva O, Bogatyrev N, Bowyer A, Pahl A (2006) Biomimetics: its practice and theory. J R Soc Interface 3:471–482
3. Clark J, Cham J, Bailey S, Froehlich E, Nahata P, Full R, Cutkosky M (2001) Biomimetic Design and Fabrication of a Hexapedal Running Robot. Proc IEEE Int Conf Robot Automat 4:3643–3649
4. Menciassi A, Accoto D, Gorini S, Dario P (2006) Development of a biomimetic miniature robotic crawler. Auton Robot 21:155–163
5. Wendell D, Patti J, Montemagno C (2006) Using Biological Inspiration to Engineer Functional Nanostructured Materials. Small 2(11):1324–1329
6. Runyon M, Johnson-Kerner B, Ismagilov R (2004) Minimal functional model of Hemostasis in a Biomimetic Microfluidic System. Angew Chem Int Ed 43:1531–1536
7. Cho S, Moon H, Kim C (2003) Creating, Transporting, Cutting, and Merging Liquid Droplets by Electrowetting-Based Actuation for Digital Microfluidic Circuits. J MEMS 12(1):70–80

Biomimicry

► Biomimetics

Biomolecular Adsorption in Microfluidics

JEONG-YEOL YOON[1], ROBIN L. GARRELL[2]
[1] Department of Agricultural & Biosystems Engineering, The University of Arizona, Tucson, AZ, USA
[2] Department of Chemistry & Biochemistry, University of California, Los Angeles, CA, USA
jyyoon@email.arizona.edu

Synonyms

Protein adsorption; Cell adhesion; Lab on a Chip

Definition

Biomolecular adsorption in microfluidics usually refers to the *nonspecific* adsorption of biomolecules (amino acids, peptides, DNA, RNA, proteins, and cells) onto the surfaces of microfluidic devices. In this sense, this is often referred as *biofouling in microfluidics*. This causes many problems including reduced device sensitivity, poorer detection limits and selectivity, and diminished device lifetime. Among the above adsorbing species, proteins (including protective proteins of cells) cause the biggest problems resulting from irreversible adsorption and subsequent denaturation.

Overview

The microfluidic device is probably the most popular lab-on-a-chip, and major breakthroughs have been made for its development over the last five years. Microfluidic devices have been demonstrated for many chemical and biological assays [1]. In the early 1990s, several problems in microfluidic actuation were identified. One problem was water stiction: the adhesion of water to microchannel walls made of hydrophilic materials such as glass, which perturbs the desired flow and prevents the channels from being rinsed for reuse [2]. This problem can be solved by passivating the channel walls, typically through modifications that alter the wettability of the surface [2]. Another serious problem is that biomolecules tend to adsorb from solution onto many of the materials commonly used for microfluidic devices [3]. The adsorbing species may include amino acids, peptides, proteins, DNA, RNA, and cells. Among these species, proteins cause the biggest problems, because they often denature and become very difficult to remove [3].

This entry reviews the physicochemical properties of microfluidic devices, mechanisms of biomolecular adsorption and denaturation at microfluidic device interfaces, and methods to minimize or to prevent biomolecular adsorption. The trade-offs between methods to reduce water stiction will also be discussed.

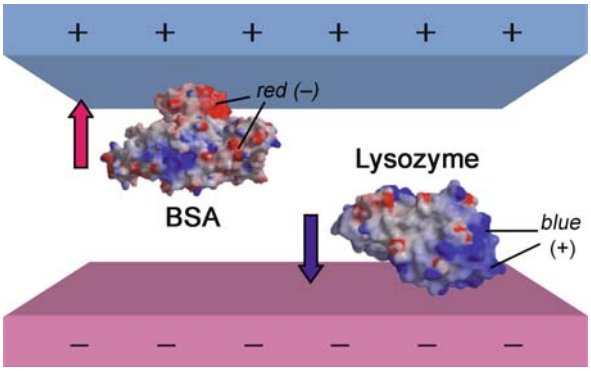

Biomolecular Adsorption in Microfluidics, Figure 1 At pH 7.2, bovine serum albumin (BSA) has negative net charge and is electrostatically attracted to the positively charged top surface. At that pH, lysozyme has positive net charge and is attracted to the negatively charged bottom surface

Basic Methodology

The interactions between protein molecules and solid surfaces can be classified into: hydrophobic interactions, electrostatic interactions, hydrogen bonding (a special type of electrostatic interactions), and van der Waals interactions [4].

Van der Waals and Electrostatic Interactions

Van der Waals interactions are a combination of several types of very weak, short-range interactions: dipole–dipole, induced dipole–induced dipole (London dispersion forces), dipole–induced dipole, and the Born repulsion. Van der Waals interactions are weak compared with electrostatic interactions, and are difficult to control through the choice of experimental conditions [4]. Hydrogen bonds, a special type of dipole–dipole interaction, are stronger and play important roles in protein folding, solvation, and adsorption. Electrostatic interactions arise from Coulombic attraction or repulsion between charged groups. Portions of protein surfaces are positively charged from terminal or side chain ammonium groups (colored blue in Fig. 1), while other portions are negatively charged from terminal or side chain carboxyl groups (colored red in Fig. 1) [4]. Depending on the pH, the net charge on a protein molecule can be positive or negative, or neutral at the isoelectric point (pI). Charged protein molecules adsorb on surfaces having the opposite charge, as illustrated in Fig. 1 [3].

Hydrophobic Interactions

In general, nonpolar substances such as hydrocarbon oils and polyethylene are considered hydrophobic. The hydrophobic effect refers to the phenomena that such species are more soluble in nonpolar solvents than in water. The effect is at least partly due to the tendency of water to form a hydrogen-bonded network structure that excludes nonpolar or non-hydrogen-bonding moieties. An attempt to transfer nonpolar moieties into the hydrogen-bonded water structure results in a decrease in entropy ($\Delta S < 0$) and almost no change in enthalpy ($\Delta H \approx 0$ at room temperature), thus leading to an increase in Gibbs free energy ($\Delta G > 0$), corresponding to a nonspontaneous process. The hydrophobic effect is especially important in biological systems. When a protein folds, the interior consists predominantly of hydrophobic domains, while the exterior is more hydrophilic.

In water, nonpolar and non-hydrogen-bonding moieties associate through hydrophobic interactions. Hydrophobic interactions can cause protein molecules to aggregate (even to the point of precipitating out of solution), and also play a major role in protein adsorption from water onto hydrophobic surfaces. At room temperature, protein molecules in solution diffuse by Brownian motion. When they come in contact with hydrophobic surfaces, they tend to remain there, adsorbing, unfolding, and eventually denaturing. Protein aggregation in solution and protein-surface hydrophobic interactions are maximized at the isoelectric point of a protein (pI), while electrostatic interactions with water are minimized at that pH [4].

Surface Wettability of Materials Used for Microfluidic Device Surfaces

Whether a surface is hydrophilic or hydrophobic, surface wettability can be assessed by measuring the contact angle, θ, of a sessile water droplet on a smooth surface. The contact angle is a consequence of the surface tensions (γ) at the liquid–vapor (LV), solid–vapor (SV), and solid–liquid (SL) interfaces, as shown by the Young equation,

$$\gamma_{SL} = \gamma_{SV} - \gamma_{LV} \cos\theta \,. \tag{1}$$

Figure 2 illustrates how static, advancing, and receding contact angles are defined. A larger contact angle indicates the surface is more hydrophobic than a reference surface.

Table 1 summarizes contact angles for water on various materials that are frequently used in direct contact with liquids for microfluidic devices. The values shown in this table are not definitive, as surface treatments such as plasma etching can dramatically change the contact angle. The advancing contact angle $\theta_{advancing}$, obtained by tilting

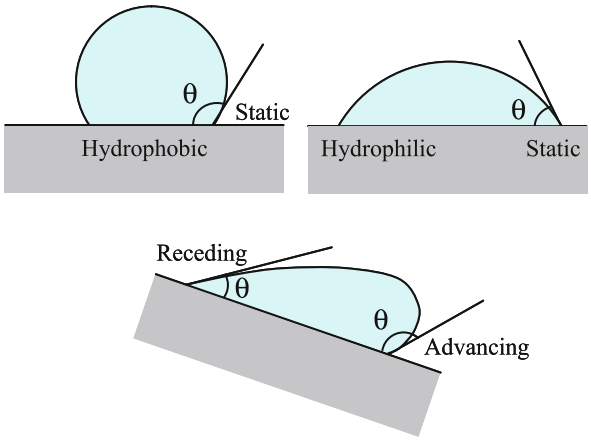

Biomolecular Adsorption in Microfluidics, Figure 2 Static, advancing, and receding contact angle as measures of surface wettability

the surface, by adding more liquid to a droplet, or by using the Wilhelmy plate method, is generally larger than the static contact angle θ_{static}; the difference depends on the surface homogeneity and roughness (Fig. 2). In general, on etching or roughening a surface, the contact angle θ typically increases, but it may decrease.

Glass, silicon dioxide (SiO_2), and poly(ethylene glycol) (PEG) are hydrophilic. Their static water contact angles are $\leqslant 30°$ as shown in Table 1. Many clean metal surfaces, including gold, show contact angles close to 0° [5]. Ordinarily, metal surfaces are contaminated, resulting in higher contact angles ($\sim 60°$ for gold) [6]. Polystyrene (PS), alkane-terminated self-assembled monolayers (SAMs), polydimethylsiloxane (PDMS), and Teflon are hydrophobic, with static water contact angles $\geqslant 90°$. All the other materials shown in Table 1, including ordinary gold, protein films, polyesters such as poly(methyl methacrylate) (PMMA), and polycarbonate (PC), can be considered as intermediate between hydrophilic and hydrophobic.

Nonspecific Protein Adsorption on the Surfaces of Microfluidic Devices

Proteins such as antibodies and enzymes can be deliberately anchored on microfluidic device surfaces by covalent bonds or molecular recognition in order to fabricate array biosensors. Nonspecific adsorption is the (usually) undesirable adsorption of molecules on the surface, and it ends up with loss of analyte. In nonspecific adsorption, the molecule–surface interactions are initially weaker, so the adsorption process is both slower and more difficult to control. Subsequent denaturation leads to stronger adhesion [7], as well as to changes in the surface hydrophilicity and roughness [8]. It is important to understand the mech-

Biomolecular Adsorption in Microfluidics, Table 1 Advancing and static water contact angles on common materials used for microfluidic device surfaces [18–43]

Materials	θ_{static} (deg)	$\theta_{advancing}$ (deg)
Glass (clean)	0	0
Glass (ordinary)	14–51	60
Gold (clean)		0
Gold (ordinary)	61–65	
Si wafer	22	
SiO_2		27
Poly(ethylene glycol) (PEG)	18	39–46
Albumin film	64–70	
Lysozyme film	58	
Polycarbonate (PC)	70	86
Poly(methyl methacrylate) (PMMA)	70–74	
Polystyrene (PS)	87–91	97
Alkanethiolate or alkylsilane self-assembled monolayers (SAMs)	108–115	110–116
Polydimethylsiloxane (PDMS)	108–113	118
Fluorohydrocarbon	115	
Teflon	112–118	

anisms of nonspecific protein adsorption in order to minimize the problems it can create.

Analyzing Protein Adsorption

Although protein adsorption from aqueous solutions onto various types of surfaces has been studied for several decades, no models accurately describe the process in detail [4]. Protein adsorption is typically analyzed by measuring a series of surface coverage data (Γ, usually in $mg \cdot m^{-2}$) against either the equilibrium protein concentration (C_{eq}, usually in $mg \cdot mL^{-1}$) or the time elapsed (t). Γ can be evaluated by measuring the amount of protein remaining in solution in contact with a particulate surface in a series of test tubes or in a stirred cell. Alternatively, the amount of protein adsorbed to an ordinary (nonparticulate) surface can be measured directly by total internal reflection fluorescence (TIRF), surface plasmon resonance (SPR), ellipsometry, optical waveguide lightmode spectroscopy (OWLS), or a thickness shear mode (TSM) resonator.

A plot of Γ vs. C_{eq} is an adsorption isotherm. Data for protein adsorption are frequently modeled by the Langmuir equation, although the validity of using this equation for

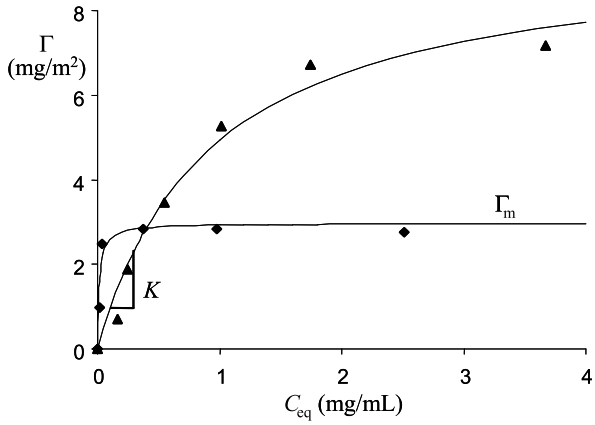

Biomolecular Adsorption in Microfluidics, Figure 3 A typical Langmuir-type adsorption isotherm, for bovine hemoglobin adsorbing from 10 mM phosphate buffer (pH 6.8) onto sulfonated polystyrene microparticles: ♦ = 0.14 sulfonate groups nm^{-2}, ▲ = 2.1 sulfonate groups nm^{-2}

protein adsorption remains an open question:

$$\Gamma = \Gamma_m \frac{KC_{eq}}{1 + KC_{eq}}. \quad (2)$$

This isotherm is characterized by the linear rise at low concentrations (slope = K, the equilibrium constant for adsorption) and the subsequent plateau (Γ_m = the saturated surface coverage of protein), as shown in Fig. 3. K is associated with the ratio of the adsorption to desorption rates, and is related to the work of adhesion: the energy required to desorb the protein from the surface. A larger K indicates slower desorption than adsorption, leading to irreversible adsorption.

To get some control over protein adsorption, one has to understand the protein-surface interactions in advance. To this end, adsorption isotherms have been obtained for a wide variety of surfaces, from hydrophilic to hydrophobic. Techniques for controlling the surface wettability include varying the terminating groups of SAMs or the ratio of monomers in copolymers. The effects on protein adsorption of factors such as liquid polarity, temperature, pH, solute type (e. g. electrolyte), and solute concentration have been widely studied [4].

Several adsorption isotherm studies [9] have shown that K, associated with the ratio of the adsorption to desorption rate, is larger for hydrophobic surfaces than for hydrophilic surfaces, indicating proteins adsorbs irreversibly to hydrophobic surfaces. This irreversibility is closely associated with the extent of structural changes of proteins adsorbed on surfaces, which will be discussed in the following section.

Structural Changes of Protein Molecules at Water–Solid Interfaces

Once a protein molecule makes contact with a hydrophobic surface, conformational fluctuations at the outside of protein molecule cause hydrophobic residues to be exposed, some of which adhere to the surface, ultimately leading to unfolding and/or flattening [4]. This conformational change is a spontaneous process ($\Delta G < 0$), driven in part by entropy gain ($\Delta S > 0$). This unfolding has been shown through circular dichroism (CD) experiments to involve a decrease in α-helix and increase in β-sheet and unordered conformations [7]. This denaturation is, for the most part, responsible for the irreversibility of adsorption through hydrophobic interactions. Protein adsorption leads to the formation of a bumpy layer, or even to the formation of irregular aggregates of protein molecules adsorbed on the surface. For example, Locascio et al. have identified large, irregular aggregates of protein molecules adsorbed on the microchannel surface in a capillary electrophoresis system [8].

Association and dissociation of protein molecules on hydrophobic surfaces may also take place. Small proteins comprised of a single polypeptide chain, such as lysozyme, associate to form dimers upon adsorption on hydrophobic surfaces, especially near the pI of 11. Proteins that have a quaternary structure, such as hemoglobin, can dissociate into subunits upon contacting a hydrophobic surface, as the subunits are held together by hydrophobic interactions.

However, such structural changes have also been found for hydrophilic surfaces, when the surface is fully covered with proteins [7] and when the proteins are in contact with the surface for a long period of time (more than several hours) [3], indicating the participation of other interactions towards structural changes.

Key Research Findings

Small Solute, DNA, and Cell Adhesion to Microfluidic Device Surfaces

DNA is a negatively charged polyelectrolyte, and so sticks to positively charged surfaces, but not hydrophobic surfaces. Ions and water-soluble polymers also do not stick to hydrophobic surfaces.

The adhesion of cells to surfaces is different from that of proteins and DNA. Cell adhesion and spreading are believed to depend primarily on the hydrophobicity of both cells and surfaces. Cell surface hydrophobicity is usually associated with the presence of fibrillar structures on cell surfaces and specific cell wall proteins. Adhesion, spreading, and growth of mammalian cells are generally promoted on hydrophilic surfaces ($\theta_{static} \approx 30 - 40°$) [10], while those of bacterial cells are generally promoted on hydrophobic surfaces [11]. The latter can be distinguished from mammalian cells by the existence of fibrils and a large number of cell wall proteins. Other factors that affect cell adhesion include surface topography [10] and the presence of certain proteins (especially albumin and fibrinogen) that may interact with cell wall proteins.

Surface Materials Used in Microfluidic Applications

To prevent biomolecular adsorption and water stiction, the surface materials for a microfluidic device should be carefully chosen with consideration of the actuation method (hydrodynamic or electrokinetic) and analytes to be manipulated (small solutes, DNA, proteins, and/or cells). Tables 2 and 3 summarize the surface materials that have been used in microfluidic applications.

Minimizing Biomolecular Adsorption with Hydrodynamic Actuation

Hydrodynamic actuation methods include pressurizing a microchannel with a syringe pump or from a nitrogen tank (pumping), applying different pressures for inlets and outlets of microchannels (ΔP), centrifuging the microchannel tubes, and utilizing gravity or osmosis. In the absence of externally applied electrical potentials, hydrophobic interactions become dominant over electrostatic interactions, unless the surface is highly polarized. Since charged analytes (ion, dye, water-soluble polymer, and DNA) and mammalian cells do not have hydrophobic interactions, all types of surfaces, including hydrophilic (glass, SiO_2, and PEG), intermediate (PC and PMMA), and hydrophobic surfaces (PDMS), can be used for hydrodynamic actuation of these species, as shown in Table 2. Among these surfaces, PDMS can prevent water stiction that leads to fluctuation in the flow rate in microchannels. However, PDMS is not the optimal choice for the solutions of proteins or bacterial cells, because they adsorb on PDMS surfaces through hydrophobic interactions. PDMS also has some swelling issues, especially with nonpolar solvents.

Minimizing Biomolecular Adsorption with Electrokinetic Actuation: Electroosmotic Flow

The most common method of electrokinetic actuation is capillary electrophoresis (CE), in which electrophoresis of analytes and electroosmotic flow (EOF) of bulk fluid usually occur at the same time. Figure 4 illustrates the working principle of CE. The surface of fused silica capillaries is negatively charged at the pH values commonly used

Biomolecular Adsorption in Microfluidics, Table 2 Surface materials used for hydrodynamic actuation

Actuation method	Analyte	Surface materials	References
ΔP / pumping	Dye	PDMS	Anal. Chem. 75, 967–972
	Water-soluble polymer	SiO_2	Sens. Actuators B 82, 111–116
		Glass	Anal. Chem. 74, 3972–3976
	DNA	PEG	Anal. Chem. 74, 3372–3377
		Glass	Anal. Chem. 74, 3972–3976
		PC	Anal. Biochem. 311, 40–49
		PDMS	Talanta 55, 909–918
	Protein	PEG	Electrophoresis 23, 799–804
		PDMS	Anal. Chem. 73, 165–169 Anal. Chem. 74, 5243–5250 Anal. Chem. 74, 379–385 Anal. Chim. Acta 468, 143–152
	Mammalian cell	PDMS	Anal. Chem. 74, 3991–4001
Centrifugation / gravity	Ion	PMMA	Anal. Chem. 73, 3940–3946
	Protein	PDMS	Sens. Actuators B 72, 129–133 Anal. Chem. 73, 5207–5213
Self-filling / capillary osmosis	Protein	PEG	Langmuir 17, 4090–4095
		PDMS	Science 276, 779–781

Note. References taken from the period 2000–2003.

in CE. A diffuse double layer of cations is attracted to the stationary negative changes on the wall. EOF occurs when an electric field is applied, which causes the outer layer of cations to migrate towards the cathode, dragging along the bulk buffer solution. In many cases, the electroosmotic force is stronger than the electrophoretic force, which causes all analytes to migrate toward the cathode, regardless of their charge. Under these conditions, as shown in Fig. 4, analyte molecules are separated according to their charge.

Because the surfaces of microchannel walls have to be ionized for EOF, they may have electrostatic interactions with charged analytes. That is, charged protein molecule could adsorb through Coulombic interactions. Because EOF scales with the charge density on the channel walls, biomolecular adsorption originating from electrostatic interactions also depends on the rate of EOF [12]; whether the surface is originally hydrophilic or hydrophobic is less important. This explains why many materials ranging from glass (hydrophilic) to PDMS (hydrophobic) can be used for chip-based CE systems, as shown in Table 3.

CE-based methods that do not utilize electrophoresis include capillary electrochromatography (CEC) or micellar electrokinetic chromatography (MEKC). In CEC, EOF acts as a pump to move analytes past a stationary phase; analytes partition into the stationary phase with different affinities, enabling separation. Other CE-based methods that do not utilize EOF include capillary isoelectric focusing (CIEF) or capillary gel electrophoresis (CGE). CIEF works on the same basic principle as IEF. The capillary is treated with polyacrylamide or methylcellulose, so there is no EOF, ensuring that the relative movement of proteins depends solely on differences in their pI values. There are no electrostatic interactions between charged analytes and the microchannel surface, so hydrophobic interactions are

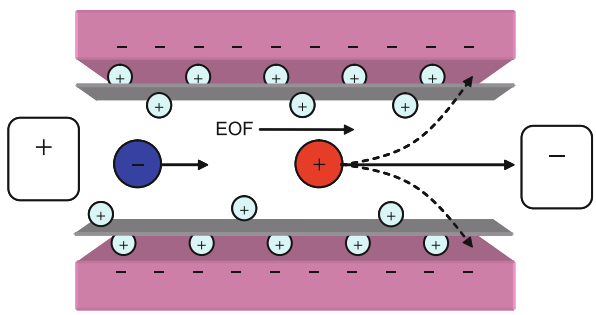

Biomolecular Adsorption in Microfluidics, Figure 4 Capillary electrophoresis (CE). Cations on a microchannel wall are pulled toward the anode, generating electroosmotic flow (EOF); positively and negatively charged analytes are separated by their differences in their electrophoretic mobilities. Depending on the rate of EOF, analytes may be attracted to a microchannel wall through electrostatic attraction, shown as dashed arrows

Biomolecular Adsorption in Microfluidics, Table 3 Surface materials used for electrokinetic actuation

Actuation method	Analytes	Surface materials	References
CE (electrophoresis and EOF)	Dye	PC	Anal. Chem. 74, 2556–2564
	Ion	PMMA	Anal. Chem. 74, 2407–2415 Anal. Chem. 74, 1968–1971
	Amino acids and sugar	Glass	Sens. Actuators B 81, 369–376
		PC	Anal. Chem. 74, 2556–2564
		PDMS	Electrophoresis 23, 3558–3566 Analyst 127, 1021–1023 Electrophoresis 23, 2347–2354 Electroanalysis 14, 1251–1255
	DNA	SiO_2	Fresenius J. Anal. Chem. 371, 112–119
		PEG	Anal. Biochem. 311, 40–49
		PC	Anal. Chem. 74, 2556–2564 Electrophoresis 21, 165–170 Electrophoresis 23, 2477–2484 Electrophoresis 22, 3939–3948
		PMMA	Electrophoresis 21, 165–170 Electrophoresis 22, 3939–3948 Sens. Actuators B 75, 142–148 Microsyst. Technol. 7, 265–268 Lab Chip 2, 88–95 Anal. Chim. Acta 470, 87–99
		SAM	Anal. Chem. 74, 1436–1441
	Protein	Protein film	Anal. Chem. 73, 4181–4189
		PC	Anal. Chem. 74, 2556–2564
		PMMA	Electrophoresis 22, 3972–3977
		PDMS	Anal. Chem. 73, 4491–4498 Anal. Chem. 74, 1772–1778 Electrophoresis 23, 740–749
CIEF (electrophoresis only)	Protein	Gold	Anal. Chem. 73, 1627–1633 Anal. Chem. 73, 658–666 Electrophoresis 23, 3638–3645
		PMMA	Electrophoresis 23, 3638–3645
CEC or other EOF-based microfluidics (EOF only)	Dye	PC	Anal. Chem. 74, 45–51
		PDMS	Sens. Actuators A 102, 223–233
	Protein	Glass	Anal. Chem. 73, 3400–3409
		PMMA	J. Chromatogr. A 857, 275–284
		PS	J. Chromatogr. A 857, 275–284
		PDMS	Sens. Actuators A 102, 223–233 Anal. Chem. 73, 5645–5650
Electrowetting	Ion	Teflon	Appl. Phys. Lett. 77, 1725–1726
	Protein	Teflon	Lab Chip 2, 19-23

Note. References taken from the period 2000–2003.

the dominant factor for separation. Materials commonly used for CIEF include polyacrylamide, cellulose, gold, and PMMA, as shown in Table 3. These materials are either hydrophilic or intermediate, and are capable of minimizing protein adsorption through hydrophobic interactions.

Surfaces of intermediate hydrophobicity, such as PC, PMMA, and protein film, are most commonly used for CE-based microfluidic chips, as they minimize water stiction as well as protein adsorption through hydrophobic interactions to some extent. The popularity of PDMS is

attributable to its ease of fabrication. However, PDMS has several problems for electrokinetic actuation. One is that CE in a PDMS channel supports lower EOF than glass or quartz because there is little negative charge on the surface. A more serious problem is that PDMS is gas permeable, allowing water vapor formed by Joule heating to permeate into the bulk material, changing the buffer concentration and the EOF rate. Salts may precipitate in PDMS channels, and affected devices have to be discarded. Another significant problem is that proteins adsorb to hydrophobic PDMS through hydrophobic interactions, leading to unstable EOF, peak tailing, and loss of sample [13].

To summarize, there is no definitive surface to be used for all types of analytes. Surfaces should be carefully chosen or modified, depending on the type of analyte and the method of actuation.

Modifying Surfaces to Prevent Biomolecular Adsorption and Water Stiction

Several microfabrication processes limit the choice of materials, and sometimes one is forced to use hydrophobic materials such as PS and PDMS. These hydrophobic surfaces can be made more hydrophilic by copolymerizing with hydrophilic monomers or coating with PEG or poly(ethylene oxide) (PEO) films [14]. The common feature of these hydrophilic modifications is the absence of functional groups that can act as hydrogen bond donors. Coating with protein films that resist certain biomolecules has also been demonstrated [15].

Water stiction on hydrophilic materials such as glass or silicon wafers can also be prevented. The surfaces can be passivated by depositing thin hydrophobic layers such as hydrocarbon/perfluorocarbon SAMs or Teflon. The nonstick nature of Teflon coatings found in many household products refers to the prevention of water stiction; the coatings do not prevent protein adsorption. Micropatterning these passivated hydrophobic layers can also be utilized to achieve microfluidic actuation of water. Zhao et al. [2] and Kataoka and Troian [16], for example, have patterned the hydrophobic surface to have a gradient from hydrophobic to hydrophilic, or alternating surfaces of hydrophobic and hydrophilic structures, to let the liquid flow over these surfaces. This *surface-directed* flow has thus far been demonstrated only for pure water. There are potential problems with protein solutions since proteins adsorb preferentially on rough rather than smooth surfaces.

Preventing Protein Adsorption in Electrowetting-Based Actuation

In several types of microfluidic actuation, hydrophobic surfaces have been used to control the rate of EOF or to manipulate droplets [3]. As noted earlier, however, it has not been possible to prevent protein adsorption that occurs through hydrophobic interactions. One way around this problem is to make the surface hydrophobic to prevent water stiction, while utilizing electrostatic repulsion to prevent biomolecular adsorption. We have recently demonstrated this strategy in electrowetting-based microfluidic actuation [3].

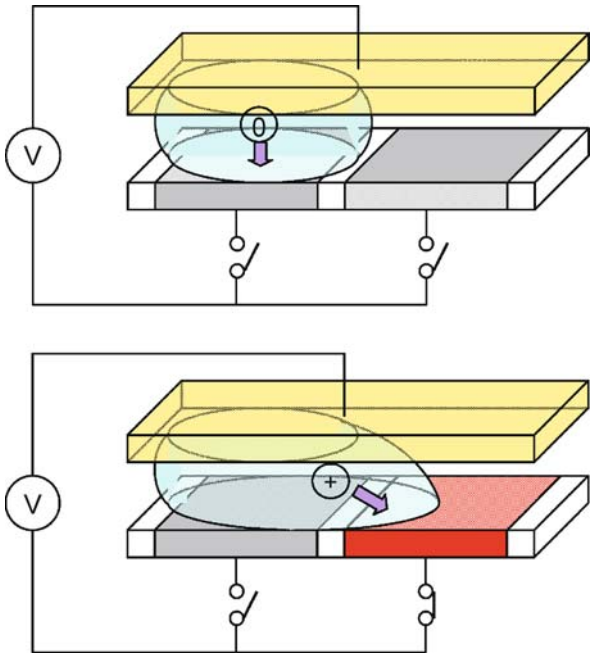

Biomolecular Adsorption in Microfluidics, Figure 5 Electrowetting-based actuation. Illustration of fluid motion induced by applying an electrical potential across dielectric-coated electrodes below a liquid droplet. By switching on the voltage at an electrode adjacent to the droplet, the surface tension is lowered, causing the droplet to move to the right. Biomolecules with neutral net charge may be attracted to electrodes while no voltage is applied. Biomolecules with positive (or negative) net charge may be attracted to electrodes while voltage is applied

Electrowetting-on-dielectric (EWOD) is a new method for moving liquids in biofluidic chips through electrical modification of the surface hydrophobicity (Fig. 5) [3]. We have demonstrated prevention of protein and DNA adsorption by minimizing hydrophobic interactions through careful choice of the bias, magnitude, and duration of the applied voltage, and by introducing electrostatic repulsions between charged proteins and the device surfaces.

Future Directions for Research

Summary of Current Approaches

The surfaces of microfluidic devices can be classified into three groups based on their surface wettability: glass, gold, Si wafer, SiO_2, and PEG as hydrophilic; PS, SAM,

PDMS, and Teflon as hydrophobic; and protein films, PMMA, and PC as intermediate. The common analytes in microfluidic devices can be classified into two groups based on their type of interactions with surfaces: small charged solutes and DNA interact primarily through electrostatic interactions, while proteins exhibit both electrostatic and hydrophobic interactions. In hydrodynamic actuation, biomolecules adsorb on surfaces largely through hydrophobic interactions. Hence small charged solute and DNA solutions are relatively easy to manipulate, as they have negligible hydrophobic interactions. For actuating protein solutions, the surface should be modified so as to be hydrophilic. In electrokinetic actuation, however, hydrophilic modification cannot be used since there are both hydrophobic and electrostatic interactions. An intermediate surface can be one possible solution, but a better way appears to be faster actuation (e. g. high EOF rate), utilizing electrostatic repulsion or changing device configuration, which have been demonstrated for electrowetting-based actuation.

Future of Biomolecular Adsorption in Microfluidics

The above summary addresses the adsorption of individual biomolecules in microfluidics. Biomolecular adsorption from real-world liquid samples such as blood will be much more complicated and probably almost impossible to prevent or control. However, we need to remember that biomolecular adsorption is not a problem unique to microfluidics; people have been working on antifouling coatings since the 1950s [17]. The future direction of this research will be related to or inspired by the research on biomaterials (e. g., prosthetic devices). Collaborations with orthopedic surgeons, dentists, and cell biologists are expected, which scientists are not really exploiting at this stage [17].

Cross References

- ► Surface Tension Driven Flow
- ► Capillary Electrophoresis (CE)
- ► Electroosmotic Flow (DC)
- ► Electrowetting

References

1. Verpoorte E, de Rooij NF (2003) Microfluidics meets MEMS. Proc. IEEE 91:930–953
2. Zhao B, Moore JS, Beebe DJ (2001) Surface-directed liquid flow inside microchannels. Science 291:1023–1026
3. Yoon JY, Garrell RL (2003) Preventing biomolecular adsorption in electrowetting-based biofluidic chips. Anal Chem 75:5097–5102
4. Kim JH, Yoon JY (2002) Protein adsorption on polymer particles. In: Hubbard A (ed) Encyclopedia of surface and colloid science. Marcel Dekker, New York
5. Adamson AW, Gast AP (1997) Physical chemistry of surfaces, 6th edn. John Wiley & Sons, New York
6. Smith T (1980) The hydrophilic nature of a clean gold surface. J Colloid Interface Sci 75:51–55
7. Horbett TA, Brash JL (1995) Proteins at interfaces II: fundamentals and applications. American Chemical Society, Washington, DC
8. Locascio LE, Hong JS, Gaitan M (2002) Liposomes as signal amplification reagents for bioassays in microfluidic channels. Electrophoresis 23:799–804
9. Yoon JY, Kim JH, Kim WS (1999) The relationship of interaction forces in the protein adsorption onto polymeric microspheres. Colloids Surf A 153:413–420
10. Ruardy TG, Schakenraad JM, van der Mei HC, Busscher HJ (1997) Preparation and characterization of chemical gradient surfaces and their application for the study of cellular interaction phenomena. Surf Sci Rep 29:3–30
11. Tsuneda S, Aikawa H, Hayashi H, Yuasa A, Hirata A (2003) Extracellular polymeric substances responsible for bacterial adhesion onto solid surface. FEMS Microbiol Lett 223:287–292
12. Locascio LE, Perso CE, Lee CS (1999) Measurement of electroosmotic flow in plastic imprinted microfluid devices and the effect of protein adsorption on flow rate. J Chromatogr A 857:275–284
13. Lee JN, Park C, Whitesides GM (2003) Solvent compatibility of poly(dimethylsiloxane)-based microfluidic devices. Anal Chem 75:6544–6554
14. Cox JD, Curry MS, Skirboll SK, Gourley PL, Sasaki DY (2002) Surface passivation of a microfluidic device to glial cell adhesion: a comparison of hydrophobic and hydrophilic SAM coatings. Biomaterials 23:929–935
15. Kingshott P, Griesser HJ (1999) Surfaces that resist bioadhesion. Curr Opin Solid State Mater Sci 4:403–412
16. Kataoka DE, Troian SM (1999) Patterning liquid flow on the microscopic scale. Nature 402:794–797
17. Mukhopadhyay R (2005) When microfluidic devices go bad. Anal Chem 77:429A–432A
18. Davies J, Nunnerley CS, Brisley AC, Edwards JC, Finlayson SD (1996) Use of dynamic contact angle profile analysis in studying the kinetics of protein removal from steel, glass, polytetrafluoroethylene, polypropylene, ethylene-propylene rubber, and silicone surfaces. J Colloid Interface Sci 182:437–443
19. Woodward RP (2000) Cleanliness measurement using contact angles. First Ten Angstroms, Portsmouth
20. Clint JH, Wicks AC (2001) Adhesion under water: surface energy considerations. Int J Adhes Adhes 21:267–273
21. Sklodowska A, Wozniak M, Matlakowska R (1999) The method of contact angle measurements and estimation of work of adhesion in bioleaching of metals. Biol Proc Online 1:114–121
22. Adamson AW, Gast AP (1997) Physical chemistry of surfaces, 6th edn. Wiley, Hoboken
23. Biederman H, Slavinska D, Boldyreva H, Lehmberg H, Takaoka G, Matsuo J, Kinpara H, Zemek J (2001) Modification of polycarbonate and polypropylene surfaces by argon ion cluster beams. J Vac Sci Technol B 19:2050–2056
24. Du YZ, Wood LL, Saavedra SS (2000) Growth behavior and structure of alkyltrichlorosilane monolayers bearing thioacetate and acetate tailgroups. Mater Sci Eng C 7:161–169

25. Klintberg L, Svedberg M, Nikolajeff F, Thornell G (2003) Fabrication of a paraffin actuator using hot embossing of polycarbonate. Sens Actuators A 103:307–316
26. van Oss CJ, Good RJ, Chaudhury MK (1988) Additive and nonadditive surface tension components and the interpretation of contact angles. Langmuir 4:884–891
27. Papra A, Bernard A, Juncker D, Larsen NB, Michel B, Delamarche E (2001) Microfluidic networks made of poly(dimethylsiloxane), Si, and Au coated with polyethylene glycol for patterning proteins onto surfaces. Langmuir 17:4090–4095
28. van der Vegt W, van der Mei HC, Busscher HJ (1994) A comparison of different approaches to calculate surface free energies of protein-coated substrata from measured contact angles of liquids. Langmuir 10:1314–1318
29. Kwok DY, Leung A, Lam CNC, Li A, Wu R, Neumann AW (1998) Low-rate dynamic contact angles on poly(methylmethacrylate) and the determination of solid surface tensions. J Colloid Interface Sci 206:44–51
30. Kwok DY, Neumann AW (1999) Contact angle measurement and contact angle interpretation. Adv Colloid Interface Sci 81:167–249
31. Aizawa H, Kurosawa S, Kobayashi K, Kashima K, Hirokawa T, Yoshimi Y, Yoshimoto M, Hirotsu T, Miyake J, Tanaka H (2000) Turning of contact angle on glass plates coated with plasma-polymerized styrene, allylamine and acrylic acid. Mater Sci Eng C 12:49–54
32. Sapsford KE, Ligler FS (2004) Real-time analysis of protein adsorption to a variety of thin films. Biosens Bioelectron 19:1045–1055
33. Clear SC, Nealey PF (1999) Chemical force microscopy study of adhesion and friction between surfaces functionalized with self-assembled monolayers and immersed in solvents. J Colloid Interface Sci 213:238–250
34. Srinivasan U, Houston MR, Howe RT, Maboudian R (1997) Self-assembled fluorocarbon films for enhanced stiction reduction. Transducers'97, pp 1399–1402
35. Abbott NL, Whitesides GM (1994) Potential-dependent wetting of aqueous solutions on self-assembled monolayers formed from 15-(ferrocenylcarbonyl)pentadecanethiol on gold. Langmuir 10:1493–1497
36. Appelhans D, Ferse D, Adler HJP, Plieth W, Fikus A, Grundke K, Schmitt FJ, Bayer T, Adolphi B (2000) Self-assembled monolayers prepared from ω-thiophene-functionalized n-alkyltrichlorosilane on silicon substrates. Colloids Surf A 161: 203–212
37. Ostuni E, Yan L, Whitesides GM (1999) The interaction of proteins and cells with self-assembled monolayers of alkanethiolates on gold and silver. Colloids Surf B 15:3–30
38. Sondag-Huethorst JAM, Fokkink LGJ (1992) Potential-dependent wetting of octadecanethiol-modified polycrystalline gold electrodes. Langmuir 8:2560–2566
39. Gillmor SD, Larson BJ, Braun JM, Mason CE, Cruz-Barba LE, Denes F, Lagally MG (2002) Low-contact-angle polydimethyl siloxane (PDMS) membranes for fabricating micro-bioarrays. IEEE-EMBS Microtechnologies in Medicine and Biology 2002, pp 51–56
40. Uilk JM, Mera AE, Fox RB, Wynne KJ (2003) Hydrosilation-cured poly(dimethylsiloxane) networks: intrinsic contact angles via dynamic contact angle analysis. Macromolecules 36:3689–3694
41. Grundke K, Werner C, Pöschel K, Jacobasch HJ (1999) Characterization of adsorbed protein layers by low-rate dynamic liquid-fluid contact angle measurements using axisymmetric drop shape analysis (part II). Colloids Surf A 156:19–31
42. Oh SJ, Jung JC, Zin WC (2001) Synthesis and surface property variations of polypropylene-graft-poly(ethylene glycol). J Colloid Interface Sci 238:43–47
43. Smith T (1980) The hydrophilic nature of a clean gold surface. J Colloid Interface Sci 75:51–55

Further Reading

Protein adsorption in general:

- Horbett TA, Brash JL (1995) Proteins at interfaces II: fundamentals and applications. American Chemical Society, Washington
- Dee KC, Puleo DA, Bizios R (2002) An introduction to tissue–biomaterial interactions. Wiley-Liss, Hoboken
- Andrade JD (1985) Surface and interfacial aspects of biomedical polymers volume 2: protein adsorption. Plenum, New York

Contact angle and hydrophobicity:

- Adamson AW, Gast AP (1997) Physical chemistry of surfaces, 6th edn. John Wiley & Sons, New York
- Shaw DJ (1992) Introduction to colloid and surface chemistry, 4th edn. Butterworth-Heinemann, Oxford

Biological and medical applications of microfluidic devices:

- Saliterman SS (2006) Fundamentals of bioMEMS and medical microdevices. Wiley Interscience and SPIE, Bellingham

Biomolecular Synthesis in Microfluids

MASAYA MIYAZAKI[1,2], HIDEAKI MAEDA[1,2,3]
[1] Nanotechnology Research Institute, National Institute of Advanced Industrial Science and Technology (AIST), Tosu, Saga, Japan
[2] Department of Molecular and Material Science, Interdisciplinary Graduate School of Engineering Sciences, Kyushu University, Kasuga, Fukuoka, Japan
[3] CREST, Japan Science and Technology Agency (JST), Kawaguchi, Saitama, Japan
m.miyazaki@aist.go.jp, maeda-h@aist.go.jp

Synonyms

Synthesis of biological molecules in microfluidics; Microfluidic reactor for biomolecular synthesis; Microreactor for synthesis of biomolecules

Definition

Biological molecules, such as proteins and peptides, oligosaccharides, nucleic acids, lipids and their related

compounds are widely used for biomaterial and pharmaceutical applications. These compounds are expensive, not so stable for long-term storage and do not require extremely large-scale synthesis. Also, the use of hazardous compounds is required in many cases. Therefore, the microreaction process is considered as a new approach which can overcome these restrictions in the synthesis of biomolecules. Several organic and biochemical syntheses have been performed using the microfluidic platform.

Overview

Biomolecules, fine chemicals and pharmaceuticals are high-value products that are produced in modest quantities. They are usually seasonal products that are customer specific and have a short shelf life. These characteristics usually place significant constraints in their production, such that it is not uncommon to see labor-intensive batch processes being used instead of the more efficient continuous process. This usually leads to a significant waste generation during the scale-up from the laboratory to production scale. In addition, the use of hazardous and often toxic homogeneous catalysts makes product purification and waste disposal important issues as regards today's stringent environmental regulations.

The microfluidic reaction system for biochemical synthesis was developed as miniaturization system of conventional synthetic chemistry. The development of microreaction processes has been much slower than that of μTAS. Lab-on-a-chip for synthetic applications is still a young research field as compared to the mature μTAS. To date, a number of gas- and liquid-phase reactions have been carried out in microfluidic systems and such microfluidic-based reactions are increasing tremendously. In this article, typical examples of biochemical syntheses within a microfluidic reactor are presented and discussed.

Peptide and Protein Synthesis

Peptide synthesis using a microfluidic reactor was reported by Watts et al. [1]. The synthesis of β-peptides has been successfully performed using a borosilicate glass microreactor (Fig. 1), in which a network of channels was produced using photolithographic and wet etching methods. The reagents were mobilized by electroosmotic flow (EOF). The microreactor was initially evaluated using a carbodiimide coupling reaction to form a dipeptide. The methodology has been extended such that the peptides may also be produced via the pentafluorophenyl ester derivatives of amino acids. It was found that performing the pentafluorophenyl ester reactions in the microreactor resulted in an increase in the reaction efficiency over the traditional batch method. Watts et al. postulated that the enhancement in the rate of reaction is an electrochemical phenomenon, due to the reaction being performed in an electric field, which is unique to microreactor systems. It has also been demonstrated that selective deprotection of the resultant dipeptides can be achieved. This approach has been used in the synthesis of a tripeptide.

Synthesis of another β-peptide was also performed. Seeberger et al. performed the synthesis of oligo β-amino acid using amino acid fluoride in a silicon microreactor [2]. They developed a method for high-efficiency synthesis that is capable of large-scale production.

Miyazaki et al. reported possible use of a microreactor as an active reaction vessel for carrying out biochemical reactions [3]. An important feature of the microchannel systems is their superior controllability of fluids, which cannot be achieved in the batchwise reactions using large reaction apparatus. The effects of a microfluidic system on chemical reactions of two different miscible solutions were examined using amino acid substitution as a model reaction. Substitution of phenylalanine in a microreaction system using separate solutions was more efficient than the batchwise reaction and microchannel reaction using a homogeneous solution. Substitution of other amino acids showed that this enhancement is caused by localization of hydrophobic amino acids at the dimethylformamide (DMF) $-$ H_2O interface. By using the rapid Michael addition reaction of the SH group of cysteine to a maleimide group, it was demonstrated that such reaction involving hydrophilic compounds diminished in a microfluidic system. These results show that the microreaction system is a novel apparatus for regulating chemical reactions, depending on the structure of the reactant molecules, by controlling the mixing of two different solutions.

In addition to these organic syntheses, biochemical production of compounds in microreactors has also been performed. A microreactor array which enables high-throughput cell-free protein synthesis was developed [4]. The microreactor array is composed of a temperature control chip and a reaction chamber chip. The temperature control chip is a glass-made chip on which temperature control devices, heaters and temperature sensors are fabricated with an indium tin oxide (ITO) resistive material. The reaction chamber chip is fabricated by micromolding of polydimethylsiloxane (PDMS), and is designed to have an array of reaction chambers and flow channels for liquid introduction. The microreactor array is assembled by placing the reaction chamber chip on the temperature control chip. The small thermal mass of the reaction chamber resulted in a short thermal time constant of 170 ms for heating and 3 s for cooling. The performance of the microreactor array was examined through experiments on cell-free protein synthesis. By measuring

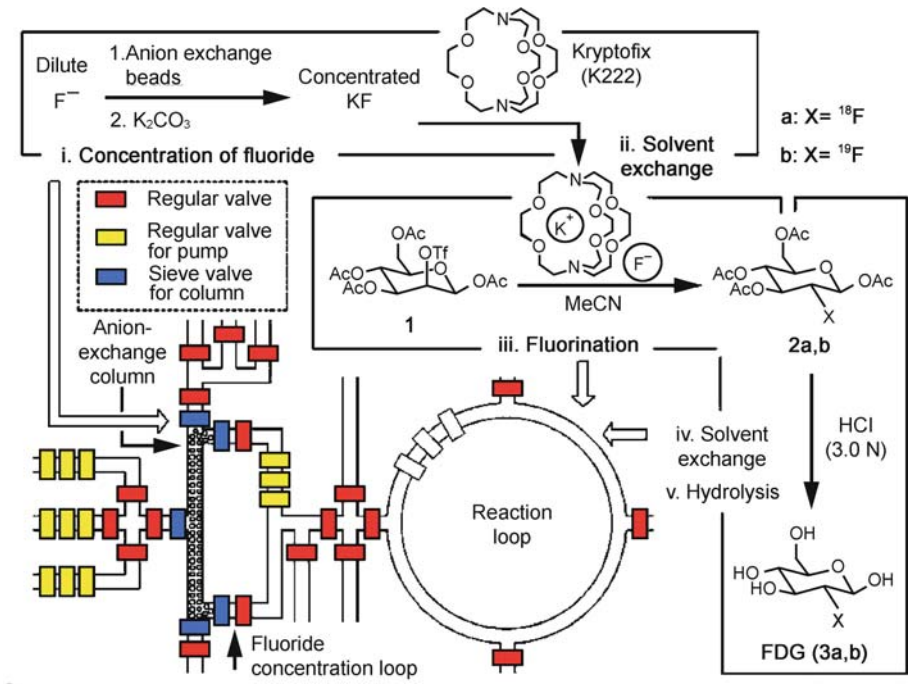

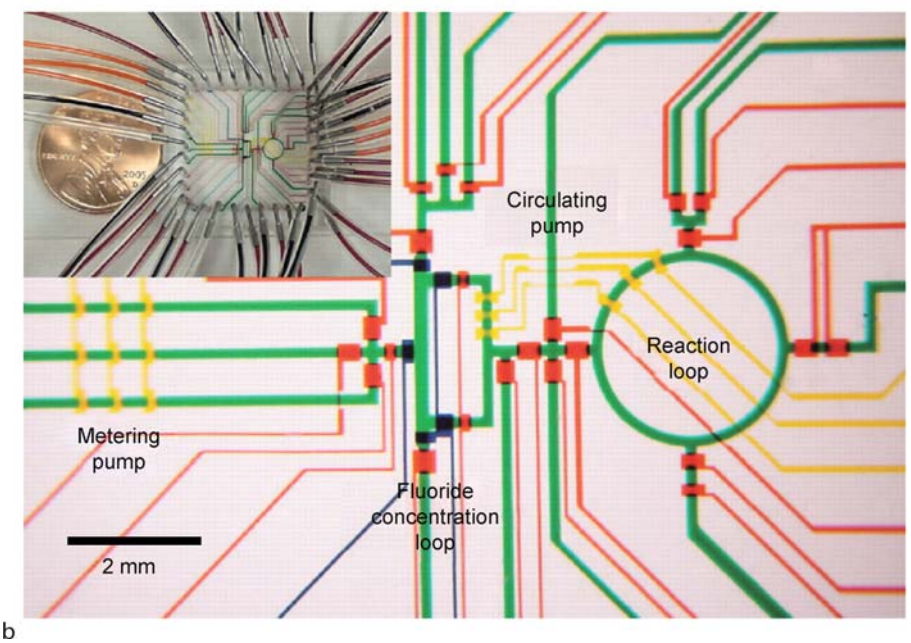

Biomolecular Synthesis in Microfluids, Figure 1 (**a**) Schematic representation of a chemical reaction circuit used in the production of 2-deoxy-2-fluoro-D-glucose (FDG). Five sequential processes are shown: (i) concentration of dilute fluoride ion with the use of a miniaturized anion exchange column located in a rectangle-shaped fluoride concentration loop, (ii) solvent exchange from water to dry MeCN, (iii) fluorination of the D-mannose triflate precursor 1, (iv) solvent exchange back to water, and (v) acidic hydrolysis of the fluorinated intermediate 2a (or 2b) in a ring-shaped reaction loop. Nanogram amounts of FDG (3a, 3b) are the final product. The operation of the circuit is controlled by pressure-driven valves, with their delegated responsibilities illustrated by their colors: red for regular valves (for isolation), yellow for pump valves (for fluidic metering circulation) and blue for sieve valves (for trapping anion exchange beads in the column module). (**b**) Optical micrograph of the central area of the circuit. The various channels have been loaded with food dyes to help visualize the different components of the microfluidic chip; colors are as in (**a**), plus green for fluidic channels. The inset shows an actual view of the device; a penny (diameter 18.9 mm) is shown for comparison. (Reproduced from [5])

the fluorescence emission from the products, it was confirmed that green fluorescent protein (GFP) and blue fluorescent protein (BFP) were successfully synthesized using *Escherichia coli* extract.

Synthesis of Sugar and Oligosaccharides

Synthesis of radiolabeled glucose has been achieved (Fig. 2) [5]. Quake et al. reported the synthesis of an [^{18}F]fluoride-radiolabeled molecular imaging probe, 2-deoxy-2-[^{18}F]fluoro-D-glucose ([^{18}F]FDG), in an integrated microfluidic device. Five sequential processes – [^{18}F]fluoride concentration, water evaporation, radiofluorination, solvent exchange and hydrolytic deprotection – proceeded with high radiochemical yield and purity and with shorter synthesis time relative to conventional automated synthesis. Multiple doses of [^{18}F]FDG for positron emission tomography imaging studies in mice were prepared. These results, which constitute a proof of principle for automated multistep syntheses at the nanogram to microgram scale, could be generalized to a range of radiolabeled substrates. Synthesis of oligosaccharides is one of the challenges in the field of synthetic organic chemistry. Generally, glycoside formation depends on the conformation, sterics and electronics of both reaction partners. The challenge in accurately predicting the reactivity of the coupling partners makes it difficult to foresee the outcome of the reaction. In addition, reaction variables such as concentration, stoichiometry, temperature, reaction time and activator play indisputable roles in the outcome of a given glycosylation. Jensen and Seeberger used continuous flow microreactors to systematically study the glycosylation reaction as an example of a challenging organic transformation (Fig. 3) [6]. A five-port silicon microreactor was designed with three primary inlets to mix and react glycosylating agent, nucleophile (acceptor) and activator (Fig. 4). Glycosylation reactions were performed rapidly over a wide range of conditions using this microreaction system. This microfluidic system enables easy handling of hazardous reagents such as trimethylsilyl trifluoromethanesulfonate at microliter scale.

In a different approach, transgalactosylation, which is the reverse reaction of the hydrolysis reaction by ►glycosidase, was carried out in organic solvent–buffer system as a reaction solvent to reduce the water concentration, and consequently the equilibrium of the reverse reaction was shifted [8]. The reaction was performed in a poly(methyl methacrylate) microreactor with two different inlets. The enzyme and reagents were loaded from these inlets by simple syringe pumping, and the reaction was terminated by heating. The reaction gave three kinds of stereoisomers, i. e. *p*-nitrophenyl-2-acetamide-2-deoxy-3-*O*-(β-D-galactopyranosyl)-β-D-glucopyranoside, *p*-nitrophenyl-2-acetamide-2-deoxy-4-*O*-(β-D-galactopyranosyl)-β-D-glucopyranoside and *p*-nitrophenyl-2-acetamide-2-deoxy-6-*O*-(β-D-galactopyranosyl)-β-D-glucopyranoside. The ratios between those isomers in the products were not determined, but the total amount of the disaccharide mixture (galactosylated *p*-nitrophenyl-2-acetamide-2-deoxy-6-*O*-(β-D-galactopyranosyl)-β-D-glucopyranoside; Gal-GlcNAcPNP) gave better yield when the reaction was conducted in the microreaction channel compared with that in the micro-test tube. This result suggests that the microreactor is an effective device for enzymatic transglycosylation.

Oligonucleotide Synthesis

The polymerase chain reaction (PCR) is the most widely used technique for oligonucleotide synthesis. Microchips/microdevices for PCR are studied extensively, and thus great progress has been made in the development and scope of microchip components of microchip-based PCR analyzers such as on-chip micromachining (fabrication, bonding and sealing), choice of substrate materials, surface chemistry and architecture of reaction vessel, handling of necessary sample fluid, control of three- or two-step temperature thermocycling, detection of amplified nucleic acid products, integration with other analytical functional units such as sample preparation, capillary electrophoresis (CE), DNA microarray hybridization, etc. The two general strategies for microchip-based PCR are flow-through and stationary chamber formats. The topic of microchip-based PCR, however, is well summarized in another article.

Chemical synthesis of oligonucleotide was also performed using a microfluidic platform. A microfluidic DNA oligonucleotide synthesizer made of PFPE which performs reaction cycles adopted from the widely used phosphoramidite method was reported [8]. PFPE is an elastomer with excellent chemical compatibility which makes it pos-

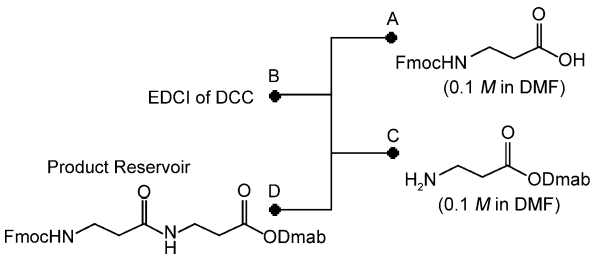

Biomolecular Synthesis in Microfluids, Figure 2 Schematic of the microreactor used in carbodiimide coupling reactions performed in [1]. (Reproduced from [1])

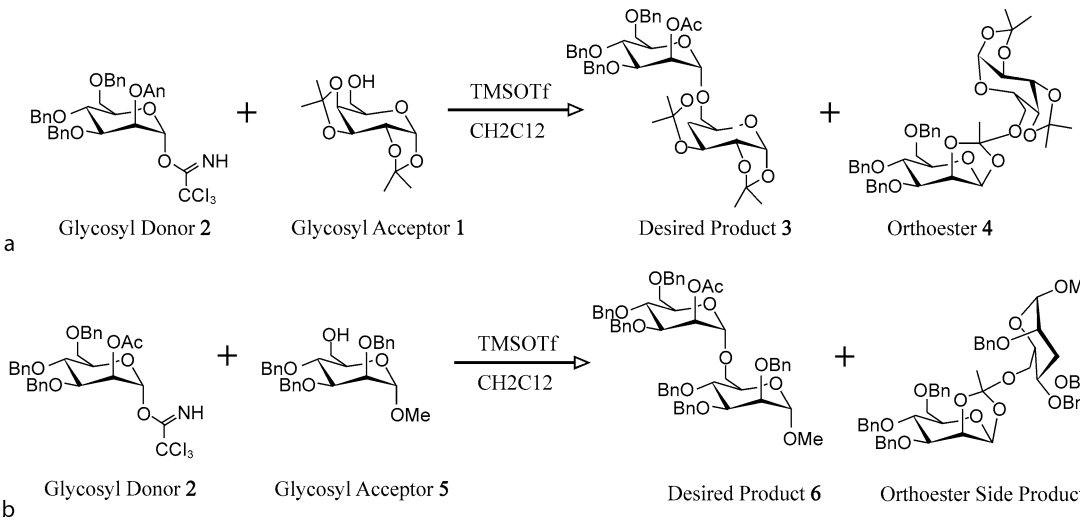

Biomolecular Synthesis in Microfluids, Figure 3 (**a**) Sample glycosylation of glycosyl donor 2 and nucleophile (acceptor) 1 to fashion disaccharide 3. Formation of orthoester 4 is also often observed. (**b**) Glycosylation reaction involving glycosylating agent 2 (mannosyl donor) and nucleophile 5 (acceptor) to fashion disaccharide 6. Formation of orthoester 7 is also often observed. (Reproduced from [6])

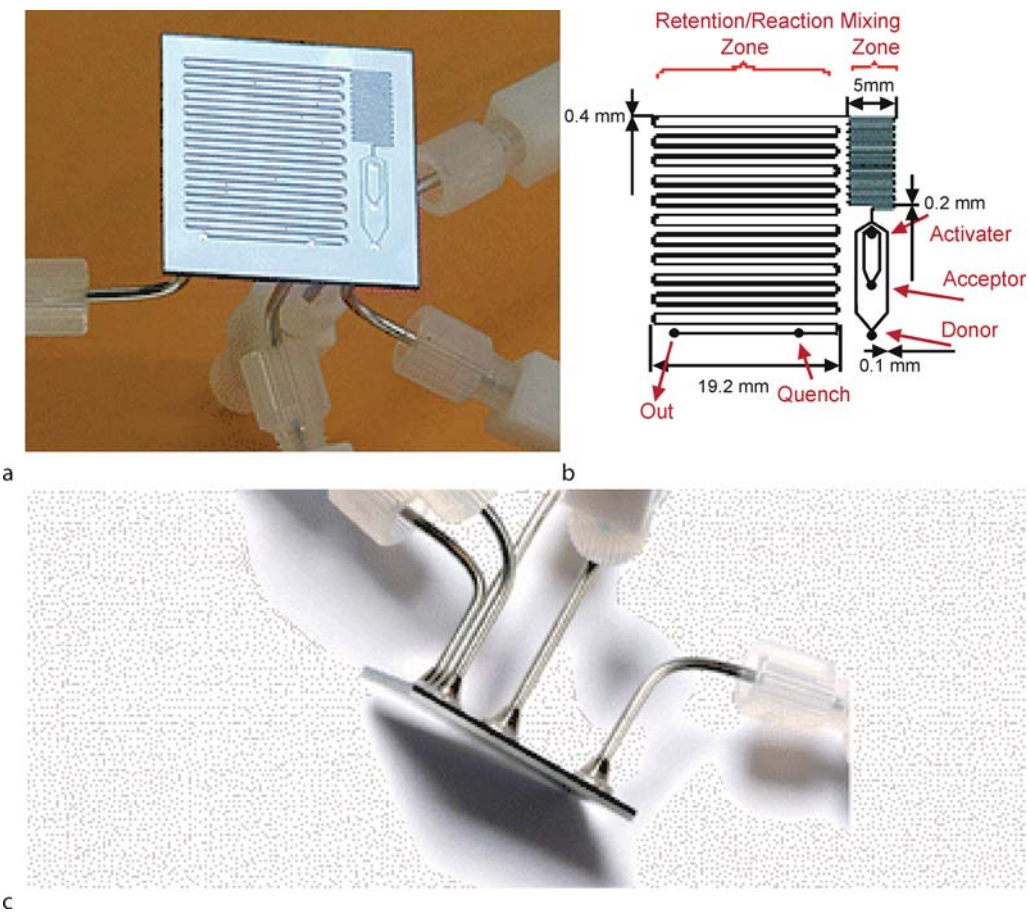

Biomolecular Synthesis in Microfluids, Figure 4 (**a**) Silicon microfluidic microreactor. (**b**) Schematic of microreactor system, comprised of three primary inlets, a mixing and reaction zone, a secondary inlet for quench and an outlet for analysis/collection. (**c**) Soldered joints of the microreactor; also perspective of the device from the side. (Reproduced from [6])

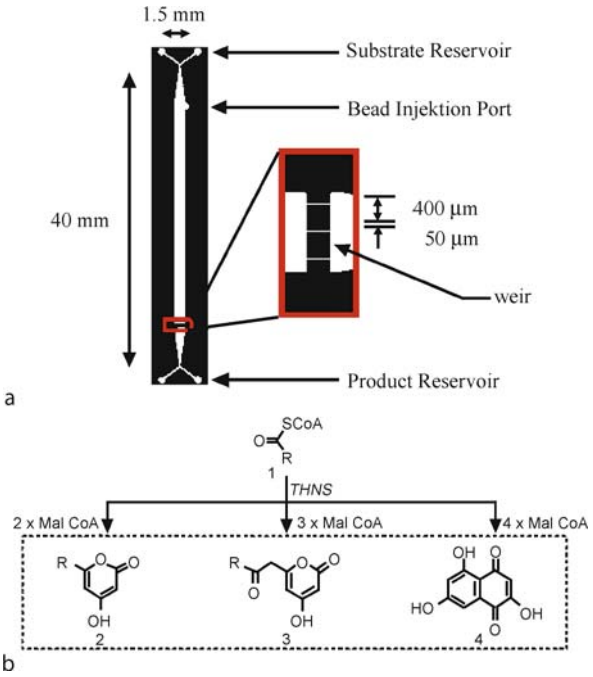

Biomolecular Synthesis in Microfluids, Figure 5 Schematic of the microreactor for polyketide synthesis. (**a**) biochip design used in this study. (**b**) Biosynthesis of flaviolin 4 and pyrone-based polyketides 2 and 3 from THNS with different starter CoA esters. (Reproduced from [11])

sible to perform organic chemical reactions. The device is capable of synthesizing 60 pmol of DNA oligonucleotides while consuming less than 500 nL of 0.1 mol L^{-1} phosphoramidite solution in each reaction cycle. The reduction of reagent consumption is significant: a 60-fold reduction over conventional automation. This approach demonstrates the usefulness of integrated micromechanical valves for complicated multistep organic synthetic reactions and enables automated chemical experiments with a wide variety of solvents.

Synthesis of Prodrugs and Other Bioactive Compounds

A microfluidic reaction system has also been used for the production of prodrugs. A multichannel membrane microreactor was fabricated and tested for ▶ Knoevenagel condensation of benzaldehyde and ethyl cyanoacetate to produce α-cyanocinnamic acid ethyl ester, a known intermediate for the production of an antihypertensive drug [9]. Knoevenagel condensations of carbonylic compounds and malonic esters yield several important key products such as nitriles used in anionic polymerization, and the α,β-unsaturated ester intermediates employed in the synthesis of several therapeutic drugs that include niphendipine and nitrendipine. Unlike most condensation reactions, Knoevenagel condensation is base-catalyzed. Strong bases such as sodium and potassium hydroxides and piperidine are traditionally used for these reactions. However, basic zeolites such as Cs-exchanged faujasite NaX and faujasite GeX, as well as amino-modified mesoporous silica are also able to catalyze these reactions. The use of heterogeneous catalysts significantly simplifies product separation and purification. It also eliminates the need for solvents. However, the water formed by the reaction is a poison for zeolite catalysts, and its removal is a must if we are to expect optimum catalyst performance. The removal of water has the added benefit of increasing the conversion for this equilibrium-limited reaction. By using Cs-exchanged faujasite NaX as the catalyst, the membrane microreactor could achieve supra-equilibrium conversion at higher product purity.

Another prodrug synthesis using a microfluidic reaction system is that of the antibiotic ciprofloacin [10]. A microreaction system developed by CPC systems (CYTOS) was used as a reaction apparatus. This system is the size of a videotape with a hold-up of 1.8 ml. The high surface-to-volume ratio for the mixing section as well as for the temperature-controlled reaction channels allow heat transfer coefficients of up to 2000 $Wm^{-2}K^{-1}$. The synthesis has demonstrated the potential for faster development, particularly in the preparation of relevant quantities for development studies, such as clinical trials, using the microreaction systems.

Enzymatic syntheses within the microfluidic platform were also reported. The construction and novel compound synthesis from a synthetic metabolic pathway consisting of a type III polyketide synthase (PKS) known as 1,3,6,8-tetrahydroxynaphthalene synthase (THNS) from *Streptomyces coelicolor* and soybean peroxidase (SBP) in a microreactor were performed (Fig. 5) [11]. THNS immobilized to Ni-NTA agarose beads was prepacked into a microfluidic channel, while SBP was covalently attached to the walls of a second microfluidic channel precoated with a reactive poly(maleic anhydride) derivative. The result was a tandem, two-step biochip that enabled synthesis of novel polyketide derivatives. The first microchannel, consisting of THNS, resulted in the conversion of malonyl-CoA to flaviolin in yields of up to 40% with a residence time of 6 min. This conversion is similar to that obtained in several-milliliter batch reactions after 2 h. Linking this microchannel to the SBP microchannel results in biflaviolin synthesis. During the course of this work, we discovered that the substrate specificity of THNS could be manipulated by simply changing the reaction pH. As a result, the starter acyl-CoA specificity can be broadened to yield a series of truncated pyrone products. When combined with variations in the ratio of acyl-CoA and

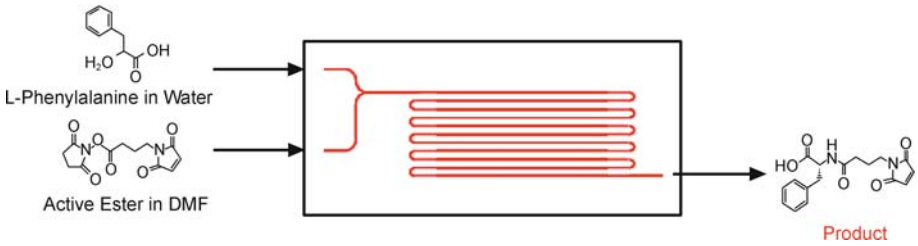

Biomolecular Synthesis in Microfluids, Figure 6 Microreactor setup used in the reaction of amino acid with active ester [3]

malonyl-CoA (extender substrate) feed rates, high yields of the pyrone products could be achieved, which is further structurally diversified from self- and cross-coupling in the SBP microchannel. The ability to rapidly evaluate the effects of reaction conditions and synthetic multienzyme pathways on a microfludic platform provides a new paradigm for performing metabolic pathway engineering, such as reconstruction of pathways for use in new compound discovery.

A monolith entrapped enzyme process was also applied to the microfluidic platform [12]. Several 10 cm long capillary tubes (made of poly(ether ether ketone) (PEEK)) with inside diameters of 0.1 – 2.0 mm were filled with silica monolith-immobilized protease derived by in situ sol–gel transition from a 1 : 4 mixture of tetramethoxysilane and methyltrimethoxysilane. ▶ Transesterification between 20 mM (*S*)-(−)-glycidol and 0.4 M vinyl *n*-butyrate in an organic solvent was used as the test reaction. The substrate solution flowed through the column at a flow rate of 0.0004 – 5.0 ml min^{-1}. The substrate conversion in the microbioreactor was higher than that in the batch reactor at high liquid flow rate. When three tubes were connected in series, the conversion at a fixed ratio of the mass of the enzyme to the liquid flow rate was increased by approximately 50% because of the tripling of the flow rate as compared to the setup with only a single tube. Changes in the tube diameter had no influence on the conversion at a fixed superficial liquid velocity. Further, the conversion increased with a decrease in the enzyme content. These results were ascribed to the apparent effect of liquid–solid mass transfer and were analyzed quantitatively using a simple mathematical model.

Basic Methodology

Basically, biomolecular synthesis reaction in a microreaction system was performed by organic synthesis or biochemical conversion. The reaction was performed by simple loading of substrate and enzyme solutions into separate inlets using syringe pumps.

Preparation of Microreaction Device

A brief overview of device fabrication was summarized to help readers, particularly the would-be microreactor users. Details can be found in other articles of this encyclopedia. From hard lithographic techniques to soft lithography and in-house-built devices, a concise description is given, and readers should refer to the appropriate articles for more details.

The foundations of microfluidic fabrication techniques lie in the well-established field of semiconductor microelectronics. For instance, the microfabrication tools of lithography, resist layers and wet and dry etching have been instrumental in the fabrication of many microfluidic systems. These methods have been used to create microfluidic systems through both direct and indirect ways. In the direct method, the microfabricated component is used directly as a channel in a device. Direct methods have the disadvantage of producing only one device for one completed fabrication. However, if the fabrication is fast, this can allow rapid prototyping of many designs. On the other hand, indirect methods use the microfabricated component as a master to transfer the design to a secondary material in a replication step. This molded material is then used as the final device. Indirect methods have the advantage of needing only one master to create many (up to hundreds) of final devices. In biomolecular synthesis, the reactions are mainly performed in organic media; therefore, silicon or glass has been widely used as the material for device preparation. These are mainly fabricated by direct method such as lithography or milling.

Performing a Microreaction

Generally, chemical syntheses using microreaction devices are performed by simple loading of reagents into the microchannel. Biomolecular synthesis depends on the molecular conformation, steric hindrance and electronics of both reaction partners. The challenge in accurately predicting the reactivity of the coupling partners makes it difficult to foresee the outcome of the reaction.

In addition, reaction variables such as concentration, stoichiometry, temperature, reaction time and activator play an indisputable role in the outcome of a given synthesis. In this article, the reaction of amino acid with active ester is shown as an example [3]. This reaction was a simple condensation reaction between amino group of amino acid and carboxyl group of active ester.

A ceramic microreaction device with a microchannel (width 400 μm × depth 400 μm × length 40 cm) was fabricated by micromachining. From two separate inlets, the solutions of active ester in DMF and amino acid with triethylamine (added for deprotonation of amino group of amino acid) in water were loaded separately by syringe pumping (Fig. 6). The resulting solution was collected and directly analyzed by HPLC to estimate the conversion rate. Each peak obtained by HPLC was confirmed by ESI-TOFMS. In the case of reaction between phenylalanine with *N*-(4-maleimidobutyloxy)succinimide (GMBS), the reaction did not proceed at higher flow rates (< 1 min, $> 50\,\mathrm{ml\,min^{-1}}$). However, the reaction yield increased at slower flow rate and even exceeded 90% in a 10 min reaction time. This result indicates that the reaction rate in the microdevice is improved dramatically over batchwise reaction which gave 80% yield after 12 h.

Key Research Findings

In the last decade, many reactions for biomolecular synthesis were performed within microfluidic reactors. The use of microreactors provides several advantages over conventional reaction systems. A microfluidic reactor allows control of mixing reagents and reaction time. This can be achieved by controlling the length of the microchannel or integrating a micromixing device. Such control of fluid enables regulation of reaction by mixing. Generally, rapid micromixing enhances the reaction yield in a microfluidic system. However, some biomolecules such as peptides are amphiphilic, and these molecules prefer the interface of organic solvent and water. In a laminar flow system, mixing of two miscible solutions occurs gradually in a straight microchannel. Construction of mixing devices enhances mixing. Also, creation of repeating tight turns produces Dean vortices and disrupts the interface. Addition of these structures in a microreaction system strongly affects the reaction yield in the synthesis of biomolecules, as in the amino acid substitution [3]. Therefore, a proper design of the microchannel structure and precise fluid control are essential for the development of efficient microreaction systems for biomolecular synthesis.

Control over thermal or concentration gradients within the microreactor allows new methods for efficient chemical transformations with high space–time yields. PCR for oligonucleotide synthesis is a typical case. Also, in most cases, chemical reaction is sensitive for factors like temperature and concentration of reactant molecules. The narrow dimension of microfluidics brings attractive mass transfer and heat flow advantages. These attributes contribute to achieving efficient chemical synthesis. Often, reactions performed within a microreactor invariably generate relatively pure products in high yield, in comparison to the equivalent bulk reactions, in much shorter times and in sufficient quantities to perform full structural characterization. These are advantageous for the optimization of reaction conditions, especially biomolecular synthesis, which is expensive in most cases. Overall, microfluidic reactors are perceived as a useful tool for the synthesis of biomolecules.

Future Directions for Research

As noted above, the great advantages of microfluidic technology have been identified as ability to achieve higher yields and selectivities, more effective use of resources and much enhanced reaction control compared with conventional systems. Most biomolecules are expensive, and therefore high reaction yield and efficiency are desired for their synthesis. To achieve this, the technology of microreaction synthesis offers a wide range of solutions. Some biomolecules and their related compounds are bioactive molecules which are important for drug development. The development of a single microreactor enables small-scale production by numbering-up; therefore, the development of synthetic microreaction processes may become a popular area of research for drug development.

In addition, a microreaction device can be constructed by an integration of various components for chemical reactions such as synthesis, analysis, extraction, separation and concentration. This possibility opens access to elegant combined reactor arrangements. The development of integrated microreaction devices is an emerging field in biomolecular synthesis.

Cross References

- ► Microfluidic Bioreactors
- ► Lab-on-a-Chip Devices for Chemical Analysis
- ► Microfluidics for Bio- and Chemical Reactions
- ► Droplet Microreactors
- ► PCR Lab-on-chip Devices

References

1. Watts P, Wiles C, Haswell SJ, Pombo-Villar E (2002) Solution phase synthesis of β-peptides using micro reactors. Tetrahedron 58:5427–5439

2. Flögel O, Codée JDC, Seebach D, Seeberger PH, (2006) Microreactor Synthesis of β-Peptides. Angew Chem Int Ed 45:7000–7003
3. Miyazaki M, Yamashita K, Yamaguchi Y, Honda T, Nakamura H, Fujii M, Maeda H (2004) Differential regulation of chemical reaction in microfluidic system. New J Chem 28:1622–1626
4. Yamamoto T, Nojima T, Fujii T, (2002) PDMS-glass hybrid microreactor array with embedded temperature control device. Application to cell-free protein synthesis. Lab Chip 2:197–202
5. Lee CC, Sui G, Elizarov A, Shu CJ, Shin YS, Dooley AN, Huang J, Daridon A, Wyatt P, Stout D, Kolb HC, Witte ON, Satyamurthy N, Heath JR, Phelps ME, Quake SR, Tseng HR (2005) Multistep synthesis of a radiolabeled imaging probe using integrated microfluidics. Science 310:1793–1796
6. Ratner DM, Murphy ER, Jhunjhunwala M, Snyder DA, Jensen KF, Seeberger PH (2005) Microreactor-based reaction optimization in organic chemistry – glycosylation as a challenge. Chem Commun 5:578–580
7. Kanno K, Maeda H, Izumo S, Ikuno M, Takeshita K, Tashiro A, Fujii M (2002) Rapid enzymatic transglycosylation and oligosaccharide synthesis in a microchip reactor. Lab Chip 2:15–18
8. Huang Y, Castrataro P, Lee CC, Quake SR (2007) Solvent resistant microfluidic DNA synthesizer. Lab Chip 7:24–26
9. Lai SM, Martin-Aranda R, Yeung KL (2003) Knoevenagel condensation reaction in a membrane microreactor. Chem Commun 22:218–219
10. Taghavi-Moghadam S, Kleeman A, Golbig KG (2001) Microreaction technology as a novel approach to drug design, process development and reliability. Org Process Res Dev 5:652–658
11. Ku B, Cha J, Srinivasan A, Kwon SJ, Jeong JC, Sherman DH, Dordick JS (2006) Chip-based polyketide biosynthesis and functionalization. Biotechnol Prog 22:1102–1107
12. Kawakami K, Sera Y, Sakai S, Ono T, Ijima H (2005) Development and characterization of a silica monolith immobilized enzyme micro-bioreactors. Ind Eng Chem Res 44:236–240

Biomolecule Detection

► Fluorescent Labeling

Bionics

► Biomimetics

Biophysics

► Biomimetics

Bioprinting on Chip

MARTINA DAUB, ROLAND ZENGERLE
Laboratory for MEMS Applications
Department of Microsystems Engineering (IMTEK),
University of Freiburg, Freiburg, Germany
daub@imtek.de, zengerle@imtek.de

Synonyms

Biochip printing; Microarray fabrication; DNA array; Protein array; Cell array

Definition

Bioprinting on chip concerns the fabrication of so-called ►microarrays or ►biochips. It comprises the deposition of a multitude of fluidic or dissolved biological agents onto solid substrates with subsequent coupling, i. e. fixation, of the organic molecules on the substrate surface. The biological substances are arranged as hundreds to hundreds of thousands of small chemical reaction areas, so-called spots, in a predetermined spatial order (ranging from the hundreds of micrometre down to the submicrometre range) to provide a 2D array. *Bioprinting on chip* involves printing techniques, microarrayers and criteria that comply with the requirements for high-quality microarray fabrication.

Overview

Generally, microarrays can be regarded as highly parallel sensors used in biomedical applications, chemical sciences, life sciences or drug discovery for studying a multitude of complex biological interactions simultaneously to determine the presence and/or amount of nucleic acids (e. g. oligonucleotides, genes, gene fragments) or proteins (e. g. antibodies, antigenes) in biological samples, e. g. in blood, cell extract or tissue extract, to investigate, for example, gene expression levels or for proteomics studies [1, 2]. Key technical challenges in creating high-content microarrays include advances in array fabrication. Additionally, to address those versatile applications, high-quality microarrays as well as high-quality microarray processing and data analysis are crucial to produce meaningful results. Quality control is needed for the whole process, including definition of microarray content, biological sample preparation, sample purification, sample quality, printing, coupling, washing, microarray quality, hybridisation, scanning, data acquisition, image analysis and data analysis [3–5]. This article focuses only on the transfer of biological molecules onto substrates.

The basic idea of all microarrays is a spatially, miniaturised arrangement of a multitude of different unique immobilised capture molecules on a two-dimensional substrate. Figure 1 shows the typical life cycle of a microarray experiment. One microarray contains hundreds to hundreds of thousands of spots. Typical substrates are glass, membranes or silicon wafers. The arranged multitude of biological agents acts as capture probes to bind molecules out of a complex biomedical sample to be

analysed in a high-throughput and parallel manner. The complex biological interactions are identified by mapping the binding event at a certain location to the specific capture molecules that were previously immobilised at that place. After hybridisation of labelled complementary molecules, i. e. binding of sterically compatible molecules, a scanning microscope detects the bound, labelled sample and measures the visualised probe to ascertain the presence and/or amount of the specific type of complementary molecule in the complex sample. Detection methods are mainly fluorescence based, but chemiluminescence, radioactivity, mass spectrometry or electrochemistry are also used.

In principle there are three main types of microarrays: DNA, protein and cell microarrays. Historically DNA microarrays were the first focus of research and gained a key position in medical and biological research. Typical applications are gene expression profiling, genotyping, sequence analysis and further gene investigations on their localisation, structure, modifications, interactions and function [6]. The proteome is the functional entity of encoded proteins by the genome. Proteins are the true targets of medicine and thus the pharmaceutical industry. Thus protein microarrays are powerful tools to provide quantitative data on a large number of samples to perform proteomics studies. The third type of microarrays, cell microarrays, provides additional functionalities not available through protein arrays where full protein functionality is only given in living organisms, e. g. through posttranslational modifications or for transmembranal proteins. Cell microarrays are intended to detect environmental toxins, to identify potential drug targets or to evaluate the specificity of drug leads by functionally characterising large numbers of gene products in cell-based assays.

The high impact of microarrays as a large-scale and high-throughput tool for biomedical applications in basic research, diagnostics and drug discovery as well as their commercial success have led to enormous efforts of different companies to provide the most suitable microarrayer system. Because of the extensive and time-consuming preparation of the precious printing agents, the reliable and effective processing of microarrayer systems is imperative. The bases for high-quality microarray printing are standardised biological and technological processes to guarantee robust biochip printing and with it reproducible microarray fabrication. Additionally, the multitude of samples shows different liquid properties which greatly influence the deposition behaviour. In contrast to the commercialized ink-jet technology, where the ink as printing medium is adapted to the printer, an ideal microarrayer would be able to deposit any liquid sample with arbitrary liquid properties. Not only the samples but also the solid substrates onto which the samples have to be deposited vary in a wide range.

Depending on the specific application, the general needs that a microarrayer should fulfil are

- to enable uniform, identical and reproducible spots in a regular array pattern with exact controllability of microarray position,
- reliable exclusion of cross-contamination (between samples) and carry-over (between successive printing processes),
- fast microarray production (speed, frequency, parallelism of printing, automation capability, short machine down times for washing steps and machine movements),
- flexibility of printing (chip layout, medium property independence, adjustability of spot size),
- minimum consumption of sample and of substrate area,
- cost-effective microarray production,
- avoid damaging of microarrayer, sample and surface chemistry of substrate,
- integrated quality control and
- robust, automated systems that are easy to handle and to maintain.

Preconditioned that the microarrayer printing properties lead to optimal results, other characteristics are crucial for high-quality microarray production. High coupling efficiency and homogeneity of the biological agent on the substrate are essential. To obtain high-quality microarrays with homogeneous spots, a further feature is homogeneous surface modification of the substrate. Environmental operation requirements include dust-free fabrication, control of temperature and relative humidity whilst printing and subsequent drying process. Associated with the wide variety of different microarray types in combination with very heterogeneous biological agents (e. g. nucleic acids, proteins, cells) there is a vast complexity of coupling types depending on coupling chemistries for the fixation of diverse biological molecules. For each application all interacting parameters have to be optimised to each other. For high binding efficiency of printed molecules onto different microarray surfaces the printing buffer has to be adapted to the kind of biological molecules and to the substrate surface chemistry. When an adequate parameter set is found, standard operating procedures enable robust microarray fabrication.

Basic Methodology

For the production of different types of microarrays a wide variety of microarray production techniques and specialised microarrayers are available. This article will focus on the three basic techniques commonly used: on-chip

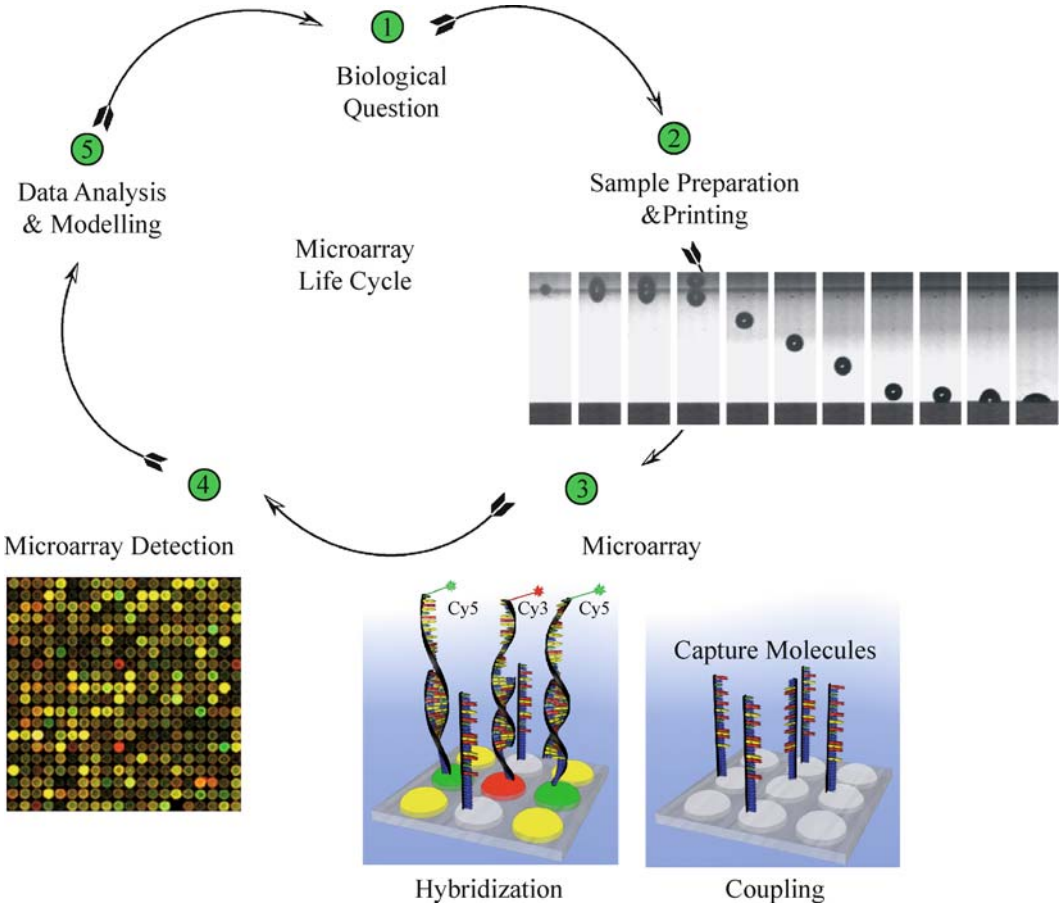

Bioprinting on Chip, Figure 1 Principle of microarray experiment. The microarray life cycle shows the five main steps needed for a microarray experiment [2]. (1) The biological question is the first step followed by (2) sample preparation including printing of the biomolecules onto the substrate. (3) The coupling of the capture molecules localised at predefined positions – so-called spots – finalises the microarray fabrication followed by the microarray reaction. A complex analyte liquid (sample) is brought into contact with the fixed capture molecules where hybridisation of matching molecules takes place. (4) In most instances the microarray analysis is fluorescence-based detection. (5) The last step includes data analysis and modelling by employing bioinformatic tools

synthesis and contact and non-contact printing techniques. In the following, currently available microarray production methods are presented, but the discussion does not claim to be exhaustive.

On-Chip Synthesis of Biomolecules

For the on-chip approaches the features of the microarray are synthesised directly on the substrate (Fig. 2). Oligonucleotides are assembled using sequential printing of oligonucleotide precursors or by photolithography approaches. On-chip approaches using printing are used exclusively by *Agilent Technologies* and called *SurePrint* technology [7]. Instead of printing the readily synthesised oligonucleotides onto the microarray surface, they are actually synthesised base by base in repeating print layers using standard phosphoramidite chemistry. An ink-jet print cartridge with four heads is used, each one filled with one of the four different phosphoramidite nucleotides (A, C, G, T), the building blocks of in situ nucleic acid synthesis. The iterative oligonucleotide synthesis loop starts when the first nucleotide of each oligonucleotide is printed onto an activated glass surface. The protective 5′-hydroxyl group of the printed nucleotide is removed chemically and oxidised to activate it enabling it to react with the 3′-group of the nucleotide printed in the next print layer. The excess of unbound nucleotides is washed away so that they will not randomly react later in the synthesis. The process of printing a nucleotide followed by de-protection, activation and washing is repeated 60 times resulting in 60 mer oligonucleotide arrays. Available microarray formats on 1 in. by 3 in. microarray glass slides

include various content microarrays, e. g. whole genome microarrays of different model organisms, as well as fully customised microarrays. Microarray densities range from 1.9 K to 244 K (K means kilo features) per array; microarray formats for multiplexed arrays on single slides include 1 × 244 K, 2 × 105 K or 4 × 44 K, 4 × 22 K, and 8 × 15 K features. The printing process involves multiple real-time quality control feedback mechanisms of each printed layer of nucleotides. This guarantees the proper synthesis of the desired oligonucleotide sequence.

In an on-chip approach using photolithography *Affymetrix* uses a process to produce high-density oligonucleotide microarrays by a combinatorial on-chip approach. Affymetrix floods the phosphoramidites and uses light-activated deprotection by the use of masks. For each oligonucleotide synthesis step another photolithographic mask is needed. Oligomers with a length of up to 25 bases and a minimum feature size of 5 μm can be produced. Up to 100 masks have to be used for the fabrication of so-called *GeneChips*. *Affymetrix* offers a multitude of high-density microarrays for whole genome, targeted genotyping, sequencing analysis, quantification and regulation of gene expression and clinical applications. The product catalogue includes microarrays from various species like human, mouse, rat, and non-mammalian model species (e. g. yeast, plants, worms). Customised arrays are also available.

For higher flexibility *NimbleGen* and *Febit* use controllable micromirror arrays instead of masks for selective deprotection. The *NimbleGen* system is based on the Digital Micromirror Device (DMD), a solid-state array of micromirrors, which are able to pattern up to 786,000 individual pixels of light, enabling minimum feature sizes of 17 μm. These flexible virtual masks replace the physical chromium masks of the *Affymetrix* approach. This on-chip approach enables a more flexible production of small batches of high-density microarrays with different array layouts. *NimbleGen* was taken over by *Affymetrix* that now is offering both technologies.

Another company called *Febit* has integrated the DMD approach providing a highly versatile platform using a set of eight microchannel structures called *DNA processor*™. A freely user designable oligonucleotide microarray is built up inside these meandering microfluidic channels overnight in their *Geniom* device. After the oligomer building process, the hybridisation and analysis by fluorescence detection is also done in the same device. It allows the synthesis of up to eight times 6000 oligonucleotides. The major applications of *Geniom* are SNP genotyping (single nucleotide polymorphism) and gene expression profiling. Others include sequencing by hybridisation, de novo genotyping and epigenetic analysis.

Advantages of the on-chip approaches are that the systems are well established and very uniform processing is practicable. But these approaches can only be applied for the production of oligonucleotide microarrays. So far, only scientific but no commercial approaches hav been undertaken to produce peptide microarrays by an on-chip approach. Additionally, depending on the specific application, low-density microarrays and only low microarray numbers are sufficient to answer particular biological questions; thus, often small batches (hundreds) of microarrays with low density (a few hundred spots) are needed. In research applications the array layout needs to be flexible. The production of protein or cell microarrays is in high demand as well.

Contact Printing

The more commonly used approach for microarray fabrication is the deposition of pre-synthesised molecules by a microarray printer onto substrate, so-called contact and non-contact microarray printing (Fig. 3a,b). Contact arrayers use different shaped steel pins for direct deposition of droplets onto the substrate by touching the surface with the pins. Non-contact arrayers are similar to commercial piezo-driven ink-jet printers and deposit a droplet onto the substrate without coming into contact with the substrate surface. Microarrayers which use other technical approaches are also commercially available and will also be discussed.

Contact printing technologies were used from the beginning of microarray technology. They are based on pin tools, which are dipped into the sample solution and take up a small volume of sample. Then they are brought in contact with the slide surface where they deliver the sample as a small spot. Whilst moving the pins away from the surface, the adhesion forces between sample and substrate lead to retention of small volumes on the substrate. In this system the spot volume metering is determined by the interaction between the pin, the transferred fluid and the substrate. *TeleChem International* is one of the major pin suppliers for contact printing [8]. The catalogue includes pins and printheads of different brands like *ChipMaker, Stealth, ArrayIt* and printheads for *BioRobotics, Robodesign, Genetix* and *NanoPrint* robots. Their pins deliver spot volumes from 0.5 nl to 12 nl, resulting in spot diameters from 62.5 μm up to 600 μm. After each deposition solid pins need to be re-dipped for sample loading. Thus, specially shaped pins were developed to allow several depositions with one dipping action, e. g. capillary tubes, tweezers, microspotting pins or split pins. They are available with reservoir capacities from 0.25 μl to 1.25 μl of sample solution. Another way to circumvent re-dipping

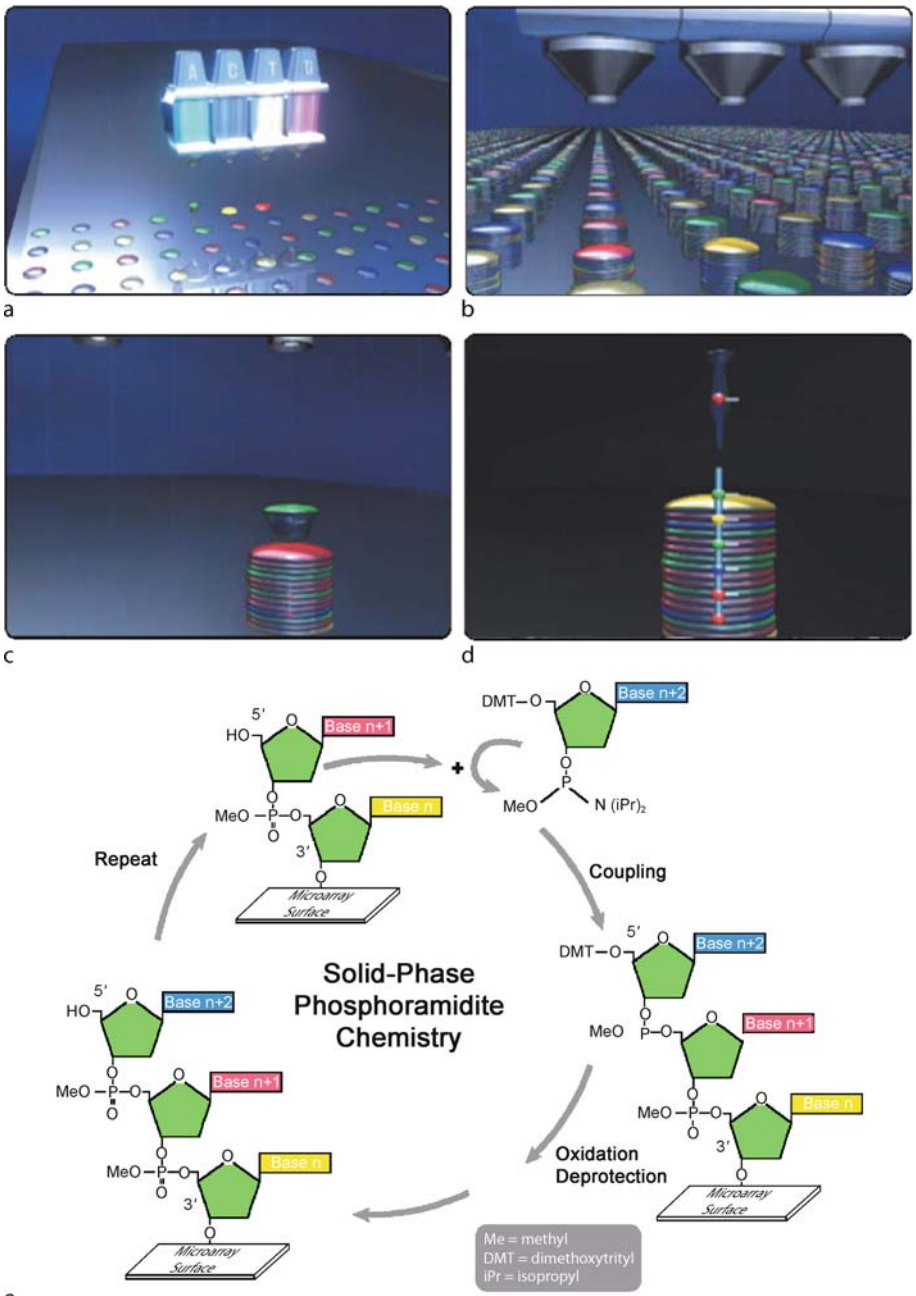

Bioprinting on Chip, Figure 2 On-chip synthesis of oligonucleotide microarrays using *SurePrint* technology of *Agilent Technologies* [7]. A schematic of the general mechanism via ink-jet printing shows (**a**) the first layer of nucleotides being deposited on the activated microarray surface. (**b**) The growth of the oligonucleotides after multiple layers of nucleotides have been precisely printed. (**c**) A close-up of one oligonucleotide as a new base is being added to the chain, which is shown in (**d**). (**e**) The general cycle of oligonucleotide synthesis via phosphoramidite chemistry (courtesy of *Agilent Technologies*)

is the pin-and-ring technology. A small ring is dipped into the sample solution. The surface tension of sample is used to form a fluid layer within the ring. A solid pin is pushed through the fluid layer and the trapped sample is deposited onto the surface. After retraction of the pin the fluid film is still intact and fluid is replenished from the ring. Commercially available contact printers are offered, for example, by *Genemachines*.

The contact printing technology is currently most commonly used to produce DNA microarrays. The advantage of pin-based printing technologies is the robust transfer of liquid by direct contact of the tip of the pin with the surface to be printed on. But this implies the risk of damaging the substrate surface by mechanical load during printing. To avoid this, the microspotting pins deposit samples without touching the pin to the substrate. Spots are produced with a 25 µm distance between pin and substrate surface. To produce a high number of arrays in a reasonable time, it is necessary to use many pins in parallel, typically up to 48. An accurate and precise volume deposition depends on the interaction between the pins, the sample and the slide surface. Therefore only mechanically very precisely produced pins will deliver the same volume consistently and reliably. Additionally, a careful pre-selection process of the pins combined with an accurate adjustment is needed to obtain a set of pins that are uniform in size, shape and height. Due to the adhesion force dependence of the contact printing process the printing media should be similar in media properties to produce equal spot sizes.

Non-Contact Printing

In non-contact printing techniques the liquid metering is not determined by the complex interplay of the pin, the liquid and substrate, but is separated from the substrate, because no contact between the printing tool and the substrate occurs (Fig. 3c–e). The fluid is ejected as a flying droplet or jet towards the surface from a certain distance, which makes metering more precise in many cases. Usually the dispensing units of non-contact printers come with a reservoir, enabling the dispensing of thousands of droplets without the need of interim refilling. Capillary forces or active pumping mechanisms are used to transport the liquid through microchannels or tubes from reservoirs to the dispensing orifices.

One concept of non-contact printing is based on syringe–solenoid-driven printers. In the syringe–solenoid concept a reservoir and a high-speed microsolenoid valve are connected to a high-resolution syringe (e. g. *synQUAD* system provided by *Genomic Solutions*). Within the *synQUAD* dispensing platform *PreSys 4040XL* containing an eight channel dispense head the system is filled with system liquid. Operating the syringe causes the sample to move into the tip. The syringe pressurises the system and if the microsolenoid valve is opened, droplets are dispensed out of the tip. This system delivers volumes from 20 nl to 20 µl per ejection process.

Further non-contact microarrayers are piezoelectrically driven. Companies like *MicroDrop*, *PerkinElmer*, *Scienion* and *GeSim* use a technology that is similar to ink-jet printer technology. The printers of *MicroDrop, PerkinElmer* and *Scienion* are based on glass tips. Each glass tip is surrounded by a piezo actuator. The dispenser tip of *GeSim* consists of bonded silicon and glass layers. A piezo actuator is fixed at the top of the dispenser tip. In all piezo tip systems the samples are aspirated into the tip by applying a slight vacuum at the back end of the capillary. The squeezing of the tip forced by the piezo actuation induces droplet ejection out of the capillary. The fast response time of the piezoelectric crystal permits fast dispensing rates (kilohertz range). The small deflection of the crystal generates droplet volumes from hundreds of picolitres to a few nanolitres.

For higher throughput, parallel systems were built with four (*PerkinElmer Piezorray*) and sixteen piezo tips (*GeSim Nano-Plotter NP 2.0*). Horizontal alignment of all tips to the substrate surface is not as critical as for contact printers. However, each tip has its own specific piezo actuator necessitating calibration of each tip to enable homogeneous droplet ejection. Usually the tips are produced in small batches in a handmade process, so an accurate quality control of tips is needed to ensure the high precision of tip geometries. Overall non-contact printing approaches provide less spot-to-spot and chip-to-chip variability than contact printing methods.

Another non-contact microarrayer using the *TopSpot* technology is offered by *Biofluidix* [9]. This technology enables high-throughput printing of microarrays. The *TopSpot* technology can be applied to the production of custom made low- to mid-density microarrays containing up to several thousands of different probes on a substrate. A key element of the *TopSpot* technology is the micromachined printhead which can be loaded with 24, 96, or up to 384 different samples. The reservoirs comprise one to several microlitres of printing medium. All liquids are printed onto a substrate simultaneously by a micronozzle array contained in the printhead. The microarray is then formed by the individual droplets on the substrate having a pitch of 500 µm. For each droplet only about one nanolitre of liquid is consumed. Therefore a printhead can create several thousand microarrays with one filling. The printhead is operated in the so-called print module, which is designed to apply a pressure pulse to the printhead via a piston such that droplet generation is initiated. For this purpose the piston is driven with a high velocity by a piezo actuator. The major advantage of the *TopSpot* technology over other nanolitre dispensing systems (e. g. an ink-jet printer) is that each nozzle can be supplied with another printing medium. The inherent parallelisation of the printhead increases the speed without the need of complicated automation systems. By using only one actuator unit to generate the pneumatic driven droplet dispensing out of

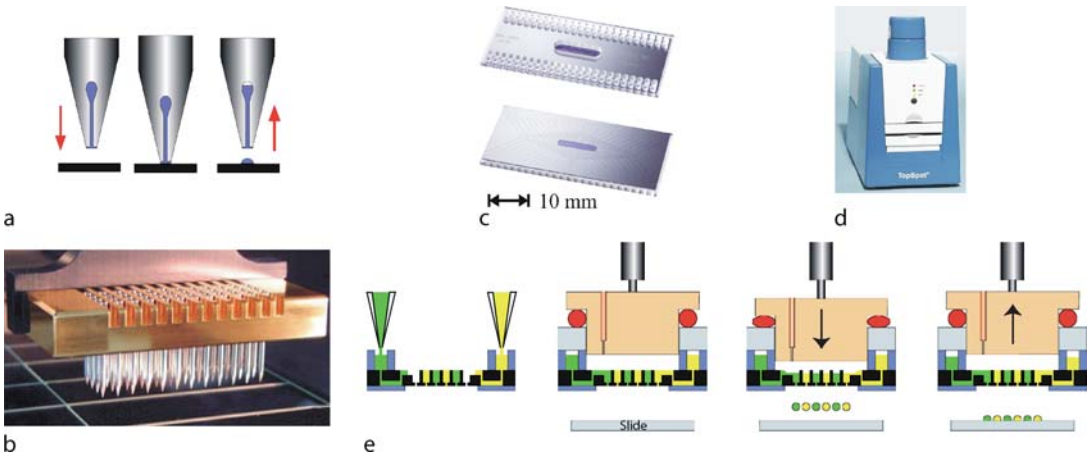

Bioprinting on Chip, Figure 3 Contact and non-contact printing. Contact printing mechanism of *TeleChem International Inc.* [8]. (**a**) *Micro-spotting pins* enable high-speed manufacture of microarrays. The pins have flat tips and defined uptake channels, which allows a thin (25 μm) layer of sample to form at the end of the pin, and printing to proceed by gentle surface contact. Printing occurs as a simple three-step *ink-stamping* process as follows: (left) downstroke, (centre) contact, and (right) upstroke. (**b**) Printing with 48 pins in parallel using the *Arrayit*® microarray technology equipped with a *Stealth 48 printhead* fitted with *48 SMP3 microarray spotting pins* ((**a**), (**b**) by courtesy of *TeleChem*). Non-contact printing of microarrays using *TopSpot*® technology of *Biofluidix GmbH*. (**c**) Core of the *TopSpot*® technology [9] is the microfabricated printhead ((top) top view, (bottom) bottom view of a 96 position printhead) allowing highly parallel microarray fabrication. (**d**) The benchtop *TopSpot*® machine operating one printhead within a print module. (**e**) Schematic cross-section of the operating principle in four steps starting with filling of the printhead reservoirs. Via a piezostack actuator an air pressure is generated within the actuation chamber above the nozzle array that simultaneously affects all nozzles resulting in droplet ejection of 96 droplets ((**c**), (**d**), (**e**) by courtesy of *Biofluidix*)

all nozzles simultaneously, no calibration of multiple actuator units is needed. Several printheads can be lined up to generate microarrays with higher content.

Other Deposition Methods

In addition to on-chip approaches and contact and non-contact printing of agents onto microarrays there are further methods for microarray fabrication. Two examples are the protein profiling chips offered by the company *Zyomyx* and the electronic microarrays offered by the company *NanoGen*.

Zyomyx offers an all-in-one system for protein profiling. The system is provided as a comprehensive package that includes an assay workstation, a biochip scanner, data analysis software, assay reagents containing the calibration analytes and internally validated biochips. Each biochip is designed to assay up to 200 different proteins in each one of six separate flow cells. Every flow cell can be run with a sample volume of 25 μl. The chips are provided ready-to-use, and fully loaded with specified capture antibodies. The protein profiling biochips are fabricated by silicon micromachining. Every flow cell contains an ordered array of 200 micropillars, each one with a height of 150 μm and a diameter of 50 μm. Specific capture agents are directionally bound to the top of each pillar.

The core of *NanoGens* technology is the *NanoChip Electronic Microarray*. It consists of a silicon chip capable of rapid identification and analysis of biological molecules. The technology utilises the natural positive or negative charge of most biological molecules. Applying an electric current to individual test sites on the *NanoChip* enables rapid movement and concentration of the molecules. Molecular binding onto the test sites is accelerated 1000 times compared to traditional passive methods. Currently *NanoChips* with 100 or 400 test sites for DNA and RNA analysis are commercially available. The sites have diameters of 80 μm and a pitch of 200 μm. The *NanoChip* microarray technology provides an open platform that allows customers to run common assays as well as customise their own assays. Applications include SNP analysis, and insertion, deletion and mutation analyses.

Another deposition method for fabricating microarrays containing functional proteins for surface immunoassays is so-called microcontact printing. The Delamarche group [10] uses a microfluidic chip that comprises a number of independent capillary systems, each of which is composed of a filling port, an appended microchannel and a capillary pump. Each capillary system fills spontaneously driven by capillary forces, the flow through the channels being driven by evaporation employing Peltier-controlled cooling and heating. The sandwich fluores-

cence immunoassay takes place on the surface of a polydimethylsiloxane (PDMS) slab, which is placed across the microchannels. After precoating of the PDMS surface with capture antibodies the binding sites of analyte molecules are localised by using the chip, then the captured analyte molecules are bound to a second fluorescently labelled antibody using a second chip that is directed orthogonally to the first chip. The assay results in a mosaic of fluorescence signals on the PDMS surface which are measured using a fluorescence scanner.

Coupling of Capture Biomolecules

An indispensable factor for high-quality microarray fabrication performed with contact or non-contact printing is the efficient and homogeneous fixation of biological molecules on the substrate surface, so-called coupling. The printing system in combination with other interacting parameters like substrate surface chemistry, type of biological agents, printing buffer composition, immobilisation protocols and washing procedures have to be optimised to each other. It is important to distinguish between, for example, nucleic acid or protein or cell microarrays.

Nucleic Acid Microarrays

Within the above mentioned microarray categories further partition into sub-categories makes it even more complex. Nucleic acids comprise various configurations and lengths, e. g. oligonucleotides, cDNA, RNA and plasmids, with diverse properties leading to different coupling requirements. First of all the choice of substrate combined with adequate surface chemistry is relevant to couple nucleic acids onto the substrate surface. For high-sensitivity measurements an important precondition is the low autofluorescence of substrate and coating and the absence of non-specific background to ensure high signal-to-noise ratios. Most commonly used are glass substrates on which functional aminosilanes are deposited to form layers on the substrate to which the capture molecules can be bound. Some examples of such functionalised organosilane compounds are APTES (3-aminopropyltriethoxysilane), AEA (*N*-(2-aminoethyl)-3-aminopropyltrimethoxysilane), AEEA (3-(2-(2-aminoethyl)-ethylamino)-propyltrimethoxysilane) and GOPS (3-glycidoxypropyltrimethoxysilane). These monovalent and multivalent cations are known to condense DNA into higher ordered structures. Another glass substrate modification is the NHS ester modification to couple the proteins by EDC-NHS chemistry (EDC is *N*-(3-dimethylaminopropyl)-*N*′-ethylcarbodiimide; NHS is *N*-hydroxysuccinimide). Thereby NHS-esters react with amines to form amide bonds. EDC is a cross-linker that effects direct coupling between carboxylates (−COOH) and primary amines ($-NH_2$). A third method is the coating of glass substrates with functional epoxy groups to react with amino-functionalised biomolecules. Substrates other than glass are nitrocellulose, nylon or cellulose acetate membranes, and polymer substrates such as COC (cyclo-olefin copolymer) or PMMA (poly(methyl methacrylate)). As for all kinds of microarrays, the coupling chemistry used has to be optimised relating to all interacting parameters like capture molecules, substrate, printing buffer, immobilisation protocol, etc. Besides a stable, reproducible and established production process, strict internal manufacturing controls are crucial for low batch-to-batch variations. The quality of biomolecule coupling onto the slide surface depends on coupling chemistry of the substrate surface and the reproducibility of the surface properties.

Parameters that have to be adapted to the specific application are printing buffer, including buffer system (e. g. phosphate, carbonate, borate based; corresponding acid–base pair; salt components), concentration, pH value and additional supplements such as DMSO (dimethylsulfoxide) and betaine. The printing buffer composition has to be optimised according to the printing molecules, the substrate surface and the immobilisation protocol used. Within this protocol varying parameters that have to be adapted are, for example, incubation times, temperature curves and relative humidity. Commonly used approaches for immobilisation are incubation in a heated water bath or in an oven. Additionally the washing procedure to remove unbound molecules after coupling has to be adapted.

Protein Microarrays

Proteomic profiling will yield more direct answers to the current biological and pharmacological questions, because the majority of known biological effector molecules, diagnostic markers and pharmaceutical targets are proteins, not mRNA or DNA. Protein microarrays are expected to significantly expedite the discovery of new markers and targets of pharmaceutical interest, and to have the potential for high-throughput applications. In particular, antibody and cell lysate microarrays have the potential to revolutionise protein expression profiling. Where functionality is only given in living cells, also cell microarrays become relevant. The main precondition for protein and cell microarrays is that the capture proteins or cells are kept in a functional state after being immobilised to the microarray substrate by exclusion of protein denaturation or cell lysis.

Protein microarrays can be classified into three general categories regarding their applications: expression profiling, interaction profiling and functional identification. Protein expression profiles reflect the concentration profile

of proteins depending on the cell or tissue status (e. g. cell type, age, environmental conditions, disease state). Antibody arrays are the main tool to perform protein expression profiling. Protein interaction profiling is most critical to drug discovery since many drugs and toxins affect protein–protein interactions. With so-called proteome arrays, which are microarrays with the whole proteome or a subset of it immobilised to the substrate surface, protein interactions can be categorised at a large scale. At the same time more precisely specific domain–domain interactions can be identified. Besides purified proteomes and proteome subsets, interaction profiling can be based on various other immobilised capture molecules, e. g. antibodies, antibody fragments, engineered binding proteins or even aptamers. Also microarrays of immobilised antigens have been developed, e. g. for profiling the reactivity of antisera. The spots of protein microarrays can also consist of complex samples, such as blood sera or cell lysates, which can be probed, for example, against a single antibody. The microarrays of this approach are termed reverse phase microarrays. The most seminal field is the decoding of protein function. At present only for a small population of proteins is the function known. The identification of the particular function for each protein connected with manifold interactions among each other is the goal of proteomics studies and to utilise the knowledge gained about regulatory processes for the healthcare and pharmacological industry.

In contrast to DNA microarrays, production of protein microarrays is an immense technological challenge. The first challenge derives from the limited availability of proteins for the fabrication of vast amounts of protein microarrays. Whereas for DNA with the *polymerase chain reaction (PCR)* a routine method exists to enormously increase the number of DNA copies and automated processes are established for oligonucleotide synthesis, for proteins such methods are missing; hence, proteins are produced in very small quantities. Furthermore, the biochemistry of proteins is orders of magnitude more complex than DNA biochemistry, so that the production of protein microarrays is much more difficult. Whereas DNA is a relatively simple polyanion and can be modified and easily immobilised on solid surfaces based on electrostatic interactions or covalent bonding, protein bonding is much more delicate. The complexity derives from a multitude of biochemical properties. Protein molecules possess particular three-dimensional structures, varying chemical and physical properties (e. g. hydrophilic and hydrophobic domains, ionic interactions) and the activity and function as well as the partial charge of domains depend on the local physical and chemical microenvironment. Additionally, complexity is further increased by posttranscriptional modifications of protein conformation; hence the well-established on-chip approaches of oligonucleotide microarrays are not applicable to protein microarrays. For protein microarray production four major requirements have to be fulfilled:

- speed of protein production and accurate purification,
- minimisation of background caused by unspecific protein binding to obtain high signal-to-noise ratios,
- native protein conformation and orientation on substrate surface and
- protein detection and identification.

A protein interacts with other molecules through specific functional domains. Hence, native conformation and orientation of the immobilised capture molecules are indispensable for meaningful results from protein microarrays. The most problematic factor is the potential of inadvertent masking or degradation of epitopes of antibodies, active sites of enzymes or binding sites of receptors. Thus surface chemistry plays a critical role in protein microarrays where the surface chemistry should provide an inherently inert surface that resists non-specific binding in combination with integrated functional groups that ensure facile, highly specific and oriented immobilisation of native proteins.

For protein immobilisation the most commonly used method is the EDC–NHS affinity ligand coupling chemistry as described for DNA bonding to glass substrates. An advanced surface coating method for protein microarrays was developed by the company *MicroSurfaces*. A *poly(ethylene glycol)* (PEG) surface coating, arranged as a high-density brush to provide a zero background surface, is functionalised with molecules that mediate biomolecular binding. The kind of molecules depends on the interaction mode and the application. Surfaces are functionalised with biotin or streptavidin, chelated copper, epoxy functional groups or NHS to mediate binding of streptavidin- or biotin-labelled proteins, polyhistidine-tagged proteins (with Cu^{2+}). The epoxy functional groups are used to covalently attach proteins in purified form via amine groups.

Cell Microarrays

For cell microarray printing additional elementary demands have to be addressed by the printing technology. A highly reproducible number of living cells per spot on microarray slides and an optimised printing process that is qualified for reproducible production of cell microarrays along with keeping their vitality and function for analysis are essential. There are two fundamental methods to produce cell microarrays. The indirect method was developed by J. Ziauddin and D.M. Sabbatini (2001) [11]. To produce

transfected cell microarrays a mixture of gelatine, acting as an anchor, containing different DNA molecules for transfection purposes is printed onto a glass substrate using a standard pin printing arrayer. After drying of gelatine–DNA spots the substrate is incubated with a cell suspension containing the transfective agent. This induces incorporation of DNA into the cells, resulting in cell microarrays of differently transfected cells. In the direct method the different cell types themselves are printed onto the substrate. In some publications contact-based microarrayers are used, but more often non-contact-based devices like modified ink-jet printers or piezo-driven tips are used.

The construction of chemically modified solid supports is of particular importance in cell-based microarrays. For cell immobilisation on substrates the most commonly used method is the binding to poly-L-lysine-coated slides. Binding of cells results from ionic interactions between the cell membrane and the positively charged poly-L-lysine surface. This method is most effective for adherent cell types. To promote cell adhesion, surfaces coated with extracellular matrix (ECM) proteins such as collagen or fibronectin have also been employed. In some cases, polymer-treated surfaces are used in conjunction with the above mentioned compounds to reduce non-specific adhesion.

Companies that offer microarrays and associated services are *Affymetrix, Agilent Technologies, GE Healthcare Bio-Sciences, Applied Biosystems Applera, BD Biosciences Clontech, BF-BIOlabs, BioCat, Biomol, Biozym Scientific, Cambrex Bio Science, Chemicon, Chipron, CLONDIAG chip technologies, Clontech Laboratories, Eppendorf, Gene Expression Center, Genetix, Greiner Bio-One, Hypromatrix, Invitrogen, KFB, Merck Biosciences, Miltenyi Biotec, MoBiTec, MWG Biotech, Panomics, Randox Laboratories, Schleicher&Schuell BioScience, Scienion, Sigma-Aldrich Chemie, SIRS-Lab* and *VBC-GENOMICS*, to name just a few.

Key Research Findings

Accelerated Molecule Interaction Research

After more than fifteen years of microarray research the technology holds a momentous position ranging from fundamental screening to clinical diagnostics. The first paper reporting the use of microarrays was published in 1989 by Ekins and co-workers. The microarray technology has since undergone numerous refinements, iterations and adaptations regarding the steadily increasing number of applications. The number of interactions to be measured and with it the variety and diversity of microarrays steadily increases. Fields of application include the investigation and treatment of various diseases (e. g. cancer, infectious diseases, autoimmune responses) to improve diagnostic accuracy and to predict treatment efficiency. This is supported by advanced elucidation of regulatory processes including cell signalling pathways, molecular interaction studies and regulation of transcription and replication where malfunction may also lead to disease development. Advanced identification of biomarkers and pharmacological target discovery accelerates pharma research and development.

Gene Expression Profiling, Deciphering Whole Genomes and the First Clinically Accredited Arrays

Most early microarrays provided gene expression profiling studies in order to identify genes of interest that may be over- or underexpressed in some defined biological condition. Fabrication of those microarrays required cloning of complementary DNA (cDNA) sequences copied from isolated messenger RNA (mRNA) out of cells or tissues, followed by subsequent amplification by PCR. The PCR product from each clone was then deposited on microarrays. The subsequent concept of oligonucleotide arrays allowed scientists a higher degree of flexibility for microarray design because of the independence of available clone sequences. Further advantages of oligonucleotide arrays vs. cDNA arrays are better reproducibility, streamlined workflow and lower fabrication costs. In combination with the complete mapping of the human genome early in 2001 (further refining of sequencing is still ongoing) and other genomes of various model organisms (e. g. the bacterium *Escherichia coli*, the yeast *Saccharomyces cerevisiae*, the roundworm *Caenorhabditis elegans*, the fruitfly *Drosophila melanogaster*, the laboratory rat *Rattus norvegicus* and the laboratory mouse *Mus musculus*) the microarray technology has opened new perspectives. Nowadays several companies (e. g. *Agilent Technologies, Affymetrix, TeleChem/ArrayIt, Applied Biosystems*) offer products that enable scientists to probe gene expression from entire genomes on one single microarray. The knowledge gained improves DNA diagnostics, genotyping, proteomics as well as pharmacogenetics studies. By data analysis using clustering tools, the resulting signatures allow typing of genes linked with, for example, cancer pathogenesis and metastasis and with it to guide treatment options and to avoid ineffective treatment. *Agendia* (based on *Agilent Technologies'* custom microarray) is the first company worldwide to be granted the ISO 17025 accreditation (2005) for its *MammaPrint* gene expression service to classify breast cancer patients as at low or high risk of developing distant metastasis in a ten-year period. In 2006 a further accreditation for *Agendias CupPrint,* to identify cancer of unknown primary that concerns 4% of all cancer diseases, was granted.

Encoded Proteins Manifest Gene Function

Additionally, research has greatly benefited from the post-genomic era. Despite the success of DNA microarrays in gene expression profiling or mutation mapping, it is the activity of encoded proteins that directly manifests the gene function. So protein microarrays have been applied in biomarker discovery, protein profiling, protein–protein interaction analysis and peptide mapping applications. It seems that especially antibody microarrays have the potential to revolutionise the progress in protein expression profiling. With it, for example in drug discovery, one seeks to develop a biological or chemical entity that will improve the disease symptomatology or actually treat the underlying pathophysiological basis of the particular disease state. Protein expression profiling in cell or tissue extracts enables one to elucidate pathways and to identify mechanisms involved in gene regulation. Antibody arrays are available from various companies (e. g. *Sigma-Aldrich, Invitrogen, Genetix, Clontech Laboratories, Hypromatrix, Chemicon, Panomics*).

To identify splicing variants of mRNA by exon-level expression profiling, exon microarrays are offered by, for example, *Affymetrix, ExonHit Therapeutics* together with *Agilent Technologies.* This approach takes into account that one gene encodes for multiple different proteins by alternative splicing, i. e. small blocks of transcribed mRNA can be rearranged in multiple various combinations to form different transcripts from the same gene. Splicing variants of proteins cannot be detected on the DNA level and are supposed to be involved in several diseases.

Cell Arrays for Interaction Studies in Life Processes

In similar fashion to DNA and protein microarrays the ability to create arrays of cells and even tissues at high-density offers the potential for the development of cell-based sensors with extremely high throughput and multiplex capability. Research on biomolecular interactions on the genomic, the proteomic and the cellular level paves the way for advanced understanding of the function of the human genome and to unravel the complexity of biological pathways and cellular networks that control life processes.

Progress in Microarray Fabrication Techniques

These advances in life science research using the highly parallel microarray technology would not have been possible without enormous progress in bioprinting on chips. For microarray fabrication the on-chip approach to synthesise capture molecules on chips is well established and highly reproducible. But it is only applicable to oligonucleotide arrays. The deposition of cDNA by contact and non-contact printing is also highly developed, and integrated quality control mechanisms guarantee high-quality microarray fabrication. The higher complexity of protein microarrays compared to nucleic acid microarrays leads to greater demands regarding bioprinting on chip. This implies correct folding of the capture molecules on the microarray surface to achieve reproducible results. Binding sites of bound proteins need to be accessible and in native conformation to act as functional capture molecules to deliver valid results. Additionally, posttranslational modifications, e. g. phosphorylation, methylation or farnesylation, might play an important role for reliable molecular interactions with other proteins as well as with nucleic acids.

Cell microarray printing implies the exclusion of shear forces during the printing process to keep the cells on the chip alive. Additional specific supplements within the printing buffer can prevent cells from breaking during the printing process. There are different approaches to couple living cells on a substrate surface. First of all – for adherent cells – the cellular adhesion can be used to keep the cells at the spot positions. This could be aided or mediated by binding of discrete areas of *poly-l-lysine* or *extracellular matrix protein* acting as kind of adhesive agent within the spot areas. An application of recent cell microarray studies is the parallel investigation of cell adhesion forces of different permanent cell lines on different polymer substrates. To couple non-adherent cells to generate a microarray containing living cells could be mediated by specific anchor molecules that are located within spots on the surface. One end of these anchor molecules binds to the substrate surface and the other end is a transmembranal region that incorporates into the cell membrane, connected by a spacer in between.

Future Directions for Research

Clinical Diagnosis and Treatment Prediction

With the progressive development of the capabilities that microarrays provide, comprehensive investigations lead to new insights into regulatory processes within cells to elucidate cellular processes like transcription and replication as well as protein expression. With the complete sets of genes of organisms available, studies of gene regulation and interactions are available for scientists. Using this technology, coherences of cellular processes and health can be discovered and used to develop new drugs and to improve healthcare by advanced diagnostics and treatment prediction by assessing related gene signatures. The first steps towards diagnostic microarrays and treatment prediction are being taken with the ISO accreditation of *MammaPrint* and *CupPrint* arrays by *Agendia*. Another

step forward into the clinic was the approval of *AmpliChip (Roche Diagnostics)* by the *FDA (US Food and Drug Administration)* in 2005. The pharmacogenetic *AmpliChip* helps physicians to tailor patient dosages of drugs that are metabolised differentially by cytochrome P450 enzyme variants. These real medical applications of microarrays will lead to a gathering of momentum towards the wide field of medical applications that was anticipated years ago. Commercialisation towards real medical application beyond pure research breaks into new markets.

Reliability of Microarray Data, Standardisation and Terminology

Currently the progress to utilise microarray studies for clinical practice is further supported by the *FDA*. Under the auspices of *FDA* scientists, combined community-wide efforts are ongoing within the *MAQC project (MicroArray Quality Control)* dealing with the objective assessment of seven microarray platforms to experimentally address the key issues surrounding the reliability of DNA microarray data. The project aims at the set-up of guidelines for using microarrays in clinical practice and regulatory decision-making. Studies aiming at intraplatform reproducibility and analytical consistency across microarray platforms that are indispensable to translate the technology from pure research to clinical application are the main subject.
An important starting point to perform reliable microarray experiments and to gain meaningful information is the biological question and with it choosing the optimal microarray type (nucleic acid vs. protein vs. cell vs. any other kind) and information content (low-, mid-, high-density array) together with an adequate platform for each experiment. Furthermore a range of quality control for all successive processes and protocols is required. In the very beginning of making sense out of microarray experiments enormous discrepancies between microarray results appeared. Furthermore standard formats for microarray data to share data and results were missing. One effort towards standard generation in microarray data handling started in 2001. Brazma et al. published in 2001 the *Minimum Information About a Microarray Experiment (MIAME)* that describes the minimum information that is needed to enable the interpretation of the results of the experiment unambiguously and potentially to reproduce the experiment and is aimed at facilitating the dissemination of those data [12]. The *Microarray Gene Expression Data Society* (MGED) further refined those efforts in 2002 with a publication of Spellmann et al. [13] with the design and implementation of *MicroArray Gene Expression Markup Language* (MAGE-ML), followed by the set-up of standards and ontologies for microarray databases and for high-throughput data sharing. Those efforts towards standardisation and community-wide usability of generated data and results lead to the accord that with careful experimental design and appropriate data transformation and analysis, microarray data can indeed be reproducible and comparable among different formats and laboratories. One major outcome is that statistical analysis in regulatory submissions and clinical diagnostics is likely to be different from that used in basic research and discovery. This study can be used as a solid foundation for combining other microarray studies to realise the comprehensive potential by accumulating microarray results to enlarge understanding of biological processes and with it pave the way for new healthcare uses.

Microarray Evolution

DNA sequencing is another challenge to unravel coherences between DNA sequence and DNA function. Deciphering the whole genome of organisms leads to new possibilities by comparison of sequence differences interacting with their resulting phenotypes. The differences between human beings are small and the unique DNA sequences differ by only about 0.1%, regardless of ethic origin. These genetic differences encode for how humans look and to what diseases they are susceptible. Furthermore they can be used for evolution studies as well as for historical migration patterns of humans across the world.
The numerous different types of microarrays in combination with the widespread fields of applications claim for advanced microarray fabrication technologies that are adapted to the specific needs regarding speed and flexibility. For all technologies reproducibility and robust processing as well as accuracy and printing precision should be taken for granted. With the ongoing and shifting usage of this tool further innovative platforms will appear.
Taken together these various capabilities that microarrays provide make high demands on bioprinting on chip technologies and therewith coupling chemistries. The important conclusion is that the microarray technology will continue to dramatically change over time as our picture of regulatory processes becomes more sophisticated and complete. With it the relevant microarray fabrication technologies and microarray platforms have to develop further associated with the increasing requirements.

Cross References

- ► Capillary Filling
- ► Cell Culture (2D and 3D) on Chip
- ► Cell Patterning on Chip
- ► DNA Micro-arrays
- ► Droplet Dispensing
- ► Droplet Evaporation

- ► Evanescent-Wave Sensing
- ► Fluorescence Measurements
- ► Fluorescent Labelling
- ► Hydrophilic/Hydrophobic Patterning
- ► Methods for Surface Modification
- ► Supersonic Micro-Nozzles
- ► Proteomics in Microfluidic Devices
- ► Surface Tension Driven Flow
- ► Capillarity and Contact Angle
- ► Van der Waals Interaction Forces

References

1. Hardiman G (2003) Microarray technologies - an overview. Pharmacogenomics 4(3):251–256
2. Schena M (2000) Microarray Biochip Technology, 1st edn. Eaton Publishing Company/Biotechniques Books, Natick
3. Allison DB, Page GP, Beasley TM, Edwards JW (eds) (2006) DNA Microarrays and Related Genomics Techniques: Design, Analysis, and Interpretation of Experiments. Chapman and Hall/CRC Press, Boca Raton
4. Zhang W, Shmulevich I, Astola J (2004) Microarray Quality Control. Wiley, New Jersey
5. Simon RM, Korn EL, McShane LM, Radmacher MD, Wright GW, Zhao Y (2004) Design and Analysis of DNA Microarray Investigations. Springer, New York, Berlin, Heidelberg, Hong Kong, London, Milan, Paris, Tokyo
6. Kronick MN (2004) Creation of the whole human genome microarray. Expert Rev Proteomics 1(1):19–28
7. Agilent Technologies, Inc. (2003) Agilent SurePrint Technology. http://www.chem.agilent.com/temp/radADA68/00039489.pdf. Accessed 17 Nov 2006
8. TeleChem International, Inc. (1998–2005) Stealth Microarray Spotting Pins and Printheads, Products, Printing Technology. http://arrayit.com/Products/Printing/Stealth/stealth.html. Accessed 17 Nov 2006
9. Biofluidix GmbH (2005–2006) http://www.biofluidix.com. Accessed 17 Nov 2006
10. Cesaro-Tadic S, Dernick G, Juncker D, Buurmann G, Kropshofer H, Michel B, Fattinger C, Delamarche E (2004) High-sensitivity miniaturized immunoassays for tumor necrosis factor alpha using microfluidic systems. Lab Chip 4(6):563–569
11. Ziauddin J, Sabatini DM (2001) Microarrays of cells expressing defined cDNAs. Nature 411(6833):107–110
12. Brazma A, Hingamp P, Quackenbush J, Sherlock G, Spellman P, Stoeckert C, Aach J, Ansorge W, Ball CA, Causton HC, Gaasterland T, Glenisson P, Holstege FC, Kim IF, Markowitz V, Matese JC, Parkinson H, Robinson A, Sarkans U, Schulze-Kremer S, Stewart J, Taylor R, Vilo J, Vingron M (2001) Minimum information about a microarray experiment (MIAME)-toward standards for microarray data. Nat Genet 29(4):365-371
13. Spellman PT, Miller M, Stewart J, Troup C, Sarkans U, Chervitz S, Bernhart D, Sherlock G, Ball C, Lepage M, Swiatek M, Marks WL, Goncalves J, Markel S, Iordan D, Shojatalab M, Pizarro A, White J, Hubley R, Deutsch E, Senger M, Aronow BJ, Robinson A, Bassett D, Stoeckert CJ Jr, Brazma A (2002) Design and implementation of microarray gene expression markup language (MAGE-ML). Genome Biol 23;3(9)

Biorecognition

Definition

Biorecognition is the ability of a biologically derived entity (molecule or pathway) to reproducibly identify an analyte target and to generate a predictable response commensurate with that recognition reaction.

Cross References

- ► Impedimetric Biosensors for Micro and Nano Fluidics

Biosafety

- ► Lab-on-Chip Devices for Biodefense Applications

Biosample Preparation by Lab-on-a-Chip Devices

JONGYOON HAN[1], JIANPING FU[2], YING-CHIH WANG[2], YONG-AK SONG[2]

[1] Department of Electrical Engineering and Computer Science and Department of Biological Engineering, Massachusetts Institute of Technology, Cambridge, MA, USA

[2] Department of Mechanical Engineering, Massachusetts Institute of Technology, Cambridge, MA, USA

jyhan@mit.edu, jpfu@mit.edu, ycwang@mit.edu, yongak@mit.edu

Synonyms

Sample pre-fractionation; Preparatory separation; Microfluidic devices; Microsystems

Definition

Sample preparation is usually defined as a series of molecular separation/fractionation steps required or recommended in order to obtain higher sensitivity and selectivity of downstream biosensing or bioanalysis.

Overview

Given the complexity of most biological samples, sample preparation has been, and will be, one of the critical challenges in bioanalysis. Typically, most biosensing involves detection of low-concentration target molecules over molecular backgrounds with much higher concentrations. In genomic biosensing, this problem is largely

resolved by polymerase chain reaction (PCR), which can be used to increase the number of nucleotides with a specific sequence by several orders of magnitudes. However, in proteomic biosensing and bioanalysis, the issue of sample preparation still remains as a serious technical bottleneck, since there is no PCR equivalent for proteins and other biomolecules. For example, blood plasma or serum from any source is valuable for proteomics-based discovery of biomarkers for diseases or for discovery of novel drug targets. Detection of these proteins has potential diagnostic values; however, the major challenge is the complexity of common biomolecule samples. It is estimated that there are more than 10 000 protein species present in a serum sample. Moreover, most biomarker proteins are generally present at very low concentrations ($\ll$ pg/ml), while others, such as albumin and immunoglobulins, are present in very large amounts ($\gg$ mg/ml). This large concentration variation poses a formidable challenge to currently existing biomolecule detection techniques, most of which do not have low enough detection sensitivity and large enough dynamic range. It is expected, therefore, that the detection of low-abundance protein species or biomarkers would be possible only by better sample preparation and sorting. Conventionally, two dimensional (2D) protein gel electrophoresis, coupled with mass spectrometry (MS) has been the norm of proteomics research for decades, while multidimensional liquid chromatography coupled with MS is getting wider use due to ease of automation. Both techniques demonstrate similar separation peak capacity (up to ~ 3000) and dynamic range of detection ($\sim 10^4$) when coupled with MS.

Microfluidic engineering has the potential to improve the proteomic sample preparation processes significantly, by the automation and integration of many, laborious fractionation steps on a chip. While microfluidic devices for 2D protein separation [1] have already been demonstrated, the following technical issues still need to be addressed before the wider application of microfluidic 2D protein separation devices.

1. Preparatory separation should be able to process large sample volume. While small sample consumption is beneficial for some applications (such as single-cell analysis), most proteomic samples (blood, for example) are available in the volume larger than $\sim 1\,\mu L$. Most microfluidic separation systems are based on miniaturized capillary electrophoresis, which is essentially an analytic (not preparatory) technique. Therefore, the overall sample throughput and the detection sensitivity in such separation are limited.
2. Any preparatory separation device should be designed with the downstream sensing in mind. Many capillary electrophoresis separations utilize polymeric sieving media or reagents like carrier ampholytes, which are detrimental to most downstream detection systems (such as MS) by causing huge background and nonspecific binding.
3. Since there is no *PCR-like signal amplification* process for proteins or peptides, there must be efficient sample pre-concentration steps in the overall process. The low-abundance molecules could be efficiently separated, but in order to cover several-order-of-magnitude concentration ranges, one needs to concentrate these purified dilute, low-abundance species into higher concentration.
4. Usually, more than one separation strategy would be needed to deal with the complexity of proteome. However, there is a need for developing separation techniques by pI (isoelectric point) or size (kD), rather than other properties such as hydrophobicity. One reason is that size-based separation would be an ideal method to eliminate most abundant proteins (albumin/globulin) from a given sample, which are typically larger than signaling molecules. Also, fractionation based on size (kD) or pI values will significantly reduce database searching time at the end of MS (or tandem MS)-based proteomic analysis.

The above issues come from the fact that technical requirements for preparatory separation are quite different from those of analytic separation. For the last decade, many microchip-based separation processes have been developed, demonstrating high resolution and speed. However, the requirement for preparatory separation/fractionation is different from that of analytical separation. Generally speaking, resolution is less stressed while sample throughput becomes more important. Accordingly, to meet the demand for high throughput, continuous-phase separation (free-flow electrophoresis, transverse electrophoresis) has been gaining increasing popularity. In this continuous-flow mode separation, molecules are fractionated continuously into different streams, based on different molecular properties (size, charge, electrophoretic mobility, etc.). As a result, the biomolecules are separated and flow to different output channels at the end of the main separation chamber, where the fractionated samples can be collected continuously, as shown in Fig. 1. This eliminates the need for careful sample loading and ensures higher throughput. Typical biosample analysis could involve many (up to ~ 10) steps, which are currently of manual operation. Therefore, integration of different separation and fractionation steps is highly important, in order to build meaningful sample preparation microsystems. Two main challenges are buffer exchange and flow rate (volume) matching between each component. Some of the techniques that are very useful for analytical separation are

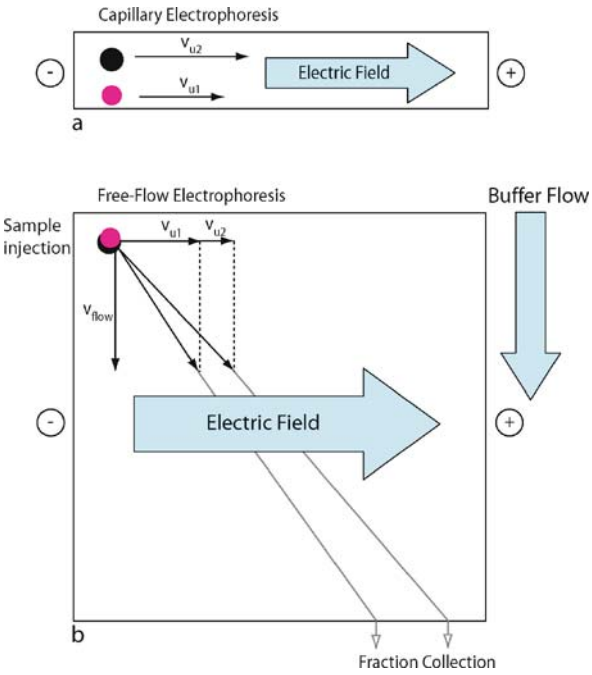

Biosample Preparation by Lab-on-a-Chip Devices, Figure 1 Comparison between (**a**) batch-mode capillary electrophoresis and (**b**) continuous-mode free-flow electrophoresis

not adequate for preparatory separation, because of specific buffer requirements or reagents to be used. Efficient buffer exchange methods in a microfluidic system have not been fully explored yet, as well as desalting of the sample (required for MS-based biosensing).

Basic Methodology

Filtration and Size-Based Separation

Gel filtration chromatography and gel electrophoresis are the two most commonly used techniques for separation of biologically relevant macromolecules (such as nucleic acids and proteins) based on size. Both techniques use gelatinous materials consisting of cross-linked three-dimensional pore networks, where the sieving interactions with the migrating biomolecules determine the separation efficiency. Depending on the relative size of the macromolecule compared with the gel mean pore size (e.g., the ratio of the radius of gyration R_g of the molecule to the gel mean pore size a), three basic separation mechanisms [2] have emerged to explain how flexible macromolecules migrate though a constraining gel medium – Ogston sieving ($R_g/a < 1$), entropic trapping ($R_g/a \sim 1$), and reptation ($R_g/a > 1$). In Ogston sieving, the macromolecule is smaller than the gel pores or constrictions, and the molecular sieving occurs because of steric interactions of the macromolecules with the gel pore network. Since $R_g/a < 1$, the molecules move rather freely through the gel matrix, assuming their unperturbed conformations. Entropic trapping applies when $R_g/a \sim 1$, and the conformation of the flexible macromolecule must deform or fluctuate to pass through the gel medium's spatial constrains. At each point, the number of accessible conformations defines the molecule's local entropy. Entropy differences derived from the gel medium's spatial heterogeneity drive molecules to partition or localize preferentially in less constrictive spaces, where their enhanced conformational freedom raises entropy. Reptation can be envisioned as a long flexible macromolecule occupying multiple pores threading its way through the gel in a snake-like fashion, which is very similar to the *reptation in a tube* process proposed by deGennes for entangled synthetic polymers. In reptation, only the end segments can escape as the molecule undergoes random curvilinear motion along the tube axis.

Both gel filtration chromatography and gel electrophoresis represent the current standard for size-based separation of biomolecules in laboratories. However, poor separation resolution in gel filtration chromatography and difficult sample recovery with gel electrophoresis make neither method optimal in separating complex mixtures for downstream analysis. Various microchip-based separation systems have been developed by using liquid or solid polymeric materials as sieving media contained in microchannels, and such systems have demonstrated fast separation of various biomolecules (e.g., DNA, proteins and carbohydrates) with rather high resolution [3, 4]. However, the foreign sieving matrices pose intrinsic difficulties for the integration of automated multistep bioanalysis microsystems. Furthermore, these microchip-based systems are limited to analytical separation of biomolecules, due to the difficulty of harvesting purified biomolecules for downstream analysis.

Recently, there has been great interest in switching from disordered porous gel media to patterned regular sieving structures, in the hope of achieving more efficient separation than gels in terms of separation speed and resolution [5]. While there are many different techniques to fabricate micrometer- or nanometer-sized sieving pores, it is sometimes more important to consider and understand the detailed molecular interaction with micro- or nanopore sieves before designing a molecular filter. Biomolecule interaction with molecular filters or sieves can be quite complicated, especially for the case of biopolymers such as long DNA. Intuitions based on filtration process of macroscopic objects can be quite misleading for the interaction between nanosized molecular sieves and nanometer-sized biomolecules in liquid environments.

Charge-Based (pI-Based) Separation

The charge density of biomolecules is related to their electrophoretic mobility; therefore electrophoresis in a free solution (*capillary zone electrophoresis (CZE)*) can be a method to separate biomolecules based on the charge density. The free solution electrophoretic mobility μ_e is a characteristic feature of each analyte, which is determined by the complicated balance among the electrical driving force on the analyte, electrical driving force on the counterions within the Debye layer on the analyte backbone and the frictional force from the surrounding fluid. Therefore, it is not a trivial matter to determine or calculate the electrophoretic mobility of a given protein/peptide *a priori* from the sequence information. Also, electrophoretic mobilities of many proteins among a given proteome can be similar. Therefore, the CZE is not an ideal technique for separating a very complex protein mixture for sample preparation purposes.

The most powerful variant for charge-based separation is *isoelectric focusing (IEF)*. To perform this separation technique, a linear pH gradient has to be established first either in the gel or in the microchannel. Once the pH gradient has been established, the biomolecules such as proteins and peptides migrate to the position where the pH equals their specific isoelectric point (pI). At this specific position, the net charge of the molecules becomes zero and they stop migrating. Molecules with different pI values focus at different positions with the pH gradient, thus allowing an effective charge-based separation of the molecules. This is a powerful fractionation technique because pI of a given target protein can be easily and accurately estimated from amino acid sequences; therefore one can collect and analyze only the pI region of interest. This could significantly cut down database searching time after MS detection, which can be quite time-consuming.

Because of its utility, IEF has been employed in many different forms even at macroscopic scales. Miniaturization of IEF would have benefits of employing small potentials. In IEF, the separation resolution does not depend of the length of the channel. The focused peak width σ can be given as the following equation:

$$\sigma = \sqrt{\frac{D\left(dx/d(\mathrm{pH})\right)}{E\left(d\mu/d(\mathrm{pH})\right)}} \sim \frac{L}{\sqrt{V}} \tag{1}$$

Here, D is the diffusion constant of the protein, E ($= V/L$, L is the channel length) is the electric field and μ is the mobility of the protein. While $\mathrm{d}\mu/\mathrm{d}(\mathrm{pH})$ is an inherent property of the protein, $\mathrm{d}x/\mathrm{d}(\mathrm{pH})$ (pH gradient in length) scales as $\sim L$ for a given pH range determined by the ampholyte used in the experiment. The separation resolution R_s is given as $\sim d/\sigma$, where d is the separation distance in the microchannel between the two peaks of interest. Since d also scales as $\sim L$, R_s is only proportional to $V^{1/2}$, independent of the length of the channel L. In other words, for a given applied potential, the separation resolution does not change as the channel length is decreased, because of increased field strength in the channel makes the focused peak narrower. However, the time it takes to achieve IEF in the channel is decreased, because of shorter channel length as well as higher electric field strength.

One important consideration for the miniaturization would be the ways to achieve a pH gradient. The best resolution can be achieved by immobiline gel, where ampholyte chemical groups are polymerized into a gel. The other method to obtain a pH gradient is to use carrier ampholytes in solution form. The ampholytes are small buffer molecules with a wide range of isoelectric points that form a pH gradient when an electric field is applied. Typically, the electric field is generated between a basic solution (catholyte) such as ammonium hydroxide at the cathode and an acidic solution (anolyte), e.g. phosphoric acid, at the anode. It is possible to establish a natural pH gradient, relying on reduction–oxidation process near the electrode [6]. However, such a natural pH gradient is not stable enough for practical applications. Instead, adding carrier is preferred, in order to obtain more stable pH gradient. This is true even when immobiline gel is used. More stable separation is achieved by adding carrier ampholytes to the gel solution. Therefore, the use of carrier ampholytes has been the method of choice for microfluidic IEF devices. This, however, can interfere with subsequent analysis such as MS.

Isotachophoresis utilizes two different buffer systems, one as the leading electrolyte and the other as the trailing electrolyte. The leading electrolyte has a higher mobility than that of the analytes while the trailing electrolyte has a lower mobility. When an electric field is applied, the ions of the leading electrolyte migrate fastest and those of the trailing electrolyte slowest. Then, the ions of the analytes spread into the gradient of the electrical strength set by the mobilities of the terminating electrolytes. However, for practical applications, it is often difficult to find the appropriate terminating electrolytes with the required mobilities. The other limiting factor for this separation technique is that the ions have to be of the same polarity in order to be separated.

Affinity-Based Separation

The affinity-based sample preparation method on microchips is another powerful tool for separation of biomolecules. Conventional affinity-based separation

methods such as liquid chromatography or affinity chromatography have been successfully implemented in microfluidic chip format. The way the chromatography works in the microchannel is essentially the same as in the conventional method. In capillary electrochromatography (CEC), which combines the separation power of both liquid chromatography and capillary electrophoresis, the analyte is forced through a column of the stationary phase by electroosmosis instead of pressure. After this step, the gradient elution with a varying solvent composition, for instance 5% to 50% methanol, flows across the column and separates the analyte mixture depending on how well it mobilizes the analyte. The more hydrophobic component will elute first if the methanol content is high. However, when the methanol concentration is low, the hydrophilic analyte will elute more readily. The affinity chromatography is based on the specific interaction between an immobilized ligand and the target protein to be separated.

The last two variants of affinity-based separation are *micellar electrokinetic chromatography (MEKC)* and *electrochromatography (EC)*. MEKC uses surfactants which form micelles as pseudo-stationary phase in the microchannel. During electrophoresis, the analytes partition into the micelles depending on their hydrophobicity. Through the interaction with the micelles, the retention time of the molecules can be increased. In this way, even neural molecules can be separated. Electrochromatography utilizes an electrokinetic flow instead of pressure-driven flow to bring the mobile phase through a packed bed consisting of silica with a large negative surface charge. This induces an electro-osmotic flow (EOF) which drives the separation. A plug-like velocity profile brings a higher efficiency than HPLC.

Signal Amplification and Preconcentration

Several research groups have reported ways to preconcentrate samples in "Lab-on-a-Chip" devices. While most on-chip preconcentration approaches evolve from conventional capillary electrophoresis and chromatographic column techniques, these preconcentration techniques play an increasingly important role in chip-based system. The basic preconcentration strategies applied on microfluidic devices can be classified into three large categories: electrokinetic preconcentration, chromatographic preconcentration and membrane preconcentration.

Electrokinetic Preconcentration

Field-amplified stacking (FAS) (Fig. 2a) is a technique with a long history, first introduced by Mikkers et al. in the late 1970s [7].

The mechanism relies on manipulating buffer concentration to achieve local field amplification. The relation between the electrical field (E) and buffer concentration (C) can be defined by the relative conductive (γ) as:

$$\gamma = \frac{c_L}{c_H} = \frac{\sigma_L}{\sigma_H} = \frac{E_{\text{buffer}}}{E_{\text{sample}}} \tag{2}$$

As a result, when we introduce low conductivity (σ_L) sample plug into capillaries or microfluidic channels with high conductivity running buffer, most of the potential drop will be applied onto the injected sample. This locally amplified field will therefore drive/stack sample to the ends of the plug by electrophoretic force. With a given plug size, one can increase the enhancement factor by increasing the relative conductivity. Even though FAS is one of the simplest preconcentration schemes to implement on microchips, the band broadening at the stacking boundary caused by hydrodynamic mixing from both flow injection and mismatched EOF makes it difficult to have highly focused peak.

Transient isotachophoresis and *micellar electrokinetic sweeping* can be viewed as extensions of the stacking concept of FAS. In the case of isotachophoresis, with the understanding of a sample's electrophoretic mobilities, the sample plug is sandwiched by leading electrolyte (LE) and terminating electrolyte (TE) instead of the same high conductivity buffer. Based on the order of descending mobilities, the constituents will separate into distinct zones between high mobility LE and low mobility TE (relative to sample constituents) upon the application of the separation voltage. Moreover, once the steady-state gradient is achieved, the boundaries between samples can be maintained by a self-focusing mechanism which alleviates the dispersion problem from which FAS suffers. Both FAS and isotachophoresis use buffer manipulation to achieve local field enhancement that helps sample stacking. Micellar electrokinetic sweeping, on the other hand, works on changing the electrophoretic mobilities of samples by labeling them with micelle compounds (surfactants). Once the correct compound is chosen, one can use a small plug of fast moving micelle compounds to sweep samples rapidly out of the sample zone by hydrophobic interaction. The enhancement factor of micellar electrokinetic sweeping can be further improved by coupling with FAS, however, it is still limited by analytes' affinity to the micellar compounds.

While FAS and its related techniques are well-established, their merit for sample preparation device is limited since these techniques usually require special buffer arrangements or reagents in the system. *Electrofocusing* (Fig.2b) is another class of techniques used to collect and concen-

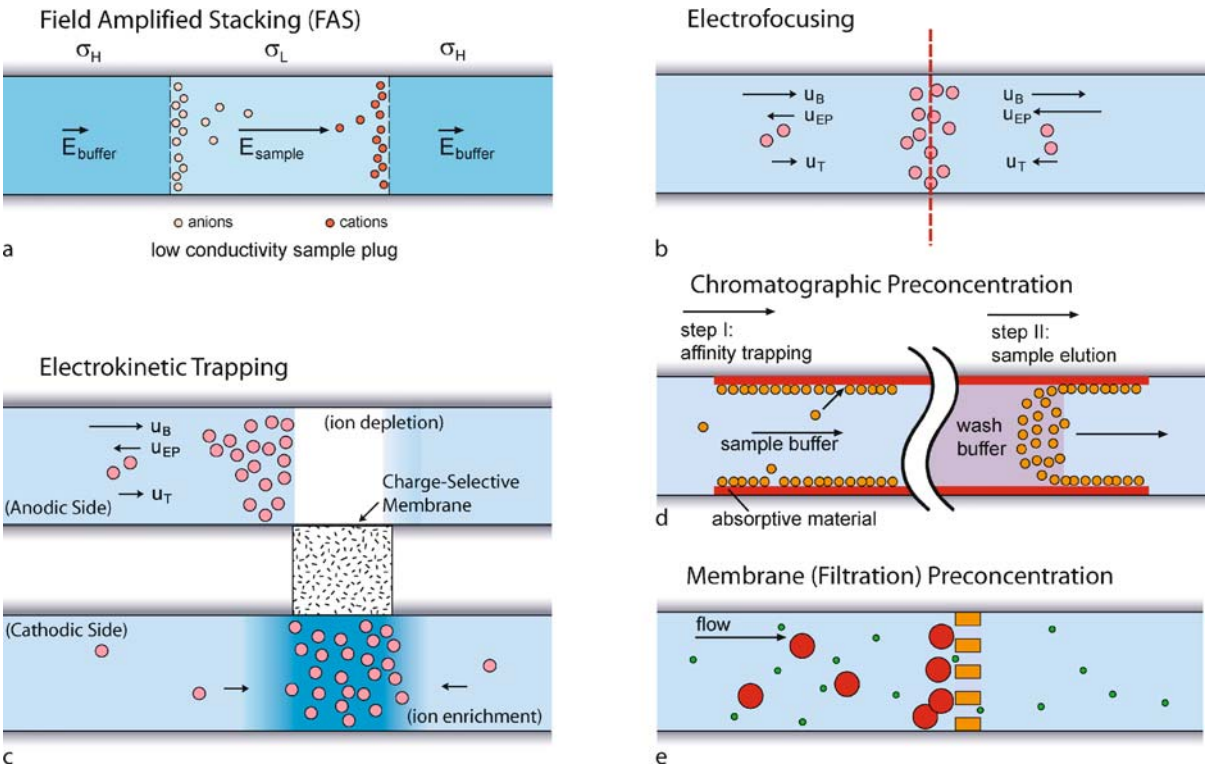

Biosample Preparation by Lab-on-a-Chip Devices, Figure 2 Various types of preconcentration strategies. (**a**) Field amplified stacking, (**b**) electrofocusing (various types), (**c**) electrokinetic trapping (both anodic and cathodic side), (**d**) chromatographic preconcentration and (**e**) membrane preconcentration

trate analytes by manipulating both hydraulic and electrophoretic driving forces in the microchannel. Electrofocusing can occur whenever the net molecular velocity profile is converging, as shown in Fig.2b, by either controlling the flow and/or electric field of the two zones. Such a condition can be obtained by changing channel geometry, electric field of each zone or temperature of each zone. Electrofocusing can be achieved in a continuous fashion (collection of molecules until enough concentration is reached), and does not require any special buffers or ionic strength arrangements. However, the collection would be critically dependent on the specific electrophoretic mobility of the target.

Another novel electrokinetic preconcentration technique is *electrokinetic trapping* (Fig.2c), utilizing unique electrokinetic properties of perm-selective membranes. As a perm-selective membrane, one can use traditional membranes (such as Nafion®), nanochannels or charged polymer monoliths. When a current is applied through such a perm-selective membrane/nanochannel, concentration polarization of ions can occur (even at moderate buffer concentrations), causing the ion concentration of anodic side to decrease (ion depletion) and that of cathodic side to increase (ion enrichment). Both phenomena can be (and have been) utilized for concentrating biomolecules. In the cathodic side, biomolecules and ions can be enriched due to the ion enrichment process. In the anodic side, ion depletion region can be used in a similar manner as a *stacking boundary*, although the physical mechanism in this case is different from FAS. Unlike FAS, both cations and anions are collected at the same boundary. This is because both ionic species are *repelled* by concentration polarization process from the membrane/nanochannel. The advantage of electrokinetic trapping is that the preconcentration can be less sensitive to specific molecular electrokinetic properties (such as electrophoretic mobility), therefore providing a generic way for various types of molecules. However, concentration polarization and related phenomena are generally poorly understood, and the linearity and stability of the trapping is sometimes an issue.

Chromatographic Preconcentration

Chromatographic preconcentration (Fig.2d) is also called solid-phase extraction. It usually involves two steps. First, analytes are retained by affinity binding force onto an

appropriate stationary subject. Then, with the application of elution buffer, the analytes can be eluted into a more concentrated form. Non-microfluidic examples of this strategy are widely used, such as commercially available trap column for mass spectrometry and SELDI (surface-enhanced laser desorption and ionization)-MS. Affinity reagents and bead systems are well-developed for trapping proteins and peptides and commercially available, which makes its implementation to microfluidic format rather straightforward. Also, chromatographic preconcentration techniques can also desalt biosamples, which is another important benefit especially for MS. One of the drawbacks of chromatographic preconcentrations, however, is that the preconcentration can be biased (hydrophobic vs. hydrophilic), and the washing (elution) step could potentially re-dilute the concentrated plugs. In addition, chromatographic preconcentration can be limited by the number of binding sites (binding surface area) in the systems.

Membrane Preconcentration

In membrane preconcentration (Fig.2e), gel or porous membranes are used to concentrate molecules bigger than the size of the pores. By adjusting the pore size, one can allow the passage of buffer ions and small molecules but exclude larger molecules of interest. With the formation of nanofilters or nanoporous membranes within the microfluidic systems, this strategy can be implemented easily. Membrane (filtration)-based preconcentration will not have any chemical bias (mainly dependent on the size of the molecule), but continuous membrane filtration could generate eventual clogging of the system, which is one of the main problems in this technique.

Key Research Findings

Filtration and Size-Based Separation

For size-separation of biomolecules, it is imperative to have a molecular sieving structure incorporated in the system. Formation of polyacrylamide gel in a microchannel is one viable option, but solid-state, artificial sieving systems are much preferred due to their mechanical and chemical stability. Artificial molecular sieving systems can be fabricated using a variety of techniques [8–13], such as colloidal templating, anodized alumina pore fabrication, packed nanospheres, superparamagnetic particle arraying, standard photolithography and e-beam lithography.

Regular arrays of micrometer- or nanometer-sized pillars have been fabricated by different groups with either photolithography (with pillar diameter and spacing down to 1 μm) or e-beam lithography (with pillar diameter and spacing down to 100 nm) on silicon substrates. The advantages of such microlithographically fabricated devices include the precise control over the sieving matrix geometry and the design flexibility. By applying two alternating electric fields of different directions and different magnitudes, Huang et al. recently devised a *DNA prism* device that can continuously separate long DNA molecules with high speed [14]. In this design, the longer DNA molecules only follow the strong electric field component while the shorter ones migrate in the direction of the sum electric field vector. However, their application was largely limited to rather large biomolecules (long DNA).

The concept of Brownian ratchets has been applied to construct asymmetric obstacle courses that provide a spatially asymmetric steric potential for biomolecule separation [15, 16]. The basic idea is to use such asymmetric obstacles to rectify the Brownian motion laterally and thereby to deflect diffusing biomolecules based on their sizes. So far, the Brownian ratchet systems have been successfully demonstrated for long DNA and phospholipids [15, 16], even though the separation resolution reported so far was not ideal.

More recently, a microfabricated nanofilter array system was developed, which can be used for separating various biomolecules such DNA molecules and proteins [17, 18]. The unique feature of this class of molecular filters is that only standard photolithography is needed to create ~ 10 nm sized molecular filters. Using the same system, one can employ different sieving mechanism. For long DNA molecules, entropic trapping mechanism is used, while small DNA and proteins can be separated by Ogston sieving mechanism. These devices demonstrated speed and resolution comparable to or better than the conventional techniques (i. e. pulsed field gel electrophoresis for long DNA, and capillary gel electrophoresis for proteins). One important advantage of a nanofilter array system is that the separation efficiency could be further improved by increasing the nanofilter density, by using advanced high-resolution (photo or e-beam) lithography techniques.

In terms of sample preparation, continuous-flow separation is also highly desirable for micro-/nanofluidic devices because of the low sample throughput. We choose two recent developments here that we believe represent the current advance of this particular exciting area: the *Tango* device (or the bump array) (by Huang et al. [19]) that separates long DNA molecules by asymmetric bifurcation of laminar flow [19], and the anisotropic nanofilter array (ANA) (by Fu et al.) that separates DNA and proteins based on the different sieving characteristics along two orthogonal directions within the ANA structure [18]. The Tango device employed arrays of micrometer-sized pillars and spacing, with each pillar column slightly shifted with respect to the previous one in a direction perpendicular to

the flow direction. Longer DNA molecules are displaced as they flow through the pillar array while shorter DNA molecules remain in the feeding streamlines (i. e. the deterministic lateral displacement), leading to efficient separation. It is believed that as the gap size of pillar array is reduced using nanofabrication, the Tango device can be used to fractionate biologically relevant molecules. The design of the ANA consists of a 2D periodic nanofilter array, and the designed structural anisotropy in the ANA causes different sized biomolecules to follow radically different trajectories leading to separation. So far, continuous-flow Ogston sieving-based separation of short DNA and proteins as well as entropic trapping-based separation of long DNA molecules have been demonstrated with the ANA structure. The design of the structural anisotropy is the key for the continuous-flow biomolecule separation, and it can be applied to any sieving mechanism across the nanofluidic sieving structure along the orthogonal direction (size-, charge- or hydrophobicity-based) that can lead to differential transport across the nanofilters. Highly efficient, continuous-flow molecular separation would be possible as long as one can create a separation system that is *anisotropic* in nature.

Charge-Based Separation

IEF-based sample fractionation devices have been developed and commercialized, but miniaturizing them into a microfluidic format is being studied actively. Especially, there have been tremendous efforts to increase the throughput of charge-based separation by operating the microfluidic device in a continuous mode. The Yager group from the University of Washington fabricated a multi-stacked Mylar continuous-flow separation device with palladium electrodes in direct contact with the solution. Since the electrodes were in direct contact with the solution, only a small voltage, 2.3 V, could be applied over a 1.27 mm wide channel [6]. Because of the small distance, however, it generated sufficient electric field, ~ 18 V/cm, for the separation of a binary mixture of proteins. The same group used the electrolysis of the buffer, H^+ at the anode and OH^- at the cathode, to generate a natural pH gradient across the microchannel without using any carrier ampholytes [6]. This low-voltage approach, however, requires a significant amount of time for separation at around 4 minutes. To reduce the separation time, Zhang et al. developed a high-voltage μ-FFE (free flow electrophoresis) device by isolating the separation channel from the electrode reservoirs using narrow (4 μm wide) microchannels [20]. Their FFE microchip with 10 μm deep channels in a polydimethylsiloxane (PDMS) substrate allowed an electric field up to 270 V/cm and they could successfully separate two fluorescent dyes, rhodamine 110 and fluorescein, as well as two amino acids in 2 s. However, the high voltage induced a strong EOF which deteriorated the separation result. The μ-FFE device developed by Kohlheyer incorporates two new improvements compared to the previous ones [21]. First, it is a multifunctional μ-FFE device which can perform free-flow zone electrophoresis and free-flow IEF. Depending on the separation method to be used, the only parameter to be changed is the width of the sample by hydrodynamic focusing. This can be performed easily on the run by changing the flow rates in the two side channels. Second, they implemented a polymerized acrylamide as the salt bridge between the main separation channel and the electrode reservoirs. This proved to be more effective in suppressing the EOF than the microchannel as the salt bridge. Isotachophoresis (ITP) has been also realized in microchip format for the free-flow electrophoresis [22]. A sample mixture of fluorescein, eosin G and acetylsalicylic was separated in less than a minute. Song et al. developed a novel ampholyte- and gel-free pI-based continuous-flow sorting technique [23]. Their method differs from previous approaches in that this continuous sorting process involves no external power supply and no special ampholytes. Instead, they utilized the diffusion potential generated by the diffusion of different ionic species in situ at the laminar flow junction.

Free-flow electrophoresis has also been successfully applied to separate subcellular particles such as organelles (mitochondria) [24]. This is facilitated by the fact that these particles contain many different proteins and amphoretic molecules. The sorting in microscale devices offers obvious advantages compared to the conventional ones. Less heat is generated by using only ~ 2 V compared to 2000 V of conventional devices and this causes less damage of organelles. The result shows that free-flow electrophoresis can be applied to various organelles, even for organelles that are larger and do not have uniform pI values.

Affinity-Based Separation

While the technology for affinity-based separation is very well developed for capillary-based separation, chromatography in microchips has not been as popular as electrophoresis, mainly due to the difficulty in packing microchannels with beads. In particular, if the channels are not straight but are curved into serpentine configurations, it is quite a challenge to achieve a uniform packing of the channels. Instead of packing affinity beads, creating a polymer monolith [25, 26] is much preferred, with controlled, relatively uniform pore sizes, variety of chemical groups one can incorporate into the system, and covalent

linkage to the channel wall (therefore no need of frits to hold the monolith stationary).

Often, fittings for microfluidic systems cannot handle the high pressure required for chromatographic separation, and electrokinetic flow can be used in lieu of pressure-driven flow. Using the microchip chromatography, driven either by elecroosmosis or pressure, a separation of low-molecular-weight neutral and basic compounds and acidic proteins has been demonstrated. He et al. demonstrated CEC of peptides in a microfabricated system [27]. They mimicked the packed bed by etching an array of support structures into a quartz substrate, the so-called collocate monolith support structures. These columns were prepared with polystyrene sulfate for stationary phase. A mixture of tryptic peptides from ovalbumin was separated in the CEC isocratically as opposed to the gradient elution mode.

In capillary-based separations, technologies based on microbeads with specific chemistry are well-developed and mature, and utilizing such bead systems in microfluidic channels would be of tremendous value. Oleschuk et al. developed a design that allows exchange of packing materials [28]. This can be utilized for solid-phase extraction (SPE) and CEC. Using CEC, a separation of BODIPY and fluorescein could be achieved with a mobile-phase composition of 30% acetonitrile / 70% aqueous 50 mM ammonium acetate. The BODIPY is hydrophobic and has a higher affinity for the column than the fluorescein, causing slower elution of BODIPY. In addition to affinity-based separations, microchannels with packed beads could provide other functionalities for microfluidic sample preparation systems, such as peptide digestions [29, 30], removal of majority proteins and extraction of DNA from cells [31]. It was shown that peptide digestion reaction can be significantly expedited ($\sim$ 10 min) compared with solution-phase digestion process.

Signal Amplification and Preconcentration

Given the importance of sample preconcentration in many biosensing applications, several sample preconcentration techniques, including field-amplified sample stacking (FAS), isotachophoresis (ITP), electrokinetic trapping, micellar electrokinetic sweeping, chromatographic preconcentration, electrofocusing (various types) and membrane filtration preconcentration have been developed. Each technique has its own advantages and disadvantages.

Field-Amplified Stacking and Other Related Techniques

FAS can be implemented on microchips in a very similar manner as capillary electrophoresis. However, the requirement of low ionic strength sample buffer for FAS puts limitation on its use as general preconcentration technique. Variations of the technique, such as transient isotachophoresis and micellar electrokinetic sweeping, have been more successfully used. Jung et al. reported on-chip transient isotachophoresis by introducing TE and LE into a T-junction simultaneously to achieve fast sample loading, preconcentration and separation [32]. Micellar electrokinetic sweeping, pioneered by the Terabe group, combines field-amplified stacking with affinity concentration using micelles [33], and provides very high concentration factors. These techniques were originally developed for capillary electrophoresis; therefore they are well suited for enhancing the sensitivity of microchip-based separation and detection. However, they require special arrangements of buffers with different ionic concentrations, which makes the coupling to the downstream biosensing challenging, limiting their use as sample preparation devices. For example, micellar electrokinetic sweeping relies on a detergent additive (sodium dodecyl sulfate), which has a negative impact on the downstream analysis.

Electrofocusing and Electrokinetic Trapping

Newer techniques such as electrofocusing and electrokinetic trapping could be ideal alternatives for proteomic sample preconcentration. One of the benefits electrofocusing offers is that the collection can be run continuously, and therefore, concentration can be arbitrarily increased (with a limitation imposed by crystallization and other technical issues). Electrofocusing can continuously collect molecules by applying two different (electrophoretic and hydraulic, typically) driving forces in the opposite direction in a microchannel or capillary to trap molecules. Various types of electrofocusing [34–37], which differ in the method to generate a gradient in electrophoretic mobility (temperature, electric field, etc.), have been demonstrated in microfluidic and capillary systems. Depending on the focusing time, these techniques can achieve typically up to $\sim 10^5$-fold concentration enhancement.

Electrokinetic trapping techniques [38–41] have been recently demonstrated as an efficient way of concentrating protein samples. Different membrane materials can be used, such as polymer monolith (Singh and coworkers), Nafion® (Swerdlow and coworkers), nanochannels (Han and coworkers) and even PDMS (Kim et al.). These techniques demonstrate impressive concentration factors (up to $\sim 10^6$) as well as the flexibility to be coupled to downstream analysis. These techniques are dependent on the ion depletion and concentration polarization, which as a generic process are quite common to most nanoporous membrane systems. Therefore, there is no specific buffer

requirement, as long as the ionic strength is moderate (~ 10 mM or less).

Chromatographic Preconcentration/Membrane Preconcentration

Several groups [42, 43] have demonstrated affinity-based molecular preconcentration systems in a microfluidic format. Affinity chemical groups can be directly coated to the surface of the glass microchannel, although techniques using microbeads (Harrison and coworkers) and polymer monoliths (Frechet and coworkers) provide better functionality, larger binding surface area and flexibility in fabrication and integration. The concentration factor in these systems is eventually determined by the surface binding area. For efficient capturing from larger sample volume (~ 1 μL or more), a larger microchannel is required.

Membrane preconcentration [44, 45] is a microscale version of membrane filtration and dialysis, which is well established. Typically gel or other polymeric materials (Singh and coworkers) as well as nanofluidic channels/solid membranes (Ramsey and coworkers) are used as a molecular filter. An advantage of this technique is that one can combine preconcentration with filtration/separation in a single step. A disadvantage of this technique would be that it becomes progressively more difficult for smaller proteins and peptides, and it is also limited by the ambiguity of the molecular weight cutoff of the nanoporous filter membrane materials. Even in the case of regular nanofilters, molecular size filtration of biomolecules can be quite complicated due to conformation changes of biomolecules.

Future Directions for Research

The importance of sample preparation in bioanalysis is expected to draw more attention in the future, since this is currently one of the major bottlenecks in biosensing. For preparatory separation, continuous-flow fractionation is much preferred over elution-type separation, due to the flexibility of integration and higher sample processing rates. More and more fractionation techniques would be made into a continuous-flow format, possibly by adopting anisotropic sieving system designs. Since typical sample preparation could easily involve many (up to ~ 10) different separation/reaction/preconcentration processes, integration of these individual steps on a single device would be highly desirable for practical application. Recent developments in sample preconcentration devices have the potential to enhance any new and existing biosensors in terms of sensitivity and selectivity, if properly integrated with preparatory separation steps.

Cross References

- ► Isoelectric Focusing
- ► Electrokinetic Flow and Ion Transport in Nanochannels

B

References

1. Rocklin RD et al (2000) A microfabricated fluidic device for performing two-dimensional liquid-phase separations. Anal Chem 72:5244–5249
2. Viovy JL (2000) Electrophoresis of DNA and other polyelectrolytes: Physical mechanisms. Rev Mod Phys 72:813–872
3. Woolley AT et al (1994) Ultra-high-speed DNA fragment separations using microfabricated capillary array electrophoresis chips. Proc Natl Acad Sci USA 91:11348–11352
4. Yao S et al (1999) SDS capillary gel electrophoresis of proteins in microfabricated channels. Proc Natl Acad Sci USA 96:5372–5377
5. Volkmuth WD et al (1992) DNA Electrophoresis in Microlithographic Arrays. Nature (London) 358:600–602
6. Macounova K et al (2000) Generation of Natural pH Gradients in Microfluidic Channels for Use in Isoelectric Focusing. Anal Chem 72:3745–3751
7. Mikkers FEP et al (1979) High-performance zone electrophoresis. J Chromatogr 169:11–20
8. Turner SW et al (1998) Monolithic nanofluid sieving structures for DNA manipulation. J Vac Sci Technol B 16:3835–3840
9. Han J et al (1999) Entropic trapping and sieving of long DNA molecules in a nanofluidic channel. J Vac Sci Technol A 17:2142–2147
10. Doyle PS et al (2002) Self-assembled magnetic matrices for DNA separation chips. Science 295:2237
11. Sano T et al (2003) Size-exclusion chromatography using self-organized nanopores in anodic porous alumina. Appl Phys Lett 83:4438–4440
12. Baba M et al (2003) DNA size separation using artificially nanostructured matrix. Appl Phys Lett 83:1468–1470
13. Tabuchi M et al (2004) Nanospheres for DNA separation chips. Nat Biotechnol 22:337–340
14. Huang LR et al (2002) A DNA prism for high-speed continuous fractionation of large DNA molecules. Nat Biotechnol 20:1048–1051
15. Chou C-F et al (1999) Sorting by diffusion: An asymmetric obstacle course for continuous molecular separation. Proc Natl Acad Sci USA 96:13762–13765
16. van Oudenaarden A et al (1999) Brownian Ratchets: Molecular Separations in Lipid Bilayers Supported on Patterned Arrays. Science 285:1046–1048
17. Han J et al (2000) Separation of Long DNA Molecules in a Microfabricated Entropic Trap Array. Science 288:1026–1029
18. Fu J et al (2006) Patterned anisotropic nanofluidic sieving structure for continuous-flow separation of DNA and protein. Nat Nanotech 2 121–128
19. Huang LR et al (2004) Continuous particle separation through deterministic lateral displacement. Science 304:987–990
20. Zhang C-X et al (2003) High-Speed Free-Flow Electrophoresis on Chip. Anal Chem 75:5759–5766
21. Kohlheyer D et al (2006) Free-flow zone electrophoresis and isoelectric focusing using a microfabricated glass device with ion permeable membranes. Lab Chip 6:374–380
22. Janasek D et al (2006) Isotachophoresis in Free-Flow Using a Miniaturized Device. Anal Chem 78:3815–3819

23. Song Y-A et al (2006) Continuous-Flow pI-Based Sorting of Proteins and Peptides in a Microfluidic Chip Using Diffusion Potential. Anal Chem 78:3528–3536
24. Lu H et al (2004) A Microfabricated Device for Subcellular Organelle Sorting. Anal Chem 76:5705–5712
25. Yu C et al (2000) Towards stationary phases for chromatography on a microchip: Modeled porous polymer monoliths prepared in capillaries by photoinitiated in situ polymerization as separation media for electrochromatography. Electrophoresis 21:120–127
26. Ericson C et al (2000) Electroosmosis- and Pressure-Driven Chromatography in Chips Using Continuous Beds. Anal Chem 72:81–87
27. He B et al (1999) Capillary electrochromatography of peptides in a microfabricated system. J Chromatogr A 853:257–262
28. Oleschuk RD et al (2000) Trapping of Bead-Based Reagents within Microfluidic Systems: On-Chip Solid-Phase Extraction and Electrochromatography. Anal Chem 72:585–590
29. Wang C et al (2000) Integration of immobilized trypsin bead bed for protein digestion within a microfluidic chip incorporating capillary electrophoresis separations and an electrospray mass spectrometry interface. Rapid Commun Mass Spectrom 14:1377–1383
30. Jin LJ et al (2003) A microchip-based proteolytic digestion system driven by electroosmotic pumping. Lab Chip 3:11–18
31. Tian H et al (2000) Evaluation of Silica Resins for Direct and Efficient Extraction of DNA from Complex Biological Matrices in a Miniaturized Format. Anal Biochem 283:175–191
32. Jung B et al (2006) On-chip Millionfold Sample Stacking Using Transient Isotachophoresis. Anal Chem 78:2319–2327
33. Quirion JP et al (1998) Exceeding 5000-Fold Concentration of Dilute Analytes in Micellar Electrokinetic Chromatography. Science 282:465–468
34. Hori A et al (1993) Electroconcentration by Using Countercurrent due to Pressurized Flow and Electrophoretic Mobility. Anal Chem 65:2882–2886
35. Huang Z et al (1999) Digitally Controlled Electrophoretic Focusing. Anal Chem 71:1628–1632
36. Ross D et al (2002) Microfluidic Temperature Gradient Focusing. Anal Chem 74:2556–2564
37. Humble PH et al (2004) Electric Field Gradient Focusing of Proteins Based on Shaped Ionically Conductive Acrylic Polymer. Anal Chem 76:5641–5648
38. Singh AK et al (2002) In: Micro Total Analysis Systems, vol 1. Kluwer, Nara, Japan, pp 347–349
39. Astorga-Wells J et al (2003) Fluidic Preconcentrator Device for Capillary Electrophoresis of Proteins. Anal Chem 75:5207–5212
40. Wang Y-C et al (2005) Million-fold Preconcentration of Proteins and Peptides by Nanofluidic Filter. Anal Chem 77:4293–4299
41. Kim SM et al (2006) Electrokinetic Protein Preconcentration Using a Simple Glass/Poly(dimethylsiloxane) Microfluidic Chip. Anal Chem 78:4779–4785
42. Li J et al (2001) Integrated system for high throughput protein identification using a microfabricated device coupled to capillary electrophoresis/nanoelectrospray mass spectrometry. Proteomics 1:975–986
43. Yu C et al (2001) Monolithic Porous Polymer for On-Chip Solid-Phase Extraction and Preconcentration Prepared by Photoinitiated in Situ Polymerization within a Microfluidic Device. Anal Chem 73:5088–5096
44. Khandurina J et al (1999) Microfabricated Porous Membrane Structure for Sample Concentration and Electrophoretic Analysis. Anal Chem 71:1815–1819
45. Song S et al (2004) Electrophoretic Concentration of Proteins at Laser-Patterned Nanoporous Membranes in Microchips. Anal Chem 76:4589–4592

Biosecurity

► Lab-on-Chip Devices for Biodefense Applications

Biosensor

Definition

A *biosensor* is a device for the detection of an analyte that combines a biological component with a physicochemical detector component.

It consists of 3 parts:

- the *sensitive biological element* , including biological material (eg. tissue, microorganisms, organelles, cell receptors, enzymes, antibodies, nucleic acids etc) and a biologically derived material or biomimic).
- the *transducer* in between (associates both components)
- the *detector element* (works in a physicochemical way; optical, piezoelectric electrochemical, thermometric, or magnetic.)

Cross References

► Biosensor
► Acoustics Based Biosensors
► Impedimetric Biosensors for Nano- and Microfluidics

Biosensors Using Atomic Force Microscopes

SUIJIAN QI, CHANGQING YI, MENGSU YANG
Department of Biology and Chemistry, City University of Hong Kong, Kowloon Tong, Hong Kong SAR
bhmyang@cityu.edu.hk

Synonyms

Biosensors using scanning force microscope; Cantilever biosensors; Force-based biosensors; AFM biosensors; Force biosensors

Definition

Biosensors using ►atomic force microscopes (AFMs) are devices which employ an atomic force microscope for biological recognition events. The principle of biosensors

using atomic force microscopy is mainly based on the mass-sensitive detection of binding events that change the deflection of a ►cantilever whose surface is modified with immobilized bioreceptors.

Overview

A ►biosensor, which exploits a biological detection or recognition system for target molecules, typically consists of three components: the transducer, the detector and the signal output. The core of a biosensor is the physicochemical transducer which converts the biological recognition event into a useable output signal. There are numerous studies that integrate various detection schemes with biosensors, which can be categorized into optical detectors (for example, UV-Vis absorption, fluorescence, and chemiluminescence), electrochemical detectors (for example, amperometry, potentiometry, and conductometry) and mass spectrometric (MS) detectors according to the different detection principles. Recently, state-of-the-art AFMs have also entered into the biosensing area as highly sensitive detectors.

AFM is a type of scanning probe microscope with very high resolution, and is one of the foremost tools for imaging, measuring and manipulating matter at nanoscale level. An AFM mainly consists of a microscale cantilever (with a sharp tip), an optical deflection system and a sample stage (Fig. 1a). AFM has basically been used as a high-resolution imaging tool to "feel" the topography of a sample and it has the ability to visualize the atomic and molecular structure of sample surfaces. In the imaging mode of AFM, the sharp tip at the end of the cantilever is raster-scanned over the surface of a sample. As the tip approaches the surface, the cantilever deflects as a result of the interaction forces between the tip and the surface of the sample, and its deflections are monitored by a laser and a photodiode and then used to reconstruct the topography of the sample [1, 2]. Besides its imaging mode, AFM is also a powerful tool for measuring the force between a single bio-molecule pair interaction with nanometer resolution, as AFM is able to measure intermolecular forces as small as a few piconewtons (as weak as a single hydrogen bond interaction). As a biosensor AFM is able to directly probe the adhesion or rupture (unbinding) force interactions between molecules, such as ligands and receptors, antibody and antigen pairs; and strength of chemical bonds, such as hydrogen bonds [3].

When AFM operates as a force sensor, the interaction force between the tip and the substrate surface can be measured by moving the tip perpendicular to the surface while measuring the force on the tip. The working principle is as follows: one type of molecule, i. e., an

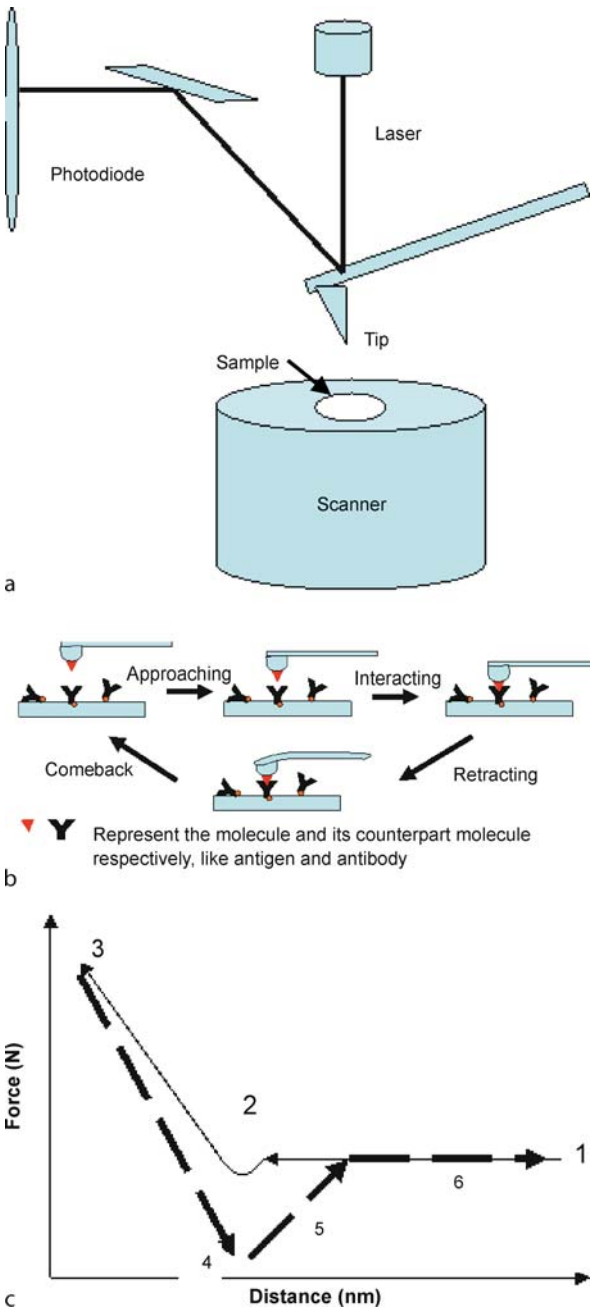

Biosensors Using Atomic Force Microscopes, Figure 1 (**a**) Basic components and working principle of AFM. A sharp tip fixed at the end of a flexible cantilever is raster-scanned over the surface of a sample. As the tip interacts with the surface, the cantilever deflects and its deflections are monitored by a laser and a photodiode and then used to reconstruct the topography of the sample. (**b**) A schematic diagram of AFM as a biosensor in detecting the force interaction between biological molecules. (**c**) Force–distance curve. During the tip (immobilized with one type of molecule, i. e., antigen) of the cantilever approaches to the substrate (immobilized with the counterpart of molecule, i. e., antibody), the *line* 1–3 is followed. By retracting the tip back, the cantilever bends downward as a function of the unbinding force between the two molecules, the line 4–6 (*dash*) is followed

antibody is attached to the tip of the cantilever and its counterpart molecule, i. e., an antigen is attached on the substrate surface. When the tip and substrate approach to each other, the two molecules interact and bonds are formed. Thus, their adhesion force can be measured. By retracting the tip back, the cantilever bends downward as a function of the unbinding force between the two molecules. Thus, the unbinding force, defined as the maximum force at the point of separation of the samples, can be recorded and measured. The force is monitored by the deflection of the cantilever and the deflection is directly proportional to the force. The schematic diagram of such an experiment and the force–distance curve are illustrated in Fig. 1b and 1c.

There have been several other powerful techniques for probing the molecular interaction between biosurfaces, including the use of shear flow detachment, surface force apparatus, biomembrane force probe, and optical tweezers [4]. The main advantages of using AFM are its high resolution, easy sample preparation, and its ability to manipulate in aqueous medium. AFM is currently the only force technique that makes mapping and analyzing single receptors with nanoscale lateral resolution possible [4]. Up to now, researchers have successfully used this system to measure interaction force between biotin and streptavidin, avidin and biotin, antibodies and their antigens, and single pairs of DNA nucleotides.

Basic Methodology

The first studies using AFM as a detection tool for intra- or intermolecular force can only measure discrete force. As the techniques for tip and sample preparation improve, single molecular interaction force detection will become the focus of AFM biosensors.

Major Factors for Single Molecular Interaction Force Detection

For real measurements of interactions between single molecules, very strict conditions are needed. Several important factors should be considered. First, the density of molecules distributed on both tip and sample should be sufficiently low to allow the formation of single molecular interactions. Second, to prevent unwanted detachment, covalent bonding of the molecules to the tip and the sample is critical. Generally, the binding between the surfaces and the molecules should be much stronger than the intermolecular force being studied. Third, a suitable molecular crosslinker (spacer) is a good choice to attach the molecules to the surfaces so that the molecules can interact with their counterparts with sufficient mobility. Forth, unspecific adsorption on the modified surfaces should be blocked to minimize the contribution of unspecific adhesion to the measured forces. Fifth, for oriented systems, site-directed coupling in which the molecule has a defined orientation may be desired [4]. Moreover, the rupture forces measured in an interaction force experiment are highly dependent on the conditions of the experiment, i. e., the spring constant of the cantilevers and the retraction rate of the cantilevers, and these factors will affect the result of the measurement.

Basic Procedures for Preparing AFM Tips and Samples

The coupling of biomolecules to the tip and to the surface has proved to be essential in the measurement of single molecular interaction force. The quality and reproducibility of the functionalization steps are the key factors leading to the success and reliability of a single-molecule experiment.

Preparing AFM Tips

Two types of surface chemistries have been developed for the functionalization of tips, they are based either on the strong chemisorption of thiols on gold surfaces or on the covalent attachment of silanes or alcohol on silicon oxide surfaces [4].

Strong Chemisorption of Thiols on Gold Surfaces

The gold coating techniques can be used to functionalize the tip. When the tip has been coated by a thin adhesive layer of gold (gold tip), proteins, oligonucleotides or carbohydrates that bear thiol groups can be attached directly onto the gold surfaces. We can also functionalize the gold tip with alkanethiols which can attach biomolecules by self-assembled monolayers (SAMs). SAMs are easily obtained by immersing gold surfaces in dilute (typically 1 mM) ethanol solutions of the interested alkanethiols. The alkanethiols may be terminated by carboxyl group or amino group. The former can be reacted with amino groups of proteins using 1-ethyl-3-(3-dimethylaminopropyl) carbodiimide (EDC) and N-hydroxysuccinimide (NHS) in aqueous solution. This method can provide both firm attachment and molecular mobility, but is restricted by the multiple attachment points which lead to broad unbinding force distributions. The latter can also be used to attach proteins [4].

When the gold tip is functionalized with alkanethiols terminated with nitrilotriacetate (NTA) group, recombinant histidine-tagged proteins can attach to it via their carboxy or amino group. This method allows the optimal exposure of the C-terminal or N-terminal domains. Moreover, it can orient the attached molecules in the same way and minimize nonspecific protein adsorption and allows low density coupling to ensure single molecule recognition. But

the binding strength between NTA and histidine-tagged protein is ten times lower than that of the covalent bond. Therefore this method is not suitable for studying strong receptor–ligand bonds [4].

Covalent Attachment of Silanes or Alcohol on Silicon Oxide Surfaces The method does not require a gold coating tip, and can be applied directly to silicon tips. Proteins can be linked to the silicon tip through a crosslinker which carries heterobifunctional group, for example, a polyethylene glycol (PEG) crosslinker with an amine-reactive NHS group on one end and 2-pyridyldithiopropionyl (PDP) on the other end. The NHS group reacts with amines on the silicon tip forming a stable amide bond while the PDP group reacts with free thiols presented by cysteines in the protein forming a stable disulfide bond.

Preparing Samples

The receptors or ligands recognized by the functionalized tip need to be firmly attached to a solid support using appropriate, nondestructive approaches. Mica, glass and silicon have proved to be excellent supports for immobilizing purified receptors. The surface of mica is negatively charged at neutral pH, positively charged proteins can adsorb to it forming a strong enough binding to withstand the pulling force during the force detection experiments. The surface chemistries that are often used to prepare the samples are the same as those for preparing the tips, including strong chemisorption of thiols on gold surfaces and covalent attachment of silanes or alcohol on silicon oxide surfaces [4].

Besides molecules and biomolecules, cells can also be attached to the tips or sample supports. It makes the detection of cell–cell, cell–support interactions possible. The most important factor when attaching cells is that the attaching methods should retain the integrity and viability of the cells while at the same the binding between the cell and tip, cell and support should firm enough. Chemical fixation using crosslinking or attaching through adhesive coating proteins (collagen, fibronectin) can be applied to the cell attachment.

Other Features for the Single Molecular Interaction Force Detection

When the tips and samples have been functionalized, the quality of the tip and sample modifications should be evaluated. A control experiment is necessary to ensure that the bonds being formed during the tip or sample preparation processes will not break during the force experiment. A block experiment is important to address the specificity of the interaction force being detected. A block experiment can be performed by masking the receptor sites with free ligands.

Key Research Findings

Detection of the Forces of Discrete Bonds

Several investigations have demonstrated the measurement of inter- or intra-molecular interactions using AFM. Lee and co-workers were the first to use AFM to measure discrete and biologically specific rupture forces between biotin and streptavidin which are one of the strongest ►noncovalent interactions in nature. The schematic diagram was similar to Fig. 1b. First, the force probe (a glass microsphere glued to a cantilever) and the surface were coated with bovine serum albumin (BSA) by nonspecific adsorption; then, biotin was covalently coupled to BAS-coated force probe and surface; subsequently, the biotin-functionalized surface was incubated with the counterpart molecule, streptavidin, resulting in a monolayer of streptavidin bound to the biotinylated BSA on the glass surface. When the force probe and surface approached each other, the biotin on the probe could interact with the streptavidin and bonds were formed. When retracting the cantilever, the bonds formed could be disrupted. This rupture occurs when the gradient of the cantilever potential exceeds the highest gradient in the unbinding pathway of the ligand–receptor interaction potential. By registering the deflection of the cantilever at rupture, the rupture force could be measured. After blocking the streptavidin by free biotin, no rupture force was measured, which showed the specificity of the interactions.

Detection of Single Molecular Interaction Force

Lee's work was very useful for measuring the unbinding forces of discrete bonds, but not for measuring the single molecular interaction force. To successfully detect the single molecular interaction force, several techniques have been developed to modify the tips and the samples, e. g., crosslinker system, intrilotriacetate (NTA)-Ni^{2+}-His system. Whatever technique is used, the key point is to make the density of the molecules distributed on both the tip and the sample sufficiently low to allow the formation of single molecular interactions. Kienberger et al. [5] have successfully detected the single molecular interaction force between abotin and avidin.

Detection of the Force Interactions of DNA in the Aqueous Medium

The most significant point of AFM is that it can be applied to detect the force interactions in aqueous medium. The

measurements are not as straightforward as those between the tips and the solid surfaces. Cengiz and co-workers [6] have constructed a biosensor for quantitative measurements of molecular nucleic acid in aqueous medium. Only an AFM head with a cantilever, a sensitive approaching unit (to control the approach of the target solution to the AFM tips) and a CCD camera were needed in such a system. The sensitive approaching unit was in fact an inchworm motor that provides precise approach positioning in the Z-direction with high stiffness and holds position even with the power turned off. This type of motor has a resolution of 1 nm and a speed range of 1 nm/s to 0.5 mm/s when used as its own controller. When using this system, a model single strand DNA (ssDNA) molecule was covalently attached onto the tips (cantilevers) of the AFM as a specific ligand. Buffer solutions with and without free ssDNA molecules were approaching to the tip ($+Z$-direction) by the inchworm motor until the tip touched to the solution. The tips interacted with the target ssDNAs in the buffer solution for about 10 min to complete hybridization and then the buffer solution was driven at the opposite direction ($-Z$-direction) and meanwhile the *separation distance* (L, in nm) that the tip got rid of the solution was measured to follow the interaction between the ligand molecules attached on the cantilever (the tip) and the target molecules in the buffer solution. The percentage separation distance (PSD) was calculated from the following equation and used as the main variable:

$$(\mathrm{PSD})(\%) = \{(L_2 - L_1)\} \times 100 \quad (1)$$

Where L_1 is the separation distance for the buffer solution without ssDNA (nm), and L_2 is the separation distance for the same buffer solution containing the target ssDNA (nm). Note that the negative value shows the decrease in the interaction between the AFM tip and the liquid phase. And in order to show the specificity of these AFM sensors, buffer solutions with the non-complementary ssDNA were also measured. The results showed that after hybridization with its complementary ssDNA, the PSD values were significantly increased when compared with the PSD values for the buffer solutions, while the PSD values for the non-complementary ssDNA increased slightly (specificity of the method). The PSD values also decreased with the concentration of the target ssDNA in the medium. It seemed that there was a correlation between the concentration of the complementary target ssDNA in the medium and the PSD value, although it was not linear.

Force Amplified Biological Sensor (FABS)

AFM biosensors have been used by researchers to measure binding or rupture forces between biological molecules.

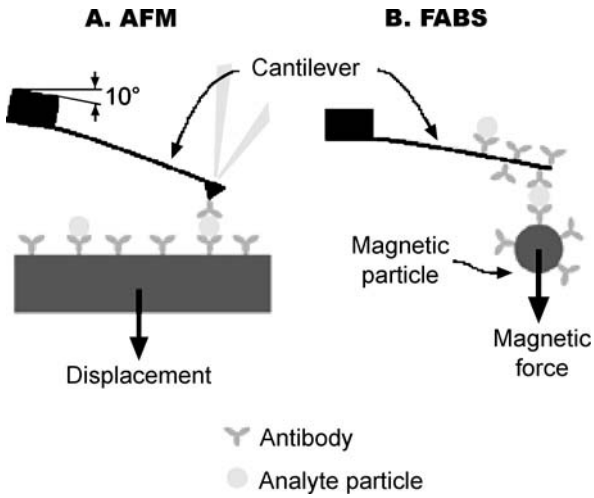

Biosensors Using Atomic Force Microscopes, Figure 2 Detection of antibody–antigen interaction forces with AFM and with FABS. (**a**) In AFM, a piezoceramic translator moves an antibody-derivitized surface away from a cantilever until a single antibody–antigen bond breaks. (**b**) In FABS, a magnetic field pulls on antibody-derivitized magnetic particles. The cantilever can bear thousands of particles, although the figure only shows one. (reproduced from [7])

However, they have a few drawbacks, for example, the nonideal geometry of AFM can produce artifacts, the result of measurement is affected by many factors and in order to obtain good results, very strict experimental conditions are required. Improvements of the AFM biosensors are being studied.

A FABS, whose working principle was very similar to that of the AFM biosensor, was a cantilever-based immunosensor [7]. However, its configuration was much simpler than that of the AFM. Rather than using a piezoceramic translator to pull on intermolecular bonds, it used magnetic particles, which eliminated the need to manually position a tip and sample next to each other with picometer precision and stability. The cantilever-beam force transducer was the only element of the AFM retained by the FABS.

Here, the measurement of antibody–antigen interactions was used to illustrate the working mechanism of a FABS (Fig. 2): one or more cantilevers with attached antibodies will capture antigen from a sample solution; 2 μm magnetic particles that also have attached antibodies will then bind to the captured antigen (at this stage the particles are not magnetized); after they have bound to the cantilever, a large magnetic field will magnetize the particles while a modulated field gradient exerts force on them. This force will cause particles bound via antibody–antigen bonds to pull on and bend the cantilever, while dislodging nonspecifically bound particles (*force discrimination*). The amount that the cantilever bends will indicate the

number of particles bound to the cantilever and, therefore, the concentration of analyte (antigen) in the sample. The FABS is capable of detecting a single bound particle, potentially corresponding to a single antigen molecule. A second detection mode might involve gradually increasing the force on the magnetic particles and determining the number of particles that detach at the expected antibody–antigen interaction force.

As can be seen from above, the magnetic particles, the Helmholtz coils, and cantilevers are the critical components of the FABS. The force generated by each magnetic particle is

$$F = 0.524Md^3(\mathrm{d}B/\mathrm{d}Z) \tag{2}$$

Where M is the volume magnetization of the magnetic material, d is the particle diameter, and $\mathrm{d}B/\mathrm{d}Z$ is the field gradient generated by the Helmholtz coils.

With its ability to detect a single bound molecule and to distinguish specific from nonspecific interactions, FABS could potentially have 6 – 8 orders of magnitude more sensitivity than commonly used immunoassays. This ability would be of value for environmental monitoring. Testing for airborne bacteria or viruses, for example, can presently require several days of air collection to accumulate detectable amounts of analyte. The high sensitivity of FABS could dramatically reduce sampling times and speed the detection of dangerous microorganisms or chemicals.

Combination of AFM and Other Techniques: AFM-Tip-Integrated Biosensors

Kueng et al. [8] have developed an AFM-tip-integrated biosensor to map molecular transport across membranes. Actually, this biosensor was a combined AFM-SECM (scanning electrochemical microscopy) probe which retained the integrity of both techniques and could be applied in dynamic-mode operation on soft biological samples. The combined AFM-SECM probe was fabricated as shown in Fig. 3a. An electroactive area with defined geometry, which was recessed from the apex of the AFM tip, allowed integration of the SECM functionality into AFM by correlating the current measured at the integrated electrode with the topographical information obtained by the AFM tip. Biological recognition elements, such as enzymes were then immobilized to the combined AFM-SECM probe as shown in Fig. 3b. In this integrated biosensor, AFM worked in its imaging dynamic mode, which was different from the above described biosensors which used AFM in a nonimaging mode.

To demonstrate the ability of this AFM-tip-integrated biosensor to study glucose membrane transport, a porous polycarbonate membrane (200 nm pore size) was mounted in a vertical diffusion cell that separated aqueous solutions in the donor and receptor compartments to mimic glucose transport through cellular membranes (Fig. 3c) and the glucose oxidase containing polymer layer was immobilized onto the probe (Fig. 3b). The combined AFM-SECM glucose oxidase electrode acted as a sensor that established concentration profiles of individual species near the sample surface. When the AFM tip was scanning in the X-direction above a synthetic membrane with 200 nm pores, the expected qualitative height and current signals were recorded (Fig. 3c). At the position of the pores, the height signal decreased, and glucose diffused through the pores toward the immobilized glucose oxidase layer, which catalyzed the conversion of glucose into gluconolactone (Fig. 4a). The current recorded at this glucose biosensor during the imaging of the pores increased as a result of the localized production of H_2O_2 when glucose diffused from the donor into the receptor compartment. Fig. 4c and 4d show AFM topography, SECM current images in the presence and absence of glucose in the donor compartment and exemplary line scans of the height and current response, respectively. The glucose signal response in the electrochemical image corresponded to the topography measured simultaneously with the AFM tip. The SECM current image of the porous membrane represented a contour map of the glucose concentration after emergence of the aqueous solution of glucose from the membrane pore and free diffusion into the receptor-compartment solution. While in the control experiment without glucose in the donor compartment, the measured current was negligible (Fig. 4f).

The glucose transport rate could be obtained by using Fick's law at appropriate boundary conditions, assuming that the pore opening was hemispherical. The concentration profile $C(r)$ at a radius r above the hemispherical pore opening could be described by Eqs. (3) and (4).

$$C(r) = (r_0/r)C_S \tag{3}$$

$$r_0 = 2a/\pi \tag{4}$$

Where C_S was the molecule concentration at the surface of the pore opening.

Earlier results showed that the radial divergence of the diffusive flux from a microscopic pore, regardless of its real shape, results in the pore appearing as if it were hemispherical in shape. For a disk-shaped pore with radius a, the radius of the corresponding hemispherical pore r_0 could be described by Eq. (4) [8].

Based on this approach, the theoretical glucose concentration at a distance (r) of 310 nm, which corresponds to

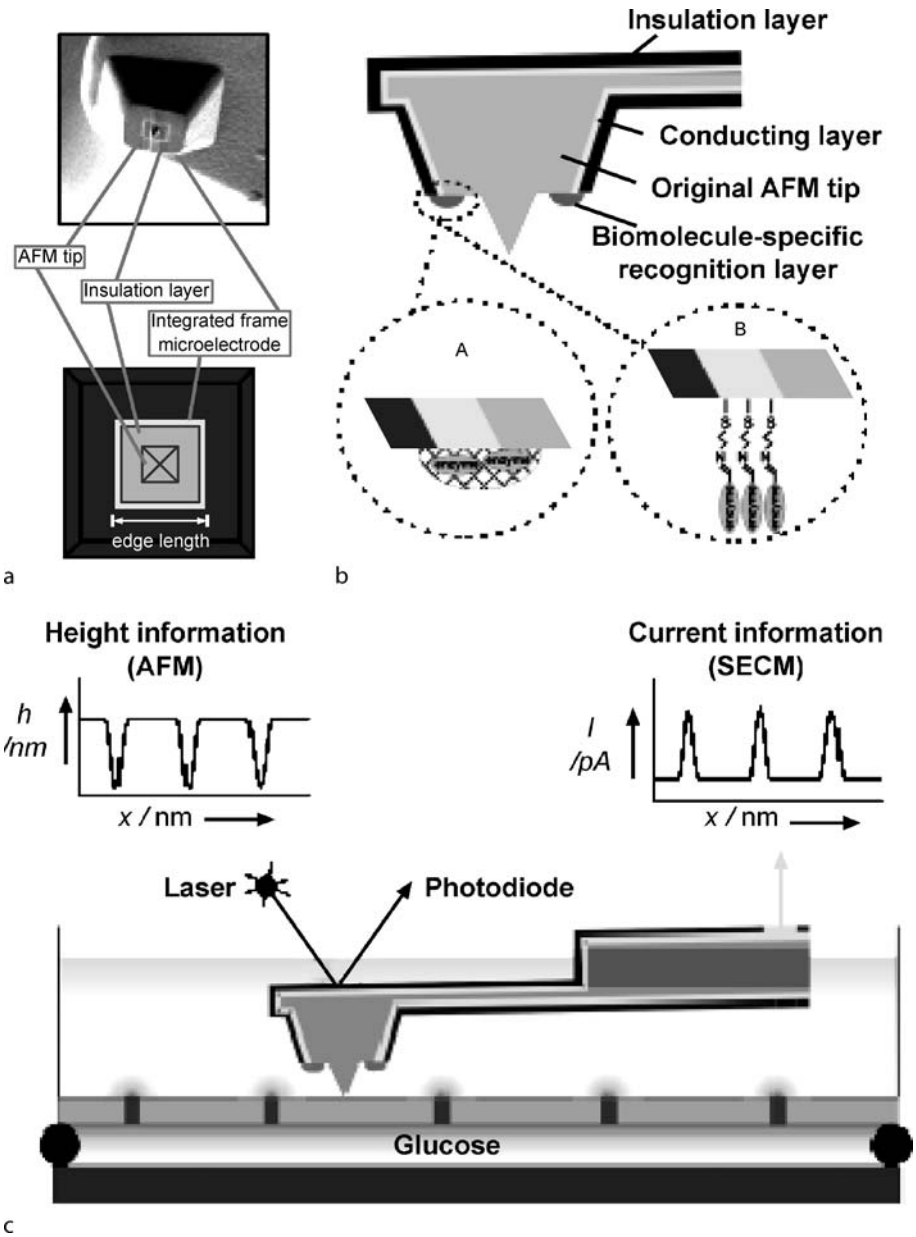

Biosensors Using Atomic Force Microscopes, Figure 3 (**a**) SEM image and schematic top view of an AFM-tip-integrated frame electrode; (**b**) schematic cross-section of an AFM-tip integrated biosensor. Enzymes can be immobilized at the surface of the scanning-probe tip-integrated electrode through self-assembled thiol monolayers with functionalized headgroups (A) or through electrochemical deposition of enzyme-containing polymer films (B). (**c**) Schematic cross-section of the experimental setup for imaging glucose transport through a porous membrane during simultaneous AFM mapping. (reproduced from [8])

the reshaped AFM tip height, above a pore opening with a radius (a) of 100 nm was estimated to be 0.62 mM for a 3 mM glucose solution. The evaluation of the current response in the SECM image (Fig. 4d) resulted in an average peak current of 1.5 ± 0.3 pA. According to the linear regression of the glucose calibration obtained at the integrated electrode (Fig. 4b), the measured glucose concentration was estimated to be 0.66 ± 0.13 mM. This semi-quantitative value corresponded well to the theoretically estimated concentration of 0.62 mM.

Glucose biosensors fabricated with this technology exhibit excellent sensitivity, response time, reproducibility, and long-term stability. This technology has a wide range of applications for biological specimens and processes.

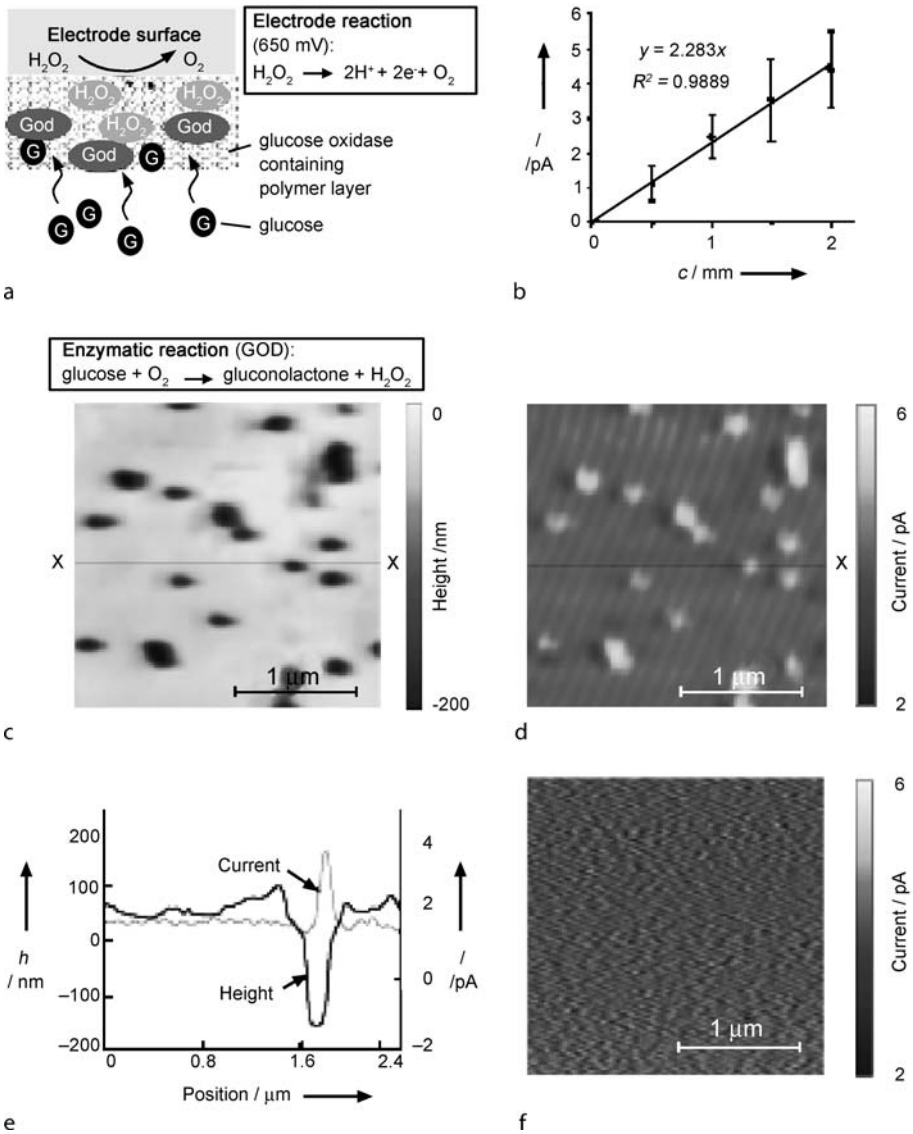

Biosensors Using Atomic Force Microscopes, Figure 4 (**a**) Reactions for glucose detection with a biosensor based on glucose oxidase (GOD). (**b**) Glucose calibration of an AFM-tip-integrated biosensor (edge length: 800 nm) fabricated by entrapment of glucose oxidase within a polymer film. Simultaneously recorded (**c**) height and (**d**) current images of glucose diffusion through a porous polycarbonate membrane (pore size: 200 nm); images recorded in AFM dynamic mode. (**e**) Exemplary corresponding line scans of height and current. (**f**) Current image recorded without glucose in the donor compartment. (reproduced from [8])

Future Directions for Research

The development of AFM and its use in detecting molecular interactions has led to the understanding of molecular recognition on a variety of biological surfaces. Researchers will continue to find more suitable surface chemistries to functionalize the AFM tip for the more precise measurement of single molecule interaction force and individual bond strength, and eventually use the AFM as a biosensor in the medical profession to screen samples for a particular chemical or biological agent. Second, the ability of the AFM to acquire movies (sequential images) under aqueous environments can be used to follow biological processes, dynamics and macromolecular assembly occurring in real time. Finally, the combination of AFM and other techniques to develop multifunctional, highly sensitive, easy operating devices for the purpose of molecular interactions study will be among future research interests.

Cross References

- ► Biosensor
- ► Atomic Force Microscope (AFM)

References

1. Kasaa S, Thomson NH, Smith BL, Hansma PK, Miklossy J, Hansma HG (1997) Biological applications of the AFM: from single molecules to organs. Int J Imag Sys Technol 8:151–161
2. Reich Z, Kapon R, Nevo R, Pilpel Y, Zmora S, Scolnik Y (2001) Scanning force microscopy in the applied biological sciences. Biotechnol Adv 19:451–485
3. Willemsen OH, Snel MME, Cambi A, Greve J, Grooth BGD, Figdor CG (2000) Biomolecular interactions measured by atomic force microscopy. Biophys J 79:3267–3281
4. Hinterdorfer P, Dufrene YF (2006) Detection and localization of single molecular recognition events using atomic force microscopy. Nature Methods 3:347–355
5. Kienberger F, Ebner A, Gruber HJ, Hinterdorfer P (2006) Molecular recognition imaging and force spectroscopy of single biomolecules. Acc Chem Res 39:29–36
6. Kocum C, Ulgen SD, Cubukcu E, Piskin E (2006) Atomic force microscopy tips (cantilevers) as molecular nucleic acid sensors. Ultramicroscopy 106:326–333
7. Baselt DR, Lee GU, Hansen KM, Chrisey LA, Colton RJ (1997) A high-sensitivity micromachined biosensor. Proc IEEE 85:672–680
8. Kueng A, Kranz C, Lugstein A, Bertagnolli E, Mizaikoff B (2005) AFM-tip-integrated amperometric microbiosensors: high-resolution imaging of membrane transport. Angew Chem (Int Ed) 44:3419–3422
9. Ebner A, Kienberger F, Kada G, Stroh CM, Geretschlager M, Kamruzzahan ASM, Wildling L, Johnson WT, Ashcroft B, Nelson J, Lindsay SM, Gruber HJ, Hinterdorfer P (2005) Localization of single avidin–biotin interactions using simultaneous topography and molecular recognition imaging. Chem Phys Chem 6:897–900

Biosensors Using Infrared Imaging

- ► Infrared Imaging and Mapping for Biosensors

Biosensors Using Lasers

JUN YANG, XIAOLIN ZHENG
Bioengineering College, Chongqing University, Chongqing, China
yjun1999@hotmail.com

Synonyms

Laser-based biosensors

Definition

Biosensors using lasers are defined as sensors for biological applications which are based on laser technology. There is a series of biosensors which use laser-based detection methods such as: surface plasmon resonance, fiber optics, waveguides, microcantilevers, and so on. Due to their high sensitivity and precision, laser-based biosensors have been widely used in many fields, including immunoassays and drug screening.

Overview

Biological sensing is a process which obtains selected information about biological macromolecular interactions in real time. Biosensors are miniaturized analytical devices based on biological sensing technology, which commonly comprise a biorecognition molecular layer immobilized on the interface between the analyte solution and a signal transducer (Fig. 1) [1]. The main part of a typical biosensor is this biologically sensitive layer that converts the biological change into a detectable signal, which is subsequently translated into a digital electronic result. The sensitive substances on the interface, which can include enzymes, antibodies, DNA segments, peptides or even a microorganism, provide the biosensor with its selectivity for the target analyte so that the molecule that is of interest can be picked out by the biosensor from a mixture of many different molecules. The extent of the biorecognition event is determined by the signal transducer and converted into an electronic signal for the end user. Popular transducers in biosensors include electrical, optical, or piezoelectric devices.

Optical biosensors are the most popular because of their high sensitivity, fast response time, in situ monitoring, and the absence of electrical interference. Due to its outstanding advantages in monochromaticity, coherence, low beam divergence, and strong irradiance, the laser is widely used as the light source in optical biosensors. For a wide range of biological systems, biosensors using lasers can be used to provide qualitative information, such as whether or not two molecules interact, and quantitative information, such as kinetic and equilibrium constants for macromolecular interactions. In a typical experiment, one molecule is attached to a surface and the other molecule, which is in solution, flows over the surface. Their interaction is transferred to a recognizable optical signal under the laser irradiation and converted to an electronic signal by optoelectronic components such as the charge coupled device (CCD) and the photomultiplier tube.

Many laser-based biosensors are derived from traditional detection methods. For example, traditional enzyme-based biological sensing analyses use the photometric detection

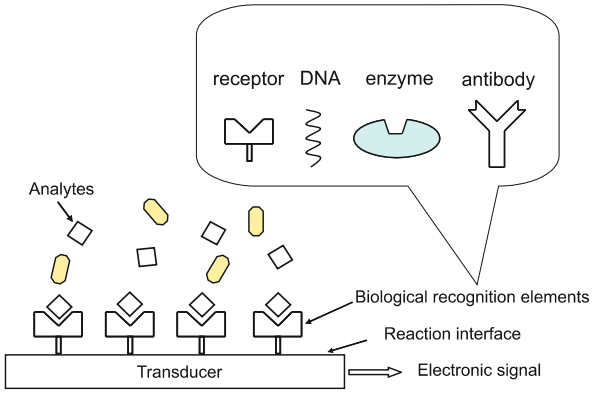

Biosensors Using Lasers, Figure 1 The biosensor comprises a biorecognition molecular layer immobilized on the interface of a signal transducer. Biological change on this interface is converted into a detectable signal and subsequently translated into a digital electronic result. Many types of sensitive molecules including enzymes, antibodies, a DNA segment, peptides or even a microorganism can be immobilized on the interface

method, where the enzyme reaction is linked to a colorimetric or fluorescent indicator. Some of these assay methods can be miniaturized and converted to solid-state systems, which were the early laser-based biosensors. This concept is now being applied to absorbance measurements by using evanescent wave detection, where the optical fiber, or in more general terms, the waveguide, itself forms the sensor surface. The binding of the immobilized biorecognition molecule and the analyte has an impact on the light propagating through the waveguide. The evanescent wave decays exponentially away from the surface of the waveguide, so that recognizable molecular interaction is limited to the layer immediately adjacent to the sensor surface, which is not affected by changes in the bulk solution.

Direct reading unlabeled immunoassay has also been sought through laser-based optoelectronics. In order to monitor the physico-chemical change produced by the interaction between an antibody and an antigen, without the secondary labels which are used in traditional biochemical assay methods, exploration of new detection techniques is required. Surface plasmon resonance (SPR) is the most outstanding of these techniques, with a sensitivity as high as 10^{-8} g/l [2]. The SPR biosensor is now the most popular optical biosensor. The microcantilever is another laser-based biological sensing method for the detection of analyte without labeling, where biological changes are monitored by using a laser optical beam deflection technique which detects the reflection of a microcantilever induced by biological interaction.

Several popular laser-based biosensors, SPR, optic fibers, waveguides, and microcantilever biosensors, will be summarized below.

Basic Methodology

Surface Plasmon Resonance

As a laser-based optical biosensor technique, SPR can measure molecular binding events at a metal surface by detecting changes in the local refractive index. The depth probed at the metal–aqueous interface is typically 200 nm, making SPR a surface-sensitive technique ideal for studying interactions between immobilized biological molecules and a solution-phase analyte.

SPR is an optical phenomenon that arises under conditions of total internal reflection of p-polarized light at an interface between a metal film and a liquid/gas phase, where a prism or grating is used as a coupling component (Fig. 2) [2]. Total internal reflection of light occurs when light traversing a medium of high refractive index (commonly a glass prism) encounters an interface with a medium of lower refractive index (usually an aqueous or gaseous environment). During total internal reflection, the energy and momentum of incident light can be transferred into the surface of the metal to create a surface plasmon. This excitation of plasmons generates an evanescent wave which propagates along the glass–metal surface, but decays exponentially over about one wavelength from the interface. For a fixed excitation wavelength, variation of the incident angle (θ) allows detection of the optimal angle associated with SPR, where most incident light is absorbed by the surface plasmon wave. This unique angle for minimal reflected light intensity is called the SPR angle (θ_{SPR}). Measurement of the intensity of reflected light as a function of the incident angle generates a SPR spectrum (Fig. 3a), which depends upon the refractive index and the thickness of the dielectric medium in the immediate vicinity of the interface. Although the evanescent field extends some 300 nm into the medium of low refractive index, the exponential decay of its amplitude gives rise to a rapidly decreasing sensitivity of response with increasing distance from the metal surface. As the detection method based on SPR angle, for a fixed incident angle, variation of the excitation wavelength allows the wavelength associated with optimal conditions for SPR to be detected. The incident angle and excitation wavelength scan are commonly used as detection methods in SPR biosensors.

The incident angle (or wavelength) where the resonance occurs strongly depends on the refractive index close to the metal surface. In a SPR biosensor, the interaction between immobilized biomolecules on the surface and analytes in solution changes the local refractive index, which results

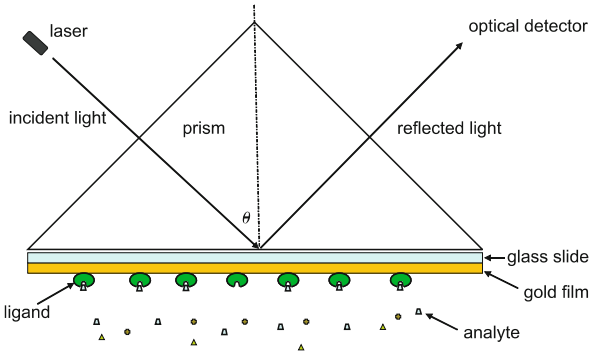

Biosensors Using Lasers, Figure 2 Schematic representation of a SPR biosensor. Laser and prism are used as the emitted light source and coupling component, respectively. Receptor molecules immobilized on the gold surface interact with analytes in solution, which induce the change in the refractive index in the immediate vicinity of the interface. This change can be detected by the SPR signal monitoring on the gold surface

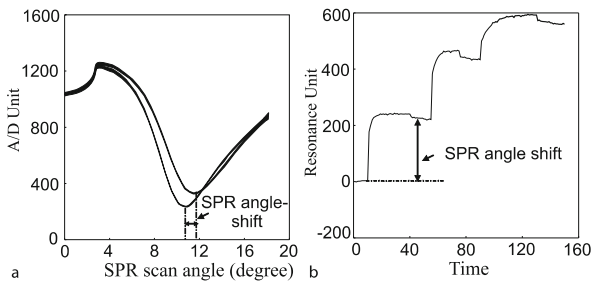

Biosensors Using Lasers, Figure 3 (a), SPR curve of a detection method based on incident angle scan. SPR angle shifts with the change in refractive index. (b), monitoring the shift of SPR angle in real time

in a shift in the SPR angle. By monitoring changes in the shift process of the SPR angle, it is possible to measure the interaction on the surface in real time (Fig. 3b). Here no label is needed. Typical biological systems examined using these instruments include antibody–antigen, ligand–receptor, and protein–nucleic acid interactions.

Traditional SPR spectroscopy biosensors, which measure the entire SPR curve as a function of the angle or wavelength, have been widely used, but offer limited throughput. The development of SPR imaging (microscopy (SPM)) allows for the simultaneous measurement of thousands of biomolecular interactions [3]. Typically, a SPM consists of a highly coherent p-polarized light source expanded by a beam expander and consequently reflected from an SPR active medium (sensing surface) to a detector. The CCD camera is frequently used as the detector in this system, which collects the reflected light intensity in an image. SPM imaging measurements are performed at a fixed incident angle that falls within a linear region of the SPR curve, so that changes in light intensity are proportional to the changes in refractive index caused by the biomolecular interaction on the surface. Thus, the gray-level intensity of the SPM image correlates with the amount of material bound to the sensing region. When combined with protein arrays, SPM imaging technology has the potential to become an invaluable tool for a broad range of applications that require high-throughput analysis of biomolecular interactions, such as proteomic analysis, drug screening, and immunoassay.

SPR offers several advantages over conventional techniques such as fluorescence or enzyme-linked immunosorbent assay. Here the analyte does not require any special characteristics or labels and can be detected directly; the measurements can be performed in real time to collect kinetic data; it is a versatile technique, capable of detecting analytes over a wide range of molecular weights and binding affinities. Because of its unique features, SPR has become a powerful tool for studying biomolecular interactions.

Fiber Optics

Fiber optic biosensors, which often use a laser as the light source are based on several different detection principles. Most existing laser-based detection methods used in large-scale instruments can be miniaturized by using optical fibers. For example, fluorescence and absorbance detection have been miniaturized by this way. In the case of absorption, the detector measures the reduction in the intensity of light from the source. This reduction is caused by an absorbent product arising from the reaction between the immobilized substance and the analyte. Absorption measurements are generally made using monochromatic wavelength light, and both the incidence and emitted beams have the same wavelength. At least two fibers are necessary in this system, one for the inward beam and one for the outward beam, because the intensities of these two beams cannot be separated at the same wavelength (Fig. 4a). The use of white light, however, can yield a complete absorption spectrum with the help of photodiode matrices or arrays. The wavelength of the rescence emission is different from its excitation wavelength, and a single fiber is sufficient to transport both the excitation and the emission radiation (Fig. 4b). A single fiber can also be used to measure fluorescence quenching, which occurs when a compound that absorbs in the same spectral region as the emission is present.

Some optical phenomena (e. g., evanescent waves) within the microscale optical environment are used to construct fiber optic biosensors [4]. In fiber optic biosensors for photometric detection, the light between the sample and the source or detector is transported along the interior of

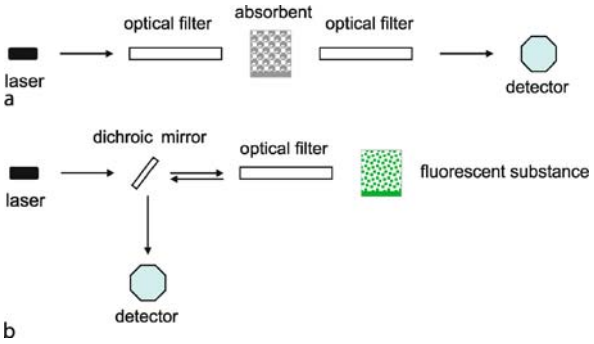

Biosensors Using Lasers, Figure 4 Fiber optic biosensors based on (a) absorbance, and (b) fluorescence detection methods

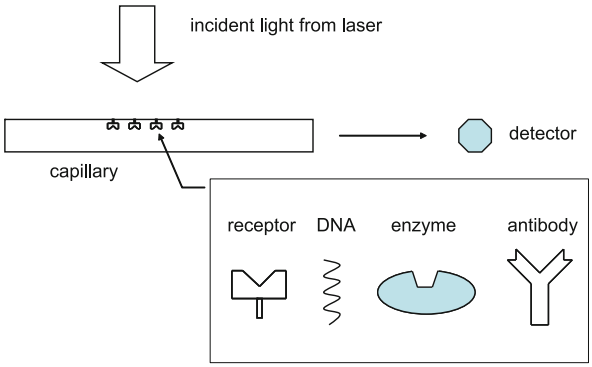

Biosensors Using Lasers, Figure 5 A capillary is used as an optical waveguide for evanescent wave-based biological sensing detection. The waveguide is perpendicularly illuminated by laser light, and the detection signal is subsequently collected from one end of the waveguide

the fibers following the principle of total reflection. The total reflection in a fiber is not perfect and some electromagnetic radiation penetrates the sheath covering the fiber. This is called the evanescent wave, and its intensity diminishes exponentially with the perpendicular distance from the interface as the surface wave in SPR. It can be used to detect the variations in optical properties of chemical and biological films placed around the fiber [5]. The laser optical detection method based on evanescent waves is widely used in biosensors. For example, a tapered optical fiber is used to analyze the total internal reflectance fluorescence. As light is propagated down the fiber, an evanescent wave excites fluorescent tracers bound to the fiber surface. Because the evanescent wave decays exponentially with the distance from the fiber surface, the excitation radius only extends about 100 nm into the buffer medium. A portion of the emission is captured and propagated back through the fiber to the detector.

Waveguides

A waveguide works on a similar principle to optical fibers, so most fiber optic detection methods can be transplanted to waveguide-based biosensors [6]. Compared with optical fibers, the waveguide is more easily integrated with other optical components (e. g., grating, interferometer) and can be integrated into miniaturized detection devices such as microfluidic chips.

The fiber optic biosensor, based on an evanescent wave, is the most popular of the biosensors using waveguides. In the early stage, a capillary is used as the waveguide to collect free propagating fluorescence [7]. For biosensor applications, probe molecules can be covalently bonded to the interior surface of the capillary to detect target molecules flowing through the capillary. Placing the probe coating on the interior surface also facilitates handling and protects against accidental damage. One detection method is achieved by illuminating the capillary (waveguide) at a 90° angle relative to the length of the waveguide and subsequently collecting the emitted fluorescence from the end of the waveguide (Fig. 5).

A waveguide can be integrated with a ating to form an optical waveguide grating coupler sensor, which responds to the change in optical refractive index of the liquid or gas cover medium. As in SPR detection, the optical refractive index in the immediate vicinity of the interface is directly related to the adsorption or binding of molecules on the surface. The optical waveguide grating coupler sensor chip is based on a fine optical grating prepared on a thin waveguide layer on a glass substrate. The optical grating couples the light of a laser at a given resonance angle into the waveguide layer. This resonance angle is very sensitive to the presence of adsorbed molecules and to any change in the refractive index of the medium covering the surface of the chip.

A planar waveguide with a corrugated surface, which can be tuned to be a resonant Bragg reflector, is also a laser-based biosensor (Fig. 6) [8]. The reflection coefficient of the light propagating through the waveguide depends on the depth of the corrugation as well as on the length of the corrugated region. A specially prepared layer, which selectively adsorbs the target biomolecules, is only covered on the surface of higher parts of the corrugation. When solution flows over this corrugation, some target biomolecules bind with the cover layer, the corrugation depth rises and the reflection coefficient changes. This change is proportional to the difference between the dielectric permittivities of the analyte and solution, and can be used to monitor the dynamics of the surface reaction. The presence and concentration of the target biomolecules in the solution can also be inferred by this method.

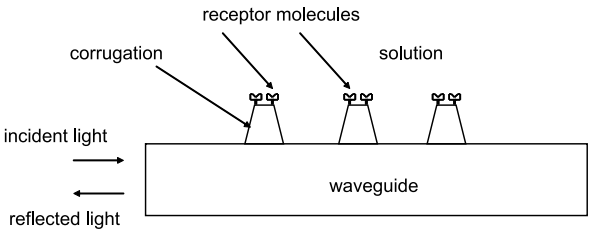

Biosensors Using Lasers, Figure 6 Schematic of a laser-based biosensor using the resonant Bragg reflector principle. A receptor molecular layer covers the surface of some corrugation that is used as sensing materials. After some target molecules bind with the receptor molecular layer, the corrugation amplitude rises and coupling coefficient changes

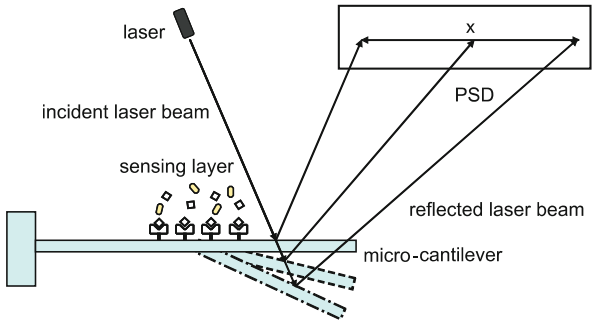

Biosensors Using Lasers, Figure 7 Scheme of the optical read-out method for a microcantilever bending evaluation. The displacement of the free end of the cantilever is measured by monitoring the optical deflection of an incident laser beam on a position-sensitive detector

Microcantilevers

Biosensors using microcantilevers have attracted considerable interest in the last few years [9, 10]. The microcantilevers transduce the recognition event from their receptor-coated surface into a mechanical deflection. As the ligands interact with the receptors, the adsorption stress leads the bending of the cantilever toward or away from the receptor side depending on the nature of the chemical bonding of the molecules. The deflection of the microcantilever can be measured using the optical beam deflection technique, which is highly sensitive and widely used in atomic force microscopy. The displacement of the free end of the cantilever is measured by detecting the optical deflection of an incident laser beam on a position-sensitive detector (PSD), which allows the absolute value of the cantilever displacement to be calculated (Fig. 7). This method provides sub-angstrom resolution and can easily be implemented. High sensitivity biological sensing thus becomes possible.

The defection (δ) of a microcantilever, which is caused by the surface stress difference of the top (receptor-coated) and the bottom surfaces, can be estimated according to

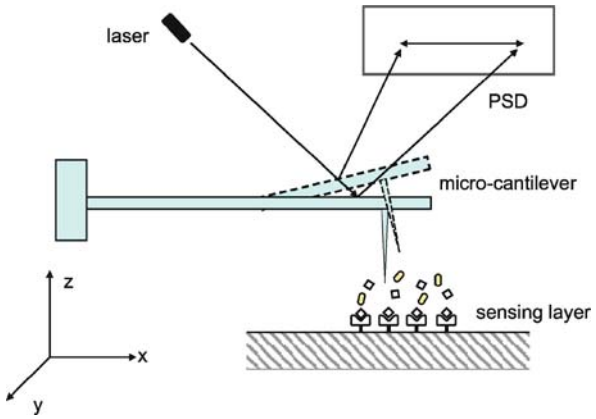

Biosensors Using Lasers, Figure 8 Working principle of the microcantilever atomic force biosensor

Stoney's formula:

$$\delta = \frac{3\,(1-v)\,(\sigma_1 - \sigma_2)\,L^2}{Ed^2}$$

where v is the Poisson ratio of the cantilever material; σ_1 and σ_2 represent the surface stress of the top and bottom surfaces, respectively. L and d are the length and the thickness of the cantilever, respectively, and E is Young's modulus of the cantilever material.

The microcantilever atomic force biosensor is another type of microcantilever-based biosensor. Its working principle is similar to that of the microcantilever biosensor. However, receptor molecules are covered on a planar other than the surface of cantilever. Biological changes are also monitored using an optical beam deflection technique. The laser illuminates the end of the microcantilever and changes in position are detected using a matching PSD. This sensor works like a profilometer by moving a microfabricated tip held at the end of a microcantilever across the sample while recording the x-, y-, and z-coordinates of the preparation being scanned (Fig. 8). The z-coordinate is calculated by detecting the laser beam reflected off the surface of the cantilever. These microcantilever biosensors are able to detect many biological systems such as single-strand DNA hybridization, and protein–protein/DNA binding, pH variations.

Future Directions for Research

In recent years, laser-based biosensors have become important tools in many fields such as analytical biochemistry, pharmaceutical research and development, and food/environmental monitoring. However, the volumes of the optic components in these biosensors limit their application in portable microdevices. In order to obtain

more powerful, miniaturized, and cheaper biosensors using lasers, novel biological sensing principles, detection means and fabrication methods need to be sought. The integration of biosensors and microfluidic chips will be an important direction for developments in laser-based biosensors. Biosensors can be used as microscale detection tools in lab-on-a-chip for the research and development of miniaturized detection devices, i. e., micro-total analysis systems.

Cross References

- ► Biosensors Using Atomic Force Microscopes
- ► Fluorescence Measurements
- ► Nanoscale Biosensors
- ► On-chip Waveguides
- ► Surface Modification
- ► Surface Plasmon Resonance Sensors

References

1. Ziegler C, Gopel W (1998) Biosensor development. Curr Opin Chem Biol 2:585–591
2. Boozer C, Kim G, Cong SX, Guan HW, Londergan T (2006) Looking towards label-free biomolecular interaction analysis in a high-throughput format: a review of new surface plasmon resonance technologies. Curr Opin Biotechnol 17:400–405
3. Rothenhausler B, Knoll W (1988) Surface-plasmon microscopy. Nature 332:615–617
4. Shriverlake LC, Breslin KA, Charles PT, Conrad DW, Golden JP, Ligler FS (1995) Detection of TNT in water using an evanescent-wave fiberoptic biosensor. Anal Chem 67:2431–2435
5. Rogers KR, Apostol A, Madsen SJ, Spencer CW (2001) Fiber optic biosensor for detection of DNA damage. Anal Chim Acta 444:51–60
6. Dhadwal HS, Kemp P, Aller J, Dantzler MM (2004) Capillary waveguide nucleic acid based biosensor. Anal Chim Acta 501:205–217
7. Zhu PX, Shelton DR, Karns JS, Sundaram A, Li SH, Amstutz P, Tang CM (2005) Detection of water-borne E-coli O157 using the integrating waveguide biosensor. Biosens Bioelectron 21:678–683
8. Dotsenko AV, Diikov AL, Vartanyan TA (2003) Label-free biosensor using an optical waveguide with induced Bragg grating of variable strength. Sens Actuators B 94:116–121
9. Zhang XR, Xu XF (2004) Development of a biosensor based on laser-fabricated polymer microcantilevers. Appl Phys Lett 85:2423–2425
10. Carrascosa LG, Moreno M, Alvarez M, Lechuga LM (2006) Nanomechanical biosensors: a new sensing tool. TRAC 25: 196–206

Biosensors Using Magnetics

CHAN HEE CHON, DONGQING LI
Department of Mechanical Engineering, Vanderbilt University, Nashville, TN, USA
Chanhee.chon@vanderbilt.edu

B

Synonyms

Magnetic biosensors; Magnetic-based biosensors

Definition

Biosensors are analytical devices incorporating biological or biologically derived sensing elements with physicochemical transducers to produce digital electronic signals [1]. These biosensors determine the concentration of substances and other parameters of biological interest. The detecting elements of biosensors work in different physicochemical ways: optical, piezoelectric, electrochemical, thermometric, and magnetic. Biosensors using magnetics utilize the magnetic field created by magnetic particles that bind to target molecules in a biological assay (Fig. 1).

Overview

There is an increasing need for higher sensitivity and specificity of detection for biosensors. Magnetic particles, by the use of the magnetoresistive (MR) effect, have been developed as labels for biosensing. These magnetic biosensors have several advantages compared to optical and electrical biosensors. The properties of magnetic particles are not affected by reagent chemistry so that they are very stable over time. Magnetic fields are also not screened by aqueous reagents or biomaterials. In addition, magnetism may be used to remotely manipulate the magnetic particles [2]. Therefore, magnetic biosensors using MR materials have been proposed as a new technology to detect low concentrations of targets in biofluids [3].

The target biomolecules in a biofluid are attached on magnetic particles. When these magnetically labeled

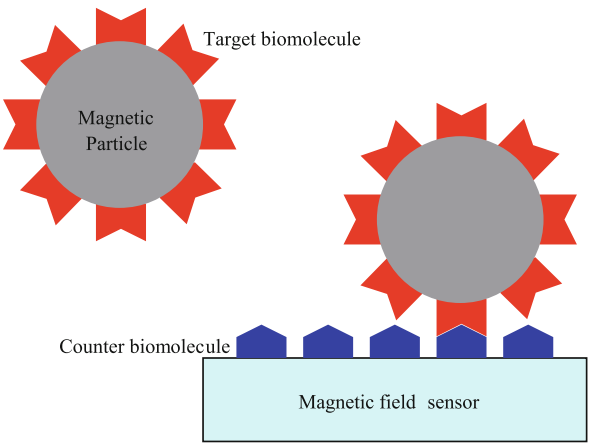

Biosensors Using Magnetics, Figure 1 Schematic of magnetically labeled biomolecule detection in a biosensor. Target biomolecules bound with a magnetic particle interact with magnetoresistive sensor-bound counter biomolecules to be detected

target biomolecules pass over the magnetic biosensor with counter biomolecules bound on its surface, these biomolecules interact with each other and the biosensor generates detecting electronic signals (Fig. 1).

A number of sensitive magnetic field detection devices have been developed as biosensors: giant magnetoresistive (GMR) sensors [4], piezoresistive cantilevers [5], inductive sensors [6], superconducting quantum interference devices (SQUIDs) [7, 8], anisotropic magnetoresistive (AMR) rings [9], and miniature Hall crosses [10].

Cross References

- ► Magnetic Field-based Lap-on-Chip Devices
- ► Biosensors Using Atomic Force Microscopes
- ► Biosensors Using Laser
- ► Infrared Imaging and Mapping for Biosensors
- ► Biosensors Using Surface-enhanced Raman Scattering

References

1. Turner APF, Karube I, Wilson GS (1987) In: Biosensors: Fundamentals and Applications. Oxford University Press, Oxford, p 770
2. Rife JC et al (2003) Design and performance of GMR sensors for the detection of magnetic microbeads in biosensors. Sens Actuators A 107:209–218
3. Graham DL, Ferreira HA, Freitas PP (2004) Magnetoresistive-based biosensors and biochip. Trends Biotechnol 22:455–462
4. Baselt DR, Lee GU, Natesan M, Metzger SW, Sheehan PE, Colton RJ (1998) A biosensor based on magnetoresistance technology. Biosens Bioelectron 13:731–739
5. Baselt DR, Lee GU, Natesan M, Hansen KM, Chrisey LA, Colton RJ (1995) A high-sensitive micromachined biosensor. Proc IEEE 85:672–680
6. Richardson J, Hill A, Luxton R, Hawkins P (2001) A novel measuring system for the determination of paramagnetic particle labels for use in magneto-immunoassays. Biosens Bioelectron 16:1127–1132
7. Lee S, Myers WR, Grossman HL, Cho HM, Chemla YR, Clarke J (2002) Magnetic gradiometer based on a high-transition temperature superconducting quantum interference device for improved sensitivity of a biosensor. Appl Phys Lett 81:3094–3096
8. Enpuku K, Hotta M, Nakahodo A (2001) High-T_c SQUID system for biological immunoassays. Physica C 357–360: 1462–1465
9. Miller MM, Prinz GA, Cheng SF, Bounnak S (2002) Detection of a micron-sized magnetic sphere using a ring-shaped anisotropic magnetoresistance-based sensor: A model for a magnetoresistance-based biosensor. Appl Phys Lett 81:2211–2213
10. Besse PA, Boero G, Demierre M, Pott V, Potovic R (2002) Detection of a single magnetic microbead using a miniaturized silicon Hall sensor. Appl Phys Lett 80:4199–4201

Biosensors Using Scanning Force Microscope

► Biosensors Using Atomic Force Microscopes

Biosensors Using Surface-Enhanced Raman Scattering

JAEBUM CHOO
Department of Applied Chemistry, Hanyang University, Ansan, Kyunggi-do, South Korea
jbchoo@hanyang.ac.kr

Synonyms

SERS-based biosensors

Definition

Devices for the highly sensitive detection of biological analytes using surface enhanced Raman scattering (SERS) spectroscopy. SERS is a highly sensitive optical detection technique in which lasers are used to excite vibrational transitions in molecule adsorbed on a metal nanoparticle surface. As a result of large optical fields, the Raman cross section for a molecule on a surface is enhanced by factors of $10^6 - 10^{10}$.

Overview

Microfluidic technology has recently been developed to perform a variety of biological or environmental trace analyses. These devices have several advantages compared with conventional techniques, such as minimal sample requirement, reduced reaction time, ease-of-use, improved product conversion, and reduced waste generation. It has long been realized that the system used for detection of the progress of the reaction is a key issue in determining the applicability of the microfluidic system. Because of the extremely small volume in a microfluidic channel, a highly sensitive detection method is essential in order to monitor the progress of the reaction. At the early development stage of a microfluidic detection, off-chip detection methods, such as high performance liquid chromatography or mass spectrometry, have been widely used to detect the small volumes of chemical species in a microfluidic channel. However, off-chip detection is very inconvenient for continuous monitoring of reactions since the sample must be removed from the reservoir of a chip on each detection occasion.

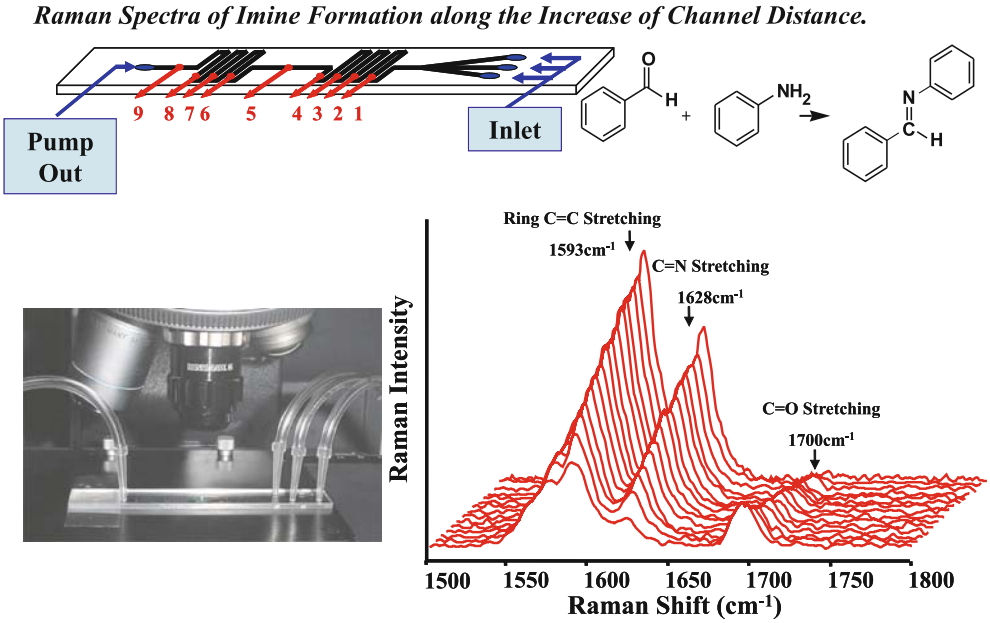

Biosensors Using Surface-Enhanced Raman Scattering, Figure 1 In situ Raman monitoring of imine formation reaction in a glass microfluidic sensor. The change in Raman spectra corresponds to the peak changes caused by the imine formation at various points along the channel

On the other hand, spectroscopic detection methods, such as laser induced fluorescence (LIF), UV/Vis absorption, chemiluminescence and thermal lens microscopy (TLM), have been used for on-chip detection. Among these methods, the fluorescence detection method has been most widely used because of its high sensitivity and low detection limits for biologically relevant species. However, the fluorescence detection technique has some disadvantages. Many chemical species do not fluoresce and so need to be treated with fluorescence tags to allow on-chip detection. Furthermore, it may have drawbacks such as a photobleaching and overlapping peaks caused by broad fluorescence emission profiles in multiplexed biological detection. Raman spectroscopy is another well-known analytical method, which offers great advantages for probing the biological and structural properties of a compound on a microscopic scale. The detection and identification of non-fluorescent samples is possible using this technique. Photodecomposition is reduced compared with fluorescent samples since the excited states are rapidly quenched and the excitation energy does not have to be in resonance with electronic transitions.

However, Raman scattering is an extremely inefficient process with low scattering cross-sections that are approximately fourteen orders of magnitude smaller than the absorption cross sections of fluorescent dye molecules. In order to achieve a high sensitivity of a biological sample, the scattering intensity should be greatly increased. Surface enhanced Raman scattering (SERS) spectroscopy, using silver nanoparticles, has shown promise in overcoming the low sensitivity problems inherent in Raman spectroscopy. Using the SERS technique, the detection sensitivity is enhanced up to 6 – 10 orders of magnitude over conventional Raman spectroscopy. As a result, the SERS technique provides a comparable sensitivity with fluorescence detection. In order to understand the enhancement mechanisms, it is instructive to refer to the following equation:

$$P = \alpha E \tag{1}$$

where P is the induced dipole moment, α is the molecular polarizability, and E is the incident electric field. The Raman scattering intensity (I) is proportional to the square of the induced dipole moment (P).

$$I = P^2 \tag{2}$$

Raman enhancement can take place by either increasing the electric field (E) experienced by the molecule (electromagnetic enhancement) or by changing the molecular polarizability of the adsorbate (chemical enhancement). The electromagnetic enhancement mechanism is explained by a phenomenon known as surface plasmon resonance. Surface plasmons are oscillations of conduction band electrons at a metal surface. At the surface

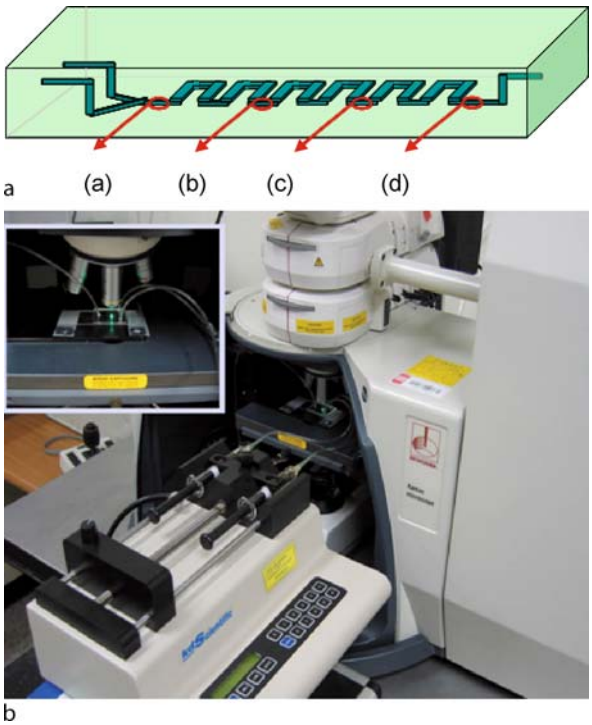

Biosensors Using Surface-Enhanced Raman Scattering, Figure 2 Schematic diagram of the experimental set-ups comprising a PDMS microfluidic channel and a microstage: (**a**) A schematic view of a 3D serpentine PDMS channel and four measurement spots along the channel distance: (a) at 0.15 mm, (b) at 28.5 mm, (c) at 68.4 mm, and (d) at 105.7 mm. (**b**) the optical arrangements for focusing the laser on the PDMS channel on the stage of confocal Raman microscope

plasmon resonance frequency, conduction band electrons move easily producing a large oscillation in the local electric field intensity. The surface plasmon frequency strongly depends on surface morphology (size and shape of particles), the dielectric properties of the metal, and the wavelength of the incident light. Electromagnetic effects are known to be decreased as a function of $1/r^3$ distance from the surface. Chemical enhancement involves the bond formation between the analyte and the metal surface. This bond makes it possible to transfer charge from the metal surface to the adsorbate molecule and this effect increases the molecular polarizability of the molecule. There have been many experimental evidences that both effects play a key role on the SERS effects. However, it is generally believed that electromagnetic enhancement may have a greater part to play than chemical enhancement. The main analytical advantages of SERS are enhanced sensitivity, surface specificity, and fluorescence noise reduction. Furthermore, it is possible to simultaneously detect multiplex analytes using SERS since its signals are much narrower than fluorescence bands.

However, the quantitative application of SERS is known to be very difficult because it is very hard to control the experimental conditions such as the degree of aggregation, the particle sizes of metal colloids, and the inhomogeneous distributions of molecules on the metal surface. As a result, under ordinary sampling conditions, the precision expected from a SERS experiment is very poor. On the other hand, a highly precise quantitative measurement can be obtained if continuous flow and homogeneous mixing conditions between analytes and silver nanoparticles are maintained. For this purpose, a functional microfluidic channel for the efficient mixing of analytes and aggregated silver colloids. Under the optimum conditions of using an an efficiently designed mixing channel and flow velocity, the quantitative SERS detection of analytes can be achieved under flowing conditions. This analytical method provides fast and reproducible results for the quantitative measurement of analytes at low detection levels. For example, the GC/MS or HPLC analysis requires longer than ten minutes for the sample pretreatments and measurements. On the other hand, only thirty seconds are needed when the SERS detection technique is applied. The SERS detection, in combination with microfluidic technology, can applied to the highly sensitive biological/environmental trace analyses.

Basic Methodology

Fabrication of an Alligator Teeth-Shaped PDMS Channel

Microfluidic channels are fabricated by stacking two PDMS layers that have upper and lower teeth patterns. These layers are produced by the pattern replication from mould masters. Two epoxy-based photoresist (EPON) mould masters, including upper and lower teeth patterns, were fabricated. By pouring the mixture of PDMS prepolymer and curing agent in a 10 : 1 ratio onto the lower mould master and by curing for 2 h on the hot plate at 80 °C, the patterned thick layer (thickness: 1.0 cm) with a lower pattern is constructed. The layer with upper teeth pattern is fabricated by the compression micro-moulding of PDMS elastomer. The PDMS pre-polymer is poured onto the mould master and compressed with transparent film and an aluminum disk. Then it is cured for 2 h. The thin upper layer (thickness: 200 μm) is produced by separating it from the mould master. For the bonding of upper and lower layers, the surfaces of both layers are activated in the oxygen plasma. Then it is aligned using the house-made aligner. Methanol is used as a surfactant between both layers. Finally, the cover glass is stacked onto the upper layer.

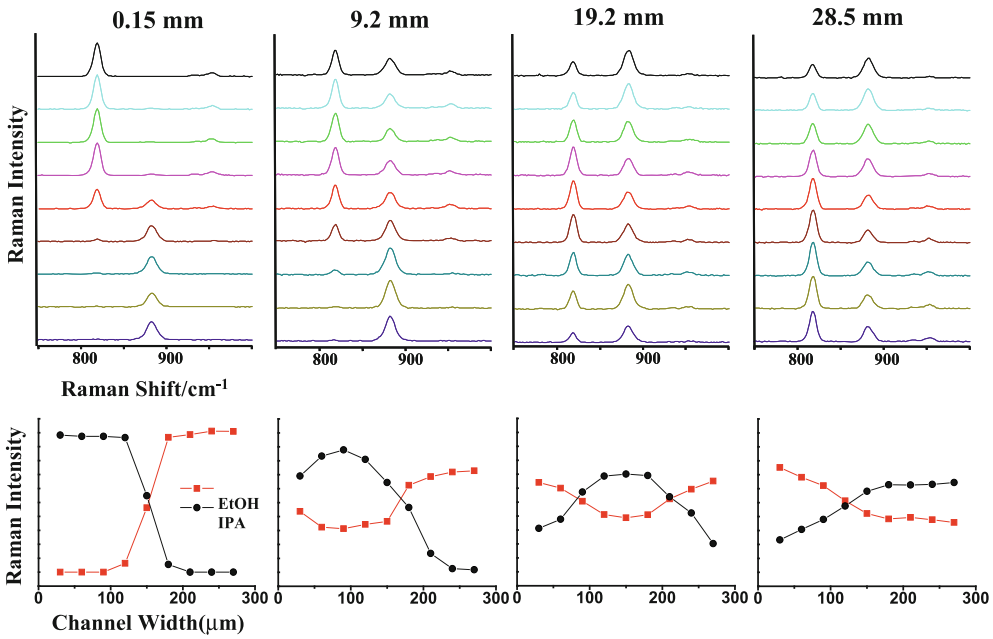

Biosensors Using Surface-Enhanced Raman Scattering, Figure 3 Raman profiling spectra and corresponding peak area changes for the C – O/C – C stretching modes of an ethanol-isopropanol mixture in a 3D serpentine channel. The upper number denotes the channel distance beyond the T-junction spot of the channel

Preparation of Silver Nanocolloids

Silver colloids are prepared by the method, as is recently reported by Leopold and Lendl. Here silver nitrate is reduced by hydroxylamine hydrochloride. The advantages of the hydroxylamine hydrochloride-reduced silver colloid are in its fast preparation at room temperature and its immediate applicability for SERS. First, 5 mL of hydroxylamine hydrochloride (3.0×10^{-2} M) is dissolved in 84 mL of triply distillated water and then 1 mL of sodium hydroxide (1.7×10^{-3} M) is added to maintain an alkaline pH condition. Next, 10 mL of silver nitrate solution (1.0×10^{-3} M) is added dropwise to the solution with continuous stirring. The solution is continuously stirred for additional 20 min. UV/Vis spectroscopy and TEM were used to characterize the particle size of produced colloids. Figure 1 shows the TEM, AFM images and UV/Vis absorption and Raman spectra of SERS-active colloidal nanoparticles.

SERS Detection

SERS measurements are performed using a Raman microscope system. An argon ion laser operating at $\lambda = 514.5$ nm is generally used as the excitation source. The Rayleigh line is removed from the collected Raman scattering by a holographic notch filter located in the collection path. Raman scattering signal is detected using a charge-coupled device (CCD) camera or photomultiplier tube (PMT). In Raman microscope, an additional CCD camera is fitted to an optical microscope to obtain optical images. A two-slit confocal arrangement is used to reduce the background Raman scattering from the unfocused laser beams. Although the laser beam is focused on the middle of the micro channel, i. e., the section between the top and the bottom in the z direction, the Raman signal from a small volume of chemicals in the micro channel cannot be completely separated from the signals originating from the surrounding PDMS material. To resolve this problem, all the Raman spectra are measured in the confocal mode. In the Raman system, the function of the pinhole is replaced by the cooperation of the entrance slit and the pixels in the CCD detector. Using the confocal technique, the background stray light, due to any out-of-focus regions of the PDMS, is effectively removed. The silver colloids and biological analytes are introduced into the channel from microsyringes connected by tubes to the inlet pipettes. The flow rate is controlled by using a microsyringe pump. The confocal SERS is measured after the analytes are effectively adsorbed on the silver nanoparticles by traveling the upper and lower alligator teeth-shaped microfluidic channel. Confocal SERS microscopy can be used as a highly sensitive sensing technique for the detection of non-fluorescent biological samples in a PDMS microfluidic channel.

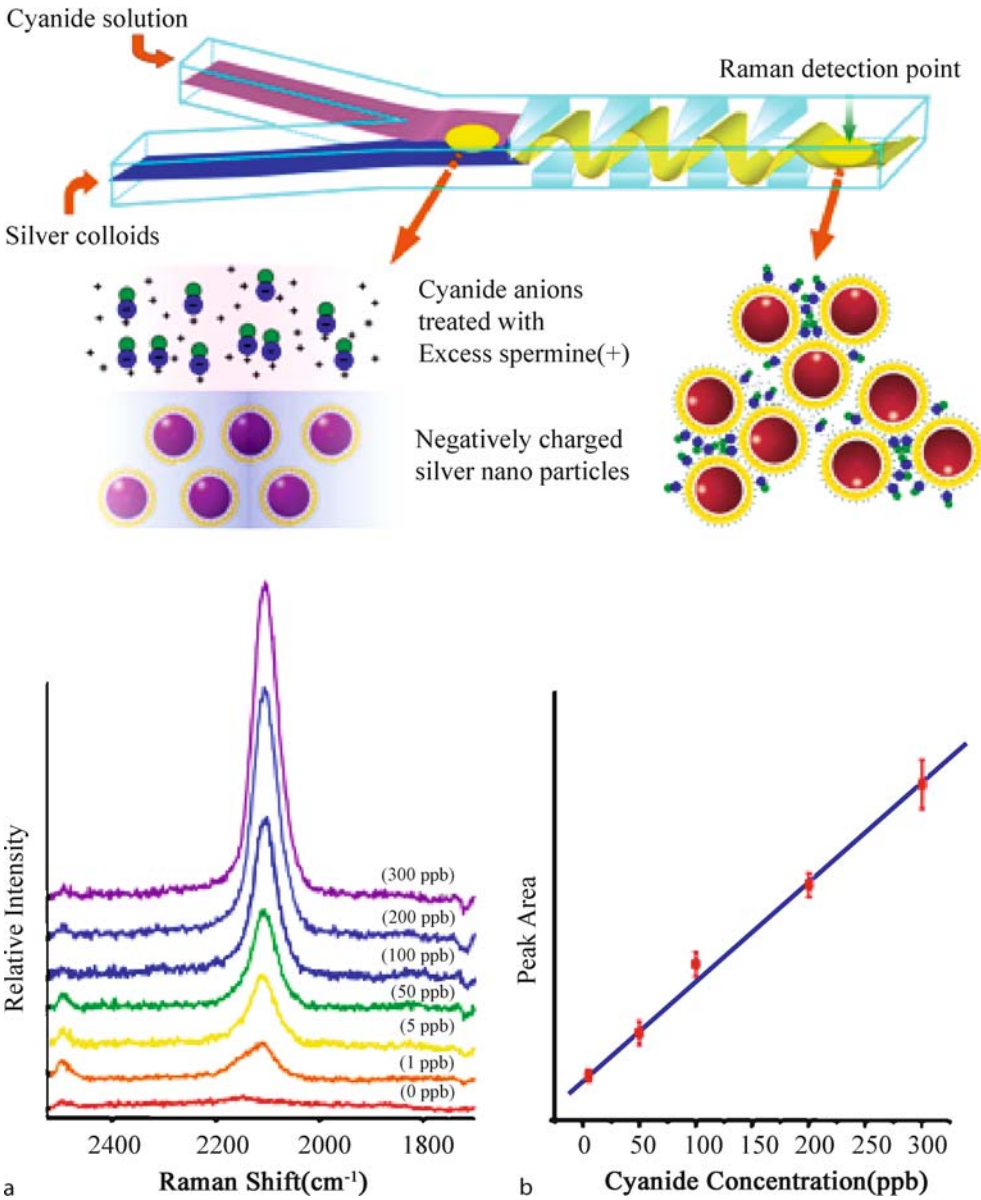

Biosensors Using Surface-Enhanced Raman Scattering, Figure 4 Schematic illustration of the alligator teeth-shaped microfluidic channel. The confluent streams of silver colloids and trace analytes were effectively mixed in the channel through the triangular structures, which are located on the upper and lower surfaces of the channel in a zigzag manner. The flow rate was 5 μL/min. (**a**) SER spectra for increasing concentrations of cyanide ion in the microfluidic channel: (a) 0 ppb, (b) 1 ppb, (c) 5 ppb, (d) 50 ppb, (e) 100 ppb, (f) 200 ppb, and (g) 300 ppb. (**b**) Variation of $C \equiv N$ stretching peak area as a function of cynide ion concentration. (correlation coefficient, $R = 0.991$)

Key Research Findings

In situ Monitoring of Chemical Reaction Using Raman Microscopy

Laser-induced Raman microscopy can be used to monitor a chemical reaction in a microfluidic channel. In situ monitoring of imine formation reaction in a glass microfluidic chip was previously performed. In order to monitor the diffusion process in a microfluidic channel, the Raman spectra are measured at various points along the channel with a constant flow rate. Time-dependent Raman spectra are also measured without flow in order to monitor the variation of Raman peaks to a complete conversion. The disappearance of the C = O stretching peak at 1700 cm^{-1} of the reactant, benzaldehyde, and the appearance of the Raman peak for the product, an imine, at

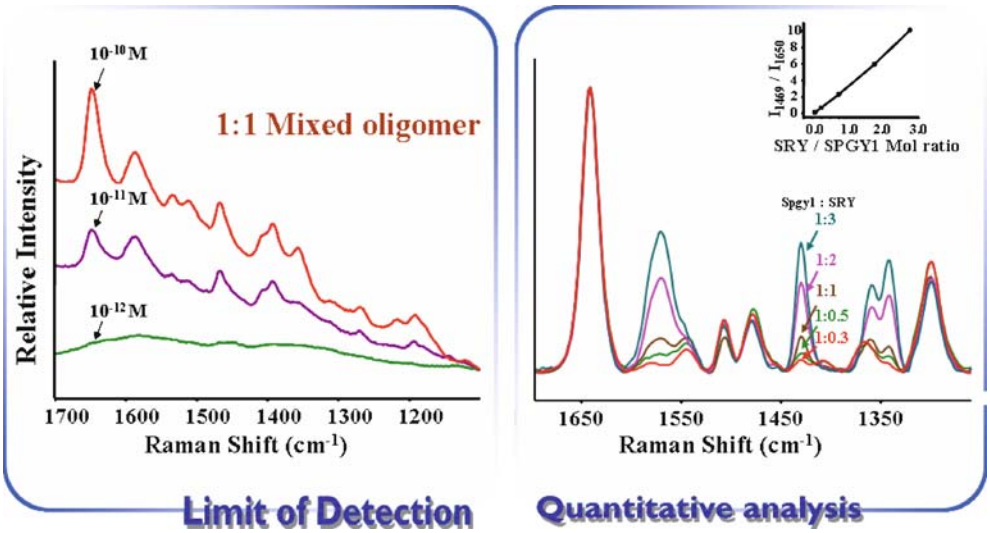

Biosensors Using Surface-Enhanced Raman Scattering, Figure 5 (**a**) Confocal SER spectra of 1 : 1 duplex DNA oligomer mixtures (Cy3-labeled SRY and TAMRA-labelled SPGY1) measured at different concentrations. The flow velocity was 74.08 mm/sec. (*b*) Confocal SER spectra of different molar ratios of duplex DNA oligomer mixtures. The molar ratio between Cy3-labeled SRY and TAMRA-labelled SPGY1 is (a) 1 : 3, (b) 1 : 2, (c) 1 : 1, (d) 2 : 1, and (e) 3 : 1, respectively. The flow velocity was 74.08 mm/sec. The insert shows the variation of peak area ratio (I_{1469}/I_{1650}) as a function of SRY/SPYG1 molar ratio

$1628\,\mathrm{cm}^{-1}$ have been successfully monitored. In addition, the intensity increases of three phenyl-stretching modes in the $1550-1630\,\mathrm{cm}^{-1}$ region have also been observed. The increase of Raman intensity for this vibrational mode is caused by an effective π electron conjugation between two phenyl rings through the $-\mathrm{C}=\mathrm{N}-$ bridging group of the product. Laser-induced Raman microscopy enables us to monitor in situ product formation as well as to get detailed structural information in a microfluidic channel. Laser-induced Raman microscopy is considered as a very sensitive detection technique with a high spatial resolution for the in situ monitoring of organic reaction in a microfluidic channel system. Figure 1 shows in situ Raman monitoring of imine formation reaction in a microfluidic sensor and the optical arrangement for laser focusing on the microfluidic channel of the channel.

Analysis of Passive Mixing Behavior in a PDMS Microfluidic Channel Using Confocal Raman Microscopy

A rapid mixing of the fluids flowing through a microfluidic channel is very important for various applications of microfluidic systems, and a number of devices have been designed to enhance the mixing on the microscale. To use this channel as a microchemical reactor, it is very important to continuously monitor the chemical changes of reaction mixtures in the channel. Confocal Raman Microscopy (CRM) offers a promising route to achieve this goal, since it provides a direct measurement of the conversion process from reactant to product. The applicability of CRM for effective evaluation of the mixing efficiency in a recently developed 3D serpentine channel has been studied. Figure 2a shows a schematic view of a 3D serpentine PDMS channel and four measurement spots along the channel distance. Figure 2b shows the experimental set-up for the confocal Raman measurements on the confluent streams in the microfluidic channels. These two streams were introduced into the PDMS channel from micro syringes connected by tubes to the inlet pipettes. The flow rates were controlled simultaneously using a KD Science micro syringe pump. For the confocal Raman spectroscopic measurements, no fluorescence dye was used during the signal measurements. Figure 3 shows the changes of profiling Raman spectra along the channel distance in the 3D serpentine channel. Ethanol and isopropanol were used for the test of mixing process in the Raman spectroscopy. The results show that the fast mixing behavior of the confluent laminar streams in the 3D serpentine channel that are driven by chaotic advection can be successfully evaluated using the confocal Raman profiling technique.

Ultra-Sensitive Trace Analysis of Cyanide Ion Water Pollutant in a PDMS Microfluidic Channel Using SERS Microscopy

Cyanide ion is one of the most hazardous toxic pollutants in ground waters. It is mainly discharged from the industries such as gold mining, electroplating, printing, tex-

tiles and leather manufacturing. Thus, it is very important to develop a highly sensitive detection system for monitoring trace amounts of cyanide ion in ground waters. SERS spectroscopic technique for a rapid and sensitive trace analysis if cyanide ion water pollutant in an alligator-teeth shaped PDMS microfluidic channel. The confluent streams of silver colloids and trace analytes were effectively mixed in the channel through the triangular structures, which are located on the upper and lower surfaces of the channel in a zigzag manner. The flow rate was controlled using a microsyringe pump. In this work, an alligator teeth-shaped PDMS channel has been fabricated and the SERS detection method has been used to achieve highly sensitive analyte detection. SERS detection, in combination with Lab-on-a-Chip technology, has been applied to the trace analysis of cyanide ion water pollutant. Compared with other methods for the trace analysis of cyanide ions, the detection sensitivity was enhanced by several orders of magnitude. Figure 4 shows the adsorption process of cyanide ions on the silver nanoparticles in a PDMS microfluidic channel. The limit of detection (LOD) is determined to be in the 0.5 – 1.0 ppb range from three standard deviations above the backgrounds.

Quantitative Analysis of Methyl Parathion Pesticides Using Confocal SERS

A quantitative analysis of the methyl parathion pesticides is performed based on the measured SERS peak height at 1246 cm^{-1}. This method has a detection limit of 0.1 ppm. This value satisfies the requirement recommended by the Collaborative International Pesticides Analytical Council (CIPAC) for the determination of methyl parathion in pesticide formulations. This study demonstrates the feasibility of using confocal SERS for the highly sensitive detection of methyl parathion pesticides in a PDMS microfluidic channel. Raman peak, centered at 1246 cm^{-1}, is used as a quantitative evaluation of methyl parathion pesticides. A very good linear response is found in the concentration range 0.1 – 1 ppm. The limit of detection (LOD) is determined to be 0.1 ppm assessed from five standard deviations above background. Compared to other methods for the trace analysis of methyl parathion pesticides, the LOD is enhanced by several orders of magnitude. We expect this analytical technique can be successfully applied to highly sensitive bioanalysis as well as to other trace analysis.

Quantitative Analysis of Duplex Dye-labelled DNA Oligonucleotides in a PDMS Microfluidic Sensor Using Confocal SERS

Rapid and highly sensitive detection of duplex dye-labelled DNA sequences in a PDMS microfluidic channel is investigated using confocal SERS microscopy. This method does not need either an immobilization procedure or a PCR amplification procedure, which are essential for a DNA microarray chip. Furthermore, Raman peaks of each dye-labelled DNA can be easily resolved since they are much narrower than the corresponding broad fluorescence bands. To find the potential applicability of confocal SERS for sensitive bio-detection in a microfluidic channel, the mixture of two different dye-labelled (TAMRA and Cy3) sex determining Y genes, SRY and SPGY1, is adsorbed on silver colloids in the alligator-teeth shaped PDMS microfluidic channel and its SERS signals are measured under flowing conditions. Its major SERS peaks were observable down to the concentration of 10^{-11} M. In the present study, we explore the feasibility of confocal SERS for the highly sensitive detection of duplex dye-labelled DNA oligonucleotides in a PDMS microfluidic channel. Figure 5a shows the confocal SERS spectra of 1 : 1 DNA oligomer mixture adsorbed on colloidal silver at the constant flow velocity. According to our spectral data, the LOD of duplex oligomer mixture is estimated to be 10^{-11} M. Figure 5b also illustrates the confocal SERS spectra for different molar ratios of two oligonucleotides in a microfluidic channel. Different amounts of Cy3-labeled SRY (from 1.65×10^{-10} to 1.5×10^{-9} M) are added to the constant concentration of TAMRA-labelled SPGY1 (5.0×10^{-10} M) to control the molar ratio between SRY and SPGY1 to be 1 : 3, 1 : 2, 1 : 1, 2 : 1, and 3 : 1, respectively. The TAMRA peak at 1650 cm^{-1} is used as an internal standard and the variations of Cy-3 Raman peaks at 1588, 1469 and 1393 cm^{-1} are monitored for their different molar ratios. The intensities of those Raman peaks increase concomitantly with the increase in the concentration of Cy3-labeled SRY. In particular, the Raman peak at 1469 cm^{-1} can be used for the quantitative evaluation of SRY since it does not overlap with any Raman peaks of SPGY1. The insert in Fig. 5b shows the linear response of peak area ratio (I_{1469}/I_{1560}) with the changes in the molar ratio of duplex DNA oligonucleotides. This means that the highly sensitive quantitative detection of duplex DNA oligonucleotide mixtures in a microfluidic channel is possible using the confocal SERS microscopic technique.

Future Directions for Research

In order to apply the SERS sensor to biological analysis, the problem for high throughput screening (HTS) should be solved. In the case of DNA microarray, the throughput is around 16 h for 1 mill oligonucleotide hybridizations. There are two possible ways to apply the microfluidic system to a high-throughput screening (HTS) of biological analysis. First, a multi-parallelization microfluidic channel

can be used for this purpose. Second, a biological assay can be performed in series by rapidly injecting the sample solutions one after the other. In this case, several thousand assays are possible within a period of a few hours if the injection time is less than 1 s.

Cross References

► Nanoparticles
► Microfluidic Optical Devices

References

1. Ruperez A, Laserna JJ (1996) Surface Enhanced Raman Spectrocopy. In: Laserna JJ (ed) Modern Techniques in Raman Spectroscopy. Wiley, Chichester
2. Pelletier MJ (1999) Introduction to Applied Raman Spectroscopy. In: Pelletier MJ (ed) Analytical Applications of Raman Spectroscopy. Blackwell Science, Oxford
3. Smith E, Dent G (2005) Surface Enhanced Raman Scattering and Surface Enhanced Resonance Raman Scattering. In: Smith E (ed) Modern Raman Spectroscopy. Wiley, Chichester
4. Zhao J, Zhang XY, Yonzon CR, Haes AJ, Van Duyne RP (2006) Localized Surface Plasmon Resonance Biosensors. Nanomedicine 1:219–228
5. Zhang XY, Young MA, Lyandres O, Van Duyne RP (2005) Rapid Detection of an Anthrax Biomarkers by Surface-enhanced Raman Spectroscopy. J Am Chem Soc 127:4484–4489
6. Lee M, Lee JP, Rhee H, Choo J, Chai YG, Lee EK (2003) Applicability of Laser-Induced Raman Microscopy for In-Situ Monitoring of Imine Formation in a Glass Microfluidic Chip. J Raman Spectrosc 34:737–742
7. Lee D, Lee S, Seong GH, Choo J, Lee EK, Gweon DG, Lee S (2006) Quantitative Analysis of Methyl Parathion Pesticides in a PDMS Microfluidic Channel Using Confocal Surface-Enhanced Raman Spectroscopy. Appl Spectrosc 60:373–377
8. Yea GH, Lee S, Kyong JB, Choo J, Lee EK, Joo SW, Lee S (2005) Ultra-Sensitive Trace Analysis of Cyanide Water Pollutant in a PDMS Microfluidic Channel Using Surface-Enhanced Raman Spectroscopy. Analyst 130:1009–1011
9. Yea GH, Lee S, Choo J, Oh CH, Lee S (2006) Fast and Sensitive Analysis of DNA Hybridization in a PDMS Microfluidic Channel Using Fluorescence Resonance Energy Transfer. Chemical Communication of RSC, UK 1509–1511
10. Park T, Lee S, Seong GH, Choo J, Lee EK, Kim YS, Ji WH, Hwang SY, Gweon DG, Lee S (2005) Highly Sensitive Signal Detection of Duplex Dye-labelled DNA Oligonucleotides in a PDMS Microfluidic Chip: Confocal Surface-Enhanced Raman Spectroscopic Study. Lab Chip 5:437–442

Biotechnology

► Biomimetics

Bioterrorism

► Lab-on-Chip Devices for Biodefense Applications

Biothreat

► Lab-on-Chip Devices for Biodefense Applications

Biotransducer

Definition

The biotransducer is the functional heart of a biosensor system. The biotransducer comprises the molecular biospecificity of the biorecognition membrane layer and the signal generating capability of the physicochemical transducer. The reproducible, intimate linking of these two parts across an interface is a key distinguishing quality of biotransducers.

Cross References

► Impedimetric Biosensors for Micro and Nano Fluidics

Bipolar Membrane

Definition

An ion-exchange membrane that consists of a layered ion structure. This typically consists of a cation exchange layer and an anion exchange layer. The use of a bipolar membrane enables many functionalities to be used such as antifouling, water dissociation, and the separation of ions. Bipolar membranes are typically unstable in high current environments.

Cross References

► Ion Exchange Membranes

Bistability

Definition

Capability to remain, without an external control action, in either one of two different stable states.
Bistability is a useful property in diverter valves with two outlets when operating in two alternative regimes, the supplied fluid leaving in each regime mainly through one of them. If the microfluidic valve operates at Reynolds numbers – related to the conditions in the inlet – higher than ~ 1000, the bistability may be obtained without use of any movable components in the valve, using the Coanda effect of alternative attachment of a fluid jet to one of two mutually opposed attachment walls. The bistable valves may be

a very useful part of sampling units used in microfluidic systems for combinatorial chemistry testing.

Cross References

► Microfluidic Systems for Combinatorial Chemistry
► Sampling Unit

Blending

► Microfluidic Mixing

Block Copolymerization

Synonyms

Block heteropolymerization

Definition

Polymerization reaction of blocks of different polymerized monomers.

Cross References

► Polymer Synthesis within Microfluidic Reactor

Block Heteropolymerization

► Block Copolymerization

Blood Analysis

► Integrated Microdevices for Medical Diagnostics

Blood–Plasma Separators

► Microfilters

Boiling and Evaporation in Microchannels

SATISH G. KANDLIKAR
Rochester Institute of Technology, Rochester, NY, USA
sgkeme@rit.edu

Synonyms

Flow boiling in microchannels; Flow boiling in narrow channels

Definition

Flow boiling in a microchannel refers to the boiling of a liquid, caused by the addition of heat through the channel walls, as it flows through a microchannel resulting in a net vapor generation at the exit.

Overview

►Microchannels are defined on the basis of the following definition by Kandlikar and Grande [1]:

Conventional channels:	$D > 3\,\text{mm}$
Minichannels:	$3\,\text{mm} \geqslant D > 200\,\mu\text{m}$
Microchannels:	$200\,\mu\text{m} \geqslant D > 10\,\mu\text{m}$
Transitional channels:	$10\,\mu\text{m} \geqslant D > 0.1\,\mu\text{m}$
Transitional microchannels:	$10\,\mu\text{m} \geqslant D > 1\,\mu\text{m}$
Transitional nanochannels:	$1\,\mu\text{m} \geqslant D > 0.1\,\mu\text{m}$
Nanochannels:	$0.1\,\mu\text{m} \geqslant D$

where D is the minimum channel dimension. This article deals with the change of phase of a liquid due to heat transfer from the channels walls while it flows through a microchannel.

The boiling process refers to nucleation of vapor bubbles and their growth resulting from heat transfer from a heated wall. Evaporation refers to change of phase from liquid to vapor at the liquid–vapor interface. Boiling is further classified as pool boiling, which refers to boiling in a pool of liquid, and flow boiling, which refers to boiling with an impressed flow.

Flow boiling in microchannels is essentially similar to the flow boiling process in ►conventional sized channels. Some differences are noted due to the effect of small channel dimensions on the flow boiling process resulting in a large surface area to flow volume ratio [2]. The surface tension forces become important at these scales as compared to the gravitational forces. This makes the boiling process in microchannels less dependent on gravity and orientation. Flow boiling in microchannels is therefore seen as a desirable heat transfer mode in ►microgravity environments.

Applications of microchannel boiling process using low-pressure water [3] or a dielectric hold great promise for chip cooling applications. The high heat transfer coefficients coupled with large heat-carrying capacity due to latent heat removal present an attractive cooling option.

The smaller channel dimensions also shift the flow towards lower Reynolds number. In general, there is a lack of available experimental data for heat transfer in microchannels and a need exists to generate new experimental data to cover the overall shift in the Reynolds numbers, heat flux and mass flux in practical applications.

Basic Methodology

Flow boiling in microchannels is currently at the research stage. The experimental methods employed are evolving as temperature and pressure measurements in the microchannels require deployment of sensors that are microfabricated. For this reason, silicon microchannels with embedded pressure and temperature sensors are being pursued. This is an area where further research is needed to establish the measurement techniques. Metal and ceramic heat exchanger devices are also being fabricated using advanced micromachining and chemical/laser etching and machining processes.

Key Research Findings

Heat Transfer During Flow Boiling in Microchannels

A limited number of experimental studies are available on flow boiling in microchannels using copper and silicon as the substrate over a limited range of heat and mass fluxes for a few fluids (water being the most widely used working fluid), e. g. Pokharna et al. [3], Lee and Mudawar [4], Kosar et al.[5], Hetsroni, et al.[6]. Early studies indicated that the heat transfer at lower mass flux and lower quality conditions is dominated by the nucleate boiling process as in the case of pool boiling. As more data become available, it is seen that the heat transfer exhibits the nucleate boiling dominant mode under low mass flux, low quality conditions, while it appears to be dependent on mass flux and independent of heat flux at higher mass fluxes and higher qualities, as in the case of the convective boiling dominant mode. However, the experimental data are seen to have a larger uncertainty band as compared to the flow boiling data in conventional sized channels due to difficulties in measuring local temperature, pressure and channel dimensions accurately. As the instrumentation, measuring techniques and experimental procedures are refined, more reliable data are expected to become available in the coming years. Further information on the research needs in this area is given by Kandlikar [2].

Heat Transfer Correlations for Flow Boiling in Minichannels and Microchannels

The flow boiling process in microchannels and minichannels has been studied over a limited range of heat and mass fluxes (mostly at the lower ends of their respective ranges employed in macroscale channels). In this range, some authors have found pool boiling type correlations to work well, while others have found the influence of convective effects. The following correlation is an extension of the Kandlikar correlation for large-diameter tubes that is derived from the low mass flux data available in the literature. In the higher mass flux regions, corresponding to the higher all-liquid Reynolds number, the correlation is expected to follow the trends in larger diameter tubes. The overall correlations for microchannels in different regions are given below [7].

Terminology

h_{TP} – two-phase heat transfer coefficient, x – quality, q – heat flux, G – mass flux, h_{LV} – latent heat of vaporization, ρ – density, k – thermal conductivity, D_h – hydraulic diameter, and $Co = [(1-x)/x]^{0.8}[\rho_V/\rho_L]^{0.5}$, $Bo = q''/(Gh_{LV})$, $Re_{LO} = G(1-x)D_h/\mu_L$, $Fr_{LO} = G^2/(\rho_L^2 g D_h)$ and $Nu_{LO} = (h_{LO}D_h/k)$. Subscripts CBD and NBD refer to nucleate boiling dominant and convective boiling dominant regions respectively, and L and V refer to liquid and vapor, respectively.

For flow boiling in microchannels and minichannels, heat transfer correlations in the NBD and CBD regions are given below:

$$h_{TP,NBD} = 0.6683\,Co^{-0.2}(1-x)^{0.8} f_2(Fr_{LO})\,h_{LO} + 1058\,Bo^{0.7}(1-x)^{0.8}\,h_{LO}F_{FL} \quad (1)$$

$$h_{TP,CBD} = 1.136\,Co^{-0.9}(1-x)^{0.8} f_2(Fr_{LO})\,h_{LO} + 667.2\,Bo^{0.7}(1-x)^{0.8} h_{LO}F_{FL} \quad (2)$$

The flow boiling heat transfer coefficient h_{TP} is then related to $h_{TP,NBD}$ and $h_{TP,CBD}$ depending on the flow regions under all-liquid flow conditions as described below.

Region I

Turbulent flow region: $Re_{LO} \geqslant 3000$

$$h_{TP} = \text{larger of } \left(h_{TP,NBD}, h_{TP,CBD}\right) \quad (3)$$

h_{LO} is given by:

For $10^4 \leqslant Re_{LO} \leqslant 5 \times 10^6$, Petukhov and Popov correlation:

$$h_{LO} = \frac{Re_{LO}\,Pr_L (f/2)(k_L/D)}{1 + 12.7\left(Pr_L^{2/3} - 1\right)(f/2)^{0.5}} \quad (4)$$

For $3000 \leqslant \mathrm{Re_{LO}} < 10^4$, Gnielinski correlation:

$$h_{\mathrm{LO}} = \frac{(\mathrm{Re_{LO}} - 1000)\,\mathrm{Pr_L}(f/2)(k_{\mathrm{L}}/D)}{1 + 12.7\left(\mathrm{Pr_L^{2/3}} - 1\right)(f/2)^{0.5}} \tag{5}$$

The friction factor f in the above equations is given by

$$f = \left[1.58\ln(\mathrm{Re_{LO}}) - 3.28\right]^{-2} \tag{6}$$

Region II

Transition region: $1600 \leqslant \mathrm{Re_{LO}} < 3000$

$$h_{\mathrm{TP}} = \text{larger of } (h_{\mathrm{TP,NBD}}, h_{\mathrm{TP,CBD}}) \tag{7}$$

With h_{LO} taken from linear interpolation between the turbulent value using the Gnielinski correlation (given under Region I above) and the appropriate laminar value (for $q'' = C$ or $T = C$) using $h_{\mathrm{LO}} = (\mathrm{Nu_{LO}}k/D_{\mathrm{h}})$.

Region III

Laminar flow region: $100 \leqslant \mathrm{Re_{LO}} < 1600$

$$h_{\mathrm{TP}} = \text{larger of } (h_{\mathrm{TP,NBD}}, h_{\mathrm{TP,CBD}}) \tag{8}$$

With h_{LO} taken from the appropriate laminar value (for $q'' = C$ or $T = C$) using $h_{\mathrm{LO}} = (\mathrm{Nu_{LO}}k/D_{\mathrm{h}})$.

Region IV

Deep laminar flow region: $\mathrm{Re_{LO}} < 100$

$$h_{\mathrm{TP}} = h_{\mathrm{TP,NBD}} \tag{9}$$

Fluid-Surface Parameter, F_{FL}

The fluid surface parameters in Eqs. (1) and (2) are given in Table 1, with h_{LO} taken from the appropriate laminar value (for $q'' = C$ or $T = C$) using $h_{\mathrm{LO}} = (\mathrm{Nu_{LO}}k/D_{\mathrm{h}})$.

Critical Heat Flux

During the flow boiling process, the walls of the channel are generally covered with liquid or a liquid film, occasionally exposing the walls to the vapor phase followed by rewetting with the liquid. At certain conditions, the liquid fails to rewet the walls leading to the condition of *dryout*. Since the vapor is unable to cool the wall as effectively as a liquid-covered wall, the local wall temperature may rise uncontrollably with further addition of heat.

The heat flux at this condition is referred to as the ►critical heat flux, or ►CHF. It depends on the flow conditions, channel geometry, local quality, fluid properties, channel material and flow history. Bergles and Kandlikar [8] discuss the CHF in microchannels from a systems perspective. It is important to establish CHF condition as a function of the mass flux and quality for a given system to ensure its safe operation. Qu and Mudawar [9] presented CHF data with water in 21 parallel minichannels of 215 μm × 821 μm cross-section over a range of $G = 86 - 268\,\mathrm{kg/(m^2 s)}$ and $q'' = 264 - 542\,\mathrm{kW/m^2}$, $x = 0.0 - 0.56$, and $P_{\mathrm{in}} = 121.3 - 139.8\,\mathrm{kPa}$. Kosar et al. [5] present low-pressure water data in microchannels enhanced with reentrant cavities. Also, the correlation by Katto [10] developed for large channels may be applied for approximate CHF estimation in the absence of an established CHF correlation for microchannels.

Boiling and Evaporation in Microchannels, Table 1 Values of F_{FL} (fluid-surface parameter) in the flow boiling correlations (Eqs. (1) and (2))

Fluid	F_{FL}
Water	1.00
R-11	1.30
R-12	1.50
R-13B1	1.31
R-22	2.20
R-113	1.30
R-114	1.24
R-134a	1.63
R-152a	1.10
R-32/R-132	3.30
R-141b	1.80
R-124	1.00
Kerosene	0.488

Future Directions for Research

Flow boiling in microchannels is currently in the research phase. Its applications include high heat flux removal in advanced computer chips and high-power electronics and electrical systems, pulsed power weapons systems, solid-state lasers and phased-array radars and sensor arrays. Microchannel heat exchangers for phase change applications offer the advantages of very compact design with large volumetric energy transfer densities. It is especially suited for the future 3D computer chip architecture by incorporating the microchannels in multiple parallel configurations. Other cooling arrangements which rely on the surface cooling techniques, such as spray or jet cooling, may not be suitable to the 3D configuration. Hot spot cooling and integration with the device architecture is also a possible application.

Another area that is expected to benefit by incorporation of microchannels is the refrigeration industry where

the potential benefits resulting from material and space savings will be quite significant. The high heat transfer coefficients and compact design makes flow boiling in microchannels very attractive in air liquefaction and cryogenic industries as well. It is expected that significant innovations and new developments will occur in this field in the near future.

One of the challenges faced in microchannel flow boiling systems is the limit posed by the critical heat flux (CHF). Establishing the CHF limits of the plain microchannels and developing new enhanced geometries with higher CHF limits is a priority that needs to be addressed in the future before widespread application of microchannel flow boiling systems can be considered.

Cross References

- ► Bubble Actuated Microfluidic Switch
- ► Bubble Dynamics in Microchannels
- ► Cavitation in Microdomains
- ► Droplet Dispensing
- ► Flow Boiling Instability
- ► Heat Transfer in Microchannel Flows

References

1. Kandlikar SG, Grande WJ (2003) Evolution of Microchannel Flow Passages – Thermohydraulic Performance and Fabrication Technology. Heat Trans Eng 24(1):3–17
2. Kandlikar SG (2002) Fundamental Issues Related to Flow Boiling in Minichannels and Microchannels. Exp Thermal Fluid Sci 26(2–4):389–407
3. Pokharna H, Masahiro K, DiStefano E, Mongia R, Barry J, Crowley C, Chen W, Izenson M (2004) Microchannel Cooling in Computing Platforms: Performance Needs and Challenges in Implementation. 2nd Int Conf Microchannels Minichannels (ICNMM2004), ASME, 109–118
4. Lee J, Mudawar I (2005) Two-Phase Flow in High-Heat Flux Micro-channel Heat Sink for Refrigeration Cooling Applications, Part II: Heat Transfer Characteristics. Int J Heat Mass Trans 48:941–955
5. Kosar A, Kuo C, Peles Y (2005) Reduced Pressure Boiling Heat Transfer in Rectangular Microchannels with Interconnected Reentrant Cavities. J Heat Trans 127:1106–1114
6. Hetsroni G, Klein D, Mosyak A, Segal Z, Pogrebnyak E (2004) Convective Boiling in Parallel Microchannels. Microscale Thermophys Eng 8:403–421
7. Kandlikar SG, Balasubramanian P (2004) An Extension of the Flow Boiling Correlation to Transition, Laminar and Deep Laminar Flows in Minichannels and Microchannels. Heat Trans Eng 25(3):86–93
8. Bergles AE, Kandlikar SG (2005) On the Nature of Critical Heat Flux in Microchannels. J Heat Trans 127(1):101–107
9. Qu WL, Mudawar I (2004) Transport Phenomena in Two-Phase Micro-channel Heat Sinks. J Electron Packag 126(2):213–22
10. Katto Y (1981) General Features of CHF of Forced Convection Boiling in Uniformly Heated Rectangular Channels. Int J Heat Mass Trans 24:1413–1419

Boltzmann Equation

Definition

Boltzmann equation determines the evolution of the velocity distribution function and reads as where $Q(ff)$ is the collision integral.

Cross References

- ► Gas Flow in Nanochannels
- ► Heat Transfer in Microchannel Flows
- ► Supersonic Micro-Nozzles
- ► Micro - and Nanoscale in Gas Dynamics
- ► Lattice Poisson-Boltzmann Method, Analysis of Electroosmotic Microfluidics

Boltzmann's Constant

Definition

A constant that relates temperature of a body to the thermal energy retained within it; $k = 1.3806504 \times 10^{-23}$ J/K.

Cross References

- ► Piezoelectric Microdispenser

Bonding of Non-Metallic Inorganic Surfaces and Polymers

- ► Glass-Polymer Bonding

Bosch Process

- ► Anisotropic Etching
- ► ICP Etching

Boundary Condition at Interface

- ► Boundary Slip of Liquids

Boundary Element Method

- ► Boundary Element Method and its Applications to the Modeling of MEMS Devices

Boundary Element Method and its Applications to the Modeling of MEMS Devices

WENJING YE
Department of Mechanical Engineering,
Hong Kong University of Science and Technology,
Hong Kong, China
mewye@ust.hk

Synonyms

Boundary element method; Boundary integral approaches

Definition

The boundary element method is a numerical method for solving integral equations. These integral equations are the integral representations of the governing equations of the underlying physical problems, often formulated based on the fundamental solutions of the problems.

Overview

The boundary element method (BEM) has been established as a powerful numerical method for solving engineering problems. Applications include, but are not limit to, electromagnetics, elasticity, acoustics, potential and viscous flow. In contrast to other numerical techniques, the governing equations are cast into a set of integral equations that are solved by collocation or Galerkin discretization. A detailed description of this method can be found in [1]. One major advantage of the BEM is that it reduces the dimensionality of the problem by one. Thus for the majority of practical cases the simple boundary discretization leads to a much smaller system of algebraic equations than any domain method. Another advantage of the BEM is that it can handle rapid transitions and steep gradients of fields since the formulation only involves unknowns on surfaces. Given the reduced complexity of data preprocessing (meshing) and smaller size of the resulting systems, the BEM is an efficient method for solving many engineering problems, especially for exterior problems and problems with free surfaces or moving boundaries.

One disadvantage of the conventional BEM is that it generates a fully populated system matrix. Also, the computation of matrix entries involves singular and nearly singular surface integrals, which are difficult to compute. This offsets some of the computer time saved by the much reduced matrix size. The recently developed accelerated BEM approaches have overcome this difficulty by combining matrix sparsification techniques, such as the fast multipole method (FMM) [2] and the precorrected-FFT technique [3], with iterative solvers. A central idea in acceleration techniques is to approximate the matrix-vector product by some computationally efficient means. In the FMM, multipole and local expansion is used to calculate the long-range interactions. In the precorrected-FFT method, a uniform grid is used to represent the long-range interactions. This grid representation allows the fast Fourier transform to be used to efficiently perform the computation. With these accelerated techniques, the BEM has emerged as one of the most efficient numerical methods for large-scale problems particularly those with complex 3D geometry. Fast BEM codes have been developed and applied successfully in a variety of applications including the modeling of complex MEMS devices, for example, the prediction of air damping in micro-resonators [4].

Basic Methodology

Boundary Integral Formulation

The BEM starts with an integral formulation of the governing equation. As an illustration, consider the potential problem governed by the Laplace equation:

$$\nabla^2 u = 0 \tag{1}$$

An integral formulation of the Laplace equation reads

$$c(\boldsymbol{x})u(\boldsymbol{x}) = -\int_{\partial\Omega} G(\boldsymbol{x},\boldsymbol{y})\frac{\partial u(\boldsymbol{y})}{\partial n(\boldsymbol{y})}\,\mathrm{d}S(\boldsymbol{y}) + \int_{\partial\Omega} \frac{\partial G(\boldsymbol{x},\boldsymbol{y})}{\partial n(\boldsymbol{y})} u(\boldsymbol{y})\,\mathrm{d}S(\boldsymbol{y}) \tag{2}$$

where

$$c(\boldsymbol{x}) = \begin{cases} 1, \boldsymbol{x} \in \Omega \\ 0, \boldsymbol{x} \notin (\Omega \cup \partial\Omega) \\ \alpha, \boldsymbol{x} \in \partial\Omega \end{cases}$$

In Eq. (2), Ω is the domain of the problem with boundary $\partial\Omega$, $n(\boldsymbol{y})$ is the outward normal vector at the field point $\boldsymbol{y}$, $\boldsymbol{x}$ is the evaluation point and α is the solid angle at $\boldsymbol{x}$ (it equals $1/2$ when $\boldsymbol{x}$ is a smooth surface point). $G(\boldsymbol{x},\boldsymbol{y})$ is the Green's function of the Laplace operator which, in a 3D space, is given by

$$G(\boldsymbol{x},\boldsymbol{y}) = \frac{1}{4\pi r}, \text{ where } r = |\boldsymbol{x} - \boldsymbol{y}| \ .$$

Note that all integrals in Eq. (2) are boundary integrals, i. e., they involve only the boundary values of the dependent variable and its derivatives. As such, this integral

equation can be employed to obtain the unknown boundary quantities based on the given boundary conditions. For example, for Dirichlet problems, the unknown boundary values are the normal derivatives of the potential, which can be calculated by solving Eq. (2) with evaluation points being on the boundary. Once all the boundary quantities are obtained, the potential at any point inside the domain is calculated again using Eq. (2) but with $c(\boldsymbol{x}) = 1$.

Discretization

To numerically solve Eq. (2), one can employ either the Galerkin scheme or the collocation scheme. In the Galerkin scheme, Eq. (2) is satisfies in a weighted integral sense while in the collocation scheme, the integral equation is satisfied at the chosen collocation points. For simplicity, the collocation scheme is used to illustrate the numerical implementation of the BEM.

First, the boundary of the problem domain is discretized into a collection of elements. On each element, quantities are assumed to be simple functions, often polynomials, which are fully determined by their nodal values. For example, a constant element has only one node located at its centroid. Over this element, quantities are assumed to be constant determined by their values at the centroid. For a general case at the i-th element

$$u = \sum_{j=1}^{p} N_j u_j^{(i)} \tag{3}$$

$$q = \frac{\partial u}{\partial n} = \sum_{j=1}^{p} N_j q_j^{(i)} \tag{4}$$

where N_j is the interpolation function, p is the number of nodes of this element and $u_j^{(i)}$ and $q_j^{(i)}$ are the nodal values at the j-th node of the i-th element. Substituting Eqs. (3) and (4) into the integral formulation (2) and enforcing Eq. (2) is satisfied at each node, a set of discretized equations in the form of Eq. (5) can be obtained:

$$\begin{aligned} c(\boldsymbol{x}_k)u(\boldsymbol{x}_k) = &- \sum_{i=1}^{n} \int_{\Gamma_i} G(\boldsymbol{x}_k, \boldsymbol{y}) \sum_{j=1}^{p} N_j(\boldsymbol{y}) q_j^{(i)} \, \mathrm{d}S(\boldsymbol{y}) \\ &+ \sum_{i=1}^{n} \int_{\Gamma_i} \frac{\partial G(\boldsymbol{x}_k, \boldsymbol{y})}{\partial n(\boldsymbol{y})} \sum_{j=1}^{p} N_j(\boldsymbol{y}) u_j^{(i)} \, \mathrm{d}S(\boldsymbol{y}) \,, \\ k = 1, 2, \cdots m \end{aligned} \tag{5}$$

In Eq. (5), n is the number of elements, Γ_i denotes the i-th element and m is the total number of nodes. This set of equations can be rearranged into a matrix form:

$$[\mathbf{G}]\{\boldsymbol{q}\} - [\mathbf{H}]\{\boldsymbol{u}\} = \mathbf{0} \tag{6}$$

where $\mathbf{G}$, $\mathbf{H}$ are matrices with entries being the element-wise integrals of the product of the kernel function (G and $\partial G/\partial n$) and the interpolation functions, and $\boldsymbol{u}$ and $\boldsymbol{q}$ are vectors comprised of nodal values of the potential and its normal derivative respectively. Equation (6) is a linear system that can be solved to obtain the unknown boundary values at each node. These values together with the given boundary conditions can be substituted into Eq. (2) to obtain potentials at interior points.

Key Research Findings

Air Damping of Laterally Oscillating Micro-Resonators

Air-packaged micro-resonators are widely used in a variety of low-frequency applications such as accelerometers, gyroscopes and sensors. In many of these applications, the quality factor of the resonator, defined as the ratio of total energy to energy dissipated per cycle, is a key performance variable but is very difficult to predict. The problem is that the dominant loss mechanism for many air-packaged resonators is viscous drag, and to predict drag it is necessary to accurately determine the detailed air flow in these typically very complicated three-dimensional resonators.

A number of approximate analytic models for drag have been developed, typically based on one-dimensional Couette or Stokes flow [5]. Such models give a good rough estimate of the drag force but they can be insufficiently accurate to correctly predict geometrical sensitivities. In particular, these one-dimensional models do not account for important finite size and edge effects. To account for these effects accurately, a detailed 3D analysis of air flow surrounding the resonators is necessary. This leads to a problem with a domain which is bounded by the complex resonator at one end and extends to infinity at the other end. For such a problem, domain methods such as the finite element method and the finite volume method, etc., could be very inefficient and are not suitable. The accelerated BEM, on the other hand, is a perfect method for handling this problem.

Micro-Resonator

The comb drive micro-resonator used for this study is shown in top and side view in Fig. 1. The main components of the resonator are a shuttle structure comprised of the connected back-to-back combs, two suspended folder beams with one end anchored to the substrate, and fixed

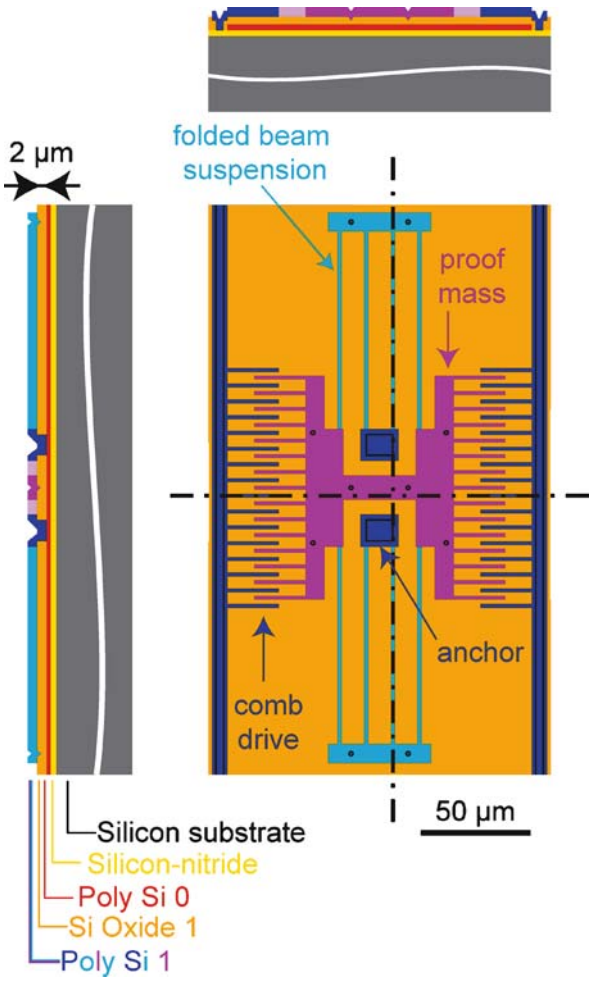

Boundary Element Method and its Applications to the Modeling of MEMS Devices, Figure 1 Schematic view of a laterally oscillating resonator

comb drives. Table 1 lists some key dimensions of the resonator.

The shuttle structure can be moved to the left or right using electrostatic forces generated by creating a potential difference between the shuttle and either the left or the right fixed combs (shown in dark blue in Fig. 1). Once the shuttle moves away, the folded beams, acting as springs, bring it back to its equilibrium position. This results in an oscillating motion.

Macro Model

Based on its operation principle, the resonator can be modeled as a simple spring–mass–dashpot system, as shown in Fig. 2, with the shuttle being the proof mass, folder beams being the spring and the surrounding air being the dashport damper. The displacement of the proof mass can then be

Boundary Element Method and its Applications to the Modeling of MEMS Devices, Table 1 Resonator dimensions

Finger gap	2.88 μm
Finger length	40.05 μm
Finger overlap	19.44 μm
Beam length	151 μm
Beam width	1.1 μm
Center plate Side plate1 × 2 Side plate2 × 4	$54.9 \times 19.26\ \mu m^2$ $28.26 \times 89.6\ \mu m^2$ $11.3 \times 40.5\ \mu m^2$
Thickness	1.96 μm
Substrate gap	2 μm
Truss length	78 μm
Truss width	13 μm

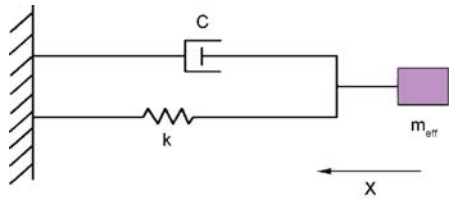

Boundary Element Method and its Applications to the Modeling of MEMS Devices, Figure 2 Spring–mass–dashpot model of a resonator

obtained by solving the second-order differential equation

$$m_{\text{eff}}\ddot{x} + c\dot{x} + kx = F_{\text{applied}} \tag{7}$$

where x is the mass displacement measured from the equilibrium position, m_{eff} is the effective mass, c is the damping coefficient, k is the stiffness of the spring and F_{applied} is the externally applied electrostatic force.

The frequency and the quality factor of the resonator are related to the parameters as

$$f_0 = \frac{1}{2\pi}\sqrt{\frac{k}{m_{\text{eff}}}} \tag{8}$$

and

$$Q = \frac{\sqrt{km_{eff}}}{c} \tag{9}$$

The effective mass for the micro-resonator is easily determined from the geometry, given fabrication process information and the density of the structure material which is polysilicon in this case. Uncertainties in polysilicon's elastic material properties and manufacturing-induced residual stress make it difficult to predict the spring constant, though the measured resonant frequency data can be

combined with the computed effective mass to determine a spring constant. What has been most difficult to determine from geometry and process information is the loss in an air-packaged micromachined device, or equivalently the dashpot constant for the spring–mass–dashpot model. The difficulty is that loss in air-packaged microresonators is primarily due to viscous drag, which in turn depends on a very complicated air flow pattern. These issues will be considered in more detail in subsequent sections, with particular emphasis given to the issue of loss prediction.

Determination of Parameters

The effective mass for a spring–mass–dashpot model of the resonator is related to geometry and the density of the polysilicon. In particular, energy considerations and an application of beam theory lead to a resonator effective mass given by

$$m_{\text{eff}} = m_{\text{p}} + m_{\text{f}} + \frac{12}{35} m_{\text{b}} + \frac{1}{4} m_{\text{t}} \tag{10}$$

where m_{p}, m_{f} are the masses of the shuttle and the moving fingers respectively, m_{b} is the mass of the beams and m_{t} is the mass of the connecting truss. With the dimensions shown in Table 1 and the density of $\rho = 2300\,\text{kg/m}^3$ for polysilicon, the effective mass of the system is 5.61×10^{-11} kg.

A simple approach to computing the spring constant for the resonator is to assume that the trusses joining the folded beam segments (shown in light blue in Fig. 2) are rigid. If there is no residual stress, beam theory predicts a spring constant of

$$k = 4Eh\left(\frac{w}{L}\right)^3 \tag{11}$$

where E is the Young's modulus of polysilicon, and h, w and L are the thickness, the width and the length of the beam respectively. If E is chosen to be 150 GPa, the calculated stiffness of the beam in our resonator is 0.454 N/m. This value, together with the effective mass, would predict a natural resonant frequency of 14,321 Hz which is far from the measured value of 19,200 Hz. This indicates that either the stiffness or the mass was predicted wrong. Because stiffness is more sensitive to measurement error than mass (mass is linearly proportional to the beam width, but stiffness is proportional to the cube of width) and it also depends on residual stress and Young's modulus of polysilicon that are difficult to predict, it is reasonable to assume that mass is more accurate than the prediction of the stiffness. In addition, since the focus is on the issue of modeling damping, the semi-empirically determined value of 0.816 N/m, obtained from Eq. (8) using the effective mass from Eq. (10) and the measured resonant frequency, was used as the stiffness in this work.

The damping coefficient, c, caused by the drag force exerted on the resonator by the air, can only be determined if the air flow velocities are known. This requires the modeling of the fluid field surrounding the resonator. In the following section several of the flow models that have been used to compute resonator drag are discussed.

Flow Models

The frequency of operation is so slow that the open air surrounding the resonator can be regarded as an incompressible fluid. In addition, the characteristic length (micrometers) and oscillation amplitude (35 nm) are both small, resulting in a small Reynolds number (8×10^{-5}, $\text{Re} = \rho UL/\mu$, where ρ and μ are the density and viscosity of the fluid, U is a characteristic velocity and L is a characteristic length, 2 μm in the resonator under study), so the nonlinear inertial force will be negligible compared to the viscous force. Finally, rarefaction effects are unlikely to be significant, as the Knudsen number (Kn) for this resonator is small (0.03, $\text{Kn} = \lambda/L$; λ is the mean free path of the gas molecules, 0.065 μm). Thus, the fluid behavior is expected to be accurately described by solutions of the incompressible Stokes equations with no-slip boundary conditions.

For the oscillating resonator, the velocity is in sinusoidal steady state and therefore the velocity $\boldsymbol{u}$ and the pressure P of the fluid satisfy the frequency domain Stokes equation. The Stokes equation consists of the continuity equation and the linear momentum equation

$$\text{i}2\pi f \rho \boldsymbol{u}(f) = -\nabla P(f) + \mu \nabla^2 \boldsymbol{u}(f) \tag{12}$$

$$\nabla \cdot \boldsymbol{u}\,(f) = 0 \tag{13}$$

where $\boldsymbol{u}(f)$ and $P(f)$ are complex amplitudes. For notational convenience, in the following the dependence on frequency will be assumed, and not stated explicitly. Note that in the case of steady flow, the only frequency-dependent term, the inertial term on the left side of Eq. (8), is zero.

To solve Eqs. (12) and (13) with oscillating velocity boundary conditions, simple models such as the Couette flow model and 1D Stokes model have been used. These models ignore the finite size and edge effects, as both of them model the device as two infinitely large parallel plates with one (the proof mass) oscillating on the top of the other (substrate). The Couette model further assumes a steady flow, resulting in a linear velocity profile between the plates. As shown later, the quality factor obtained by these two models is over-predicted by a factor of two, indicating the importance of 3D effects.

To account properly for all the edge and finite size effects and possible pressure gradients created by the motion of plates, a full 3D analysis is required. With the infinite domain and rather complicated resonator geometry, the BEM accelerated with the precorrected-FFT technique is chosen to numerically solve the 3D Stokes problem. To do so, an integral formulation must be introduced first:

$$u_j(\boldsymbol{x}) = -\frac{1}{8\pi\mu}\int_{\partial\Omega} G_{ij}(\boldsymbol{x},\boldsymbol{y}) f_j(\boldsymbol{y})\,\mathrm{d}S(\boldsymbol{y}) \tag{14}$$

where $\partial\Omega$ is the surface of the resonator, and the Greens function is given by

$$G_{ij}(\boldsymbol{x},\boldsymbol{y}) = \frac{\delta_{ij}}{r}A(R) + \frac{\hat{x}_i\hat{x}_j}{r^3}B(R) \tag{15}$$

$$A(R) = 2\mathrm{e}^{-R}\left(1+\frac{1}{R}+\frac{1}{R^2}\right) - \frac{2}{R^2}$$

$$B(R) = -2\mathrm{e}^{-R}\left(1+\frac{3}{R}+\frac{3}{R^2}\right) + \frac{6}{R^2}$$

$$R = \lambda r\,.$$

In Eq. (14), $u_j(\boldsymbol{x})$ is the j-th component of the velocity vector at the evaluation point $\boldsymbol{x}$, $\boldsymbol{f}$ is the Stokeslet density function, and the real part of $\boldsymbol{f}$ corresponds to the real part of the surface traction if there is a single moving object that rigidly moves in the fluid, $\hat{x}_i$ is the i-th component of the relative position vector between the evaluation point and the field point, i. e., $\hat{x}_i = y_i - x_i$, and λ is the frequency parameter which is defined as

$$\lambda^2 = i\frac{2\pi f\rho}{\mu}$$

Numerical Solution of 3D Stokes Model

The surface of the resonator is discretized into n small elements. A collocation scheme and constant elements were employed. A system of equations for the unknowns is derived by insisting that the integral Eq. (4) is satisfied exactly at each element centroid. The result is a linear system which relates the known quantities (velocity $\boldsymbol{u}$) to the unknown quantities (traction force $\boldsymbol{f}$), as in

$$\begin{Bmatrix} \boldsymbol{u}^1 \\ \boldsymbol{u}^2 \\ \vdots \\ \boldsymbol{u}^n \end{Bmatrix} = P(\omega) \begin{Bmatrix} \boldsymbol{f}^1 \\ \boldsymbol{f}^2 \\ \vdots \\ \boldsymbol{f}^n \end{Bmatrix} \tag{16}$$

where $\boldsymbol{u}^i$ and $\boldsymbol{f}^i$ are the velocity and traction force for the i-th element, and P is a $3n \times 3n$ dense matrix whose elements are given by

$$P_{kl}^{ij} = \int_{\Gamma_j}\left[\frac{\delta_{kl}A(R)}{r} + \frac{(x_k^i - y_k)(x_l^i - y_l)B(R)}{r^3}\right]\mathrm{d}s$$

$$k, l = 1, 2, 3\,. \tag{17}$$

Here, $\boldsymbol{x}^i$ denotes the centroid of the i-th element and Γ_j denotes the surface of the j-th element.

The dense linear system in Eq. (16), without any sparsification, could be very expensive to solve for large-scale systems. The computational time of a direct solver, for example, the Gaussian elimination, grows as the cube of the number of unknowns. For the resonator example, there are near 60,000 unknowns in the discretization shown in Fig. 3. Gaussian elimination would require more than 300,000 gigaflops to solve. In addition, the memory required to store the matrix grows as the square of the number of unknowns, and for the resonator example it would require more than 40 gigabytes.

Even with an iterative method which does not use the entries of the matrix P explicitly, but only requires matrix-vector products, the cost of computing dense matrix-vector products grows with the square of the number of unknowns. So just using an iterative method still results in a computationally expensive algorithm. However, there are a number of techniques for quickly computing approximate matrix-vector products for matrices associated with discretized integral equations.

The FastStokes program [6, 7] was used to compute the drag forces on the micro-resonator shown schematically in Fig. 2. FastStokes combines the iterative method GMRES [8] with the precorrected-FFT [3] technique for computing fast matrix-vector products. The discretized, or meshed, structure is shown in Fig. 3. Note that both the

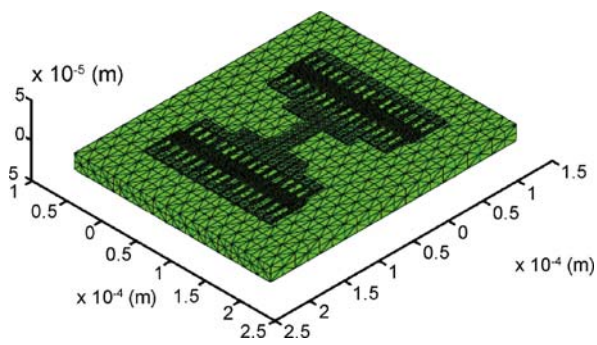

Boundary Element Method and its Applications to the Modeling of MEMS Devices, Figure 3 The meshed resonator

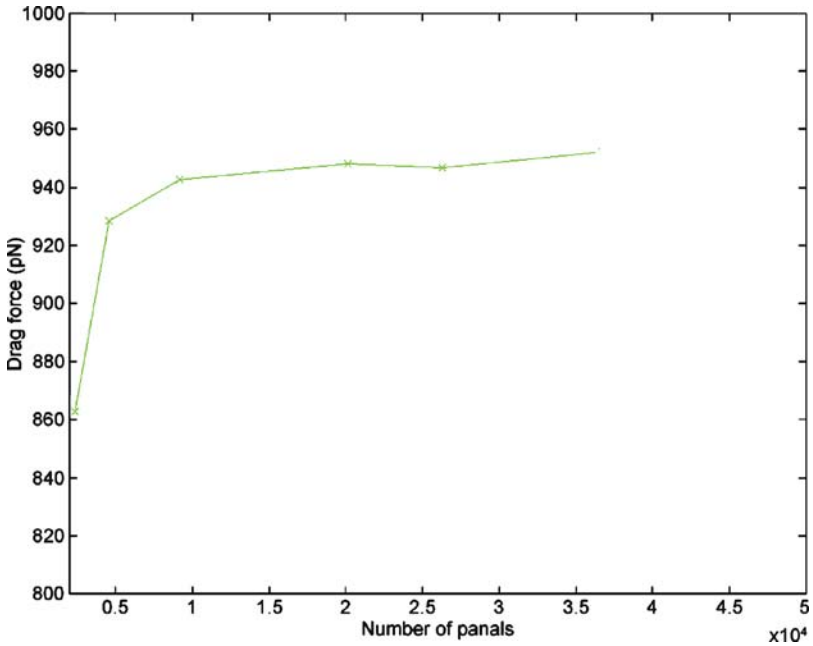

Boundary Element Method and its Applications to the Modeling of MEMS Devices, Figure 4 A convergence plot of the simulated drag force

Boundary Element Method and its Applications to the Modeling of MEMS Devices, Table 2 A comparison of drag force

Drag (pN)	Bottom	Side	Top
Couette	424.37	57.33	0
1D Stokes	437.93	57.37	52.67
FastStokes	510.72	294.50	142.80

polysilicon structures and the substrate are discretized, for a total of 20,148 panels.

The viscous drag forces on the resonator oscillating at $f = 19{,}200$ Hz were computed using progressively finer discretizations, to ensure that the discretization error was sufficiently small. Figure 4 is a plot of how the drag force converges with discretization refinement. As is clear from the plot, the results have converged to within 1% with as few as 10,000 panels. For these simulations, the kinematic viscosity and the density of air were assumed to be $0.157\ \text{cm}^2/\text{s}$ and $1.177\ \text{kg/m}^3$ respectively.

Table 2 shows the distribution of drag forces obtained from FastStokes (with a total of 36,700 panels) together with results obtained from the Couette model and the 1D Stokes model.

The contribution to the drag from the fluid between the resonator and the substrate (denoted as the bottom force) is predicted reasonably well by two simple 1D models. It is not surprising that the two 1D models are in such close agreement. The small gap ($g = 2\,\mu$m) and slow motion imply that the penetration depth, defined as the distance over which the motion amplitude has dropped to 1% of its maximum value, is 37 times larger than the gap. This indicates that the flow between the resonator and the substrate is fully developed and the velocity profile will be reasonably predicted by the Couette model. That the two 1D models are so close also suggests that the difference between the drag forces obtained from the 1D and 3D models is mostly due to the finite size effects.

Both 1D models seriously underestimate the drag force coming from the side. Due to the infinite-long plate assumption, only drag coming from the fluid between fingers is included in the 1D models. Result from the 3D calculation indicates that side forces are a significant contributor to resonator drag.

In the Couette model, in order to satisfy zero velocity at infinity, the velocity gradient at the top plate is zero. Thus there is no drag force from the top flow. By including the inertial term, the 1D Stokes model predicted about 52.67 pN of drag due to the fluid on the top. However, this value is much smaller than the drag predicted from the 3D Stokes model. This fact, again, indicates the significance of the finite size effects on the drag force.

Results

Quality Factor The quality factor, Q, of the resonator was calculated based on the computed drag force, the

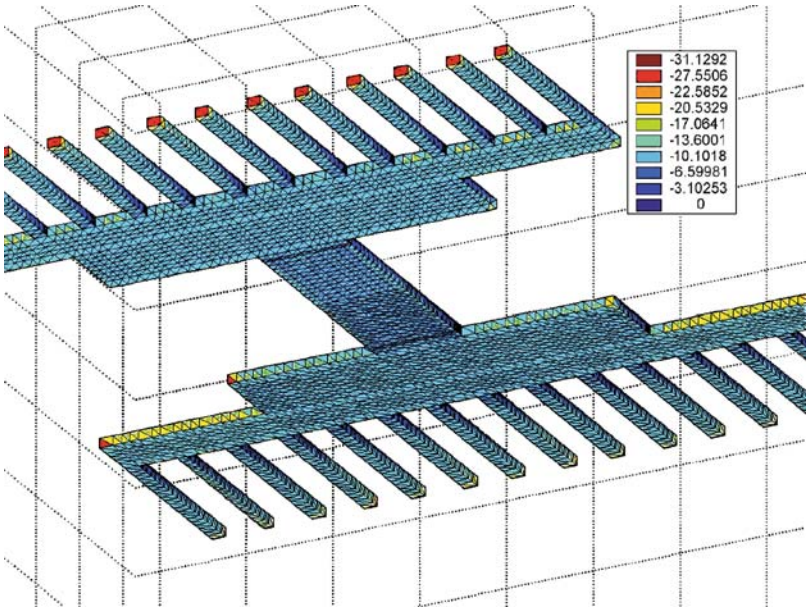

Boundary Element Method and its Applications to the Modeling of MEMS Devices, Figure 5 Drag force distribution on the resonator, bottom view

effective mass and the spring stiffness (9). Results are shown in Table 3 together with the measurement data.

It is clear that both the Couette model and the 1D Stokes model fail to predict the quality factor correctly. They overestimated the value of the quality factor by a factor of two. On the other hand, results from the 3D analysis agree well with the experimental result, with an error of 10%. This indicates that 3D effects are profound in this resonator. Figure 5 shows the detailed drag force distribution for the resonator. The drag force from the ambient air on the top of the resonator contributes 15.7% to the total drag, and the drag force from the air between the resonator and the substrate contributes 55% to the total drag. Side forces contribute almost 29.3%.

Impact of Frequency on Drag Force It is of interest to find out if the unsteady Stokes solver is necessary for computing drag forces on resonators because the unsteady Stokes solver is more expensive than a steady Stokes solver. The integrals in the matrix elements in a unsteady Stokes solver are more expensive to evaluate and both the matrix and vectors are complex. To study the impact of frequency on the drag force, a plot of drag force versus the frequency is shown in Fig. 6. The number of elements used in this simulation is 20,148. At $f = 19{,}200$ Hz, the difference in drag force obtained from the steady Stokes solver and the unsteady Stokes solver is under 6% (see Table 4). As an examination of Table 4 indicates, ignoring the inertial term results in under-predicting top force by nearly one third. Therefore, even at these low frequencies, it is necessary to include the inertial term.

Sensitivity of Drag Force on the Film Thickness A sensitivity test has been performed by varying the film thickness and simulating the drag force on the resonator. Results (obtained by using 20,148 panels) are shown in Table 5.

Boundary Element Method and its Applications to the Modeling of MEMS Devices, Table 3 Quality factor of the resonator: simulation results and experimental data

Method	Total drag (pN)	Q
Couette	481.70	58.9
1D Stokes	547.97	51.8
FastStokes	948.02	29.7
Measurement		27

Boundary Element Method and its Applications to the Modeling of MEMS Devices, Table 4 Distribution of drag force: steady versus unsteady

Drag force (pN)	Steady	Unsteady
Bottom	508.75	510.72
Side	284.84	294.50
Top	102.31	142.8
Total	895.9	948.02

Boundary Element Method and its Applications to the Modeling of MEMS Devices, Table 5 Sensitivity of drag force on the film thickness

Film thickness (% change compared with 2 μm)	Drag force (nN) (% change compared with that of 2 μm)
2 μm (0%)	948.02 (0%)
2.01 μm (0.5%)	945.26 (0.28%)
2.02 μm (1%)	942.70 (0.56%)
2.04 μm (2%)	937.57 (1.1%)
2.06 μm (3%)	932.59 (1.6%)
2.2 μm (10%)	900.10 (5.1%)

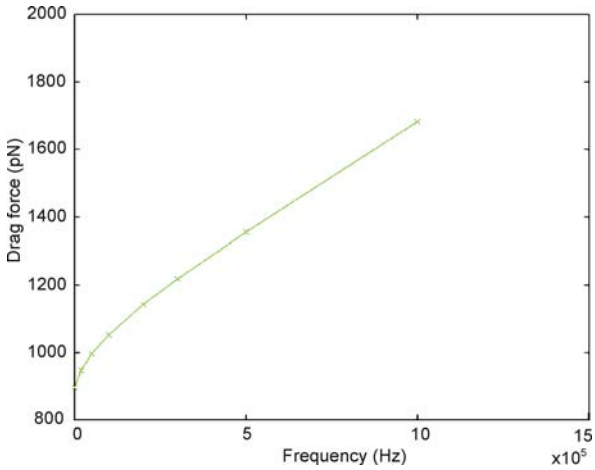

Boundary Element Method and its Applications to the Modeling of MEMS Devices, Figure 6 Drag force as a function of frequency

It has been found from the simulations that the perturbation of the drag force is roughly proportional to the perturbation of the film thickness times a factor of 0.55 for small perturbations. This can be explained using the Couette model because

- the bottom force (drag force coming from air between the resonator and the substrate) is affected the most by changes in gap and
- the Couette model predicts the bottom force pretty well for small gaps (as indicated in Table 2).

In the Couette model, the bottom force is inversely proportional to the gap. Thus, the relative change in bottom force is the same as the relative change in gap. However, the bottom force contributes only 55% of the total drag force. Therefore the relative change in total drag force is 0.55 times the relative change in gap.

Future Directions for Research

To date, most successful applications of the BEM are limited to linear and homogeneous problems. The extension to nonlinear problems is hindered by the existence of the volume integrals in the integral formulations of nonlinear problems. The evaluation of these volume integrals requires a volume discretization of the nonlinear region if standard methods are employed. As such, the boundary-only nature of the method is lost and the BEM loses its advantage in mesh generation as compared to domain methods. An efficient treatment of volume integrals would greatly expand the application scope of the BEM as many practical problems such as those encountered in MEMS devices and systems are inherently nonlinear. Research efforts have been made [9, 10] in this direction, but need to be continued and expanded.

Cross References

- ► Boundary Slip of Liquids
- ► Combined Pressure-Driven Flow and Electroosmotic Flow
- ► Electroosmotic Flow (DC)
- ► AC Electro-Osmotic Flow
- ► Volume and Finite Difference Method for Modeling and Simulation
- ► Finite Volume and Finite Difference Methods for Modeling and Simulation
- ► Gas Flow in Nanochannels
- ► Heat Transfer in Microchannel Flows
- ► Immersed Boundary Method
- ► Lattice Boltzmann Method (LBM)
- ► Meshless Methods
- ► Model Order Reduction (MOR)
- ► Molecular Dynamics Simulation Method
- ► Multiscale Modeling and Numerical Simulations
- ► Non-Continuous Approaches
- ► Pressure Driven Single Phase Gas Flows
- ► Spectral Methods

References

1. Banerjee PK (1994) The Boundary Element Methods in Engineering. McGraw-Hill, England
2. Greengard L, Rokhlin V (1997) A New Version of the Fast Multipole Method for the Laplace Equation in Three Dimensions. Acta Numerica 229–269
3. Phillips JR, White JA (1997) Precorrected-FFT Method for Electrostatic Analysis of Complicated 3D Structures. IEEE Trans Computer-Aided Des Integrated Circ Syst 16(10):1059–1072
4. Ye W, Wang X, Hemmert W, Freeman D, White J (2003) Air Damping in Lateral Oscillating Micro Resonators: a Numerical and Experimental Study. J Microelectromech Syst 12(5):557–566
5. Cho YH, Pisano AP, Howe RT (1994) Viscous damping model for laterally oscillating microstructures. J Microelectromech Syst 3(2):81–87

6. Aluru NR, White J (1998) A Fast integral equation technique for analysis of microflow sensors based on drag force calculations. Proc. of the International Conference on Modeling and Simulation of Microsystems, Semiconductors, Sensors and Actuators, 283–286, Santa Clara
7. Ye W, Wang X, White J (1999) A fast 3D solver for unsteady Stokes flow with applications to Micro-Electro-Mechanical Systems. Proc. of the International Conference on Modeling and Simulation of Microsystems, Semiconductors, Sensors and Actuators, 518–521, Puerto Rico
8. Saad Y, Schultz M (1986) GMRES: A generalized minimal residual algorithm for solving symmetric linear systems, SIAM. J Sci Statis Comput 7:856–869
9. Partridge PW, Brebbia CA, Wrobel LC (1992) The Dual Reciprocity Boundary Element Method. Elsevier, London
10. Ding J, Ye W (2006) A Grid Based Integral Approach for Quasi-linear Problems. Comput Mech 38(2):114–118

Boundary Integral Approaches

► Boundary Element Method and its Applications to the Modeling of MEMS Devices

Boundary Slip of Liquids

PRADIPTA KUMAR PANIGRAHI, MOHAMMED ASFER
Department of Mechanical Engineering, IIT Kanpur, Kanpur, India
panig@iitk.ac.in

Synonyms

Perfect slip; Apparent slip; Boundary condition at interface

Definition

The Navier–Stokes equation is one of the basic governing equations for study of fluid flow related to various disciplines of engineering and sciences. It is a partial differential equation whose integration leads to the appearance of some constants. These constants need to be evaluated for exact solutions of the flow field, which are obtained by imposing suitable boundary conditions. These boundary conditions have been proposed based on physical observation or theoretical analysis. One of the important boundary conditions is the no-slip condition, which states that the velocity of the fluid at the boundary is the same as that of the boundary. Accordingly, the velocity of the fluid adjacent to the wall is zero if the boundary surface is stationary and it is equal to the velocity of the surface if the surface is moving. This boundary condition is successful in representing a wide range of fluid flow problems. However, it has been observed that the no-slip boundary condition is not valid for all situations and there is a difference between velocity of the surface and the fluid particles near the boundary. This boundary condition is termed as slip condition.

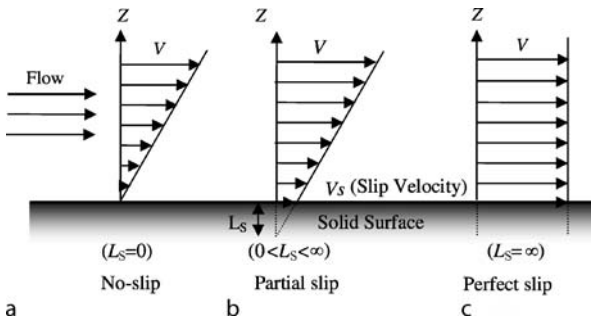

Boundary Slip of Liquids, Figure 1 Schematic representation of the no-slip, partial slip and perfect slip boundary conditions. Under no-slip boundary condition the relative velocity, V_s, between the fluid and the solid wall is zero at the wall. When slip occurs at the wall V_s is finite. The extent of slip is characterized by the slip length L_s (see text)

Overview

Three possible velocity profiles near a solid boundary are shown in Fig. 1. Figure 1a shows that the velocity of fluid particles near the stationary solid wall is equal to zero and represents the no-slip boundary condition. Figure 1b shows that the velocity near the stationary solid wall is non-zero with a relative velocity between the two and represents the slip boundary condition. Figure 1c shows the perfect slip condition, for which there is no influence of the boundary surface on the velocity profile. The velocity when extrapolated towards the wall matches that of the wall at some distance L_s away from it (Fig. 1b), which is known as the slip length and is used as a measure of the slip. The slip length is a fictitious distance below the surface at which the velocity would be equal to zero if extrapolated linearly. The velocity difference between the boundary surface and the adjacent fluid particles is known as the slip velocity, V_s, and is related to the velocity gradient ($\delta V/\delta y$) near the solid boundary as [1]

$$V_s = \frac{\mu}{C_s}\frac{\delta V(y)}{\delta y} \tag{1}$$

where C_s is the coefficient of slip and μ is the coefficient of viscosity of the fluid. The slip length L_s is the ratio of coefficient of viscosity (μ) to the coefficient of slip (C_s). The no-slip boundary condition is equivalent to $C_s = \infty$ and the perfect slip condition is equivalent to $C_s = 0$.

The slip flow near the boundary surface can be analysed based on the type of fluid, i. e. gas, Newtonian and non-Newtonian liquids. The slip flow in gases has been derived based on Maxwell's kinetic theory. In gases, the concept of mean free path is well defined. Slip flow is observed when characteristic flow length scale is of the order of the mean free path of the gas molecules. An estimate of the mean free path of ideal gas is $l_m \approx 1/(\sqrt{2}\pi\sigma^2\rho)$, where ρ is the gas density (here taken as the number of molecules per unit volume) and σ is the molecular diameter. The mean free path l_m depends strongly on pressure and temperature due to density variation. The Knudsen number is defined as the ratio of the mean free path to the characteristic length scale, i. e. $\mathrm{Kn} = l_m/L$. The characteristic length scale (L) can be the overall dimension of the flow or scale of a macroscopic quantity ($L = \rho / |\delta\rho/\delta y|$). The slip velocity is expressed as a function of the Knudsen number and the velocity gradient at the wall as

$$V_s = \frac{2-\sigma_v}{\sigma_v}\left(\mathrm{Kn}\left(\frac{\delta V}{\delta n}\right)_s + \mathrm{Kn}^2\left(\frac{\delta^2 V}{\delta n^2}\right)_s + \ldots\right) \quad (2)$$

where σ_v is the momentum accommodation coefficient, which is a function of the wall and gas interaction. The slip velocity is zero when the Knudsen number is small, i. e. the no-slip boundary condition is valid. The slip condition is valid for large Knudsen number, i. e. when $\mathrm{Kn} \geqslant 0.1$.

Liquid slip has implications to various macroscopic applications, i. e. flow through porous media, particle aggregation, liquid coating and lubrication, etc., in addition to small-scale, i. e. MEMS and bio-MEMS, applications. The movement of a three-phase contact line between two immiscible fluids and solid on a substrate during the advancing or receding film motion indicates the importance of the slip flow boundary condition. The visible contact angle from measurement differs from that predicted using the Young–Laplace equation. The buoyancy and Marangoni effect due to temperature and composition distribution is attributed to the slip flow nature of contact line movement. The conventional hydrodynamics with classical no-slip condition on the substrate generates multi-valued velocity and infinite drag force near the contact line. The imposition of slip condition eliminates this viscous stress singularity at the contact line. Molecular dynamics simulation has also confirmed the local slip near the contact line. Similarly, flows of polymer solutions also show significant apparent slip. Therefore, for liquids, the slip flow characteristics are different from those of gases and need a different explanation.

The liquid slip phenomenon is presented in the following sections. The experimental investigation quantifying the liquid slip is discussed to begin with followed by the results from molecular dynamics simulation. Subsequently, the factors responsible for liquid slip and possible mechanism responsible for liquid slip are discussed.

Basic Methodology

The applicability of slip flow is not well accepted to date by the academic community. One of the problems is the small length scale of the slip flow regime (if present) in comparison to the length scale of the flow or system. The hydrodynamic boundary condition appears to be one of no-slip, unless the flow is examined on a length scale comparable to the slip length. Hence, very accurate techniques with high spatial resolution capable of interfacial flow measurements are required to detect the effects of slip. Some of the experimental techniques for quantification of liquid slip are presented in the following sections.

Flow Rate

Macroscopic quantities, i. e. flow rate and pressure drop measurement, can be used for indirect determination of liquid slip. In this approach, a known pressure gradient ΔP is applied between the two ends of a capillary or a microchannel and the flow rate Q is measured. The flow rate for the slip flow condition is higher than that predicted from the no-slip boundary condition. For Poiseuille flow of fluid with viscosity μ through a narrow cylindrical channel of radius R and length L, the flow rate assuming no-slip boundary condition is

$$Q_{th} = \left(\frac{\Delta P \pi R^4}{8\mu L}\right) \quad (3)$$

If there is slip at the walls of the channel, the Poiseuille flow velocity profile will be modified to

$$u(r) = \left(\frac{\Delta P}{4\mu}\right)\left[(R+L_s)^2 - r^2\right] \quad (4)$$

The flow rate can be obtained using the above slip flow boundary condition, and (assuming $L_s/R \ll 1$) it can be derived that

$$Q_{slip} = Q_{th}\left(1 + \frac{4L_s}{R}\right) \quad (5)$$

For any particular slip length of fluid flow, the slip flow rate increases with decreasing radius of the cylindrical channel. For the slip length $L_s = 200\,\mathrm{nm}$, the flow rate with slip (Q_{slip}) is about 6% and 23% higher than the theoretical flow rate with no-slip (Q_{th}) for capillary radii of 13.3 μm and 3.48 μm respectively.

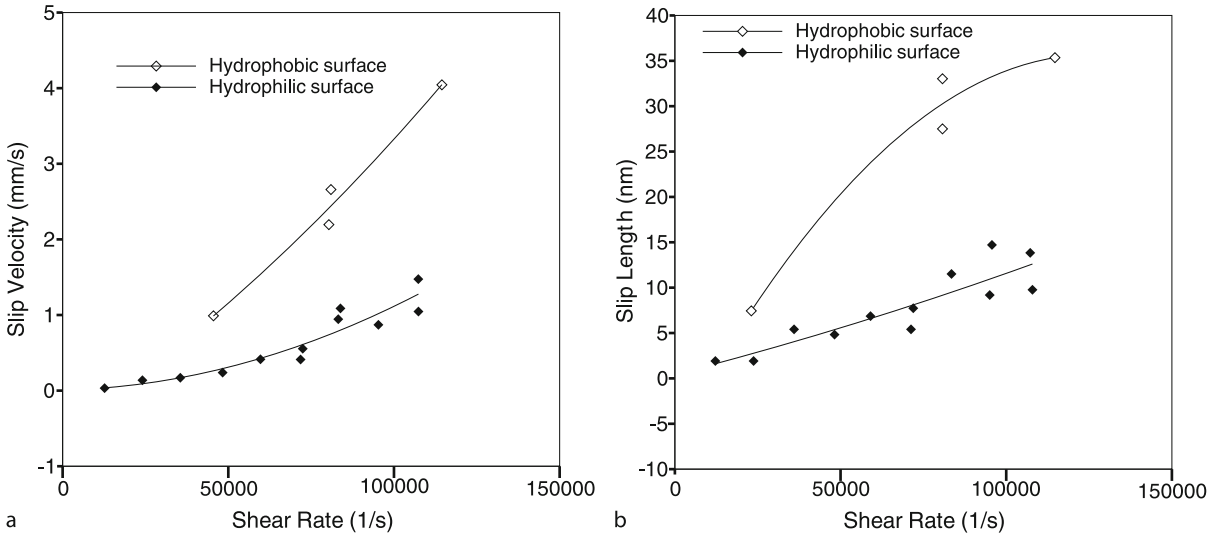

Boundary Slip of Liquids, Figure 2 Comparison of slip velocity and slip length between hydrophilic and hydrophobic surfaces as a function of shear rate

Choi et al. [4] presented the slip velocity and slip length of hydrophilic and hydrophobic microchannels (1 and 2 μm depth) based on flow rate and pressure drop measurements. Sample results from their study are compiled in Fig. 2. The flow rate for the hydrophobic surface is higher than that for the hydrophilic surface. The corresponding slip velocity and slip length for the hydrophobic surface are also higher than those for the hydrophilic surface. The slip velocity and slip length increase with strain rate.

Cheng and Giordano [5] reported the slip length data for different Newtonian fluids, i. e. silicone oil, hexane, decane and hexadecane (fluids having different molecular diameter), as a function of channel height (see Fig. 3). They observed the no-slip condition to be valid when water is the working fluid. However, the slip length is definite for other working fluids. The slip flow effect is insignificant for channel size greater than about 140 nm. Their study indicates the dependence of slip flow on the molecular diameter of the fluid and the fluid–channel wall interaction.

Hydrodynamic Force

The motion (steady or oscillatory) of a sphere towards a flat surface experiences a resistance to the motion. This resistance is due to the combined contribution from Stokes drag on the sphere, the drainage force and the drag force on the cantilever attached between the sphere and the force measuring apparatus, i. e. atomic force microscopy (AFM) or surface force apparatus (SFA). The exact hydrodynamic solutions of this resistance force for a sphere of radius a, approach velocity V, viscosity μ and closest separation distance h can be derived as [3]

$$F = f_{\text{slip}} \frac{6\pi\mu a^2 V}{h} \tag{6}$$

For the no-slip boundary condition, $f_{\text{slip}} = 1$. Otherwise when there is slip, $f_{\text{slip}} < 1$, i. e.

$$f_{\text{slip}} = \frac{h}{3L_s}\left[\left(1+\frac{h}{6L_s}\right)\ln\left(1+\frac{6L_s}{h}\right)-1\right] \tag{7}$$

Thus the hydrodynamic force for the slip flow case is smaller in magnitude than that for the no-slip case.

Figure 4a shows a schematic of the device for drainage force measurement. Fig. 4b shows the hydrodynamic force versus inverse separation distance for fluids of different viscosity based on the measurements by Neto et al. [3]. The predicted drainage force based on the no-slip flow condition is also compared in Fig. 4b. It is clearly evident that the no-slip boundary condition is unable to describe the experimental data. The slip length obtained based on Eq. (6) and (7) is equal to 4 nm and 12 nm for lower and higher viscosity values respectively. Figure 4c shows the slip length as a function of the approach velocity and fluid viscosity indicating that slip length is a function of both the fluid type, i. e. viscosity, and strain rate, i. e. the approach velocity.

Particle Image Velocimetry (PIV)

Micrometre-resolution particle image velocimetry (PIV) can also be used for direct observation of slip length by

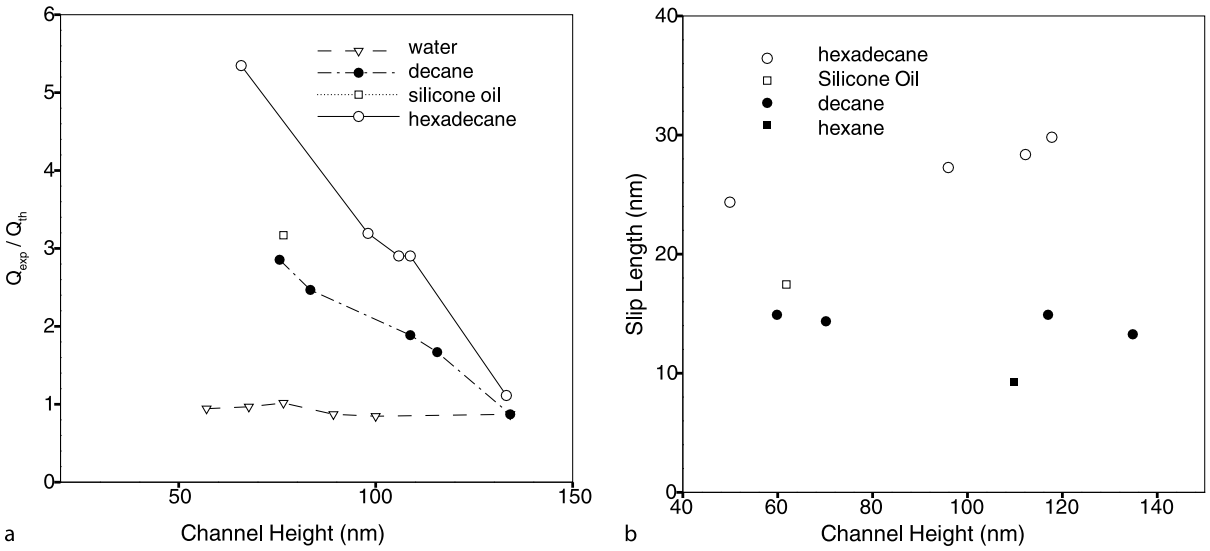

Boundary Slip of Liquids, Figure 3 (**a**) The ratio of experimental flow rate (Q_{exp}) to theoretical flow rate (Q_{th}) based on no-slip boundary condition and (**b**) the slip length as a function of channel height for different fluids (water, silicone oil, decane, hexane and hexadecane)

measuring the velocity profile in the near-wall region. Figure 5a shows a typical μ-PIV setup for microchannel velocity measurement. The velocity measurement in hydrophilic (uncoated glass) and hydrophobic (octadecyltrichlorosilane (OTS) coating) channels adopted from Trethway and Meinhart [6] is shown in Fig. 5b. Fluorescently dyed polystyrene particle of 300 nm diameter absorbs green (532 nm) Nd:YAG laser light which emits red (575 nm) light. The emitted light from the particles is collected by a CCD camera through an epi-fluorescent filter. The cross correlation between pair of particle images provides the velocity field information. The near-wall velocity field measurement of the microchannel (30 μm deep and 300 μm wide) shown in Fig. 5b indicates different velocity profile behaviour between the hydrophilic and hydrophobic channel. The hydrophobic channel shows a shifting of the velocity profile towards higher value and a finite non-zero velocity near the bottom wall, i. e. at about 450 nm from the wall surface, indicating slip flow behaviour.

Other Techniques

Sedimentation velocity and streaming potential measurements also provide indirect information about the slip length.

The sedimentation velocity of particles under gravity can be measured and compared with the predicted values based on no-slip and slip flow boundary conditions. The ratio of the sedimentation velocity as a function of slip length can be derived as

$$\frac{V_{slip}}{V_{NS}} = \frac{1 + 3L_s/a}{1 + 2L_s/a} \tag{8}$$

For small particles with radius a, the sedimentation velocity with slip (V_{slip}) for slip length L_s is larger than that with no-slip (V_{NS}). The comparison of actual velocity with the predicted velocity based on no-slip condition provides the slip length.

Streaming potential measurement of electrolyte flow inside a capillary depends on the slip length. The surface of the capillary acquires a net charge in contact with the electrolyte. The pressure-driven flow of the capillary creates an advection of charges resulting in surplus ions at one end of the capillary compared to the other end. If the two ends of the capillary are not short-circuited, a net steady-state potential difference, termed the streaming potential, develops. The streaming potential depends on the extent of slip. The ratio of streaming potential for slip (ΔV_{slip}) and no-slip (ΔV_{NS}) is given by

$$\frac{\Delta V_{slip}}{\Delta V_{NS}} = 1 + L_s\kappa \tag{9}$$

where κ is the Debye screening parameter, which gives the typical distance close to the surface where there is a net charge density in the liquid and $\kappa^{-1} = \left(\varepsilon_r \varepsilon_0 k_B T / 2e^2 n_0\right)^{1/2}$. Here ε_r is the dielectric constant of the liquid, ε_0 the permittivity of the vacuum, k_B Boltzmann's constant, T the temperature, e the electron charge

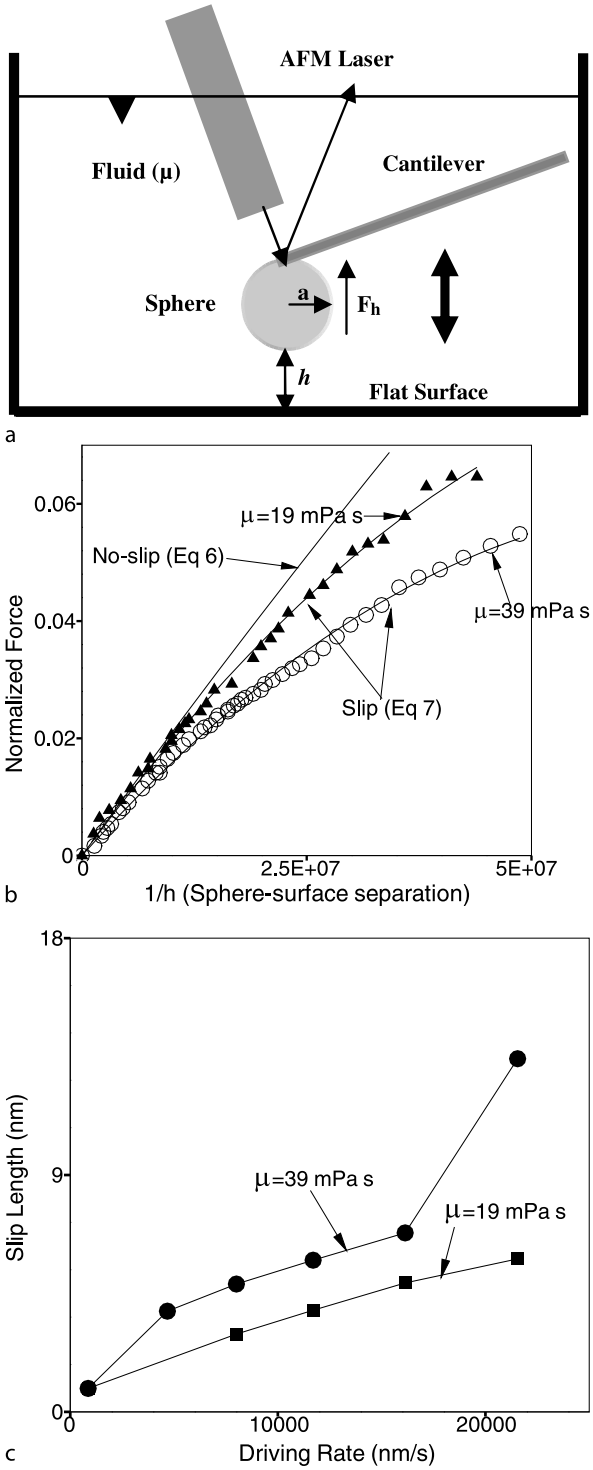

Boundary Slip of Liquids, Figure 4 (**a**) Schematic of the arrangement for slip length characterization, (**b**) the normalized hydrodynamic force versus inverse of separation for fluid of different viscosities and comparison with no-slip flow calculation and (**c**) slip length as a function of viscosity and driving rate

and n_0 the number density of ions in the bulk of the solution.

Molecular Dynamics Simulation

Molecular dynamics (MD) simulation is a useful tool for studying small-scale fluid flows. Numerical integration of Newton's law of motion for particles (atoms or molecules) is carried out:

$$m_i \frac{\mathrm{d}^2 r_i}{\mathrm{d}t^2} = \sum_j F_{ij} \tag{10}$$

where m_i is the particle mass, r_i the position of particle i and F_{ij} the interatomic or intermolecular force between particles i and j ($F_{ij} = -\nabla_i V_{ij}$). The Lennard-Jones two-body potential (V_{ij}) between particles is frequently used which is given by

$$V_{ij} = \varepsilon \left[\left(\frac{\sigma}{r_{ij}} \right)^{12} - c_{ij} \left(\frac{\sigma}{r_{ij}} \right)^{6} \right] \tag{11}$$

where ε is an energy scale, σ the particle size and r_{ij} the distance between particles i and j. The constants c_{ij} allow variation of the relative intermolecular attraction between liquids and solids, which therefore represents wetting behaviour.

Barrat and Bocquet [7] carried out the molecular dynamics simulation of Couette and Poiseuille flows. In Couette flow, the upper wall is moved with a constant velocity and in Poiseuille flow an external force drives the flow. Sample results from molecular dynamics simulation are reproduced in Fig. 6. The application of no-slip boundary condition leads to the expected linear and parabolic velocity profile respectively for Couette and Poiseuille flow. However, the velocity profile obtained from molecular dynamics simulation shows a sudden change of velocity in the near-wall region indicating slip flow. The velocity profile for Couette flow away from the solid surface is linear with slope different from that of the no-slip case. The velocity for the slip flow case is higher than that observed for the no-slip case for Poiseuille flow. For both Couette and Poiseuille flow, the partial slip boundary condition at the wall predict similar bulk flow as that observed by molecular dynamics simulation. Some discrepancy in the velocity profile is observed in the near-wall region.

Physical Parameters Affecting Slip

The results reported in the previous section have established the occurrence of slip flow from both experimental and simulation studies. It is important to know various physical parameters affecting slip. The physical

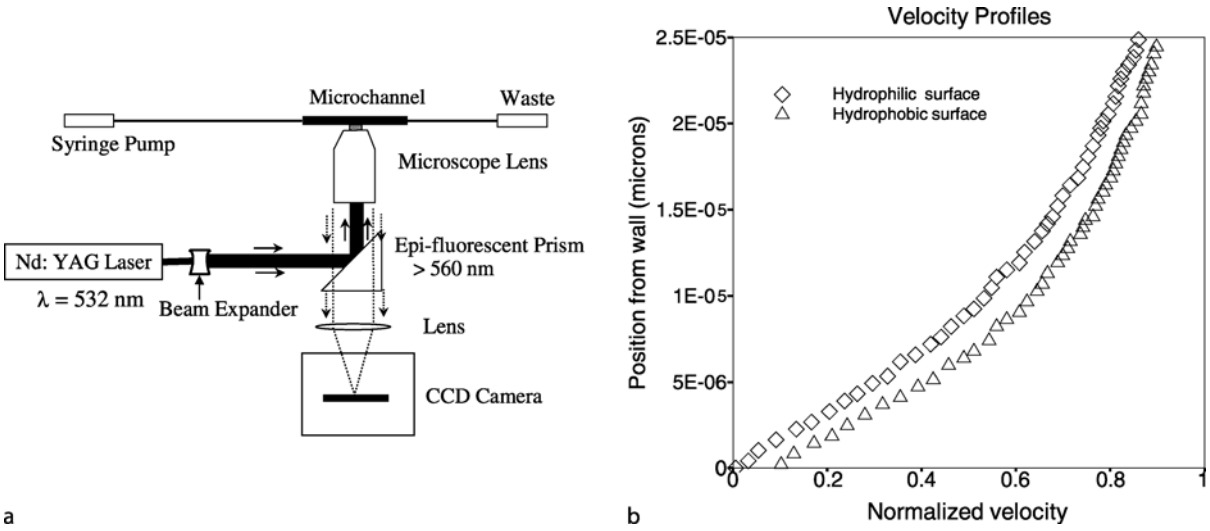

Boundary Slip of Liquids, Figure 5 (**a**) Experimental arrangement for μ-PIV measurement and (**b**) velocity profile for hydrophobic and hydrophilic surfaces obtained from μ-PIV measurement

parameters affecting slip are summarized in the following sections.

Surface Roughness

Roughness influences the behaviour at liquid–solid interfaces. Roughness induces flow around it that leads to dissipation of the mechanical energy. Therefore, there is an increase in the overall resistance to flow and the tendency of slip decreases due to surface roughness. The roughness also influences the dewetting behaviour of the liquid. A high contact angle is indicative of a weak interaction between liquid and solid, and thus causing the fluid molecules to slide across the solid. Roughness can increase the tendency to produce a gas–liquid interface at the solid boundary. The surface behaves like a super-hydrophobic surface and the slip tendency increases.

However, systematic study of surface roughness is not easy to implement. It is difficult to produce suitable surfaces of controlled roughness. Most efforts to alter the surface roughness result in additional undesired changes to the interface properties.

Surface Wettability

It is generally believed that a liquid has a larger slip tendency for poorly wetted surfaces. Higher contact angle indicates weak interaction between the solid and liquid and therefore is easy to overcome. Many experiments and molecular dynamic simulations have confirmed that the level of hydrophobicity is one of the primary factors determining the level of slip.

Shear Rate

The slip length also depends on the shear rate imposed on the fluid particles. Thompson and Troian [2] have reported the molecular dynamics simulation of Couette flow at different shear rates. At lower shear rate, the velocity profile follows the no-slip boundary condition. The slip length increases with increase in shear rate. The critical shear rate for slip is very high for simple liquids, i. e. $10^{11}\ s^{-1}$ for water, indicating that slip flow can be achieved experimentally in very small devices at very high speeds. Experiments performed with SFA and AFM have also showed shear dependence slip in the hydrodynamic force measurements.

Dissolved Gas and Bubbles

Dissolved gases or bubbles near a solid also influence the slip flow behaviour. It has been observed experimentally that the amount of slip depends on the type and quantity of dissolved gas in the fluid. From sedimentation studies it has been reported that slip is not observed in vacuum conditions while there is a clear slip when a liquid sample is in contact with air. Slip in non-wetting systems depends strongly on the environment in which the experiment is performed. Dissolved gases or nano-bubbles in the near-wall region are thought to create localized defects increasing the possibility of slip.

Polarity

For electrolyte solutions and polar liquids, the amount of slip depends on the electrical properties of the liquid. Sed-

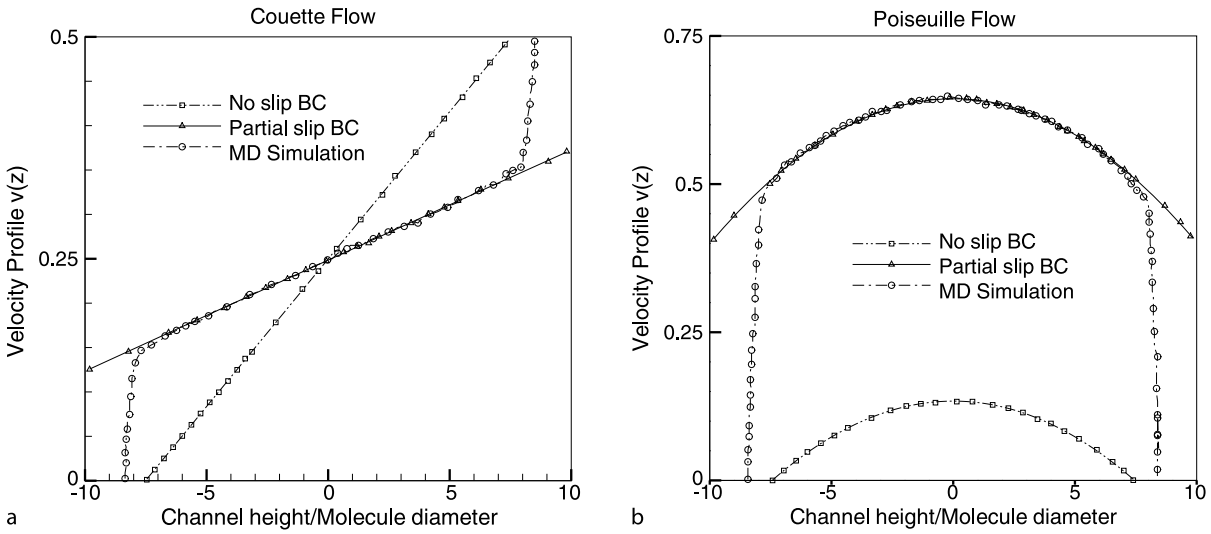

Boundary Slip of Liquids, Figure 6 Velocity profile for (**a**) Couette and (**b**) Poiseuille flow. Comparison between molecular dynamics simulation, no-slip boundary condition and partial slip boundary condition

imentation experiments report that slip is only observed for polar liquids. Drainage force experiments report slip to increase with increase in the dipolar moment of the liquid when liquids are polar. This phenomenon is attributed to the super-lattice structure in liquids due to the dipole–dipole interactions.

Possible Liquid Slip Mechanism

Slip flow phenomena can be explained by some possible mechanism. The fluid slip can be described as true or apparent slip. The true slip occurs at a molecular level, where liquid molecules are effectively sliding on the solid surface. The apparent slip occurs not at the solid–fluid interface but at the fluid–fluid interface where a thin layer of liquid/gas molecules is tightly bound to the solid surface. For apparent slip the velocity gradient close to the solid surface is so high that the bulk molecules beyond the layer of liquid/gas molecules appear to slide on the surface.

The true slip phenomena can be attributed to the liquid–liquid and liquid–solid interaction. If the viscous friction between liquid molecules at the interface is stronger than between molecules of the liquid and molecules of the solid, then the molecules can slide on the surface. This is true for hydrophobic surfaces but might also hold for hydrophilic surfaces. If the dimensions of the liquid molecules are of comparable size as the corrugation on the solid surface, then the molecules are trapped in the pits on the surface giving no-slip boundary conditions. But if their size is much smaller or much larger, they can slide on the surface.

For apparent slip, thin gas/liquid layers with a modified viscosity and/or mobility are created near the solid surface. At room temperature and pressure, there is always some residual gas dissolved in a liquid. Critical level of shear might induce cavitations in a liquid and the generated gas bubbles might adhere to the solid surface forming a thin gas layer at the solid surface onto which the liquid can slip. The other factor can be the critical shear rate at which a microscopic surface roughness or corrugation can favour the generation of turbulent flow layer at the interface, and thus modify the viscosity of this layer with respect to the bulk, even if the overall flow is laminar.

Key Research Findings

The correct specification of boundary condition of fluid flow near an interface or solid boundary is essential to obtain the analytical and numerical solution of fluid flow problems. The no-slip boundary condition is successful in describing a class of fluid flow problems. The applicability of the slip flow condition and the condition at which the no-slip boundary condition is invalid is of both academic interest and of practical interest. The recent developments of small-scale microfluidic systems have raised the importance of the specification of the correct boundary condition.

Barrat and Bocquet [7] reported slip in Couette and Poiseuille flow using molecular dynamics simulation (Fig. 6). Tretheway and Meinhart [6] reported a micrometre-resolution velocity profile in hydrophilic and hydrophobic microchannels of cross-section $30 \times 300\,\mu m^2$ using the μ-PIV technique (Fig. 5). Their

results showed significant fluid velocity near a hydrophobic (octadecyltrichlorosilane or OTS coated) microchannel wall and no-slip for a hydrophilic surface. Cheng and Giordano [5] reported pressure-driven flow of several classical fluids (hexane, decane, hexadecane and silicon oil) through lithographically produced channels. The results for water agree well with the theoretical prediction of no-slip boundary condition, for a channel height as small as 40 nm. However, for hexane, decane, hexadecane and silicone oil slip flow is observed when channel separation is reduced below about 100 nm (Fig. 3).

Choi et al. [4] examined the apparent slip effects of water in hydrophobic and hydrophilic microchannels experimentally using precision measurements of flow rate versus pressure drop. They compared their experimental results to that from analytical solution of flow through a channel with slip velocity at the wall. There was a clear difference between the flow of water on a hydrophilic and hydrophobic surface indicating the effect of slip flow (Fig. 2). Craig et al. [3] have reported clear evidence of boundary slip for a sphere–flat geometry from drainage force measurements using atomic force microscopy. The degree of slip is observed to be a function of both liquid viscosity and shear rate (Fig. 4).

Yang and Kwok [8] presented the analytical solution of fully developed electrokinetic flow subjected to sinusoidal pressure gradient or sinusoidal external electric field. The combined effect of slip flow and electrokinetics was demonstrated on the velocity profile in confined geometries. The velocity profile was observed to be a function of both slip coefficient and external electric field. They observed that both these effects play important roles for flow inside microchannels.

Ou and Rothstein [9] developed an ultra-hydrophobic surface with micrometre-sized ridges (20 – 30 μm wide) placed 20 – 120 μm apart aligned in the flow direction. They demonstrated maximum 25% drag reduction for flow inside these channels. From μ-PIV measurements, they showed the existence of slip flow at the air–water interface between the ridges, while the flow over the ridges obeys the no-slip condition. They attributed the existence of slip flow for drag reduction.

Future Directions for Research

The studies carried out so far have explained the slip flow phenomena to a great extent. However, the use of slip phenomena for analysis of different fluid flow problems is limited. The effect of various flow parameters, i. e. roughness, wettabilty, polarity and presence of nanobubbles or residual gases, on slip flow phenomena needs to be conclusively and systematically studied. The effect of temperature and concentration gradient on slip flow parameters needs to be properly characterized based on both molecular dynamics simulation and experiments. The effect of slip flow on turbulence production mechanism needs to be established. The development of advanced micro-/nano-manufacturing and measurement technology is expected to facilitate the systematic study of these parameters.

Manipulation of conditions required for generation of slip flow can have many practical applications. This will be beneficial in development of drag reduction and mixing enhancement technologies. This is particularly important for micro- and nanotechnologies, where the pressure penalty is very high and mixing is difficult due to the difficulty in generation of turbulent flow.

Cross References

- ► μ-PIV
- ► Molecular Dynamics Simulation
- ► Atomic Force Microscope (AFM)

References

1. Blake TD (1990) Slip between a liquid and a solid: D. M. Tolstoi's theory reconsidered. Colloids surf, 135–145
2. Thompson PA, Troian SM (1997) A general boundary condition for liquid flow at solid surfaces. Nature 389:360–362
3. Neto C, Craig VSJ, Williams DRM (2003) Evidence of shear-dependent boundary slip in Newtonian liquids. Eur Phys J E 12:71–74
4. Choi CH, Westin JA, Breuer KS (2003) Apparent slip flows in hydrophilic and hydrophobic micro channels. Phys Fluids 15:2897–2902
5. Cheng JT, Giordano N (2002) Fluid flow through nanometer-scale channels. Phys Rev E 65:1–5
6. Tretheway D, Meinhart C (2002) Apparent Fluid Slip at Hydrophobic Microchannel Walls. Phys Fluids 14:9–12
7. Barrat J, Bocquet L (1999) Large slip effect at a nonwetting fluid–solid interface. Phys Rev Lett 82:4671–4674
8. Yang J, Kwok DY (2003) Effect of liquid slip in electrokinetic parallel-plate microchannel flow. J Colloid Interf Sci 260:225–233
9. Ou J, Rothstein JP (2005) Direct velocity measurements of the flow past drag-reducing ultrahydrophobic surfaces. Phys Fluids 17:103606–10

Bragg Diffraction Equation or Bragg's Law

Definition

If a crystal is irradiated with x-ray radiation most of the radiation passes through unhindered. But some part of the radiation will be deflected by the crystal, which is called Raylight scattering and can be visualized on photographic plates. But the equation can only be achieved (and thereby the reflection be observed), if the pitch length

(which is although the phase shift of the radiation before and after the deflection) is an integer multiple of the wavelength. The Bragg diffraction equation was developed by William Henry Bragg and his son William Lawrence Bragg in 1912.

Bridging Instability

► Interfacial Instability

Brownian Diffusion

► Brownian Motion

Brownian Dynamics

► Simulating Migration of Polymer Chains, Methods

Brownian Motion

Synonyms

Brownian diffusion

Definition

Brownian motion refers to the random thermal diffusion of a particle suspended in a fluid due to collisions between the particle and the fluid molecules that are in continual, random motion.

Cross References

► Temperature Measurement, Methods

Brownian Noise

► Micro-PIV-Based Diffusometry

Bubble Actuated Microfluidic Switch

CHENG-HSIEN LIU
Department of Power Mechanical Engineering, National Tsing Hua University, Hsinchu, Taiwan
Liuch@pme.nthu.edu.tw

Synonyms

Microflow switch; Multi-channel micro switch pumping; Capillarity-driven stop valve and sample injection switch; Multi-channel micro liquid dosing system

Definition

The bubble actuated microfluidic switch is actuated by either thermal bubble or electrolysis bubble. The microfluid is driven by capillary force and stop by design of hydrophobic property in the microchannels. The switch function of the microfluidic system is to control the fluid sample into the individual desired outlet reservoir for the applications such as selective on-chip sample dosing, microfluidic/bio-sample on-chip transportation and Lab-on-a-Chip microsystem integration.

Overview

Some design concepts and prototypes of microfluidic switches have been demonstrated over the past decade. Doring et al. [1] demonstrated that a laminar flow could be steered into one of two outlet ports using a thermal bimorph cantilever, which was made by a bimetal structure and used as an active component for flow switching. Blankenstein et al. [2] reported that the differential hydrodynamic pressures, which were generated by external pumps, between the inlet ports were used to guide specific fluid sample stream into the desired outlet port. The sample injection into one of the five outlet ports has been demonstrated in their study. Gebhard et al. [3] demonstrated a fluidic oscillator employing a V-shaped fluidic circuit with feedback micro channels, in which a part of the output flow was fed back into the inlet region to control the main flow to be redirected to the other desired microchannel. Gebhard's work demonstrated that the fluid could be switched between two output microchannels via their design. Lee et al. [4] reported that $M \times N$ pre-focused microfluidic switches have been successfully demonstrated with several external pumps to switch continuous liquid from an inlet channel to any desired outlet channel in multi-ported outlet microchannels. In their studies, the theoretical model based on the potential flow theory was built to predict the performance of single and multiple flow switching. Also, Lemoff and Lee [5] reported an AC magnetohydrodynamic (MHD) microfluidic switch, in which the Lorentz force was used to propel an electrolytic solution. Their switch took advantage of integrating two AC MHD pumps into different arms of a fluidic Y-channel to make the fluid switch into or out of either arm. In these proposed research studies, various microfluidic switches have been successfully

demonstrated. Anyway, most proposed studies still suffer from the disadvantages such as the need of several external pumps and mechanical moving parts inside the fluidic chip. In addition, most of them could not perform precise fluidic switch into tiny microchannels due to leakage problems.

Some MEMS technologies have been drawn toward taking advantage of surface tension, which becomes a dominant force in microscale. The continuous electrowetting (CEW) requires a liquid metal in a filler liquid, limiting the medium that can be driven. A droplet movement of aqueous liquid based on electrical control of surface tension has been demonstrated with an electrolyte droplet in a filler fluid [6], still requiring two liquids in the system. In addition, the electrowetting (EW) [7] and electrowetting on dielectric (EWOD) [8] can be used to handle aqueous liquid in microscale without any second liquid medium. In these cases, the change in contact angle or the wettability shift is caused by the change in the solid-liquid surface tension.

A novel microfluidic switch based on surface tension and distributed hydrophobic-patch design was just developed and reported in our group [9]. Both the capillary force and the barrier pressure are utilized in our proposed design to achieve the switching function. The trigger driving actuator in our reported concept-proof prototype relies only on the embedded heater, which generates thermal actuation bubbles, with time-sequence power control. The bubble actuator could be replaced by the electrolysis bubble actuator in a modified chip design. This kind of proposed fluidic switch devices could resolve the disadvantages in early proposed various microfluidic switches, such as the complicated electrical connections, the need of several external pumps, the mechanical moving parts inside the fluidic chip, and the leakage problems. Compared with other actuation mechanisms, the bubble actuator has the features of simple structure, no moving parts and being easy to be integrated with the control circuitry. However, for bio-applications by using thermal bubble actuation, the bio-samples might be broken or degraded either by the shear-stress acting on them due to the hydrodynamic movement of the fluids when the bubble grows and collapses, or by the local high temperature induced by the transient generation of the thermal bubble. It has been found that some pretreatment of the bioactive samples could lower these kinds of damage. For example, Okamoto et al. [10] successfully ejected DNA segments in a DNA micro-array device by using the thermal bubble jet-printing technology. To avoid the high temperature and high shear-stress damage from the thermal bubble, they optimized the DNA ejection solvent to improve volatility, solubility, wettability, viscosity and surface tension of DNA solution, and to promote spot separation by adding some additional chemicals. Maxwell et al. [11] also reported a microbubble bioparticle actuator that uses the micro thermal bubble actuation to manipulate the bioparticles. So far, they have demonstrated that bubble actuation could be used to actuate cell-sized particles and will use the bioparticle actuator to capture living cells. Besides, our group also successfully demonstrated cell sorting feature for liver cells by using electrolysis bubble actuator to actuate MEMS T-shape structure [12]. The MEMS design gets rid of PH value actuation to get high survival rate for delicate sorted liver cells. All of these results demonstrate promising research efforts for the MEMS bubble actuation technique to be integrated in biochips for bio-applications. In the following sections, we focus on the thermal-bubble actuated microfluidic switch based on surface tension and distributed hydrophobic-patch design. This device is taken as an example to understand the details about design concept, basic theory, operation principle as well as take a look at the function demonstration.

Basic Methodology

Design Concept of Bubble Actuated Microfluidic Switch

To introduce the concept and design details, a schematic representation of the 1×4 microfluidic switch with one inlet port and four outlet ports as shown in Fig. 1 is taken as a case study here. This case-study device, as shown in Fig. 1, consists of an embedded heater, a capillary system with hydrophilic microchannels, and a specific arrangement of hydrophobic patches. This device could be expanded to $1\times N$ microfluidic switch via the similar design. Also the embedded heater could be replaced by electrolysis electrodes. In Fig. 1, L_i represents the length of each hydrophobic patch in the microchannel #i. From microchannel #1 to #4, L_i decreases with an increase of patch number in each microchannel. For the device design shown in Fig. 1, there are 1, 2, 3, and 4 separated hydrophobic patches in microchannel #1, #2, #3, and #4, respectively. These distributed patches have the same length in each microchannel.

In the $1\times N$ microfluidic switch design, the switch mechanism among different microchannels is dominated by controlling the format and the timing of power input that generates thermal bubble actuation. During the growing process of the thermal bubble, the meniscus of the liquid in each microchannel stopping at the edges of the hydrophobic patches will be pushed forward as shown in Fig. 2. When the thermal bubble begins collapsing, the meniscus of the liquid in each microchannel will flow back till leaving the hydrophobic patch due to the barrier pressure if it stays on a hydrophobic patch. On the contrary, it will

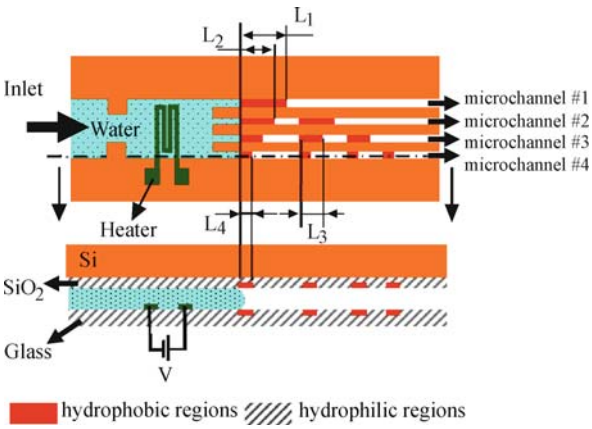

Bubble Actuated Microfluidic Switch, Figure 1 The design concept of the microfluidic switches where $L_i > L_{i+1}$, i. e. $L_1 > L_2 > L_3 > L_4$. L_i represents the length of each hydrophobic patch in microchannel #*i*. All other regions in the microchannels are hydrophilic

flow forward till reaching the edge of the next hydrophobic patch region due to the capillary force if it stays on a hydrophilic region.

Figure 2 illustrates the operation principles of a 1×4 microfluidic switch based on the proposed design concept by using specific separated hydrophobic patches in microchannels. As a fluid sample is first introduced into the inlet from the left, the fluid is driven forward to the right by the capillary force and then stops at the edges of the first hydrophobic patches of each microchannel as shown in Fig. 1. For instance, if we want to control and guide the continuous liquid into the microchannel #1, the volume control of the actuating bubble is required to push the fluid to pass through the first hydrophobic patch region of the microchannel #1 but not to pass through all the second hydrophobic patches in other microchannels. Because the length of the hydrophobic patch in microchannel #1 is the longest, the fluid could pass through all the first patches of all microchannels if the volume of the actuating bubble could push the fluid to pass through the first hydrophobic patch region in the microchannel #1. Then, the continuous liquid could be driven along the microchannel #1 by the capillary force, and stopped at second patches of other microchannels by the barrier pressure, as shown in Fig. 2a. One challenge on this capillary system design, for this case, is to drive the fluid through the microchannel #1 and precisely stop the fluid before the second hydrophobic patches in the other microchannels via the micro design of the separation gaps between hydrophobic patches and the time-sequence control of bubble volume.

For another example, if we want to control the liquid to flow into the microchannel #3 only, we could control the bubble volume via heater power control to overcome the barrier pressures of all the hydrophobic patches in microchannel #3 step by step. As soon as the fluid passes through each one of hydrophobic patches of the microchannel #3, the thermal bubble immediately begins collapsing via the voltage control on the heater. At this moment, the meniscuses of fluid staying on the hydrophilic region will flow forward due to capillary force till reaching the next hydrophobic patch in the microchannel #3 and #4. However, the meniscuses staying on the hydrophobic patches will flow back due to barrier pressure till leaving the hydrophobic patch in the microchannel #1 and #2. After we generate the growth and collapse of the thermal bubble three times, the continuous liquid could be driven through the microchannel #3 due to the capillary force, as shown in Fig. 2b. Based on the similar operation principles, the fluid could be controlled and guided into any desired microchannel or multiple microchannels based on the needs. As shown in Fig. 2c, the fluid is simultaneously switched into two desired outlet ports, the microchannel #2 and #4. Firstly, we generate the large bubble twice to make the fluid pass through all hydrophobic patch regions of microchannel #2. Afterwards, we generate the small bubble twice to make the fluid pass through the last two of the hydrophobic patch regions in microchannel #4. Based on the hydrophobic-patch design and programmed time-sequence bubble actuation, the fluid could be switched into desired outlet ports in the capillary system without the need of external pumps and complicated MEMS moving parts.

Microfabrication of Case-Study Microfluidic Switch Prototype

The micro fabrication of our capillary system with microfluidic switch function is a four-mask process, as illustrated in Fig. 3. A standard p-type <100> silicon wafer is grown with 5000 Å thermal oxide that is patterned and etched as the oxide mask, and then etched by KOH solution to define 20 μm-depth microchannels. Then, this silicon substrate is grown with another 7000 Å thermal oxide to form the hydrophilic layer. Next, the 1% Teflon solution is spin-coated on the oxide layer to define our designed hydrophobic patch regions by a lift-off process. On the Pyrex glass substrate, photoresist and HF solution are used to define the patterns and form the recesses of 1 μm-depth. A 5000 Å aluminum layer is, then, evaporated and patterned as the heater and electrodes by another lift-off process. Next, another 1% Teflon solution is also spin-coated on the Pyrex glass to define the hydrophobic pattern regions by another lift-off process. Finally, the silicon wafer and Pyrex glass are aligned for the anodic bonding process.

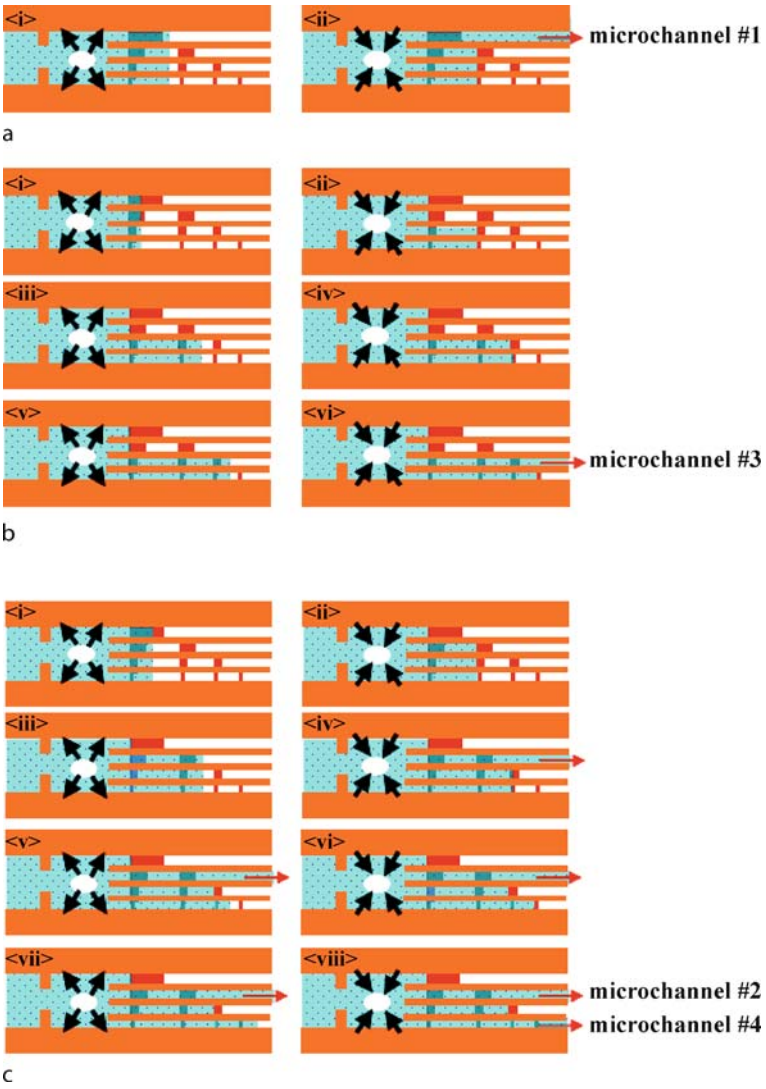

Bubble Actuated Microfluidic Switch, Figure 2 Illustration of design concept and operation principles for a 1×4 microfluidic switch via bubble actuator control, capillary force and hydrophobic patch distribution design. The liquid is controlled and switched into (**a**) microchannel #1, (**b**) microchannel #3, (**c**) microchannel #2 and #4 simultaneously

Background and Theory

Barrier Pressure Analysis

To study and design the capillary system with $1 \times N$ microfluidic switches, a theoretical model based on early literatures is proposed. The liquid actuation and control in the capillary system with microfluidic switch function is dominated by both barrier pressure and capillary force. Here, we model the liquid motion by using the total surface energy approach [13]. The surface energies are related to the equilibrium contact angle θ_c by Young's equation

$$\gamma_{sa} = \gamma_{sl} + \gamma_{la} \cos \theta_c \tag{1}$$

The total interfacial energy of the system could be modeled as

$$\begin{aligned} U_T &= A_{sl}\gamma_{sl} + A_{sa}\gamma_{sa} + A_{la}\gamma_{la} \\ &= (A_{sl} + A_{sa})\gamma_{sa} - A_{sl}\gamma_{la} \cos \theta_c + A_{la}\gamma_{la} \\ &= U_0 - A_{sl}\gamma_{la} \cos \theta_c + A_{la}\gamma_{la} \end{aligned} \tag{2}$$

where A_{sl}, A_{sa} and A_{la} are interface areas of solid-liquid, solid-air, and liquid-air, respectively, and γ_{sl}, γ_{sa}, and γ_{la} are the surface energies per unit area. The sum of $(A_{sl} + A_{sa})$ is invariant, so U_0 is a constant value.

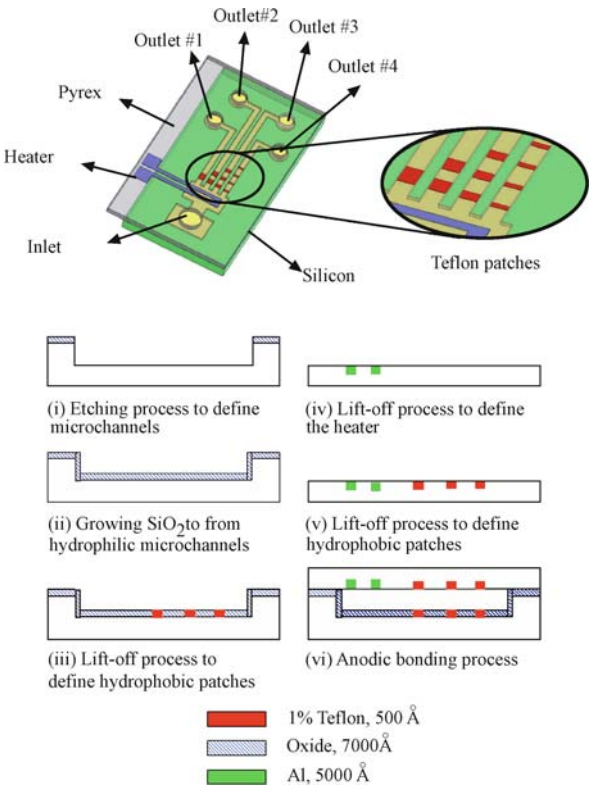

Bubble Actuated Microfluidic Switch, Figure 3 Microfabrication processes for the capillary system

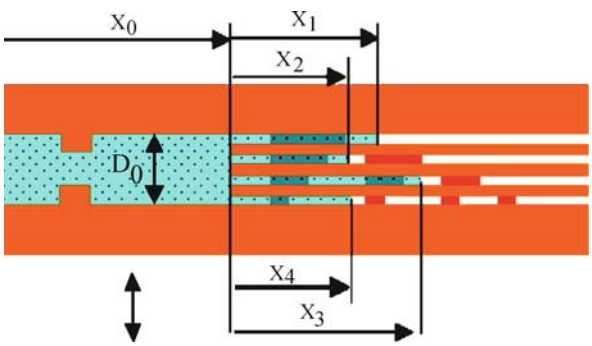

Bubble Actuated Microfluidic Switch, Figure 4 The meniscuses of the liquid stay at position x_1, x_2, x_3, x_4 in microchannel 1, 2, 3, 4, respectively, for a transient state. This is a general case for the analysis of pulling force and backward barrier pressure in the capillary system

When a liquid sample is introduced into the capillary system with a 1×4 microfluidic switch as shown in Fig. 1, it wicks by the capillary force and stops at the edges of hydrophobic patches due to the barrier pressure. To study the pulling force and backward barrier pressure in each microchannel, Fig. 4 illustrates a general case for the transient state with the liquid positions at x_1, x_2, x_3, and x_4 in microchannel #1, #2, #3, #4, respectively. The width of each outlet microchannel is much larger than the microchannel height, h, in the device, so the meniscus shape could be simplified as a one dimension problem. The effect of gravity is neglected because of shallow microchannels in the device. The meniscus is assumed to be a circular arc with a 2α angle where α is equal to $\pi/2-\theta_c$, as shown in Fig. 5. The total energy U_T is a function of the injected liquid volume V_L. The total energy U_T and the pressure P could be derived as follows [13].

$$U_T = U_0^* + \sum_{i=1}^{4}\left[-2D_i x_i \gamma_{la}\cos\theta_{c,i} + \gamma_{la}\frac{D_i h\alpha_i}{\sin\alpha_i}\right] \quad (3)$$

$$V_L = D_0 x_0 h + \sum_{i=1}^{4}\left[D_i x_i h - \frac{D_i h^2}{4\sin\alpha_i}\left(\frac{\alpha_i}{\sin\alpha_i} - \cos\alpha_i\right)\right] \quad (4)$$

where U_0^* is a constant value, D_i is the width of the microchannel #i, x_i is the meniscus in the microchannel #i, and $\theta_{c,i}$ is the contact angle between liquid and microchannel wall in microchannel #i. The pressure on the liquid is hence

$$\begin{aligned}
P_1 &= \frac{\partial U_T/\partial x_1}{\partial V_L/\partial x_1} = \frac{-2\gamma_{la}\cos\theta_{c,1}}{h},\\
P_2 &= \frac{\partial U_T/\partial x_2}{\partial V_L/\partial x_2} = \frac{-2\gamma_{la}\cos\theta_{c,2}}{h},\\
P_3 &= \frac{\partial U_T/\partial x_3}{\partial V_L/\partial x_3} = \frac{-2\gamma_{la}\cos\theta_{c,3}}{h},\\
P_4 &= \frac{\partial U_T/\partial x_4}{\partial V_L/\partial x_4} = \frac{-2\gamma_{la}\cos\theta_{c,4}}{h}
\end{aligned} \quad (5)$$

$$P = \frac{dU_T}{dV_L} = \sum_{i=1}^{4} P_i = \sum_{i=1}^{4}\left[\frac{\partial U_T/\partial x_i}{\partial V_L/\partial x_i}\right] = -\sum_{i=1}^{4}\frac{2\gamma_{la}\cos\theta_{c,i}}{h} \quad (6)$$

where P_1, P_2, P_3, and P_4 are the individual forward/backward pressure in the microchannel #1, #2, #3, and #4, respectively. P is the total pressure applied to the fluid due to capillary force and barrier pressure. When all the fluid in each microchannel stays at the hydrophobic regions, $P_1=P_2=P_3=P_4$ with the same contact angle θ_c.

In the device design, the sample liquid is DI water, the height is 20 μm and the width of each microchannel is 100 μm. According to Eq. (5), the internal liquid pressure is a function of the contact angle, which is related

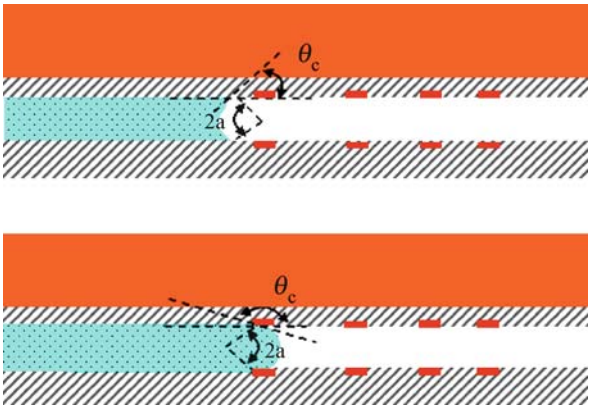

Bubble Actuated Microfluidic Switch, Figure 5 The definition for the angles of meniscus shape stayed at (**a**) hydrophilic region (**b**) hydrophobic region

to the meniscus positions, x_1, x_2, x_3 and x_4. The contact angle $\theta_c = 20°$ of hydrophilic microchannels could produce a negative pressure of nearly 7 kPa to make the liquid flow forward. The contact angle $\theta_c = 120°$ of hydrophobic patches could generate a positive barrier pressure of nearly 4 kPa to stop the liquid. Figure 6 shows the pressure distribution in each microchannel of the device based on the above contact angle parameters. The positive sign on the pressure means a backward barrier pressure on the hydrophobic patch regions. The negative sign means a forward pulling pressure on the hydrophilic region in the capillary microchannels.

Based on the above, we could extend 1×4 microfluidic switch system to $1 \times N$ microfluidic switch system with similar derivation to obtain the mathematical models for the injected volume, the total energy and the total pressure as follows.

$$U_T = U_0^* + \sum_{i=1}^{N} \left[-2D_i x_i \gamma_{la} \cos\theta_{c,i} + \gamma_{la} \frac{D_i h \alpha_i}{\sin\alpha_i} \right] \quad (7)$$

$$V_L = Dx_0 h + \sum_{i=1}^{N} \left[D_i x_i h - \frac{D_i h^2}{4 \sin\alpha_i} \left(\frac{\alpha_i}{\sin\alpha_i} - \cos\alpha_i \right) \right] \quad (8)$$

$$P = \frac{dU_T}{dV_L} = \sum_{i=1}^{N} P_i = \sum_{i=1}^{N} \left[\frac{\partial U_T / \partial x_i}{\partial V_L / \partial x_i} \right]$$

$$= -\sum_{i=1}^{N} \frac{2\gamma_{la} \cos\theta_{c,i}}{h} \quad (9)$$

Thermal Bubble Nucleation

The growth and collapse of a micro-bubble via a micro-heater actuator, with the applications to ink-jet printers, have been studied extensively in the decades. It has been demonstrated that the pressure inside the bubble could reach several MPa during the initial bubble growth period, with the heating duration of within several microseconds. It should be highlighted that most previous researches regarding the bubble generation under a pulse heating show a nearly symmetric bubble growth and collapse periods, where the width of heating pulse was kept at several microseconds. In other words, the bubble growth velocity is nearly equal to the bubble collapse velocity, so there will be no net fluid flow after one cycle of bubble growth and collapse period. Recently, P. Deng et al. [14] have studied the bubble behavior under pulse heating with pulse width in the range from microseconds to milliseconds. They report that a relatively long pulse heating duration could change the near-symmetric bubble growth-collapse pattern by prolonging the vapor bubble condensation process.

Thermal Bubble Volume

The thermal bubble growth could be mainly classified into two modes in macro-scale bubble nucleation experiments, as described in an early literature report [15]. The first mode occurs at the initial stage of bubble growth that is hydrodynamically controlled and dominated by liquid inertia. For this first mode, the bubble diameter increases proportionally with heating time. The second mode occurs at the later stage of bubble growth that is dominated by the heat diffusion. The bubble grows at a slower rate and is proportional to the square root of heating time in this second mode. Recently, Tsai et al. [16] have investigated the transient bubble formation experiments on polysilicon micro-resistors. These studies demonstrate that the micro bubble nucleation processes could be classified into three groups depending on the input current. When the input current is low, no bubble is nucleated. For the middle range of the input current, a single spherical bubble is nucleated with a waiting period up to 2 s depending on the magnitude of the input current. After the resister temperature rises and reaches a steady state, the bubble growth rate is found proportional to the square root of heating time that is similar to the heat diffusion dominant model as proposed for the macro scale boiling experiments. From the experimental data, it is found that the bubble diameter, D, could be represented as $D = 2Ct^{1/2}$, where t is the heating time, and C is the bubble growth rate constant and determined by the heating rate.

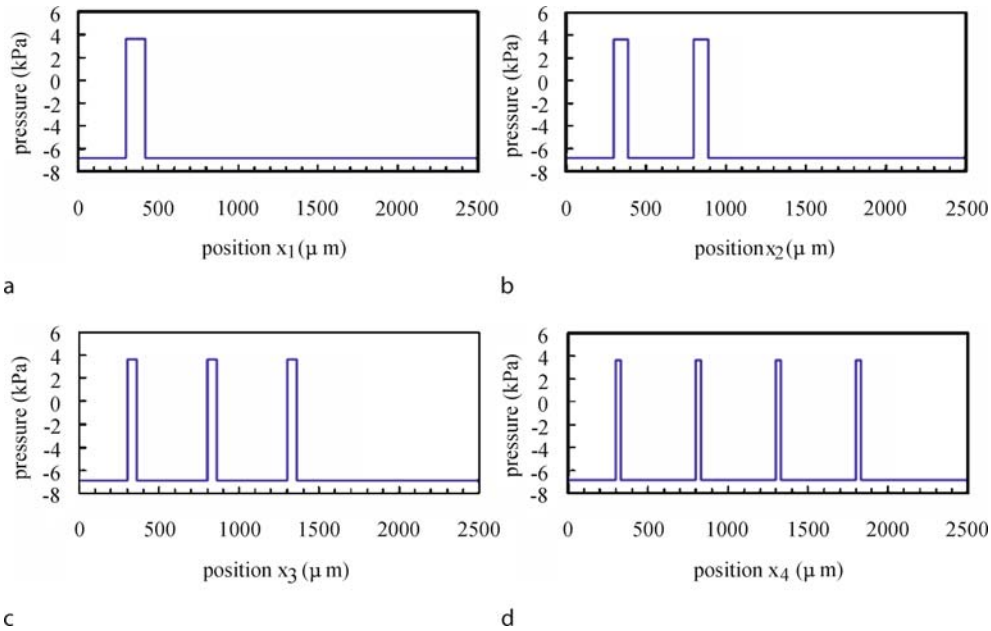

Bubble Actuated Microfluidic Switch, Figure 6 Hydrophobic barrier pressure distribution versus meniscus positions x_1, x_2, x_3, x_4 along (**a**) microchannel #1 (**b**) microchannel #2 (**c**) microchannel #3 (**d**) microchannel #4, respectively. The positive sign on pressure means a backward barrier pressure. The negative sign means a forward pulling pressure on the hydrophilic region in the capillary microchannels

Furthermore, a further assumption of a perfectly spherical bubble is made for the shape of the vapor layer generated on a thin-film heater surface, the bubble volume, V, could be modeled as [17]

$$V(t) = \frac{\pi D^3}{6} = \frac{4\pi}{3} C^3 t^{3/2} \tag{10}$$

In the design, the width of each microchannel is much larger than its height, so the bubble volume could be simplified as a two-dimension problem.

$$V(t) = \frac{\pi D^2}{4} h = \pi h C^2 t \tag{11}$$

The bubble volume increases linearly with time in the case, so we could control the bubble volume via the time of applied voltage to control the liquid positions through hydrophobic patches of different length. In addition, the bubble growth rate is also affected by the amplitude of the applied regulation voltage, so we could shorten the heating duration by increasing the amplitude of the applied voltage. Thus, the bubble volume could be controlled by the heating duration and the applied-voltage amplitude.

Thermal Energy

In fact, the heating rate is not fixed even if the heater is applied with a constant voltage. The power input to the heater is not constant because the heater resistance is continuously increasing with the temperature during the application of the heating pulse. For the square electrical voltage pulse with a time period, the thermal energy, Q, which is produced via a thin-film micro heater, could be derived by the following equation.

$$\begin{aligned} Q &= \int_0^{t_N} V_e I_e(t)\,dt = \int_0^{t_N} \frac{V_e^2}{R(T)}\,dt \\ &= \int_0^{t_N} \frac{V_e^2}{R_0(1+\alpha_T(T(t)-T_0))}\,dt \end{aligned} \tag{12}$$

where V_e, I_e, R and T are the applied voltage, the applied current, the heater resistance and temperature, respectively, α_T is the temperature coefficient of the Al wire resistor, t_N is the duration of the applied voltage pulse, and R_0 is the heater resistance at a reference temperature T_0. In the concept-proof prototype devices, the micro-heaters, as shown in Fig. 12a, are 30 μm wide Al wires with different resistances. In the following experimental demonstration, the micro-heater that we use for thermal bubble generation is characterized and has the resistance of 64.6 Ω at room temperature.

The relationship between thermal energy and the pulse duration would change due to the temperature effect. However, the thermal energy would increase with the applied heating duration. To characterize heater temperature, the

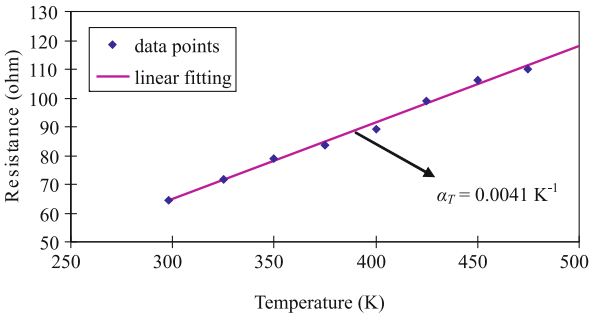

Bubble Actuated Microfluidic Switch, Figure 7 The characterized resistance for the micro heater versus the heater temperature. The Al micro heater has a nominal resistance of 64.6 Ω at the room temperature

relationship between the electric resistance and the temperature of the micro Al heater is studied. First, the heater is calibrated to obtain the temperature coefficient, α_T. The fluidic chip with the Al wire resistor is placed on a hot plate, whose temperature is controlled by a controller, and then the pad of the heater are connected to the input ports of a HP3457A multimeter. The resistance of the heater versus the temperature is characterized and recorded, as shown in Fig. 7. The temperature coefficient of the heater $\alpha_T = 0.0041\ K^{-1}$ is obtained by a linear fitting of the measured data which could help us to approach the real-time heater maximum temperature during the pulse heating process.

Mechanical Work

While a bubble expands or contracts in a liquid, mechanical work is transferred between the bubble and the surrounding liquid. The kinetic energy transferred from the expanding vapor microlayer on a thin-film heater surface could be used, in principle, to drive electromechanical microdevices such as micro actuators and micro pumps. The useful work converted from the thermal energy on the surface of a microheater is critical for these applications. The mechanical work, E_m, done by a vapor volume expansion on the surrounding liquid is [16]

$$E_m = \int P_v \, dV = \int_0^t P_v \frac{dV(t)}{dt} \, dt \tag{13}$$

where P_v is the pressure within a bubble and $V(t)$ is the bubble volume. The microfluidic switch is activated to drive fluid forward when the bubble pressure overcomes the total barrier pressure, $P_v > P$. Therefore, the mechanical work is used to overcome the barrier pressure and to increase the bubble volume. For reliability and controllability, we have to keep the total barrier pressure constant before the thermal bubble is activated each time, to make the mechanical work completely dominated by the bubble volume. The best way to keep the total barrier pressure constant is that the fluid must simultaneously pass all last hydrophobic patches at the desired turn-on microchannels. This is related to the operation principles that we will address next.

Bubble Actuated Microfluidic Switch, Table 1 Fifteen operation modes for the capillary system with a 1×4 microfluidic switch

Number of outlet ports on	Desired outlet ports (microchannel #*i*) on
One	1; 2; 3; 4
Two	1,2; 1,3; 1,4; 2,3; 2,4; 3,4
Three	1,2,3; 1,2,4; 1,3,4; 2,3,4
Fthe	1,2,3,4

Operation Principles

There are 15 operation modes for the capillary system with a 1×4 microfluidic switch, which could simultaneously switch the liquid into the desired outlet ports, as listed in Table 1. The operation modes could be divided into two parts, namely single and multiple output modes. We will discuss the required time-sequence power control for the bubble nucleation to function the fluidic switch appropriately for the capillary system as follows.

Single Output Modes

The sample liquid is assumed to be able to be pushed and pass the lengths of hydrophobic patches L_1, L_2, L_3 and L_4 in each microchannel, as shown in Fig. 1, with the voltage pulse widths T_1, T_2, T_3 and T_4 on the heater in capillary micro system. According to Eq. (11), the bubble volume increases proportionally to the heating time under a constant applied voltage. Thus, the relationship $T_1 > T_2 > T_3 > T_4$ is reasonably predicted. Therefore, we could control the fluid into one of microchannels by controlling the format and timing of heater power input, as shown in Fig. 8. For a $1 \times N$ microfluidic switch, if we desire to guide the liquid into the microchannel #*i*, the voltage pulse width t applied on the heater to generate actuating bubble must be $T_i \leqq t < T_{i-1}$ and the times of the bubble nucleation, i, is required to pass through all hydrophobic patches of microchannel #*i*. Also, the design on the separation gap between adjacent hydrophobic patches must be far enough to prohibit the fluid from passing through the microchannel #$i-1$ when we only intend to turn on microchannel #*i*.

Multiple Output Modes

Appling the similar principles, we could control the fluid into multiple microchannels based on the needs. For such multiple output modes, there are three different operation methods, as shown in Fig. 9, to control the fluid into the microchannel #2 and #4, for example, in the capillary system with a 1×4 microfluidic switch. The time-sequence actuation as shown in Fig. 9a, we would generate the growth and collapse of the thermal bubble six times to control the fluid to pass through the microchannel #4 and #2. The bubble pressure overcomes the barrier pressure to make the fluid pass through all hydrophobic patches of microchannel #2 and #4. Then, the capillary force pulls the fluid through to turn on microchannel #2 and #4. However, Fig. 9b demonstrates the same switch function with only four-time thermal-bubble actuation. These two methods have the common point which is firstly to control the fluid to pass through one of desired microchannels. According to Eq. (6), the total barrier pressure would decrease due to the effect of the capillary force which would produce a negative pressure. Hence, the magnitude of the total barrier pressure would be affected after the fluid pass through one of the microchannels. The total barrier pressure would decrease with the number of the turn-on microchannels which the fluid has passed through via capillary force.

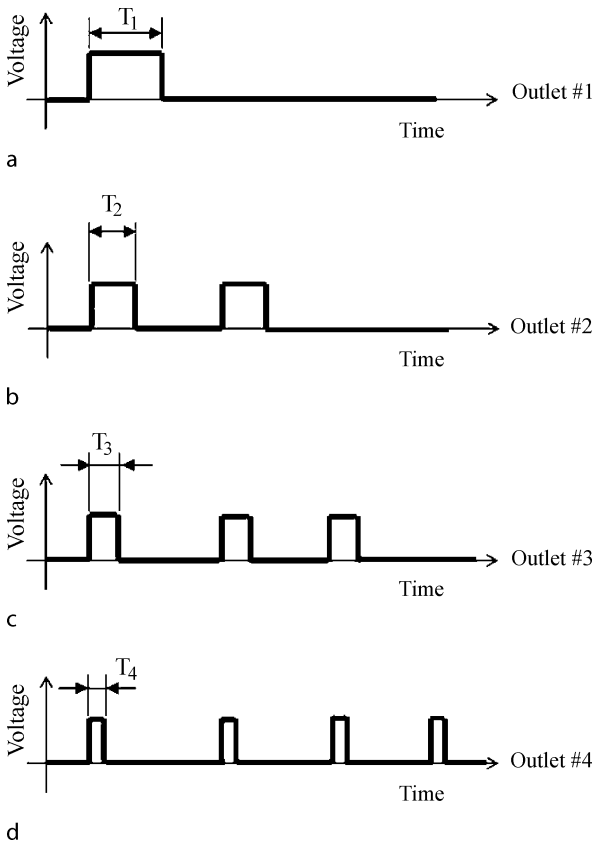

Bubble Actuated Microfluidic Switch, Figure 8 Pulse widths and the times of bubble nucleation management in a single output mode (**a**) for the power control to turn on microchannel #1 only (**b**) for the power control to turn on microchannel #2 only (**c**) for the power control to turn on microchannel #3 only (**d**) for the power control to turn on microchannel #4 only

To ensure the controllability and reliability of the microfluidic switches, the same total barrier pressure is set as the requirement in the design when the thermal bubble is activated each time. This means that the fluid has to be steady-state and stop at hydrophobic patches of each microchannels before each bubble starts being generated. For example, if we desire to control the fluid into the microchannel #2 and #4 simultaneously, we could follow the third method, as illustrated in Fig. 9c, which makes the microchannel #2 and #4 turned on simultaneously on the last time of bubble growth actuation. This procedure could also minimize the times of the bubble nucleation for the same fluidic switch purpose.

For a $1\times N$ general microfluidic switch, we want the fluid liquid to be controlled into five specific outlet ports, for example, which are connected with microchannels $\#X$, $\#Y$, $\#Z$, $\#V$ and $\#W$. The lengths of hydrophobic patches in these five microchannels have the relationship of $L_X > L_Y > L_Z > L_V > L_W$. Here, L_X, L_Y, L_Z, L_V and L_W represent the length of hydrophobic patches in microchannel $\#X$, $\#Y$, $\#Z$, $\#V$ and $\#W$, respectively. Then, we could design the required time-sequence power control logics to control the thermal bubble actuator via the control of voltage pulse width and bubble-actuation times. The control logics for the voltage pulse width and the bubble actuation times is described and optimized as follows.

Step 1: $T_X \leqq t_1 < T_{X-1}$, and $(X-1)$ times bubble actuation with the voltage pulse time width t_1.

Step 2: $T_Y \leqq t_2 < T_{Y-1}$, and $[(Y-1)-(X-1))] = (Y-X)$ times bubble actuation with the voltage pulse time width t_2.

Step 3: $T_Z \leqq t_3 < T_{Z-1}$, and $[(Z-1)-(Y-1)] = (Z-Y)$ times bubble actuation with the voltage pulse time width t_3.

Step 4: $T_V \leqq t_4 < T_{V-1}$, and $[(V-1)-(Z-1)] = (V-Z)$ times bubble actuation with the voltage pulse time width t_4.

Step 5: $T_W \leqq t_5 < T_{W-1}$, and $[(W-1)-(V-1)] = (W-V)$ times bubble actuation with the voltage pulse time width t_5.

Step 6: $T_X \leqq t_6 < T_{X-1}$, and one more time bubble actuation with the voltage pulse time width t_6,

where t_i represents the required voltage pulse time width at each step; T_i is the required voltage pulse time width

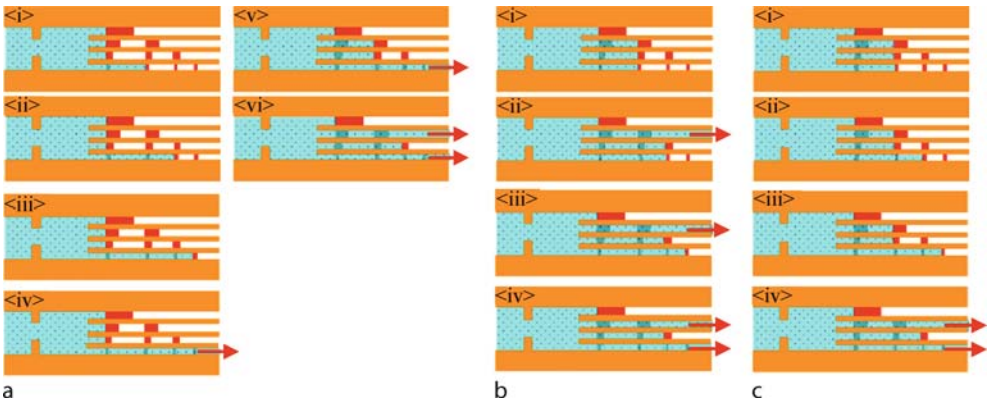

Bubble Actuated Microfluidic Switch, Figure 9 The three different time-sequence power control logics to turn on microchannel #2 and #4 in the capillary system with the 1×4 microfluidic switch function

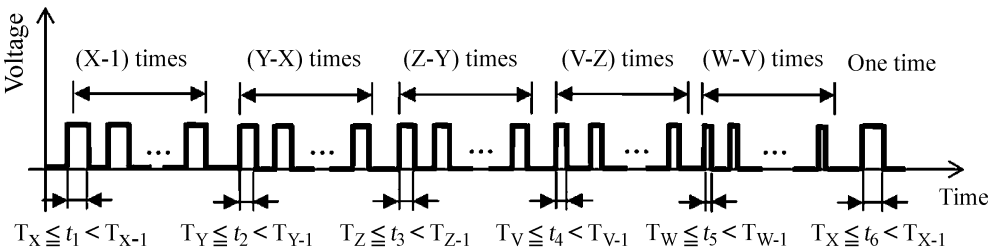

Bubble Actuated Microfluidic Switch, Figure 10 The optimized control logics to turn on microchannel #*X*, #*Y*, #*Z*, #*V* and #*W*. The t_i represents the required power pulse time width at each step. T_i is the required voltage pulse width on the heater to push the fluid to pass the first hydrophobic patch region in microchannel #*i*

on the heater to make the fluid pass through the first hydrophobic patch region in microchannel #*i*; *X*, *Y*, *Z*, *V* and *W* represent the desired turned-on microchannels. Therefore, we could simultaneously guide the fluid into specific desired microchannels by controlling the format and timing of power input based on the above generalized optimal operation steps, which are also summarized and shown in Fig. 10. The control logics could be applied to the capillary system with $1 \times N$ microfluidic switch function.

Experimental Results

Experimental Setup

The experimental setup which is utilized to observe the switch function is schematically represented in Fig. 11a. The volume of thermal bubble is controlled by the input pulse power of the heater with a preset duration which is programmed by the controller, composed of the Complex Programmable Logic Devices (CPLD) card, a buck circuit, and adaptors, as shown in Fig. 11a. In Fig. 11b, the programmable CPLD card is utilized to control the duration of the heating and to regulate the voltage amplitude by means of a buck circuit and a pulse width modulation (PWM) method. An optical microscope with a CCD camera is utilized to observe and record the switching process of the capillary system with $1 \times N$ microfluidic switches.

Experimental Demonstration

There are 15 operation modes, as shown in Table 1, for the controller design to operate the capillary system with a 1×4 microfluidic switch. In Fig. 12, two kinds of operation modes were recorded to demonstrate the fluidic switch functions for the capillary system with a 1×4 microfluidic switch. In Table 2, these designed dimensions of the hydrophobic patches are shown. The dyed DI water is introduced into the inlet, as shown in Fig. 12a, driven forward by the capillary force and finally stops at the edge of first hydrophobic patch in each microchannel, as shown in Fig. 12b. Figures 12c–f shows the results of the single-output mode demonstration – the continuous liquid is switched into the single desired outlet port via the control of the programmed bubble volume and the time sequence power control. Figure 12g demonstrates

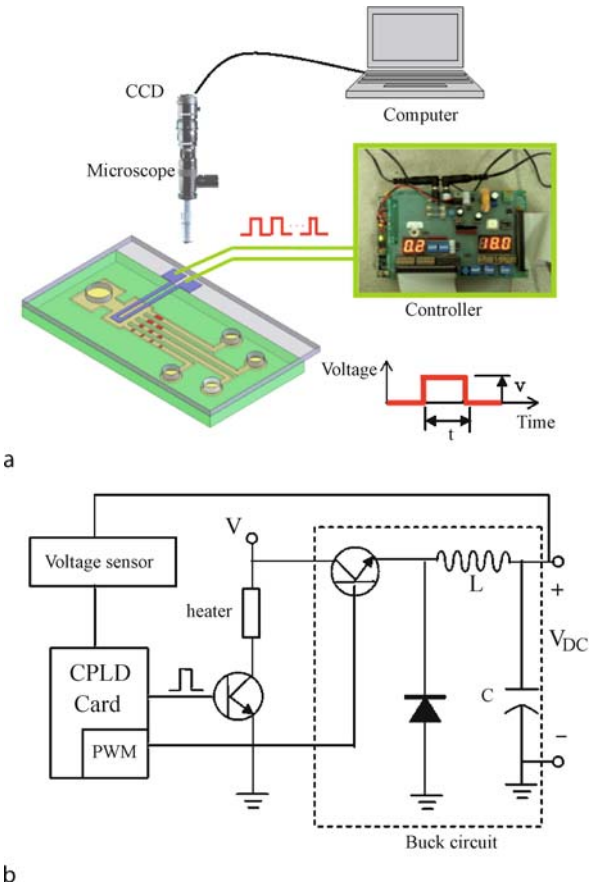

Bubble Actuated Microfluidic Switch, Figure 11 (**a**) Schematic diagram of the experimental setup (**b**) the control circuit of the micro heater for a square voltage pulse with a preset duration

Bubble Actuated Microfluidic Switch, Table 2 Geometry parameters of the 1×4 microfluidic switch (unit: μm)

	Geometry parameters
Hydrophobic length	$L_1 = 120$; $L_2 = 90$; $L_3 = 60$; $L_4 = 30$
Microchannel width	$D_1 = D_2 = D_3 = D_4 = 100$
Microchannel depth	$h = 20$

the result of the multiple-output modes – the continuous liquid is simultaneously switched into two desired outlet ports, microchannel #1 and #4. This operation mode in the controller breaks the barrier pressures of all hydrophobic patches in microchannel #1 and #4 to continuously drive liquid forward by the capillary force.

According to Eq. (11), the relationship between bubble volume and heating duration is linear for the case. Here, the bubble volume is characterized via the captured images by a CCD camera, and recorded along with the heating time under two different applied voltages, 5 V and 10 V, on the 30 μm wide micro heater, as shown in Fig. 13. The bubble growth rate constant, C, could be experimentally determined by the slope of the fitting curve. The bubble growth rate constants are characterized to be 56 and 105 $\mu m/s^{1/2}$ for the applied voltage of 5 V and 10 V, respectively. These experimental results imply that the bubble volume could be controlled by the heating duration and the applied-voltage amplitude. Therefore, the bubble volume can be controlled via the time of applied voltage to control the liquid positions through hydrophobic patches of different length in the device design.

The experimental results in Fig. 14a show the pulse width versus the length of hydrophobic patches in a 1×4 microfluidic switch under different applied voltages, 5 V and 10 V. The required voltage pulse width could be shortened by the lager voltage or the shorter hydrophobic patches. Thus, the magnitude of the applied voltage on heater and the dimension design of the hydrophobic patches would dominate the operation speed of the microfluidic switches. Besides, the relationship between the length of hydrophobic patch and the required voltage pulse width is nearly linear. However, the required pulse width must be increasing with the length of hydrophobic patch. Therefore, the bubble volume can be controlled to push the fluid through the hydrophobic patches with different length by managing the voltage pulse width, and then to drive the continuous fluid into specific outlet ports based on the operational rules and control logics. Also, the maximum temperature of the heater during the heating period can be derived by means of measuring the resistance of the heater at the end of heating based on the curve shown in Fig. 7. The relationship between the heating-pulse width and the maximum temperature is shown in Fig. 14b.

The design in this case-study prototype device remains an issue for the reversible motion of the liquid. This case-study prototype device could be effectively used for the one shot of liquid in both single-output and multi-output modes on demand. For continuous random switch function, another problem appears if we turn on microchannel #X first and desire to next turn on only microchannel #Y where $X > Y$. In this continuous switch function, the microchannel #$(X + 1)$ will be also turned on in this case-study prototype device. Anyway, above issues could be resolved via the two-way bubble actuator design [18, 19], which could make the fluid flow backwards in the unwanted microchannel. In addition, this micro fluidic switch has the potential to be integrated into a wider fluidic network system with stop valves or micro flow discretizers which could be used for separation of liquid segments from a continuous source.

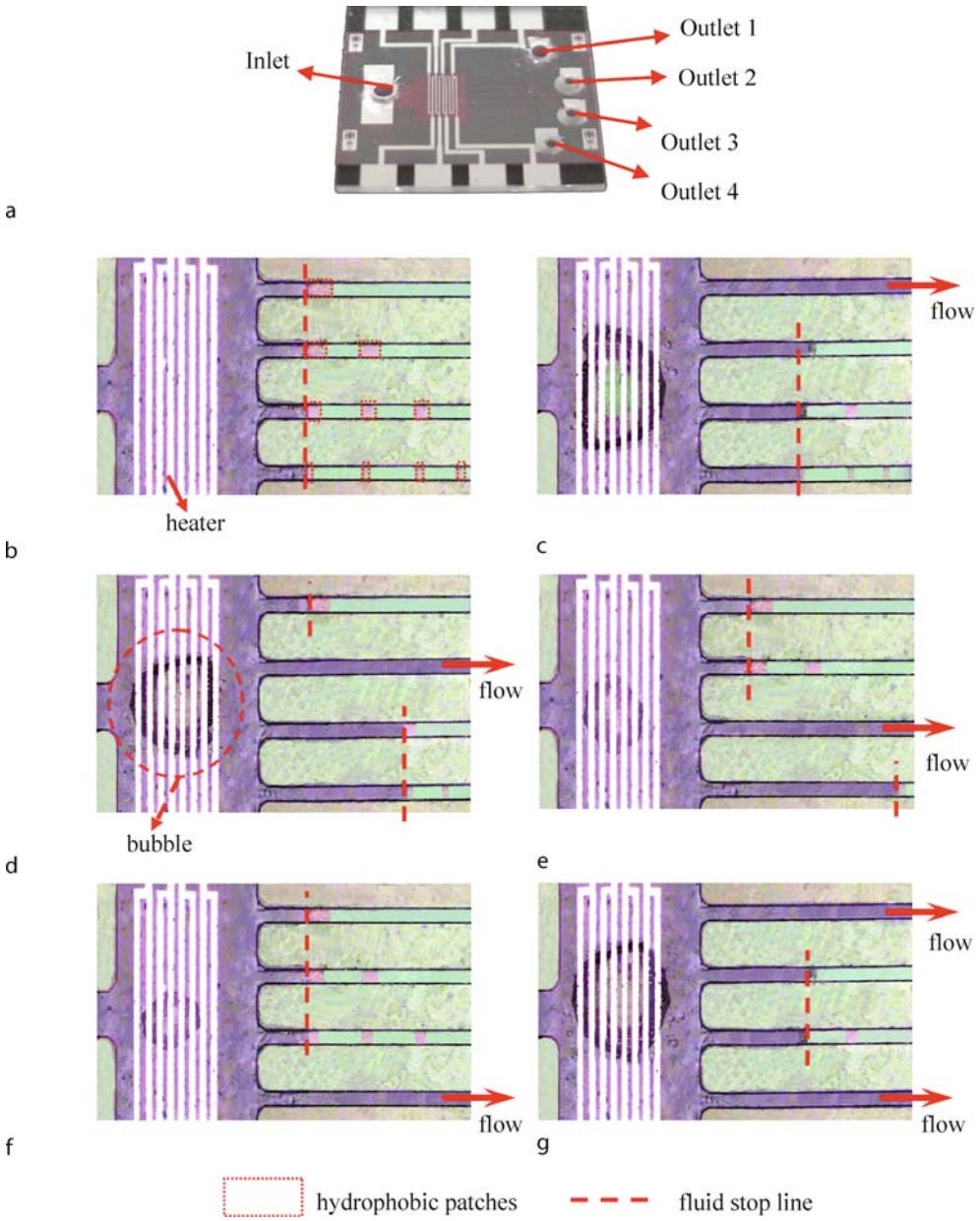

Bubble Actuated Microfluidic Switch, Figure 12 Experimental demonstration for different switch modes. (**a**) The 1×4 microfluidic switch prototype device. (**b**) DI water starts being ejected. (**c**)–(**f**) show the single-output switch mode to single desired outlet, microchannel #1, microchannel #2, microchannel #3 and microchannel #4, respectively. (**g**) shows simultaneous multiple- output mode to two desired outlets, microchannel #1 and #4

Key Research Findings

A capillary system with the appropriate design of bubble-actuated $1 \times N$ microfluidic switches is successfully demonstrated to control continuous liquid into the desired outlets without the need of external pumps and MEMS mechanical moving parts. Theoretical models are proposed to study the liquid motion, which is dominated by both the barrier pressure and the capillary force in the device. This capillary micro-fluidic switch system is a valveless switch by means of the triggering bubble-actuator, the capillary force, the design of the distributed hydrophobic patches in the microchannels, and the time-sequence power control. The switch mechanism among

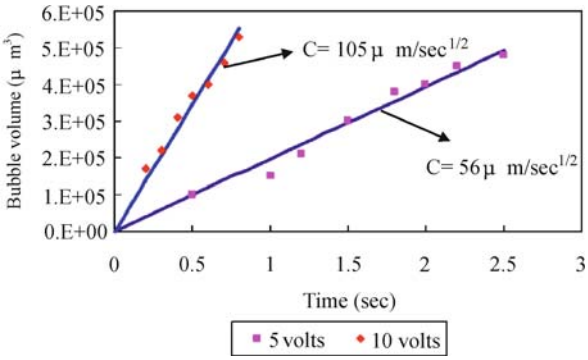

Bubble Actuated Microfluidic Switch, Figure 13 The bubble volume versus the heating period (pulse width) for a 1×4 microfluidic switch with the applied voltage of 5 V and 10 V

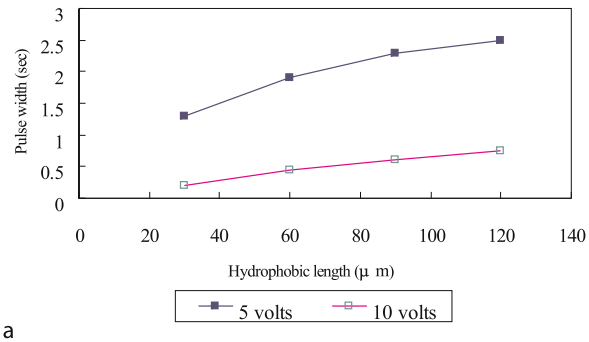

a

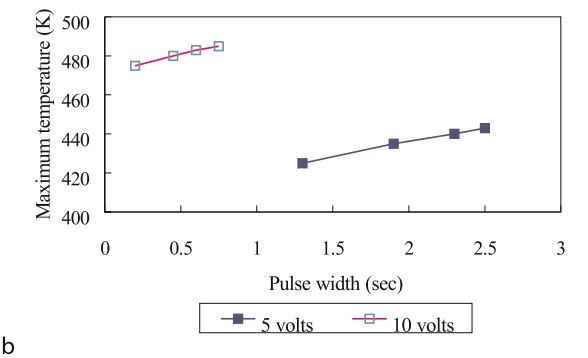

b

Bubble Actuated Microfluidic Switch, Figure 14 (**a**) Heating-pulse width versus length of hydrophobic patches (**b**) Maximum temperature versus heating-pulse width for the capillary system with a 1×4 microfluidic switch with the applied voltage of 5 V and 10 V

different microchannels in the case-study device is dominated by controlling the format and timing of power input that generates actuation bubbles. The design, synthesis and bubble control with its time-sequence control logics are presented via a case-study example of 1×4 thermal-bubble actuated microfluidic switches.

Future Directions for Research

This bubble actuated microfluidic switch could be effectively used for the one shot of liquid in both single-output and multi-output modes on demand. The reversible motion of the liquid is one further research direction. The long-term goal of this research work could be to develop integrated bio-analytical devices with the functions for specific flow guiding, specific flow injection, and precise liquid volume control.

Cross References

- Bubble Jet
- Surface Tension Driven Flow
- Hydrophilic/Hydrophobic Patterning
- Thermal Bubbles
- Bubble Dynamics in Microchannels
- Bubble Actuated Microfluidic Switch

References

1. Doring C, Grauer T, Marek J, Mettner MS, Trah HP, Willmann M (1992) Micromachined Thermoelectrically driven cantilever structures for fluid jet deflection. In: IEEE Micro Electro Mechanical Systems Workshop (MEM'92), pp 12–18
2. Blankenstein G, Larsen UD (1998) Modular concept of a laboratory on a chip for chemical and biochemical analysis. Biosens Bioelectron 13(3–4):427–438
3. Gebhard U, Hein H, Just E, Ruther P (1997) Combination of a fluidic micro-oscillator and micro-actuator in LIGA-technique for medical application. In: Solid-State Sensors and Actuators (Transducers'97), pp 761–764
4. Lee GB, Hwei BH, Huang GR (2001) Micromachined prefocused M×N flow switches for continuous multi-sample injection. J Micromech Microeng 11:654–661
5. Lemoff AV, Lee AP (2003) An AC Magnetohydrodynamic Microfluidic Switch for Micro Total Analysis Systems. Biomed Microdevices 5(1):55–60
6. Pollack MG, Fair RB, Shenderov AD (2000) Electrowetting-based microactuation of liquid droplets for microfluidic applications. Appl Phys Lett 77(11):1725–1726
7. Matsumoto H, Colgate JE (1990) Preliminary investigation of micropumping based on electrical control of interfacial tension. In: Proc MEMS, Napa Valley, pp 105–110
8. Verheijen HJJ, Prins MWJ (1999) Reversible electrowetting and trapping of charge: model and experiments. Langmuir 15(20):6616–6620
9. Cheng CM, Liu CH (2006) A Capillary System with Thermal-Bubble-Actuated 1×N Micro Fluidic Switches via Time-Sequence Power Control for Continuous Liquid Handling. J MEMS 15(2):296–307
10. Okamoto T, Suzuki T, Yamamoto N (2000) Microarrary fabrication with covalent attachment of DNA using bubble jet technology. Nat Biotechnol 18(4):438–441
11. Maxwell RB, Gerhardt AL, Schmidt MA, Toner M (2003) A Microbubble Powered Bioparticle Actuator. J MEMS 12(5):630–640

12. Ho CT, Lin RZ, Chang HY, Liu CH (2005) Micromachined Electrochemical T-switches for cell sorting applications. Lab Chip 5(11):1248–1258
13. Man PF, Mastrangelo CH, Burns MA, Burke DT (1999) Microfabricated Plastic Capillary Systems With Photo-Definable Hydrophilic and Hydrophobic Regions. In: Solid-State Sensors and Actuators (Transducers'99), pp 738–741
14. Deng P, Lee YK, Cheng P (2003) The growth and collapse of a micro-bubble under pulse heating. J Heat Mass Transf 46(21):4041–4050
15. Stralen SV, Cole R (1979) Boiling Phenomena, vol 1. Hemisphere, Bristol, pp 454–456
16. Tsai JH, Lin LW (2002) Transient thermal bubble formation on polysilicon micro-resisters. J Heat Transf 124(2):375–382
17. Zhao Z, Glod S, Poulikakos D (2000) Pressure and power generation during explosive vaporization on a thin-film microheater. J Heat Mass Transf 43:281–296
18. Jun TK, Kim CJ (1998) Valveless Pumping using Traversing Vapor Bubbles in Microchannels. J Appl Phys 83:5658–5664
19. Bohm S, Olthuis W, Bergveld P (2000) A bi-directional electrochemically driven micro liquid dosing system with integrated sensor/actuator electrodes. In: IEEE MEMS Workshop (MEM'00), pp 92–95

Bubble Dynamics in Microchannels

SATISH G. KANDLIKAR
Gleason Professor of Mechanical Engineering, Rochester Institute of Technology, Rochester, NY, USA
sgkeme@rit.edu

Synonyms

Bubble growth; Explosive Boiling in Microchannels; Confined bubble growth

Definition

Bubble dynamics in a microchannel refers to the nucleation of a bubble on heated flow channel walls and its subsequent interaction with the single-phase or two-phase flow field. ►Subcooled flow boiling refers to the boiling process with the mean flow enthalpy below the saturated liquid enthalpy at the local pressure, while ►saturated flow boiling refers to the boiling process with the mean flow enthalpy at or above the saturated liquid enthalpy but below saturated vapor enthalpy at the local pressure.

Overview

The formation and subsequent growth of a vapor bubble on a heated wall covered with a liquid is controlled by the forces arising from the excess pressure inside the bubble, the surface tension forces at the liquid–vapor interface and at the ►contact line formed by the interface at the heater surface, and the inertia forces resulting from the motion of the flow as well as the interface. The resistance to the phase change process at the liquid–vapor interface is quite small in comparison to the conduction resistance in the liquid surrounding a bubble and is generally neglected in analyzing the bubble dynamics.

Basic Methodology

The bubble dynamics during flow boiling in microchannels has been studied using high-speed video imaging and numerical techniques. The ►nucleation of a bubble and its growth leading to a confined bubble, vapor plug and annular flow have been analyzed under flow boiling studies. The research has primarily been conducted with water and several refrigerants such as R-123 and FC72 as the working fluids.

Key Research Findings

►Nucleation and *bubble growth*. Liquid enters a microchannel in a subcooled state and experiences a rise in temperature, while the local pressure falls due to frictional pressure drop along the channel in the flow direction. At some point downstream, the local saturation condition is reached. However, bubble nucleation will not occur immediately at this location as a certain degree of wall superheat is needed to activate a cavity according to the conditions originally suggested by Hsu [1]. The effect of the receding contact angle and the local flow field in front of a bubble was incorporated and the following equation is recommended [2] for nucleation of minimum and maximum cavity radii, $r_{c,min}$ and $r_{c,max}$:

$$\{r_{c,min}, r_{c,max}\} = \frac{\delta_t \sin\theta_r}{2.2}\left(\frac{\Delta T_{Sat}}{\Delta T_{Sat} + \Delta T_{Sub}}\right) \cdot \left[1 \mp \sqrt{1 - \frac{8.8\sigma T_{Sat}(\Delta T_{Sat} + \Delta T_{Sub})}{\rho_V h_{LV} \delta_t \Delta T_{Sat}^2}}\right] \quad (1)$$

where $\delta_t = k/h$; k – thermal conductivity of the fluid, W/(mK); h – single-phase heat transfer coefficient prior to nucleation; θ_r – receding contact angle of the bubble interface on the microchannel wall; ΔT_{sat} – local wall superheat ($= T_{wall} - T_{sat}$), °C; ΔT_{sub} – local liquid subcooling ($= T_{sat} - T_{fluid}$), °C; σ – surface tension, N/m; h_{LV} – latent heat of vaporization, J/kg; and ρ_V – vapor density, kg/m^3.

The experimental studies of Zhang et al. [3] and Li et al. [4], among others, confirm that the conventional nucleation theories of nucleation and bubble growth are valid for microchannel flows as well. The complex interactions due to nucleation, bubble growth and local heat transfer in

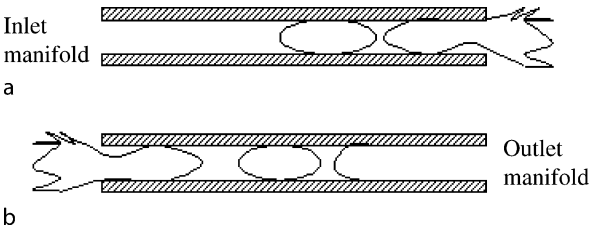

Bubble Dynamics in Microchannels, Figure 1 Flow boiling in microchannels with rapid evaporation leading to reversed flow in (**b**) [2]

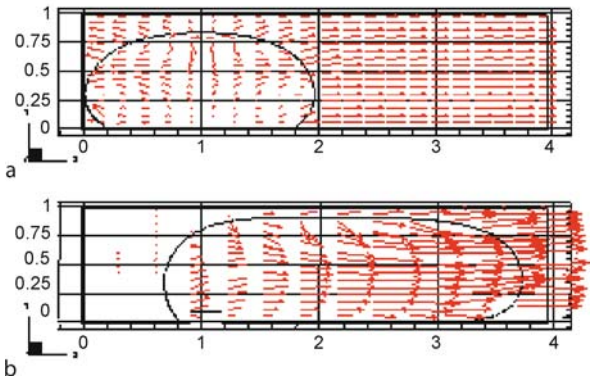

Bubble Dynamics in Microchannels, Figure 2 Bubble interface movement (**a**) without and (**b**) with a flow restrictor on the left side in a 200 μm square microchannel [9]

smooth circular and rectangular glass channels were studied by Yen et al. [5]. Their results showed that the corners in a rectangular microchannel provided nucleation cavities that initiated the boiling process at lower qualities and resulted in a higher heat transfer coefficient.

As a result of the very high single-phase heat transfer coefficients in microchannels, combined with the small radii of available nucleation cavities on the channel walls, the local liquid subcooling could be very low at the inception of nucleation. Under low flow conditions, it may even be negative, indicating that the bulk liquid is in a superheated state at the location of bubble nucleation [2]. The resulting rapid evaporation at the bubble interface raises the local pressure, creating a condition for fluid backflow. Experimental and numerical studies available in the literature indicate that the instability is predominant at the low heat fluxes [6, 7]. Figure 1 shows the effects of the explosive nature of the bubble growth under high liquid superheat conditions at the onset of nucleate boiling. If the nucleation occurs near the entrance region, the liquid vapor mixture is pushed back into the inlet manifold causing flow instabilities due to vapor condensation in the inlet manifold. If the nucleation occurs near the exit of the channel, the explosive growth propels the forward interface of the expanding bubble into the exit manifold. Backflow is prevented because of the inertia and frictional resistance in the microchannel prior to the nucleation site.

The flow instabilities due to nucleation and explosive bubble growth can be prevented by incorporating a flow restrictor at the inlet to each channel [2, 8]. Mukherjee and Kandlikar [9] analyzed the bubble growth process numerically. Their results, shown in Fig. 2, confirmed that the backflow of the interface can be substantially reduced by controlling the flow resistance at the inlet of the microchannel.

The ▶ flow patterns observed in the microchannels are largely similar to those observed in the conventional sized channels. However, the range of conditions and their transitions are somewhat different in microchannels than those observed in conventional sized channels. The influence of heat flux is more apparent during flow boiling in microchannels as compared to the adiabatic two-phase flows. As the bubbles are nucleated, they grow rapidly because surrounding liquid is superheated and the volume of the subcooled or lower temperature bulk core is limited due to small channel dimensions. The bubbly flow therefore does not exist for any appreciable length. The rapid growth of a bubble following its nucleation causes a succession of expanding vapor plugs that are separated by thinning liquid slugs. Eventually the flow assumes an annular flow pattern. Kandlikar [10] modeled the heat transfer process as an extension of pool boiling, in which the microchannel surfaces act as a bubble base that is periodically swept by rapidly moving liquid–vapor interface. This model is supported by the strong dependence of heat transfer coefficient on the heat flux experimentally observed at lower mass fluxes. Several investigators have applied the annular flow model, but prediction of the liquid film thickness poses considerable difficulties. There is a need for experimental data covering wider ranges of heat and mass fluxes and channel geometries for validating these models before they can be successfully applied to practical cases of interest.

Future Directions for Research

Bubble dynamics in microchannels is of great interest in a number of applications, including microchannel evaporators, high-flux heat removal systems for chip cooling applications, ink-jet printers, atomization nozzles and bubble pumps. The high heat transfer coupled with multidimensional heat conduction in the channel wall, and the rapid growth of the bubble at the microscale make it difficult to verify the analytical models. Future research is needed in understanding the heat transfer mechanism

during bubble growth. In this regard, the presence of a ►microlayer, if present, and its thickness and evaporation rate are areas where fundamental understanding is lacking.

Cross References

- ► Boiling and Evaporation in Microchannels
- ► Bubble Actuated Microfluidic Switch
- ► Cavitation in Microdomains
- ► Droplet Dispensing
- ► Flow Boiling Instability
- ► Heat Transfer in Microchannel Flows

References

1. Hsu YY (1962) On the Size Range of Active Nucleation Cavities on a Heating Surface. J Heat Transf 84:207–216
2. Kandlikar SG (2006) Nucleation Characteristics and Stability Considerations during Flow Boiling in Microchannels. Exp Thermal Fluid Sci 30:441–447
3. Zhang L, Wang EN, Goodson KE, Kenney TW (2005) Phase Change Phenomena in Silicon Microchannels. Int J Heat Mass Transf 48:1572–1582
4. Li HY, Tseng FG, Pan C (2004) Bubble Dynamics in Microchannels. Part II: Two Parallel Microchannels. Int J Heat Mass Transf 47:5591–5601
5. Yen T-H, Shoji M, Takemura F, Suzuki Y, Kasagi N (2006) Visualization of Convective Heat Transfer in Single Microchannels with different Shaped Cross-sections. Int J Heat Mass Transf 49:3884–3894
6. Kandlikar SG, Steinke ME, Tian S, Campbell LA (2001) High-Speed Photographic Observation of Flow Boiling of Water in Parallel Minichannels. In: 35th Proceedings of National Heat Transfer Conference, June 2001, Anaheim, CA. Paper # NHTC01-11262. ASME Publications, New York
7. Qu WL, Mudawar I (2004) Transport Phenomena in Two-Phase Micro-channel Heat Sinks. J Electron Packag 126(2):213–224
8. Kosar A, Kuo C, Peles Y (2005) Reduced Pressure Boiling Heat Transfer in Rectangular Microchannels with Interconnected Reentrant Cavities. J Heat Transf 127:1106–1114
9. Mukherjee A, Kandlikar SG (2005) Numerical simulation of growth of a vapor bubble during flow boiling of water in a microchannel. Microfluid Nanofluid 1(2):137–145
10. Kandlikar SG (2002) Fundamental Issues Related to Flow Boiling in Minichannels and Microchannels. Exp Thermal Fluid Sci 26(2-4):389–407

Further Reading

- Kandlikar SG, Garimella S, Li D, Colin S, King MR (2005) Heat Transfer and Fluid Flow in Minichannels in Minichannels and Microchannels. Elsevier, Oxford
- Zhang L, Goodson KE, Kenny TW (2004) Silicon Microchannel Heat Sinks. Springer, Berlin/Heidelberg

Bubble Formation

► Cavitation

Bubble Growth

► Bubble Dynamics in Microchannels

Bubble Jet

Definition

The functional principle of a thermal *bubble jet* printhead is based on a current pulse applied to a microheater which leads to a very short heating pulse at the solid–liquid interface. This heating pulse leads to a small vapor bubble which expands explosively. The increasing vapor bubble leads to a volume displacement of the ink towards the nozzle and finally to a droplet ejection. The detaching of the vapor bubble from the hot surface results in a concurrent cooling down of the bubble which results in condensation and collapse of the bubble. The suction of the collapsing bubble and the capillary forces inside the printhead lead to refilling of the nozzle chamber that it is finished before the next shot after approximately 10 µs. The fast explosion of the bubble leads to a characteristic pressure behavior inside the liquid. Starting instantaneously with a very high pressure of about 7 MPa to 9 MPa right at the beginning of the vaporization, the pressure decreases exponentially during a few microseconds.

Cross References

- ► Bioprinting on Chip
- ► DNA Micro-arrays
- ► Droplet and Bubble Formation in Microchannels
- ► Droplet Based Lab-on-Chip Devices
- ► Electrowetting and Droplets
- ► Inkjet
- ► Piezoelectric Microdispenser
- ► Thermal Bubble

Bubble Train Flow

► Taylor Flow in Microchannels

Bulk Materials

► Materials Used in Microfluidic Devices

Bulk Micromachining

CHE-HSIN LIN
Department of Mechanical and Electromechanical Engineering, National Sun Yat-sen University, Kaohsiung, Taiwan
chehsin@mail.nsysu.edu.tw

Synonyms

Bulk micromachining of silicon; Anisotropic silicon micromachining

Definition

Bulk micromachining (BMM) is a set of processes that enable the 3D sculpting of various materials (mainly silicon) to make small structures that serve as components for MEMS devices. Bulk micromachining builds mechanical elements by starting with a bulk material, and then etching away unwanted parts, and being left with useful mechanical devices. Typically, the substrate is ►photo–patterned, leaving a protective layer on the parts of the substrate that are to be retained. The substrate is then etched using a ►wet chemical etch process, ►dry chemical etch process, reactive plasma etch process or photo-etch process. The etch process "eats away" any exposed substrate material on the substrate. Bulk micromachining is a relatively simple and inexpensive fabrication technology to fabricate a micromachined device. It is especially well suited for applications that require only simple microstructures like microchannels, microcavities and free-standing microstructures such as micro-pit or micro-tip.

Overview

Bulk micromachining makes 3D micromechanical devices by etching deeply into a bulk material such as silicon, quartz, glass, plastic or even metal, where silicon and glass are the most common materials used in MEMS technology. These processes have been broadly applied in the fabrication of micromachined sensors, actuators, transducers and some functional structures. In practical applications, single-crystalline silicon is the most popular substrate to be used as the bulk material for bulk micromachining processes. The excellent electrical and mechanical properties of single-crystalline silicon make it a desirable material in the MEMS field and semiconductor industry. On the other hand, glass-based materials have also been extensively used in fabricating microfluidic channels for bioanalytical applications due to their low price and excellent material properties. These two materials have become the major materials for microfluidic and nanofluidic applications. They have also led to a focus on the development of different machining technologies to fabricate functional microfluidic devices in these two materials.

Table 1 summarizes the basic fabrication characteristics for these materials. Because of the rapid growth of the semiconductor industry, silicon has become one of the best-known materials in the world and can be obtained as a single-crystal structure at a reasonable price. The rapid growth of the demand for miniaturized devices also makes single-crystalline silicon the most popular material for bulk micromachining processes. However, silicon substrate is opaque in the UV-visible wavelength range such that it is difficult to observe micro- or nanofluids inside the fabricated microdevices. Also, the fabrication process is comparatively delicate and expensive even though the techniques for machining silicon substrates have been well developed, and there are plenty of tools to machine silicon into various kinds of structures.

Alternatively, silica-based devices are also important in micro- and nanofluidics since they provide advantages over other materials, including high chemical resistance and mechanical strength, large optical transmission range and good electrical insulation. Silica-based materials also have good biocompatibilities for most living cells. These materials in their native state have Si–OH functional groups on their surface, which provide an easy way to chemically modify the surface properties. However, silica-based materials such as quartz and borofloat glass are relatively expensive and rare in compare with general-purpose glass slides. These materials also have a low etch rate in hydrofluoric acid (HF)-based etchants. They also require expensive etching masks such as metal/polysilicon/nitride layer. Alternatively, soda-lime glass has several advantages over borofloat glass and quartz. The cost is much lower and the fabrication process is also much simpler and cheaper. The only drawback is that the impurities in the soda-lime glass is much more than the quartz and borofloat glasses, which may produce insoluble precipitates during etching process. In general, the amorphous structure of glass-based results in an isotropic etching pattern during wet chemical etching. As a result, the aspect ratio of the patterned structures is typically less than 0.5, which could limit their use for high-aspect-ratio microfluidic applications. Microfabrication of miniature analytical instruments on glass substrates for chemical and biomedical application has recently been widely studied. Various microfluidic devices have been fabricated on planar glass and quartz chips for μ-TAS such as capillary electrophoresis, electrochromatagraphy, DNA separations and semen testing. Planar glass chips fabricated by micromachining technologies meet the requirements of miniaturized total analysis

Bulk Micromachining, Table 1 Characteristics of typical materials for bulk micromachining in MEMS field

	Silicon	Quartz	Glass
Transparency	No	Yes	Yes
Cost	High	High	Low
Fabrication technique	Delicate	Cheap but difficult	Cheap, easy
Bonding method	Anodic, Fusion	HF, Adhesive, Sodium silicate	Fusion, Adhesive, Sodium silicate
Surface modification	Moderate – Easy	Easy	Easy
Biocompatibility	Fair	Good	Good
Surface property	Hydrophobic	Hydrophilic	Hydrophilic
Structure aspect ratio	Wide range	Typically < 0.5	Typically < 0.5

systems. Considerable attention is now directed towards how to simplify, reduce the cost and reduce the time of the manufacturing processes.

In this article, bulk micromachining techniques for fabricating microfluidic devices in silicon and glass materials are summarized. The details of the fabrication characteristics and fabrication protocols are described.

Basic Methodology

Bulk Micromachining of Silicon-Based Materials

Bulk micromachining of silicon uses wet- or dry-etching techniques in conjunction with etch masks and etch-stop techniques to sculpt a microstructure from the silicon substrate. The purpose of silicon bulk micromachining is to selectively remove significant amounts of silicon from a substrate to fabricate 3D structures in bulk micromachined silicon. The available etching methods fall into three categories in terms of the state of the etchant: wet, vapor and plasma. Wet chemical etch is the most popular method among these techniques due to the process being cheap and easy. However, the geometries of etched features using the wet chemical etching technique are usually greatly corresponding to the crystal orientation of the silicon substrate. The etch rate of dry etching may depend on the selected etching recipe and the etching mechanism of the equipment. In general, silicon wafers are usually cut to give top surfaces that roughly correspond to the main crystal planes in silicon given by the Miller indices (100), (110) and (111). Figure 1 shows the geometrical shape of a wafer and the crystal direction and polarity. For microfluidic and nanofluidic purposes, (100) wafers are the most popular because of the possibilities for the crystallographic-dependent wet etching.

Wet bulk micromachining was first developed in the Bell Telephone Laboratories in the mid-1960s. Anisotropic etching of silicon was achieved in a wet chemical solution composed of KOH, alcohol and water. Bulk micromachining using chemical and electrochemical etching processes

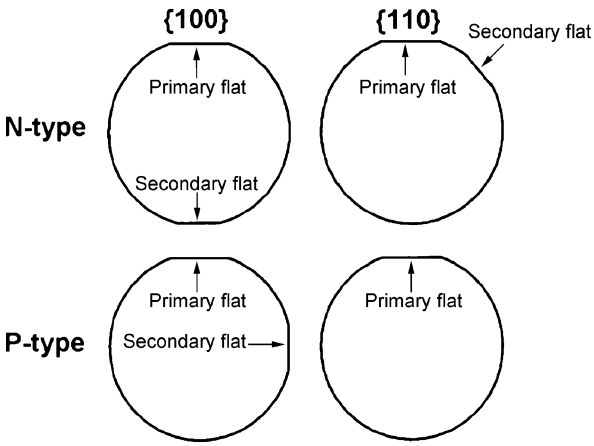

Bulk Micromachining, Figure 1 The geometrical shape of a wafer reveals the crystal direction and polarity

was pursued and became an extension of IC technology for the fabrication of 3D structures [1]. There are two major strategies, isotropic etching (crystal orientation independent) and anisotropic etching (crystal orientation dependent), adopted for this process. Figure 2 illustrates the possible features of the cross-section of a water substrate created using isotropic (Fig. 2a) and anisotropic (Fig. 2b) etching techniques. In general, the etched side wall is in round feature for a channel fabricated using ►isotropic etching since the etch rates in all directions are equal. However, a shallow dish-like feature would be obtained if the agitation during etching process is poor. On the other hand, the features created using ►anisotropic etching typically exhibit perfectly flat surfaces and are well defined. V-groove, U-groove and pyramidal pits can be fabricated with this approach. One can also form a famous feature of 54.74° sidewall while anisotropic etching (100) silicon. Figure 3 presents the typical structures which can be fabricated in (100) silicon using the anisotropic etching technique. The chemical reactions of wet etching rely on the oxidation of silicon to form compounds that can be physi-

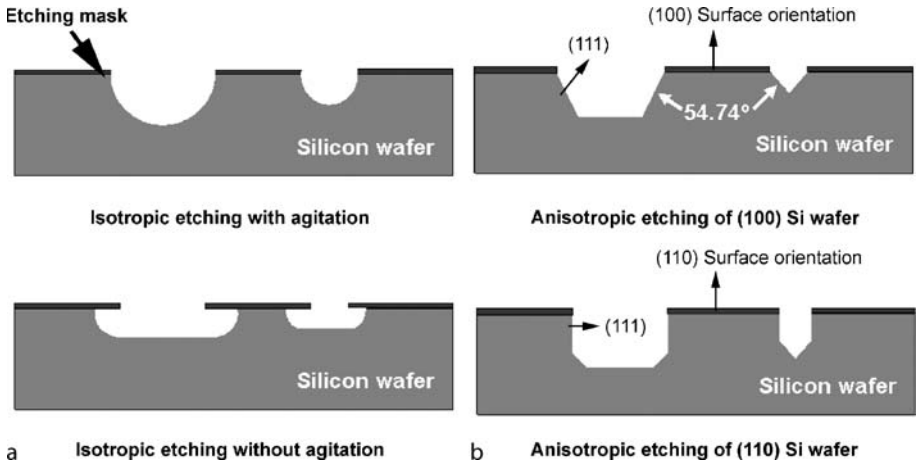

Bulk Micromachining, Figure 2 The possible features of the cross-section of a water substrate created using isotropic (**a**) and anisotropic (**b**) etching techniques

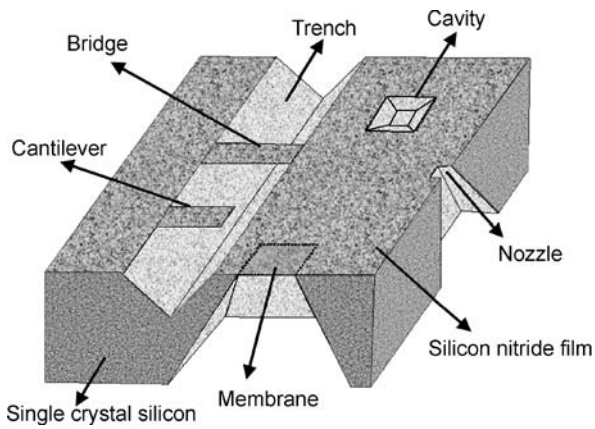

Bulk Micromachining, Figure 3 Typical structures which can be fabricated in single-crystal silicon using the anisotropic etching technique

cally removed from the substrate. The etching characteristics of the etching result are defined by the compositions of the etching chemicals, the material exchange rate of reactants and products, and some other minor factors. These include the temperature of the etching solution, the existence of additives and the shapes of the masks used to define the etched regions [2]. Table 2 provides a generalized comparison of the various etchants in terms of many of these important properties [3]. An excellent review article describing the techniques for silicon bulk micromachining can be found in Ref. [3].

Isotropic Etching of Silicon

HNA is the most popular etchant for silicon isotropic etching. The etchant is usually composed of hydrofluoric acid (HF)/nitric acid (HNO_3)/acetic acid (CH_3COOH) with a volume ratio of 1:3:8. Regarding the chemical reaction mechanism, silicon is firstly oxidized by nitric acid to form silicon oxide which is then etched away by hydrofluoric acid. Acetic acid in the recipe acts as the diluent which is essential for achieving the reaction. Water can also be used to dilute the mixture of HF and HNO_3, but this leads to dissociation of nitric acid and significantly reduces the etching speed. The rate-determining reaction of the HNA etching process is the oxidation of silicon. Therefore, increasing the ratio of nitric acid in the HNA solution will increase the reaction rate of the process. However, the surface will be slightly rougher in comparison with the surface etched using a normal HNA solution. Some negatively charged additives such as bromide, iodine or CrO_3^- can be used to reduce the surface roughness. Note also that the HNA isotropic etch is sensitive to the doping concentration of the silicon substrate. The etch process is slowed down in rate about 150 times by regions of light doping (10^{17} cm^{-3} n- or p-type) relative to more heavily doped regions [4, 5]. The overall reaction can be expressed as:

$$6HF + HNO_3 + Si \rightarrow H_2SiF_6 + HNO_2 + H_2O + H_2$$

Anisotropic Etching of Silicon

The most often used etchant for silicon anisotropic etching is KOH. The recipe is often mixed with isopropyl alcohol (IPA) to saturate the solution to increase the etch selectivity for (111) versus (100) planes. Generally, the etch selectivity on the (111) plane can be up to 400 times slower than on the (100) plane while using alkali hydroxide solutions as etchants for silicon anisotropic etching. In addition, the etch rate for KOH anisotropic etching

Bulk Micromachining, Table 2 Basic fabrication characteristics of typical materials in MEMS field

	Comparison of Example Bulk Silicon Etchants						
	HNA (HF + HNO_3 + Acetic Acid)	Alkali-OH	EDP (ethylene diamine pyrochate-chol)	TMAH (tetramethyl-ammonium hydroxide)	XeF_2	SF_6 Plasma	DRIE (Deep Reactive Ion Etch)
Etch Type	wet	wet	wet	wet	dry[1]	dry	dry
Anisotropic	no	yes	yes	yes	no	varies	yes
Availability	common	common	moderate	moderate	limited	common	limited
Si Etch Rate μm/min	1 to 3	1 to 2	0.02 to 1	~ 1	1 to 3	~ 1	~ 1
Si Roughness	low	low	low	variable[2]	high[3]	variable	low
Nitride Etch	low	low	low	1 to 10 nm/min	?	low	low
Oxide Etch	10 to 30 nm/min	1 to 10 nm/min	1 to 80 nm/min	~ 1 nm/min	low	low	low
Al Selective	no	no	no[4]	yes[5]	yes	yes	yes
Au Selective	likely	yes	yes	yes	yes	yes	yes
P^{++} Etch Stop?	no (n slows)	yes	yes	yes	no	no (some dopant effects)	no
Electrochemical Stop?	?	yes	yes	yes	no	no	no
CMOS Compatible?[6]	no	no	yes	yes	yes	yes	yes
Cost[7]	low	low	moderate	moderate	moderate	high	high
Disposal	low	easy	difficult	moderate	N/A	N/A	N/A
Safety	moderate	moderate	low	high	moderate	high	high

[1] Sublimation from solid source.
[2] Varies with wt% TMAH, can be controlled to yield very low roughness.
[3] Addition of Xe to vary stoichiometry in F or Br etch systems can yield optically smooth surfaces.
[4] Some formulations do not attack Al, but are not common.
[5] With added Si, polysilicic acid or pH control.
[6] Defined as 1) allowing wafer to be immersed directly with no special measures and 2) no alkali ions.
[7] Includes cost of equipment.

of silicon is highly dependent on the concentration and the temperature of KOH. A concentration in the range of 40–[%wt]50 and temperature in the range of 70 – 80 °C are typically adopted for the KOH etch process. Note that concentrations below [%wt]20 are not used due to high surface roughness and the formation of potential insoluble precipitates.

The reaction mechanism of the etch process is not fully clear. Several researchers proposed physical models for silicon anisotropic etching from the viewpoints of energy band gap [4, 5] and Gibbs free energy [6]. Over these models, one equation describing the simplified reaction mechanism is addressed as follow:

$$Si + 2OH^- + 2H_2O \rightarrow SiO_2(OH)_2^{2-} + 2H_2$$

Impurity doping can also be applied for slowing down the etch rate for silicon anisotropic etching in alkali hydroxide solutions. The etch rate was drastically slowed down in regions doped with boron to a concentration of $2 \times 10^{19}\,cm^{-3}$ [7]. However, fabricating microstructures of complex and arbitrary geometry is very difficult since the geometry of the microstructure fabricated using anisotropic etching process is limited by the crystal orientation. In order to overcome this drawback, an advanced deep etching technique utilizing high-density plasma and a wafer bonding process were developed. Reactive ions can perform consecutive etching of Si wafers up to a depth of a few hundred micrometers, while maintaining smooth vertical sidewall profiles. The other technology, wafer bonding, permits a Si substrate to be attached to another substrate, typically Si or glass. Three-dimensional complex microstructures can be achieved with this combination [3].

Figure 4a presents photo images of a micro gas sensor array fabricated using wet bulk micromachining, a typi-

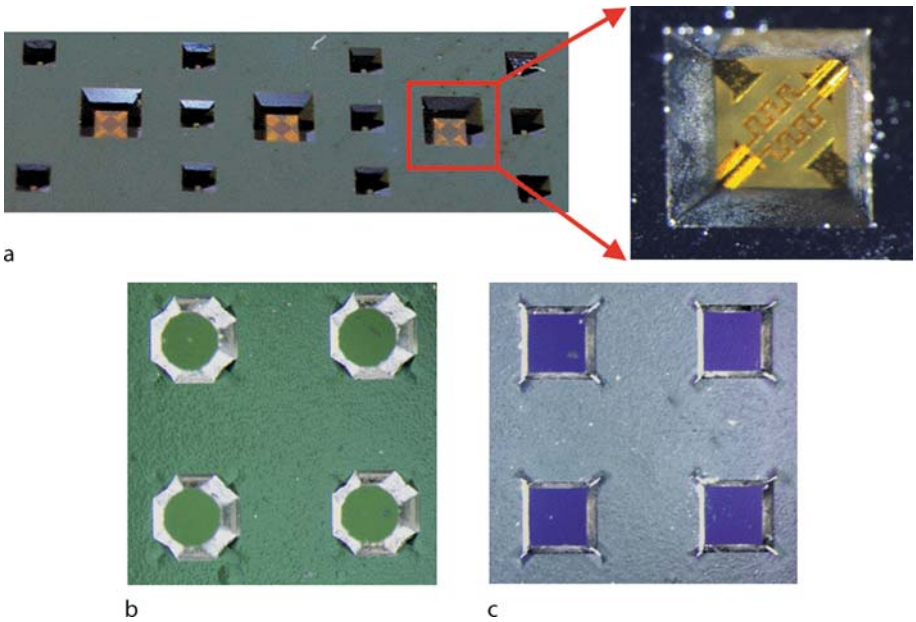

Bulk Micromachining, Figure 4 (**a**) Micro gas sensor array comprising micro-hotplates. (**b**) Etched mesa structures without convex corner compensation mask. (**c**) Etched mesa structures with convex corner compensation mask

cal application of silicon bulk micromachining. A micro gas sensor array comprising micro-hotplates with Pt resistance heaters was fabricated on a suspension silicon nitride film of 2 μm in thickness. The inset shows a close-up picture of a micro gas sensor. A wet bulk micromachining process was used to sculpt the silicon structure under the suspension micro-hotplates in order to eliminate thermal conduction and reduce thermal budget during operation. In addition to the cavity structure, mesa structures with convex corners are usually fabricated using wet bulk micromachining. However, convex corners where (111) planes meet are not stable during silicon anisotropic etching. These convex corners are rapidly undercut along {212} planes and other exposed unstable planes. Figure 4b shows the etched mesa structures with convex corner attacking features. This problem can be easily solved using corner compensation masks which preserve convex corners during the wet etching process. Figure 4c shows the etched mesa structures with the corner compensation design. A sharp convex corner was preserved after the etching process. On the other hand, undercut at convex corners also permits the creation of suspended structures such as cantilever beam and bridge structure. One special case for undercut of silicon substrate in anisotropic etch is mask misalignment. Mask misalignment with respect to the crystal lattice will result in uneven undercutting since the etching will proceed along crystal planes. The effect of misalignment is to enlarge the etched region. In general, if etched long enough, any mask-layer feature will result in a rectangular V-groove pit beneath a rectangular shape that is tangent to the mask features. Furthermore, the edges of the formed rectangular are oriented along ⟨110⟩ directions. A number of commercial and home-built computer simulation software packages have been developed to predict the etched pattern for silicon anisotropic etch [8].

Bulk Micromachining of Glass-Based Materials

Bulk micromachining of glass-based materials is a simple, fast and low-cost way to fabricate planar microfluidic devices. Here we present a fast process for bulk micromachining the glass-based materials especially for ►soda-lime glass. Rather than using a time-consuming vacuum deposition process to fabricate the mask required to etch the plates in an HF-based etchant, a 3 μm thick AZ4620 photoresist layer can be used as the masking material in the wet chemical etching process. An excellent surface quality can be obtained by an improved etching procedure. We also describe a shorter thermal bonding process without sophisticated polishing and cleaning procedures. A high bonding yield is obtained by using sintered alumina flats as the upper and underlying supports. This simple fabrication method will enable fabrication of microfluidic structures in an efficient way. The major contributions of the method is a novel process to remove the formed participant during the wet etching pro-

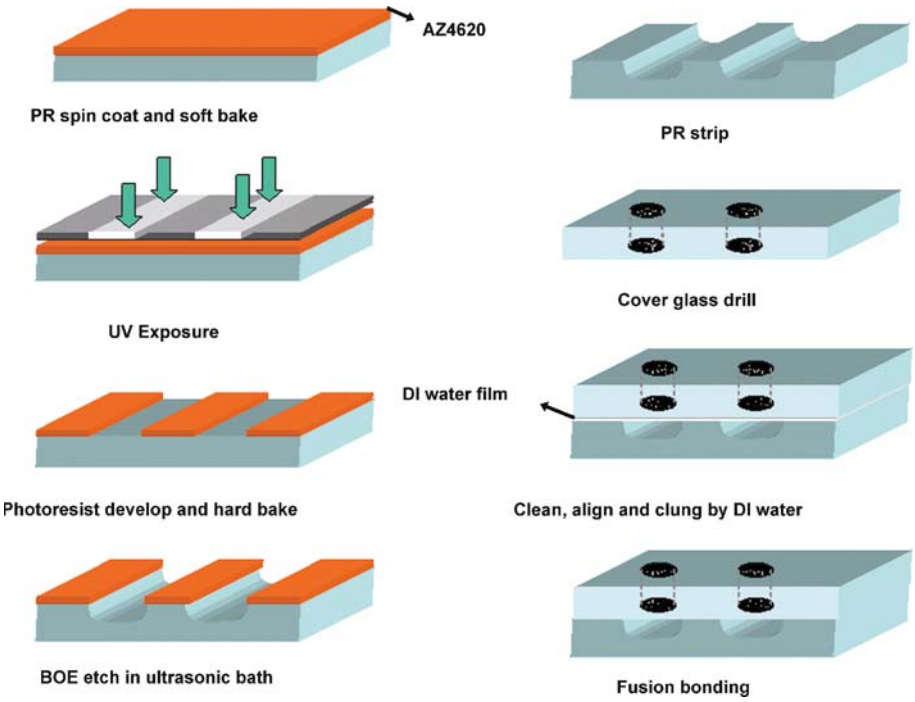

Bulk Micromachining, Figure 5 A simplified overview of the fabrication process which was used to form planar microfluidic channels on glass substrates

cess and a two-step baking process to prolong the survival time of the photoresist etch mask in the etchant. In the following we describe the details of the proposed method.

Soda-lime glass is a multicomponent mixture of SiO_2 (72.8%), Na_2O (13.7%), CaO (8.8%), MgO (4.0%) and small amounts of Fe_2O_3 (0.12%) and Al_2O_3 (0.1%). Insoluble products will be present and crystalline precipitates will be formed while etching soda-lime glass in HF-containing solution [10]. Since K_{sp} (solubility product constant at 25 °C) values of CaF_2 and MgF_2 are 4.0×10^{-11} and 6.4×10^{-9}, respectively, it is believed that most insoluble products are mainly CaF_2 and MgF_2. In order to solve the problem, 1 M HCl solution can be used to turn the precipitates into soluble products of $CaCl_2$ and $MgCl_2$. The equation below describes the chemical reaction for glass-based materials etched using HF-based etchants. The etch rate is about 0.9 μm/min for soda-lime glass etched in buffered HF solution (BOE, buffered oxide etchant) at room temperature and, with undoubtedly, the etching is isotropic inherently:

$$6HF + SiO_2 \rightarrow H_2SiF_6 + 2H_2O$$

In general, polished soda-lime glass or commercial microscope glass slides are preferred for this process. Note that the glass slides need to be annealed at 400 °C for 4 hours to relieve the residual stress inside the slides prior to the fabrication process. Otherwise, needle-like structures may form on the etched surface due to the stress corrosion effect, which may blur the glass and result in a rough surface. The simplified schematic for the fabrication process is shown in Fig. 5. The following describes the details of the fabrication process for wet bulk micromachining of microfluidic device in soda-lime glass [9].

Substrate Cleaning The glass substrates were firstly cleaned in a boiling Piranha solution (H_2SO_4 [%] : H_2O_2 [%] = 3 : 1; *Caution: Piranha solution is a very strong oxidant and is severely exothermic during reaction: it should be handled with extreme care*) for 10 min, then rinsed in DI water and blown-dry with nitrogen gas or CDA (clean dry air). The dehydration process was done by baking the glasses on a hot plate (100 °C) for 3 min to remove residual water molecules.

Lithography The glasses were then spin-coated with HMDS solution and baked on a hot plate (100 °C) for 3 min in order to improve the adhesion of the PR. The primer-treated substrates were coated with AZ 4620 positive PR, and a novel two-step baking process was used in this study. First, a soft-baking process was carried out

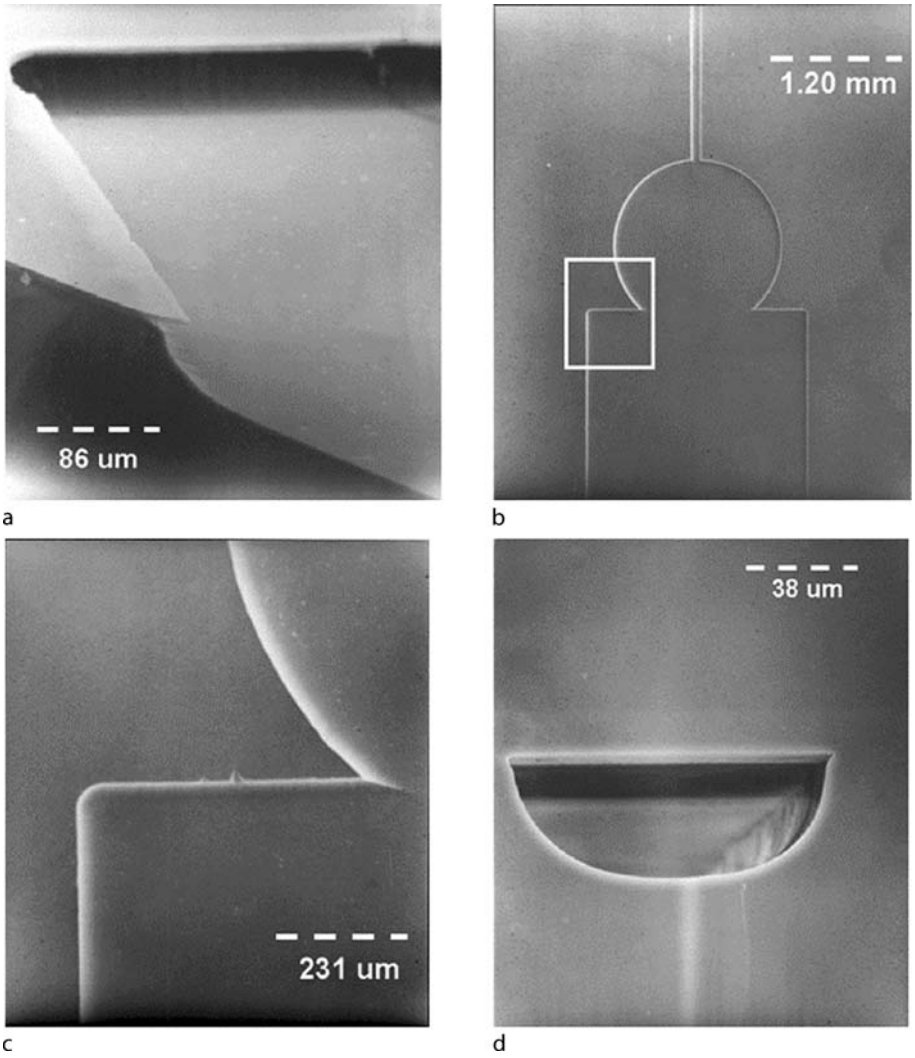

Bulk Micromachining, Figure 6 SEM images of the fabrication results of the proposed method. (**a**) Etched glass surface with PR etch mask. (**b**) After removing the PR mask. (**c**) Close-up view of a sharp corner. (**d**) Cross-sectional view of the sealed microfluidic channel after fusion bonding

at 100 °C for 1 min, 120 °C for 1.5 min, and then maintained at 100 °C for another 1 min. This two-step process can reduce the thermal stress between the glass substrate and the PR, resulting in longer survival time of the positive PR in BOE etchant. The thickness of the PR was approximately 3 μm after soft-baking. The UV lithography was carried out using a mask aligner and exposure dose was 180 mJ/cm^2. The developing of the PR was accomplished in 70 s by immersing the exposed substrate into the developer (one part AZ A400K developer : three parts DI water). After rinsing with DI water and blown-dry by N_2 gas, hard-baking of the PR was carried out at 120 °C for 1 min, 145 °C for 10 min, and then returned to 120 °C for 1 min.

Glass Etching After baking of the PR, the glass substrates were immersed in the BOE (6:1) etchant. The etching was done in an ultrasonic bath. In order to remove precipitated particles, we interrupted the etching process every 5 min and dipped the substrates in a 1 M HCl solution for 10 s during the etching process. After the HCl dipping, the substrates were then cleaned by dipping in DI water and then immersed into BOE etchant again. The etching and de-precipitation processes were iterated until the etching process was finished.

Glass Bonding The etched glass substrate and another cover glass with drilled via-holes were cleaned using boiling Piranha solution for 10 min and then rinsed by DI

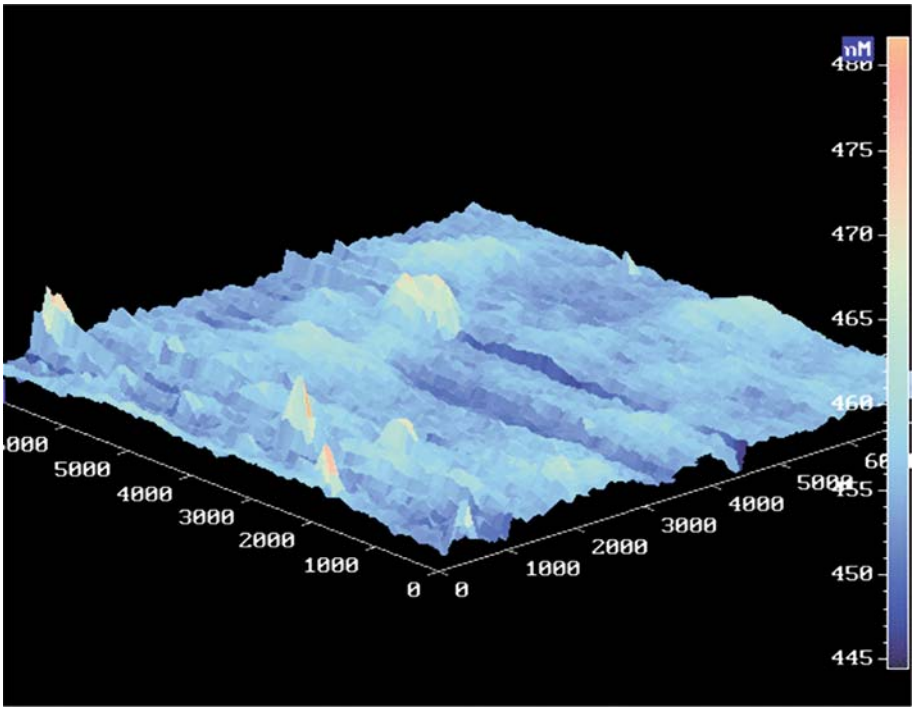

Bulk Micromachining, Figure 7 The surface profile of an etched glass substrate by using an atomic force microscope

water in ultrasonic bath for 3 min. The two glass flats were then carefully aligned and clung to each other by DI water. The atmospheric pressure will hold the two glasses tightly prior to ►thermal fusion bonding process. Bonding was performed by fusing the two glass substrates in a sintering oven at 580 °C for 20 min with a ramp rate of 5 °C/min. Polished alumina flats were stacked as upper and underlying plates which prevented the formation of fusion between glass substrate and alumina flats and kept the glass surface smooth. A sealed microfluidic device could be formed after bonding of the two glass plates.

Figure 6 shows SEM images of the fabrication results of the proposed method. Figure 6a is the etched glass substrate with PR etch mask. The feature of isotropic etching with an undercut structure of the glass substrate can be clearly seen. An etched microfluidic channel and a reservoir structure after removing the PR etch mask are shown in Fig. 6b. An etched microfluidic channel with a sharp geometry and smooth etched surface structures was observed. The close-up image of the inset in Fig. 6b is shown in Fig. 6c. It indicates that the edge of the sidewall is well defined due to good adhesion of PR on the glass substrate. Figure 6d shows a cross-sectional view of the bonded channel. The etched channel remained its original shape and the interface between the two glass substrates disappeared after the fusion bonding process. The bonding process can seal microfluidic channels of up to 3 mm in width without collapsing. It is also found that bonding temperature and holding time are the major factors for the fusion bonding process. Applied pressure and temperature ramping procedure only have minor effects on bonding quality. Temperature below 570 °C caused an incomplete bonding even though two plates were held for a long period of time. While temperature was higher than 580 °C and holding time was longer than 30 min, it resulted in fusion of the glass substrates and the alumina plates, causing cracking of the device due to the difference of the thermal expansion coefficients of the two materials. The bonding process can reduce the operation time, and, more importantly, preserve the original geometry of the etched channel with large area.

The depth and the surface roughness of the etched glass substrates were measured using a surface profilometer (Alpha-step 500). Three different locations on each glass substrate were measured. The average depth of the etched channels is 35.95 μm and the standard deviation is 0.39 μm for all 30 measured values. The etch rate is about 0.9 μm/min at room temperature and the etching is isotropic inherently. The high etch rate and uniformity of the wet etching process was due to the

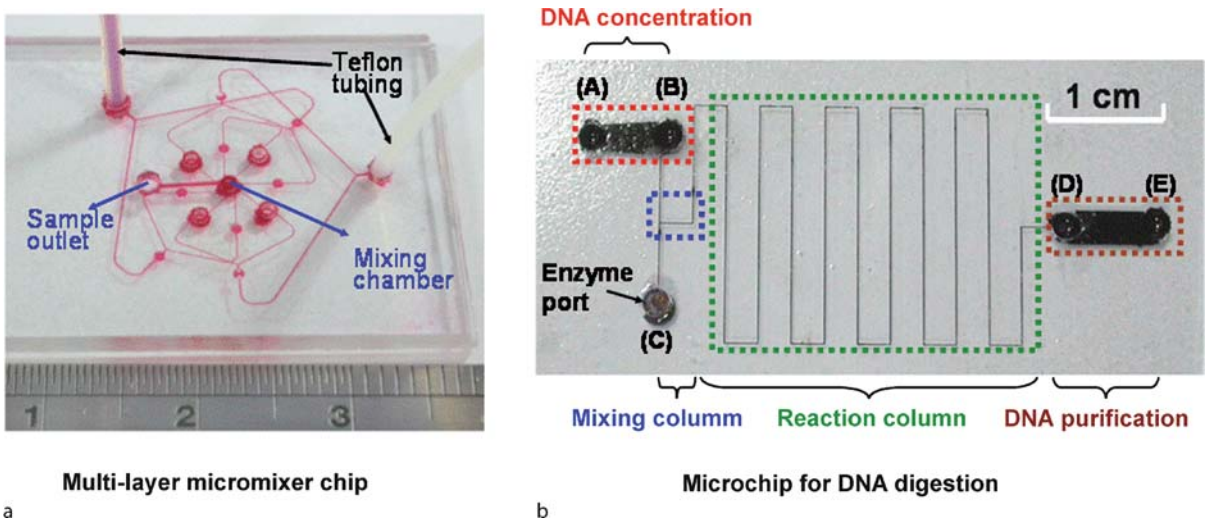

Bulk Micromachining, Figure 8 Optical images of two microfluidic devices fabricated using the proposed fabrication process. (**a**) Microfluidic vortex mixer. (**b**) Microfluidic chip for rapid DNA digestion and purification

fact that appropriate agitation was achieved by performing the etching process in an ultrasonic bath. Furthermore, ultrasonic agitation will make the insoluble precipitate, such as Al_2O_3, suspend in the solution instead of being deposited on the glass substrates. Figure 7 shows the surface profile of an etched glass substrate by using a scanning probe microscope (Solver P7LS). The maximum peak-to-peak roughness is around 0.71 Å and the average surface roughness (R_a) is less than 0.1 Å inside a 3.0 μm × 5.0 μm scanned area. Figure 8 shows the optical images of two microfluidic devices fabricated using the proposed fabrication process. Figure 8a is a microfluidic vortex mixer fabricated in a three-layer glass substrate and Fig. 8b shows a microfluidic chip for rapid DNA digestion and purification. It is observed that the fabricated microfluidic devices have good surface flatness and good optical transmittance which are beneficial for optical detection afterwards. This simple fabrication process is suitable for fast prototyping and mass production of the microfluidic systems in low-cost glass substrates.

Future Directions for Research

The anisotropic wet etching of silicon is a unique fabrication process in the MEMS field. The need to develop new processes to fabricate functional 3D microstructures in various materials is urgent for progress in microfluidic systems, micro-sensors, micro-actuators and micro-instrumentation. At present, to integrate surface micromachined devices and standard IC devices with bulk micromachined structures to demonstrate a new functional MEMS application is still a challenge for researchers who work in this field. The cooperation of multidisciplinary researchers will be required to develop miniature systems with the most appropriate building philosophy and the best operation performance.

Cross References

- ► Anisotropic Etching
- ► Isotropic Etching
- ► Laser Based Micromachining
- ► Micromolding
- ► Silicon Micromachining

References

1. Madou MJ (2002) Chapter 4 Fundamentals of Microfabrication: The Science of Miniaturization. CRC Press LLC, Florida
2. Petersen KE (1982) Silicon as a mechanical material. Proc IEEE 70(5):420–457
3. Kovacs GTA, Maluf NI, Petersen KE (1998) Bulk Micromachining of Silicon. Proc IEEE 86(8):1536–1551
4. Seidel H, Csepregi L, Heuberger A, Baumgartel H (1990) Anisotropic etching of crystalline silicon in alkaline solutions I: Orientation dependence and behavior of passivation layers. J Electrochem Soc 137(11):3612–3626
5. Seidel H, Csepregi L, Heuberger A, Baumgartel H (1990) Anisotropic etching of crystalline silicon in alkaline solutions II: Influence of dopants. J Electrochem Soc 137(11):3626–3632
6. Elwenspoek M (1996) The form of etch rate minima in wet chemical anisotropic etching of silicon. J Micromech Microeng 6:405–409
7. Williams KR, Muller RS (1996) Etch rates for Micromachining Processing. IEEE/ASME J Microelectromech Syst 5(4):256–269

8. Zhu Z, Liu C (2000) Micromachining process simulation using a continous cellular method. IEEE/ASME J Microelectromech Syst 9(2):252–261
9. Lin CH, Lee GB, Lin YH, Chang GL (2001) A Fast Prototyping Process for Fabrication of Microfluidic Systems on Soda-Lime Glass. J Micromech Microeng 11(6):726–732
10. Spierings G, Van D (1987) The dissolution of Na_2O-MgO-CaO-SiO_2 glass in aqueous HF solutions. J Mat Sci 22:1869–1874

Bulk Micromachining of Silicon

► Bulk Micromachining

Buried Channel Waveguides

► On Chip Waveguides